Star Formation Activity of Galaxies and its Relationship to Environment in Distant Universe

by

Kei Ito

Dissertation

submitted to the Department of Astronomical Science

in partial fulfillment of the requirements for the degree of

Doctor of Philosophy

The Graduate University for Advanced Studies, SOKENDAI

January 2022

Acknowledgments

I would like to thank the following people who kindly helped my five years of my Ph.D. course in SOKENDAI. Firstly, I would like to represent my sincere gratitude to my main supervisors, Prof. Nobunari Kashikawa and Assoc Prof. Masayuki Tanaka.

Prof. Kashikawa opened my career as a researcher on the galaxy evolution. When I was a second-year undergraduate student, I experienced the basics of astronomical researches with him in the “Subaru Autumn School 2015". It was the first time to feel what astronomical research is like. I was amazed by hunting distant galaxies, and this is when I wanted to study galaxy evolution through distant galaxies. During these five years, I have learned many things from him. I learned how to start research and what to do when stuck. He read drafts of my papers and proposal and check presentation slides anytime I needed and gave helpful comments. I could not complete my Ph.D. studies without his support.

Assoc Prof. Tanaka has broadened my capabilities. He first invited me to join the observation team for Hyper Suprime-Cam Subaru Strategic Program (HSC-SSP). It was a wonderful experience for me to use the Subaru Telescope constantly. I have learned how to observe with the optical/near-infrared telescopes. After he became my another main supervisor, we started studies on quiescent galaxies. He introduced me to various researchers abroad and expanded my connections during this research. In addition, through the “Galaxy Cruise" project, I learned how to introduce Astronomy to the public.

Assis Prof. Yuichi Matsuda and Assis Prof. Yusei Koyama supported me during the Ph.D. course. They often gave me helpful comments, which improved my research. Moreover, the cluster seminar, which Assis Prof. Yusei Koyama invited me, was a suitable place to study the current status of the environmental effect and galaxy

cluster researches. I also want to thank the core members of the HSC-SSP protocluster team, Jun Toshikawa, Mariko Kubo, and Hisakazu Uchiyama. They provided me with a protocluster catalog and suggestions, which were essential for completing this thesis research. Roderik Overzier helped me brush up on my published papers and invited me to several workshops and conferences in Brazil. The stay in Brazil was one of the most exciting times in these five years. I also discussed regularly with other group members, Shogo Ishikawa, Masafusa Onoue, Yongming Liang, Rikako Ishimoto, Takehiro Yoshioka, Yoshihiro Takeda, and Junya Arita. Many of the ideas in my researches are hit upon during these discussions.

I would like to express my appreciation to other co-authors of my published papers, Ryo Higuchi, Song Huang, Olivier Ilbert, Olivier Kauffmann, Anton. Koekemoer, Yutaka Komiyama, Chien-Hsiu Lee, Yen-Ting Lin, Stefano Marchesi, Murilo Marinello, Crystal L. Martin, Takamitsu Miyaji, Takatoshi Shibuya, Marko Shuntov, Sune Toft, Francesco Valentino, and John Weaver. In particular, the COSMOS2020 team gave me the COSMOS2020 catalog before being released. Thanks to their generosity, we now have the results in Chapter 4.

I appreciate the referee of this thesis, Assoc Prof. Tadafumi Takata, Assoc Prof. Daisuke Iono, Assis Prof. Masato Onodera, Assis. Prof. Hidenobu Yajima, and Prof. Tadayuki Kodama. My colleagues and roommates in NAOJ gave me great advice and cheered me up. Here, I would like to thank them, Takuma Izumi, Jun Hashimoto, Rhythm Shimakawa, Masao Hayashi, Masatoshi Imanishi, Taiki Kawamuro, Yuu Niino, Shunsuke Baba, Tomoko L. Suzuki, Kotomi Taniguchi, Haruka Baba, Tsuguru Ryu, Moegi Yamamoto, Tomonari Michiyama, Takafumi Matsuno, Satoshi Kikuta, Hiroyuki Tako Ishikawa, Ko Hosokawa, Shigeru Namiki, Takafumi Tsukui, Ryohtaroh Ishikawa, Yuta Tanimoto, Ikki Mitsuhashi, Suzuka Nakano, Yui Kasagi, Kanako Sugimori, and Abdurrahman Naufal. Without the Subaru office, I could not go on business trips or purchase goods needed for research. It should be noted that the graduate office of the astronomical course always helped me during these five years.

Finally, I deeply thank my partner and my family, in particular my brother and parents, Kaito, Takeharu, and Keiko Ito. They always understand me and support my life. My career is based on your kindness.

I acknowledge the support from Japan Society for the Promotion of Science in the

Research Fellowship for Young Scientists (DC2) and KAKENHI 20J12461. In addition, a part of this thesis were supported by Overseas Travel Fund for Students (2018, 2019) of the Department of Astronomical Science, the Graduate University for Advanced Studies (SOKENDAI).

The Hyper Suprime-Cam (HSC) collaboration includes the astronomical communities of Japan and Taiwan, and Princeton University. The HSC instrumentation and software were developed by the National Astronomical Observatory of Japan (NAOJ), the Kavli Institute for the Physics and Mathematics of the Universe (Kavli IPMU), the University of Tokyo, the High Energy Accelerator Research Organization (KEK), the Academia Sinica Institute for Astronomy and Astrophysics in Taiwan (ASIAA), and Princeton University. Funding was contributed by the FIRST program from the Japanese Cabinet Office, the Ministry of Education, Culture, Sports, Science and Technology (MEXT), the Japan Society for the Promotion of Science (JSPS), Japan Science and Technology Agency (JST), the Toray Science Foundation, NAOJ, Kavli IPMU, KEK, ASIAA, and Princeton University.

This paper makes use of software developed for the Large Synoptic Survey Telescope. We thank the LSST Project for making their code available as free software at `http://dm.lsst.org`.

This paper is based on data collected at the Subaru Telescope and retrieved from the HSC data archive system, which is operated by Subaru Telescope and Astronomy Data Center (ADC) at NAOJ. Data analysis was in part carried out with the cooperation of Center for Computational Astrophysics (CfCA), NAOJ.

The Pan-STARRS1 Surveys (PS1) and the PS1 public science archive have been made possible through contributions by the Institute for Astronomy, the University of Hawaii, the Pan-STARRS Project Office, the Max Planck Society and its participating institutes, the Max Planck Institute for Astronomy, Heidelberg, and the Max Planck Institute for Extraterrestrial Physics, Garching, The Johns Hopkins University, Durham University, the University of Edinburgh, the Queen's University Belfast, the Harvard-Smithsonian Center for Astrophysics, the Las Cumbres Observatory Global Telescope Network Incorporated, the National Central University of Taiwan, the Space Telescope Science Institute, the National Aeronautics and Space Administration under grant No. NNX08AR22G issued through the Planetary Science Division of the NASA Science Mission Directorate, the National Science Foundation grant No. AST-1238877, the

University of Maryland, Eotvos Lorand University (ELTE), the Los Alamos National Laboratory, and the Gordon and Betty Moore Foundation.

The scientific results reported in Chapter 4 are based on observations made by the Chandra X-ray Observatory. This research has used software provided by the Chandra X-ray Center (CXC) in the PIMMS application package. Data analysis was in part carried out on the Multi-wavelength Data Analysis System operated by the Astronomy Data Center (ADC), National Astronomical Observatory of Japan.

January 6, 2022

K.I.

Abstract

The formation and evolution of galaxies are essential topics in modern astronomy. Galaxy properties are correlated with their living environments, which is called the “environmental effect". In the local universe, galaxies in dense environments, such as clusters, are often in the quiescent phase. To reveal the origin of the environmental effect, it is essential to explore its initial condition in the distant universe. Protoclusters are one of the ideal laboratories at that point, but due to the small sample size, their properties are totally in mystery at $z > 3$. Moreover, recent studies suggest that the different galaxy populations probe the different spatial distribution in protoclusters, although it is not yet clear how this impacts the environment related studies and whether it is the same in the general field. Moreover, recent observations with deep surveys and sensitive near-infrared spectrograph have revealed the existence of galaxies with suppressed star formation even at $\sim 1-2$ Gyr after the big bang (redshift of $z \sim 4-6$). However, it is not yet explored whether the quenching mechanism of these high redshift galaxies is related to the environment or other mechanisms, such as active galactic nuclei (AGNs).

In this thesis, we report exploring the star formation activity of galaxies mainly at high redshift and its connection to their living environment. Based on the wide-field survey of the Hyper Suprime-Cam Subaru Strategic Program (HSC-SSP) and the Cosmic Evolution Survey (COSMOS), we conduct three studies with the statistical approaches.

Firstly, we derive the rest-frame UV luminosity function of galaxies in protoclusters (PC UVLF) at $z \sim 4$. This protocluster sample is selected from the overdensity map of Lyman break galaxies at $z \sim 4$ from the HSC-SSP, and the largest sample at this redshift. After the statistical correction for the incompleteness and contamination for

protocluster galaxies, we successfully determine the PC UVLF for the first time. From this function, we find that protocluster galaxies tend to be brighter in the rest-frame UV than field galaxies. It is not likely due to AGNs, suggesting that protocluster galaxies are more active in star formation. The PC UVLF also suggests that protoclusters at $z \sim 4$ contribute to the $\simeq 6 - 20\%$ of the total star formation occurring in the universe. These suggest that the environment has already affected the galaxy evolution at $z \sim 4$, and protocluster galaxies may evolve earlier than field galaxies.

Secondly, we evaluate the general spatial distribution difference among different galaxy populations at $2 < z < 4.5$ in the COSMOS field. We construct a massive star-forming and quiescent galaxy (SFG and QG) sample from the photometric redshift, and Lyα emitter (LAE) sample of the Slicing COSMOS with 4K Lyα emitters (SC4K) survey is used. We conduct two analyses: clustering and overdensity measurement. The cross-correlation signal of SFGs and QGs is as expected from their autocorrelation signal. However, the cross-correlation signal of SFGs and LAEs is significantly lower than their autocorrelation signal. This low signal suggests that some physics segregate LAEs in addition to the halo mass difference. The overdensity distribution measured by SFGs as a tracer supports this trend, showing that LAEs are in less dense regions than SFGs and QGs. These results reinforce the importance of exploring multiple galaxy populations in quantifying the intrinsic galaxy environment of the distant universe. In addition, we discuss the connection between SFR and the living environment from the derived overdensity. However, we do not find any correlation. Based on the clustering analysis and the overdensity, this work suggests that the environmental quenching is insignificant at $z > 2$.

Lastly, we explore the connection between galaxy quenching and AGNs at $0 < z < 5$, which is another plausible mechanism for quenching. We conduct the X-ray and radio image stacking for X-ray undetected QGs selected from the latest COSMOS2020 catalog. We successfully detect signals of X-ray and radio for up to $z \sim 5$ for the first time. The X-ray and radio luminosity cannot be explained by the only X-ray binaries and star formation-related emissions, respectively, suggesting that QGs ubiquitously possess low-luminosity AGNs. Moreover, QGs have higher AGN luminosity than SFGs at $z > 1.5$. We conclude that this trend indicates that AGNs have an essential role in galaxy quenching, possibly through “radio-mode” feedback. This enhanced AGN luminosity of QGs is not seen at $z < 1.5$, which might reflect that other mechanisms,

such as environmental quenching, are dominant for quenching.

This thesis observationally suggests that the overdense environments at the high redshift ($z > 2$) have a role in enhancing the star formation, not in quenching, and it already starts as early as $z \sim 4$. Quenching at high redshift is likely to be caused by AGNs. On the other hand, it also suggests the importance of mapping the multiple galaxy populations to examine the real environment.

Contents

List of Figures

List of Tables

1 Introduction

1.1 Galaxies throughout the cosmic time

Galaxies are gravitationally-bounded structures of stars, gases, dust, and dark matter. The first recognition that they are extra-galactic objects is not as soon as the 1920s when Edwin Hubble identified a relation between distance and velocity from Cepheid variables (Hubble, 1929). Galaxies are essential components of this universe, and understanding how they form and evolve is one of the most important topics in modern astronomy.

Through extensive studies with the modern telescopes, we are now close to understanding some aspects of galaxy evolution throughout cosmic time. One of the essential properties of galaxies is star formation rate (SFR), which is the number of stars produced in a year. SFR is measured by the various light of galaxies, such as the UV continuum emission, line emission, FIR emission, and radio emission (see Kennicutt, 1998, for the review). The late-type galaxies have a relatively high SFR, but the early-type galaxies have only a little or no SFR. This difference implies that

galaxies are not unalterable, but they have a lifetime of twists and turns throughout cosmic time. This means that they have some period of active star formation, and then their star formation gets suppressed, i.e., “quenched".

The evolution of the cosmic star formation rate density (CSFRD) shows the average picture of star formation history in the universe. The CSFRD is determined from the number density of galaxies and their luminosity in the ultraviolet (UV) and infrared (IR) wavelength. The rest-frame UV light is generally emitted from short-lived massive stars and thus a good tracer of SFR (Kennicutt, 1998). The UV radiation absorbed by the dust is reradiated in the rest-frame FIR. Therefore, the luminosity function, the number density of galaxies as a function of the luminosity, is an important tool for unraveling CSFRD. In particular, the rest-frame UV luminosity function (UVLF) is often used for high redshift galaxies since the rest-frame UV light is shifted to the optical in the observed frame, which is relatively easy to observe (e.g., Yoshida et al., 2006; Reddy & Steidel, 2009; Cucciati et al., 2012; Bouwens et al., 2012a,b, 2015; Harikane et al., 2021). The FIR luminosity function is also now measured (e.g., Magnelli et al., 2011, 2013; Zavala et al., 2021). By summarizing the results of various studies, the CSFRD $\Psi(z)$ is known to follow the functional form as $\Psi(z) = 0.015\frac{(1+z)^{2.7}}{1+[(1+z)/2.9]^{5.9}}\ \mathrm{M_\odot yr^{-1}Mpc^{-3}}$ at $z < 8$ (see Madau & Dickinson, 2014, for the comprehensive review), which is shown in Figure 1.1. According to this function, about 10 Gyrs ago (i.e., $z \sim 2$) was the peak of star formation in the universe, referred to as “cosmic noon" and the CSFRD gradually slows down toward the local universe. This implies that galaxy evolution has different phases depending on the epoch of the universe, and thus it is important to understand it across cosmic history.

In addition, the extensive wide-field surveys, such as Sloan Digital Sky Survey (SDSS, e.g., York et al., 2000), show the nearby large-scale structure of the universe from the $\sim 10^6$ galaxies and $\sim 10^5$ quasars. From their spectroscopic redshifts, the clear network-like structure is revealed. The densest structures of matter are called galaxy clusters, and they are connected to each other by filaments. On the contrary, there are sparse regions with almost no galaxies called voids. According to simulations (e.g., Springel et al., 2005), such a large-scale structure is expected to form from the early epoch of the universe gradually. Galaxies live in various “environments."

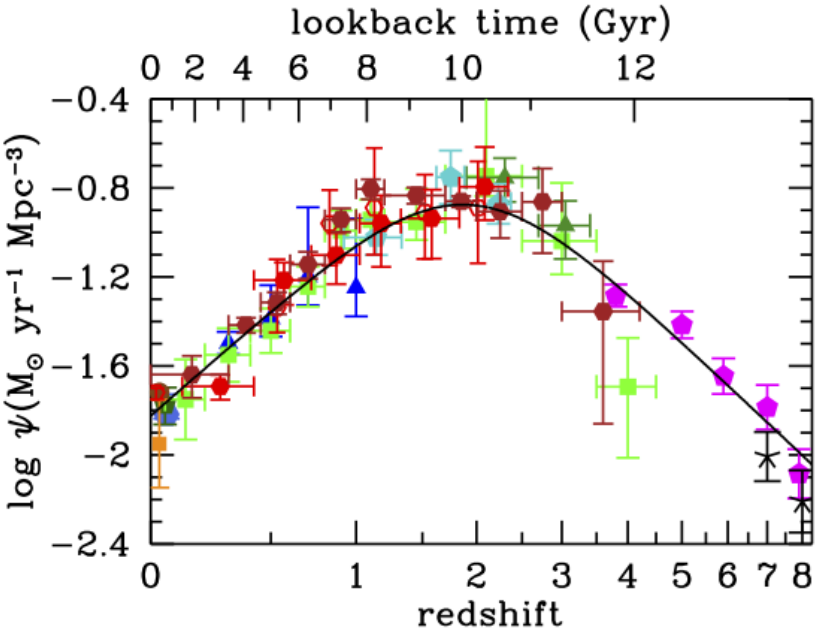

Figure 1.1: Evolution of the cosmic star formation rate density taken from Madau & Dickinson (2014). The detailed information of data points is summarized in their Table 1. The solid line is the best-fit $\Psi(z)$.

1.2 Environmental effects on galaxy evolution

Properties of galaxies are indeed correlated to their environments, often referred to as “environmental effect". Back in the 1980s', Dressler (1980) find that galaxies in local clusters are more likely to be early-type galaxies than galaxies in the general field. After that, a number of studies shows such an environmental effect. For example, Dressler's finding is supported by a larger sample (e.g., Bamford et al., 2009). In addition, Peng et al. (2010b) show that galaxies tend to be redder in more overdense regions, which is often called “environmental quenching” and its efficiency is independent of the stellar mass. The existence of the environmental quenching is also supported by the large sample from the large survey, such as SDSS and 2dF galaxy redshift survey, which shows that the quiescent fraction monotonically increases for denser regions (e.g., Balogh et al., 2004) or towards the cluster center (e.g., Wetzel et al., 2012). Not only quenching but also other properties are affected by their living environment. For example, Thomas et al. (2005) show galaxies in overdense regions are older than field galaxies based on their spectra. All above studies implies that the environment should play an essential role in the galaxy evolution.

At almost the same time of Dressler (1980), Butcher & Oemler, A. (1978) show the fraction of blue galaxies increases in higher redshift clusters, suggesting that the environmental effects also differ along with the redshift. Exploring the high redshift galaxies and their connection to their living environment is thus important to reveal when and how the environment starts to affect galaxy properties.

It is argued that the effect from the living environment has two sides, i.e., “nature" and “nurture" (De Lucia, 2006). Firstly, halos in high-density regions generally form earlier than others, leading to the possible earlier formation of galaxies. This means that galaxies in rich environments are expected to have different evolution tracks from their birth, referred to as the “nature" effect. On the other hand, some physical phenomena can be induced by a unique environment of overdense regions. For example, due to the high number of galaxies, merger, which is an important process to induce the starburst/AGN activity (e.g., Hopkins et al., 2008), can be more frequently occurred in overdense regions. Also, the ram-pressure stripping and tidal stripping, which are introduced as one of the favored processes inducing the environmental quenching (e.g., Gunn & Gott, J. Richard, 1972), are one of these processes. Galaxies can be greatly

affected by them while they are in overdense regions leading to different properties from field galaxies, which is referred to as the “nurture" effect. These two sides can have different redshift evolution. The “nature" effect may occur in the early epoch of the universe, whereas “nurture" effect may occur later since the above phenomena are closely related to the halo evolution. However, we do not know which has a more effective impact on galactic evolution at different redshift and different aspects. In order to distinguish between the two, we need to explore the distant universe.

1.3 Exploration of high redshift galaxies

In the last few decades, galaxies at $z \geq 2$ have been vigorously explored. There have been various prompts to select high redshift (high-z) galaxies. One of the famous ones is based on multi-band colors. Lyman break method is one of them and detects Lyman break at the rest-frame 1216Å (e.g., Steidel et al., 1996; Yoshida et al., 2006; Hildebrandt et al., 2009; van der Burg et al., 2010; Bouwens et al., 2009; Ono et al., 2018). Lights from high-z galaxies pass through the intergalactic gas clouds located toward the line of sight at various redshifts. Since their hydrogen absorbs Lyα emission, the spectrum of high-z galaxies has a lot of absorption line below $\lambda = 1216 \times (1 + z)$ Å, where z is the redshift of that galaxy. In the Lyman break method, we can select high-z galaxies by choosing objects with a red color between the two broad bands across the observed Lyα wavelength. These selected galaxies are often called Lyman break galaxies (LBGs). They should have bright UV-continuum, generally star-forming galaxies (SFGs).

Also, by using colors of narrow (or intermediate) band and broad band, line-emitting galaxies, such as Lyα emitters (LAEs) (e.g, Shimasaku et al., 2006; Sobral et al., 2018), O[III] emitters (e.g., Suzuki et al., 2015), and Hα emitters (HAEs, e.g., Geach et al., 2008; Sobral et al., 2013; Kodama et al., 2012) have been selected. These line-emitting galaxies can be selected with smaller redshift uncertainty than LBGs, and they are also SFGs. Especially, LAEs are known to have lower stellar masses ($\log (M_\star/M_\odot) \sim 9$) (e.g., Santos et al., 2020), younger stellar populations (e.g., Gawiser et al., 2007; Hagen et al., 2014), and less dust obscuration (e.g., Kusakabe et al., 2015; Gawiser et al., 2006) than other galaxies. In terms of their host dark matter halos, LAEs tend to reside in less massive halos than other SFGs (e.g., Khostovan et al., 2019; Kusakabe et al., 2018; Ouchi et al., 2018).

Other studies have selected high-z galaxies based on the photometric redshift (photo-z) by using all photometry based on the spectral energy distribution (SED) fitting (e.g., Scoville et al., 2007; Laigle et al., 2016). This method enables us to select not only SFGs but also galaxies with the suppressed star formation (i.e., quiescent galaxies, QGs). (e.g., Ilbert et al., 2009; Laigle et al., 2016; Mortlock et al., 2015; Davidzon et al., 2017; Mawatari et al., 2020). There are two well-known methods of selecting QGs. One is based on their colors such as by the rest-frame UVJ or $NUVrJ$ colors (e.g., Wuyts et al., 2007; Muzzin et al., 2013; Straatman et al., 2014). This method is suitable for selecting QGs from the limited information. However, it may miss recently quenched galaxies with short star-formation time scales, which are more likely to exist in the high redshift (e.g., Merlin et al., 2018). Indeed, some spectroscopically confirmed QGs at $z \sim 3-4$ are not satisfied with these color selections, even though their star formation rate is suppressed (Schreiber et al., 2018; Valentino et al., 2020). Therefore, an extended color selection is also proposed to select recently quenched post-starburst like galaxies (Belli et al., 2019). The other method is based on the specific SFR (sSFR). This method can directly define QGs based on their star formation activities. Based on these methods, QGs have been selected photometrically up to $z \sim 6$ (e.g., Ilbert et al., 2013; Davidzon et al., 2017; Merlin et al., 2019), and recent near-infrared spectroscopy observations confirm their existence up to $z \sim 4$ (e.g., Kriek et al., 2009; Glazebrook et al., 2017; Schreiber et al., 2018; Tanaka et al., 2019; Belli et al., 2019; Forrest et al., 2020; Valentino et al., 2020; D'Eugenio et al., 2021). Their star formation history inferred from the SED modeling implies their intense star formation followed by quenching in a short time scale, in agreement with star formation histories of massive elliptical galaxies in the local universe. On the other hand, their quenching mechanism is still in mystery. Especially, we do not know whether such rapid quenching is induced by the environment-related process, similar to most elliptical galaxies in local clusters, or related to other galaxy-scale processes.

The last high-z galaxy population that should be noted is dusty star-forming galaxies, which are often missed by optical/NIR observations. They are often selected by the strong sub-millimeter emission (submillimeter galaxies, SMGs, e.g., Smail et al., 1997; Yun et al., 2012). Since their SFR is often higher than that of the main sequence galaxies, their strong emission is powered by gas-rich mergers or gas accretion from the cosmic web (e.g., Tacconi et al., 2008; Umehata et al., 2019). Since their high SFR

and short gas depletion time scale, they are possible candidates of the progenitor of compact QGs (e.g., Toft et al., 2014).

1.4 Current status of protocluster studies

Even at higher redshifts ($z \geq 2$), we now have some overdense regions called protoclusters, which are defined as structures that will collapse into virialized objects with $M_{\rm halo} \geq 10^{14} {\rm M}_{\odot}$ at $z \sim 0$ (see Overzier, 2016, for a comprehensive review). These high-z structures are valuable laboratories to explore the primitive feature of the environmental effect in the distant universe. The first protocluster is serendipitously found by a spectroscopic follow-up observation of $z \sim 3$ LBGs, which is called "SSA22" protocluster at $z = 3.09$ (Steidel et al., 1998). After the discovery of this protocluster, a number of protoclusters have been found. The overdensity (significance), which is defined as the excess of the number density of galaxies normalized by the average number density (its standard deviation), is often used to trace the massive structures. Photo-z galaxies (e.g., Chiang et al., 2014), LBGs (e.g., Miley et al., 2004; Overzier et al., 2008; Utsumi et al., 2010; Toshikawa et al., 2016), LAEs (e.g., Le Fèvre et al., 1996; Venemans et al., 2002; Shimasaku et al., 2003; Ouchi et al., 2005; Venemans et al., 2007; Toshikawa et al., 2012; Jiang et al., 2018; Higuchi et al., 2019; Harikane et al., 2019), SMGs (e.g., Miller et al., 2018; Oteo et al., 2018; Mitsuhashi et al., 2021; Koyama et al., 2021), and HAEs (e.g., Hatch et al., 2011b; Hayashi et al., 2012; Shimakawa et al., 2018; Darvish et al., 2020) are used to draw the density map. Also, several studies have used the information of intergalactic medium (IGM) as tracers, such as from Lyα tomography (e.g., Lee et al., 2014, 2016) or with strong coherent Lyα absorption along the line of sight, so-called "CoSLAs" (e.g., Cai et al., 2016; Liang et al., 2021; Shi et al., 2021).

The number density of protoclusters is extremely small, so it is not easy to find. Several studies target regions around radio galaxies based on the hypothesis that they are massive and thus located in massive halos (e.g., Le Fèvre et al., 1996; Miley et al., 2004; Venemans et al., 2007; Hatch et al., 2011b,a; Hayashi et al., 2012; Wylezalek et al., 2013; Cooke et al., 2014). Systematic wide-area surveys have recently found protoclusters without relying on such peculiar targets. (e.g., Steidel et al., 1998; Shimasaku et al., 2003; Ouchi et al., 2005; Toshikawa et al., 2012, 2016; Jiang et al., 2018;

Higuchi et al., 2019; Harikane et al., 2019).

Many protocluster studies are focused on single galaxy populations, but several studies have conducted follow-up observations to map various galaxy populations. For example, SSA22, which is one of the most explored protoclusters, are known to be an overdense region not only from LBGs (Steidel et al., 1998), but also from LAEs (Steidel et al., 2000; Hayashino et al., 2004), K-band selected galaxies (Kubo et al., 2013), and SMGs (Umehata et al., 2018). Kubo et al. (2021) confirmed a massive quiescent galaxy in this structure. Also, other studies, such as Shi et al. (2020) and Yonekura et al. (2021), discuss distribution of massive galaxies population in other protoclusters at $z \sim 2-3$. On the other hand, some studies have reported that LAEs and massive SFGs trace different large-scale structures (e.g., Shimakawa et al., 2017; Shi et al., 2019a, 2020). These studies argue that such segregation of LAEs and massive galaxies can be related to the assembly time difference of host dark matter halo (e.g., Shi et al., 2019a) or baryonic physics, such as the relation of surrounding HI gas and Lyα emission (e.g., Shimakawa et al., 2017). These observational results might suggest that it is important to comprehensively understand the interrelationship of the distributions of multiple galaxy populations. Before concluding any remarks, we should examine whether this occurs only in peculiar protoclusters or this is seen in the general field.

Theoretical studies also have provided valuable insights for understanding protoclusters. A large computation volume is needed to capture the general properties of protoclusters, which are quite rare. Therefore, N-body simulations with semi-analytic models have been often used. For example, Chiang et al. (2013) use Millennium Run dark-matter N-body simulation (Springel et al., 2005) and the semi-analytic models. They discuss the effective radius of protoclusters as a function of the dark matter halo mass and show the correlation between the galaxy overdensity and the expected halo mass at $z = 0$ (referred to as descendant halo mass), which are useful to characterize observed overdense structures. Recently, Chiang et al. (2017) discuss the contribution of protoclusters to the cosmic star formation history. They show that protoclusters contributed to 20 (50) % of the cosmic star formation rate density at $z = 2$ (10). Based on the protocluster structure and their star formation activity, they argue that there are three evolutionary phases of (proto)clusters (Figure 1.2): (1) inside-out growth at $z \sim 5-10$, (2) extend star formation at $z \sim 1.5-5$, (3) galaxy infalling and quenching at z<1.5. Phase 3 is already seen in observational studies, which show the enhanced

quiescent fraction in cluster regions (c.f., Section 1.2). In this scheme, we expect that the star formation in protoclusters is more active than in the general field at $z > 1.5$, which shows the necessity of its observational examination at a higher redshift. In addition, several studies predict the connection between protocluster environment and galaxy properties, such as the fraction of active galactic nuclei (AGNs) or stellar mass function (Muldrew et al., 2015; Lovell et al., 2018).

Recent sophisticated hydrodynamic simulation has also studied the detailed properties of protocluster galaxies (e.g., Lovell et al., 2020; Yajima et al., 2021; Trebitsch et al., 2021). In particular, Yajima et al. (2021) have shown that protoclusters at $z > 2$ generally contain active star formation, and some massive galaxies are so highly dust-obscured that they can be detected as SMGs, which are in line with the known concentrated structure of SMGs (e.g., Oteo et al., 2018; Miller et al., 2018; Koyama et al., 2021). They argue that the halo growth in protoclusters is much faster than in the mean-density field, and therefore more massive galaxies are being formed inside protoclusters.

On the other hand, several obstacles prevent us from characterizing protoclusters observationally. Firstly, the number of protoclusters at $z > 3$ is too small to observationally discuss the general properties of protoclusters and galaxies therein (Figure 1.3). At $2 < z < 3$, reasonably many protoclusters have been found so far, but if we focus only $z > 3$, there are only less than 20 protoclusters. Moreover, protoclusters are found through different galaxy tracers and target field selection, as mentioned above. This makes the direct comparison among known protoclusters difficult. In this situation, exploring protocluster and protocluster galaxy properties at $z > 3$ is only limited to case studies. The systematically selected and large protocluster sample has been long waited to overcome these obstacles.

1.5 Primordial environmental effect in the distant universe

To understand the onset of the effect from the environment to galaxy properties, statistical studies have explored the galaxy properties as a function of overdensity in the distant universe. One of the most notable topics is the primordial environmental

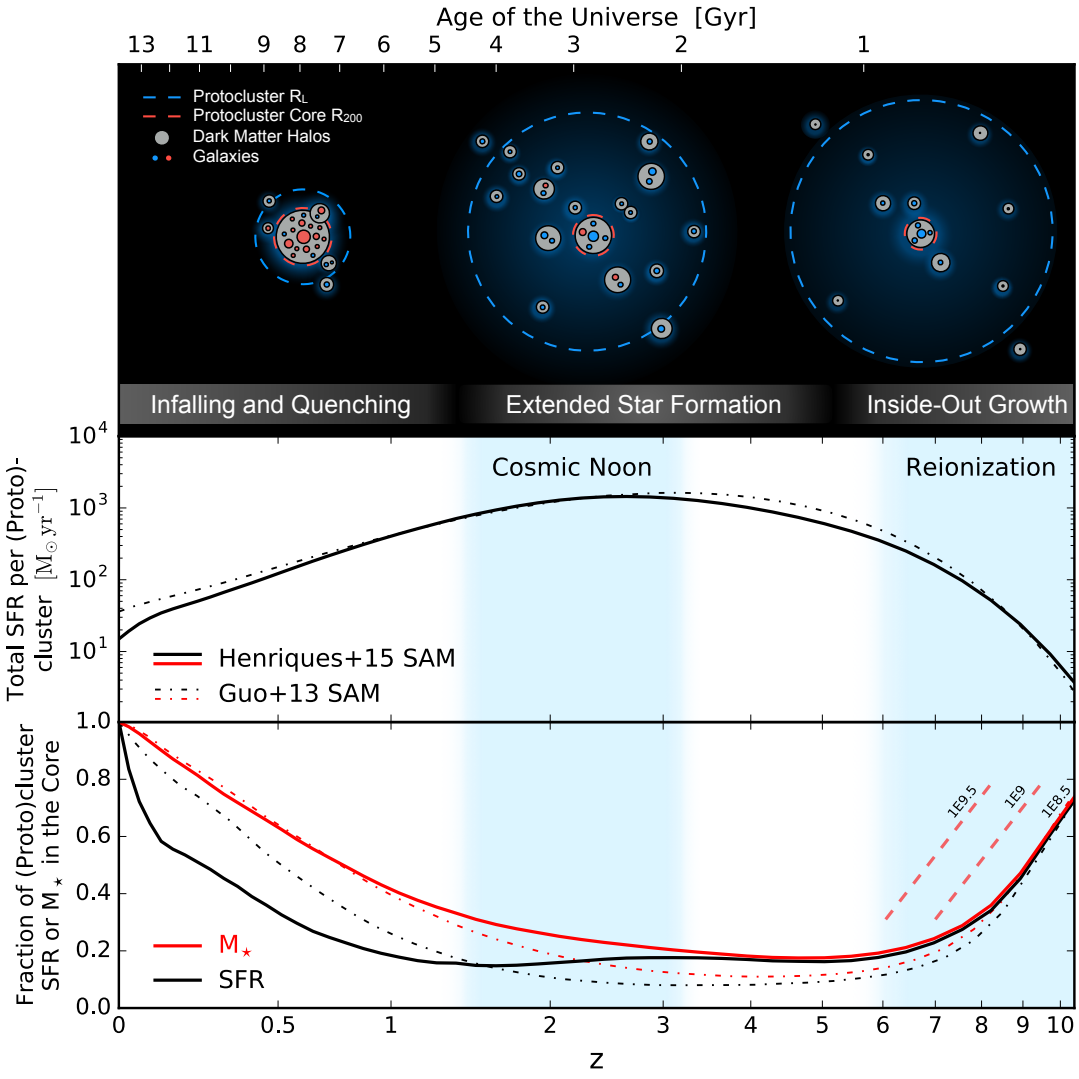

Figure 1.2: **Top panel**: The schematic view of protoclusters evolution suggested in Chiang et al. (2017). **Middle panel**: The evolution of the star formation rate in protoclusters. **Bottom panel**: Fraction of SFR or stellar mass inside protocluster core.

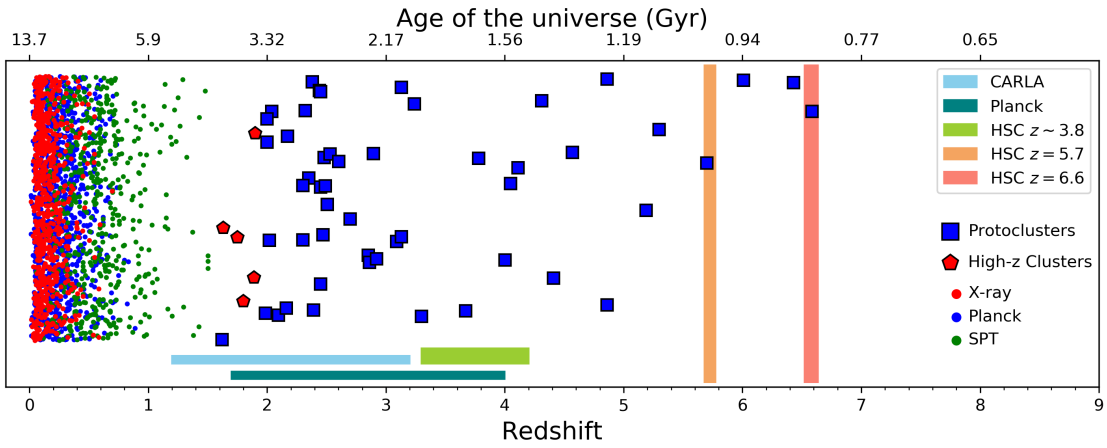

Figure 1.3: Redshift distribution of known (proto)clusters summarized in Overzier & Kashikawa (2019). Red, blue, and green circles are clusters selected by the X-ray, Plank, and South Pole Telescope (SPT) observation summarized in Bleem et al. (2015).

quenching. A higher quiescent fraction of galaxies in overdense regions than that of field galaxies proves the existence of the environmental quenching at $1 < z < 2$ (e.g., Lin et al., 2016; Kawinwanichakij et al., 2017; Nantais et al., 2017; van der Burg et al., 2020; Strazzullo et al., 2019; Reeves et al., 2021). At $z > 2$, the insignificant dependence on the overdensity to the quiescent fraction is reported (e.g., Lin et al., 2016). On the contrary, the positive correlation between the local density and SFR (i.e., higher SFR in more overdense regions) is also reported in Lemaux et al. (2020), which is the opposite trend expected from the environmental quenching. However, other studies report the negative correlation Chartab et al. (2020), and we do not know whether quenching is accelerated in the rich environment at $z > 2$.

Properties of protocluster galaxies are also energetically explored. At $z \sim 2-3$, protocluster galaxies tend to have higher SFR. For example, Shimakawa et al. (2018) estimate SFR of HAEs in a protocluster at $z = 2.5$ and find that HAEs in the densest regions tend to have a higher SFR than those in the outskirts. Koyama et al. (2013) report a similar trend from HAEs in protoclusters at $z \sim 2$. This contrasts with the local color picture, and the overdense regions somehow enhance the star formation compared to the general field. Also, they tend to have larger stellar mass (above references and Cooke et al., 2014; Hatch et al., 2011b; Steidel et al., 2005) than field galaxies, which is in good agreement with the some of above studies. Their specific

star formation rate (sSFR) does not differ depending on the environment (e.g., Koyama et al., 2013; Long et al., 2020), so these suggest that the galaxy formation is earlier in protoclusters, as supported by several theoretical studies (Chiang et al., 2017; Lovell et al., 2018; Muldrew et al., 2015). On the other hand, again, we do not know whether this trend has already emerged at $z > 3$ due to the limitation mentioned in Section 1.4. Its exploration towards a higher redshift will examine whether such environmental dependence of galaxy properties is due to early formation or other physics that emerge at $z \sim 2-3$ for the first time. Therefore, a systematic investigation of galaxy properties in protoclusters at $z > 3$ is crucial for understanding the effects of the environment on galaxy evolution.

1.6 Objectives

To summarize the above descriptions, the environment has been known as one of the most important factors to characterize the galaxy evolution. Especially, many studies have discussed the role of the environment in star formation activity and its quenching. Exploring the environmental dependence in the high redshift universe is essential. However, due to the small size of the protocluster samples and the galaxy sample, we do not know the complete picture at $z \geq 3$. Moreover, some studies report different spatial distributions for different galaxy populations, especially in high-density regions. It is necessary to examine how this relates to the environment and whether it is the same in general.

The main objective of this thesis is to explore the connection between the galaxy evolution and the environment in the distant universe. In particular, I focus on the star formation activity, including SFR and galaxy quenching. There are four topics which I attack, based on the current situation of this field.

- When do galaxies begin to be affected by their environment, especially on their star formation rate? (Chapter 2)
- Does all galaxy populations generally trace the same spatial distribution in any region? (Chapter 3)
- Does the environmental quenching exist even at cosmic noon ($z \sim 2-3$)?

- If not, what quenches the star formation around the cosmic noon? (Chapter 4)

To answer these questions, I conduct three studies. The first question is to be approached by the rest-frame UV luminosity function of protocluster galaxies at $z \sim 4$ in the Hyper Suprime-Cam Subaru Strategic Program (HSC-SSP), which shed light on the SFR distribution difference between protoclusters and field. The sample from HSC-SSP is the largest one for protoclusters at $z \sim 4$, which provides the average properties of protoclusters and galaxies therein for the first time. The second and third questions will be answered by plenty of photometry and archival catalog in the Cosmic Evolution Survey (COSMOS, Scoville et al., 2007) and conducting the clustering analysis and overdensity analysis. For the fourth question, I explore the signature of active galactic nuclei (AGNs) contribution to the quenching with deep X-ray and radio imaging in the COSMOS field. This study was not conducted for $z > 3$ due to the small number of QGs and lack of deep X-ray and radio observations.

Plentiful datasets and the statistical approach used in this study, i.e., HSC-SSP and COSMOS, will give us new observational insights. Moreover, using these two different catalogs is complementary. The HSC-SSP has deeper and larger images than any other surveys, while COSMOS has plenty of multi-photometry data in the wide wavelength range. The former provides the average properties from the largest protocluster sample, and the latter gives us a more detailed and precise view. The combination of three studies will discuss the big picture of how the star formation activity of galaxies is correlated to the environment at distant universe. These three studies are published as Ito et al. (2019, 2020, 2021), or submitted to the Astrophysical Journal.

1.7 Structure of this thesis

This thesis consisted of 6 chapters. In Chapter 2, we explore the environmental dependence of star formation rate from the largest protocluster sample at $z \sim 4$ by deriving the rest-frame UV luminosity function. In addition to the luminosity function, detailed analyses, such as the size estimation and SED fitting analysis, are conducted. Chapter 3 discusses the difference of the spatial distribution among multiple galaxy populations at high redshift ($2 < z < 4.5$). Also, we examine whether quenching is affected by the environment at such a high redshift. In Chapter 4, we discuss another

possible mechanism to quench galaxies, i.e., AGNs, by conducting the stacking analysis of the X-ray and radio images for typical QGs in the COSMOS field. By comparing the X-ray/radio properties of QGs with those of SFGs, we examine the contribution of AGN feedback to quenching. In Chapter 5, we discuss the implications of these three studies and introduce the future prospects. Lastly, we summarize this thesis in Chapter 6.

In this thesis, we assume that cosmological parameters are $H_0 = 70$ km s^{-1} Mpc^{-1}, $\Omega_{\rm m} = 0.3$, and $\Omega_\Lambda = 0.7$. All magnitude shown in the thesis is AB magnitude (Oke & Gunn, 1983). we also use cMpc and pMpc to refer to comoving and physical scales, respectively.

2

Rest-frame UV Luminosity Function of Protocluster Galaxies at $z \sim 4$

- Based on Ito et al. (2019, 2020)

2.1 Background of Chapter 2

The effect of the living environment at high redshift is an essential topic for understanding galaxy evolution, especially related to star formation activity. On the other hand, the SFR in protoclusters at $z \geq 3$ has not yet been comprehensively assessed. As mentioned in Section 1.1, the UVLF of field galaxies is one of the most valuable informations for understanding the cosmic star formation rate density (e.g., Bouwens et al., 2015; Cucciati et al., 2012; van der Burg et al., 2010, and see Madau & Dickinson 2014 for a comprehensive review), and it provides the probability distribution function of SFR. In addition, by assuming a relation between the stellar mass and SFR, so-called "main sequence" (e.g., Speagle et al., 2014; Song et al., 2016; Tomczak et al., 2016; Leslie

et al., 2020, and references therein.), UVLFs provide shapes of galaxy stellar mass functions (SMFs). Therefore, estimating a UVLF of protocluster galaxies (PC UVLF) at $z \geq 3$ will provide us with an opportunity of revealing the general properties of galaxies in high-density regions. On the other hand, an accurate measurement of the PC UVLF requires a large number of protocluster samples, which has been the biggest obstacle, and there has not been any study that measures the PC UVLF.

In this chapter, we report a study of the UVLF measurement for galaxies in protoclusters found through HSC-SSP (Aihara et al., 2018), whose main results I published as Ito et al. (2020) as a corresponding author. Mainly using the protocluster sample summarized in Toshikawa et al. (2018), which are the largest and homogeneously selected one, and from the latest data release for the supplement purpose, we discuss whether the environmental dependence on the SFR exists even at high redshift.

2.2 Data Summary, Sample Selection

We use protocluster candidates and the galaxy catalog constructed from HSC-SSP data. There are three versions of HSC-SSP products used here; S16A data, S20A data, and the joint catalog based on S18A data. In this section, I first overview the HSC-SSP survey and summarize each dataset. After that, I will introduce our galaxy and protocluster selection.

2.2.1 Overview of HSC-SSP and data summary

Hyper Suprime-Cam (HSC) is a wide-field imaging instrument on the prime focus of the Subaru Telescope located in Maunakea, Hawaii. It has 104 main science CCDs, 8 and 4 CCDs for focusing and auto-guiding, respectively. The diameter of HSC is 1.5 deg, and its pixel scale is 0.17 arcsec. Its large field of view is superior to any other instrument in other telescopes. There are multiple broadband and narrow-band filters for HSC. The HSC data was firstly analyzed on-site (Furusawa et al., 2018). The filter and the dewar design are described in Kawanomoto et al. (2018); Komiyama et al. (2018), respectively.

The HSC-SSP is an extensive survey program awarded more than 300 nights from 2014 using the Subaru Telescope. This survey consists of three layers, i.e., WIDE,

DEEP, UltraDEEP. Differences among the three layers are their survey area and depth. The WIDE layer covers $\sim$ 1400 deg^2 and the 5σ limiting magnitude is expected to be 25.9 mag in i band. The DEEP layer only covers $\sim$ 26 deg^2 but reaches deeper, such as the 5σ limiting magnitude of 26.8 mag in i band. The UltraDEEP layer aims to reach deeper, such as the 5σ limiting magnitude of 27.4 mag in i band, in $\sim$ 4 deg^2. In HSC-SSP, g, r, i, z, y, NB387, NB816, NB921-band are used. HSC-SSP data is processed via `hscpipe` (Bosch et al., 2018), which is a modified version of the Legacy Survey of Space and Time software (Jurić et al., 2015; Axelrod et al., 2010; Ivezić et al., 2019).

We use three versions of HSC-SSP products. The S16A data release covers $\sim$ 140 deg^2 and released in 2016. Based on this data release, Toshikawa et al. (2018) select protocluster catalog at $z \sim 4$, which will be introduced later, and we use the WIDE layer of this catalog in deriving the UVLF. Secondly, the S20A data release is a relatively new product of the HSC-SSP. We use this for the DEEP/UltraDEEP layer covering the 27.74 deg^2. In S16A and S20A data releases, we only focus on the continuum selected sources, so we only use broadband photometry (i.e., grizy). Lastly, the joint catalog is a combined catalog of the HSC-SSP and other surveys in the near-ultraviolet and near-infrared. The additional photometry comes from the U-band of Megacam/Canada–France–Hawaii Telescope in CLAUDS (Sawicki et al., 2019), JHK band of the WFCAM/UKIRT in DUNES[2], HSC-SSP narrow-band photometry of the CHORUS (Inoue et al., 2020), and the archival data of WFCAM from the UKIDSS DR11 (Lawrence et al., 2007) and VISTA InfraRed Camera (VIRCAM) from the UltraVISTA DR4 (McCracken et al., 2012). It covers only the DEEP/UltraDEEP layer. We use the joint data to conduct the SED fitting analysis (Section 2.5.3), so all broadband photometry is used.

In this study, we use the data of the S16A WIDE layer to constrain the general features of protoclusters thanks to the large survey field and protocluster sample. The S20A and joint catalog in the DEEP/UltraDEEP layer are used to obtain an insight of individual galaxies in protoclusters from the multiband photometry and better images.

2.2.2 Target galaxy selection

Toshikawa et al. (2018) construct a g-dropout galaxy sample from the gri band photometry. In the WIDE layer, only five regions in the Wide layer have enough

depth (XMM-LSS, WIDE12H, GAMA15H, HECTOMAP, and VVDS) to construct a homogeneous map of the galaxy distribution in the S16A data release. We use all four regions for the DEEP/UltraDEEP layer (i.e., COSMOS, DEEP2-3, ELAIS-N1, XMM-LSS).

The g-dropout galaxies are selected by the following the color and magnitude selection;

$$1.0 < g - r \tag{2.1}$$
$$-1.0 < r - i < 1.0 \tag{2.2}$$
$$1.5(r - i) < (g - r) - 0.8 \tag{2.3}$$
$$r < r_{\mathrm{lim},3\sigma} \tag{2.4}$$
$$i < i_{\mathrm{lim},5\sigma}. \tag{2.5}$$

$r_{\mathrm{lim},3\sigma}$ and $i_{\mathrm{lim},5\sigma}$ is the 3σ and 5σ limiting magnitude in r and i bands, respectively. In S16A data, the `Cmodel` magnitude is used for the selection (Bosch et al., 2018). In S20A, the `undeblended_convolvedflux` is used. It is because the `Cmodel` magnitude provides incorrectly bright magnitude for bright sources from HSC-SSP PDR2 (Aihara et al., 2019). This problem is caused by the failure in the deblending procedure for the deep images. In addition, various flags are used to select objects with clean photometry and not affected by cosmic rays and so on. The detailed selection criteria of the flags are summarized below (Table 2.1). They slightly differ depending on the data release version.

Table 2.1: Flags used for g-dropout selection

Parameter	Value	Band
S16A		
`detect_is_primary`	True	–
`flags_pixel_edge`	False	*grizy*
`flags_pixel_interpolated_center`	False	*grizy*
`flags_pixel_saturated_center`	False	*grizy*
`flags_pixel_cr_center`	False	*grizy*
`flags_pixel_bad`	False	*grizy*
`flags_pixel_bright_object_center`	False	*grizy*
`flags_pixel_bright_object_any`	False	*grizy*
`input_count_value`	> 3	*gr*

Parameter	Value	Band
input_count_value	> 5	*izy*
S20A		
sdsscentroid_flag	False	*ri*
undebldended_convolvedflux_2_20_flag	False	*gri*
merge_peak	True	*ri*
mask_brightstar_ghost	False	*grizy*
mask_brightstar_halo	False	*grizy*
mask_brightstar_blooming	False	*grizy*
blendedness_abs_flux	< 0.2	*ri*
input_count_value	> 3	*gr*
input_count_value	> 5	*izy*

2.2.3 Protocluster selection for S16A data

Toshikawa et al. (2018) select protocluster candidates according to the peak value of the overdensity significance of g-dropout galaxies of S16A. The overdensity map is drawn from their surface number density through the fixed aperture method. This method distributes circular apertures on an every $1'$ grid and estimates the surface number density of galaxies from the number of galaxies inside the apertures. They define the aperture size of $1.8'$, which corresponds to ~ 0.75 physical Mpc at $z \sim 3.8$. This is the smallest size expected for protoclusters of "Fornax-type" clusters ($M_{\rm halo} \sim 1 - 3 \times 10^{14} {\rm M}_\odot$ at $z \sim 0$), as predicted by simulations (Chiang et al., 2013).

Toshikawa et al. (2018) only focuses on regions whose limiting 5σ magnitudes for g, r, i band are deeper than 26.0, 25.5, and 25.5 mag, respectively, giving an effective survey area of 121 deg^2. For drawing the overdensity map, Toshikawa et al. (2018) utilizes the g-dropout galaxies that are brighter than 25 mag in i band. Finally, Toshikawa et al. (2018) select 179 overdense regions whose peak overdensity significance is greater than 4σ as protocluster candidates, following Toshikawa et al. (2016). Toshikawa et al. (2018) evaluate that about $\geq 76\%$ of such regions will evolve into halos with a mass greater than $10^{14} {\rm M}_\odot$ at $z \sim 0$.

This large sample of protoclusters allowed Toshikawa et al. (2018) to conduct an angular clustering analyses and estimate the mean dark matter halo mass as $\langle M_{\rm halo} \rangle = 2.3^{+0.5}_{-0.5} \times 10^{13} h^{-1} {\rm M}_\odot$. According to the extended Press-Schechter model, halos with such a large mass is indeed expected to evolve into those with $\langle M_{\rm halo} \rangle = 4.1^{+0.7}_{-0.7} \times 10^{14} h^{-1} {\rm M}_\odot$

at $z \sim 0$.

2.2.4 Protocluster selection for S20A data

We apply the same selection method described in Section 2.2.3 to S20A data (Toshikawa et al. in prep.). The only difference is the magnitude range of the galaxies used to draw the overdensity map. Since we only focus on the DEEP/UltraDEEP field, which has deeper photometry than the WIDE layer, galaxies brighter than 26 mag in the i band are used. Forty overdense regions are selected as protocluster candidates.

2.2.5 Definition of protocluster region

We have to define the volume of protoclusters to measure their UVLF. We approximate the shape of protoclusters as cylinders. The cross-section of the cylinder is a circle with a radius of 1.8′ corresponding to 0.75 pMpc, which is the same size as the aperture in the overdensity map. The line-of-sight length is equivalent to the diameter of the cross-section. Therefore, we define protocluster member galaxies as galaxies located within a projected $< 1.8'$ from the center of the overdensity peak. It should be noted that these protocluster candidates and their members have the redshift uncertainty ($\delta z \sim 1$) since this method is based on the dropout technique. Therefore, we will statistically exclude galaxies outside the protocluster from this member sample (c.f., Section 2.3.1). We also consider a masked region in determining the protocluster volume.

Note that we do not consider the particular morphology of each protocluster. For example, some protoclusters, particularly more massive ones, can be bigger (e.g., Chiang et al., 2013; Muldrew et al., 2015). Some studies also argue that the shape of protoclusters can be described in the triaxial model (Lovell et al., 2018). The radius for selecting member galaxies in the study is the minimum size of protoclusters predicted by the simulation (Chiang et al., 2013). Therefore, our selected regions are expected to contain pure protocluster members, but we might miss some members in the outermost regions of the protoclusters. As we discuss in Section 2.7.2, our results for the shape of UVLF do not significantly change even if we change the radius of the cross-section and the depth.

2.3 Rest-frame UV Luminosity Function Measurement

2.3.1 Formulation of protocluster luminosity function

We estimate the UV absolute magnitude, which is the absolute magnitude at 1500Å in the rest-frame from the apparent magnitude. As mentioned in Section 2.2.5, our protocluster galaxies have a significant redshift uncertainty since they are selected from g-dropout galaxies. Therefore, we fix $\bar{z} = 3.8$ as the typical redshift. We convert the i band magnitude (m_i) by using the following equation;

$$M_{\rm UV} = m_i + 2.5\log(1+\bar{z}) - 5\log(\frac{d_L(\bar{z})}{10\ {\rm pc}}) + (m_{1500(1+\lambda)} - m_i) \tag{2.6}$$

Here, $d_L(\bar{z})$ is the luminosity distance at $z = \bar{z}$ in the unit of pc. We assume that the g-dropout galaxies' SED at rest-UV is flat in f_ν, which leads to a k-correction factor $(m_{1500(1+\lambda)} - m_i)$ of zero, following Ono et al. (2018).

We measure only the projected number density from the photometric data; therefore, our protocluster galaxy sample has some possible contaminants. One is fore/background g-dropout galaxies outside the protocluster region, hereafter called "field galaxies". The effective redshift range of g-dropout galaxies is significantly larger than the protocluster's transverse size, so we must subtract the contribution of field galaxies from the measured surface number density in the protocluster regions. The number density of field galaxies can be approximated by the UVLF of field galaxies (field UVLF) since the volume fraction of the protocluster is small compared to the total survey volume. In addition to field galaxies, g-dropout galaxies themselves may inevitably have some contaminants such as stars and low-redshift galaxies due to the color selection uncertainties, which should be removed from the sample. These objects can be assumed to be homogeneously distributed if we combine all protoclusters, which are separated on the whole sky; therefore, their contamination rate should be the same both inside and outside of the protocluster regions. This implies that the subtraction of the field UVLF without contamination correction provides a clean estimate of the number density of protocluster galaxies.

One possible contamination source that might not be distributed homogeneously is low-z galaxy clusters at $0.3 < z < 0.6$, where Balmer breaks are hardly distinguishable

from Lyman break at $z \sim 4$. Oguri et al. (2018) construct a galaxy cluster sample at $0.1 < z < 1.1$ from 232 deg^2 WIDE layer of the HSC-SSP data. They find 620 clusters at $0.3 < z < 0.6$, implying their surface number density as 2.67 deg^{-2}. The possibility that our protoclusters in WIDE layer are overlapped with galaxy clusters at $0.3 < z < 0.6$ within $1.8'$ (i.e., protocluster size) is only 0.59%. Therefore, we conclude that all contamination is negligible to estimate the the PC UVLF.

We correct the effective volume of g-dropout galaxies to the protocluster effective volume by a factor F defined as;

$$F(M_{\rm UV}) = \frac{\langle C(M_{\rm UV}, z) \frac{dV(z)}{dz} \delta z \rangle}{V_{\rm eff}(M_{\rm UV})}. \tag{2.7}$$

Here, $C(M_{\rm UV}, z)$ is the completeness function of the g-dropout selection estimated in Section 2.3.3. δz is the redshift interval that corresponds to the depth of the cylinder volume of protoclusters (see Section 2.2.5). $dV(z)/dz$ is the differential comoving volume. The $V_{\rm eff}(M_{\rm UV})$ is the effective volume for g-dropout galaxies in $1.8'$ aperture, which is defined as follows (e.g., Hogg, 1999);

$$V_{\rm eff}(M_{\rm UV}) = \int C(M_{\rm UV}, z) \frac{dV(z)}{dz} dz. \tag{2.8}$$

The numerator of $F(M_{\rm UV})$ corresponds to the effective volume of a protocluster, whose shape is defined in Section 2.2.5. Therefore, $F(M_{\rm UV})$ is the ratio of the effective volume of the protoclusters and the effective volume of the redshift range of the entire g-dropout selection. Since we do not know the exact redshifts of each system, we use the average numerator weighted by the redshift selection function (i.e., the completeness function).

Then, the PC UVLF is described as follows,

$$\Phi_{\rm PC}(M_{\rm UV}) = \frac{1}{F(M_{\rm UV})} \left(\frac{n_{\rm obs,PC}(M_{\rm UV})}{V_{\rm eff}(M_{\rm UV})} - \Phi_{\rm field}(M_{\rm UV}) \right), \tag{2.9}$$

where $n_{\rm obs,PC}(M_{\rm UV})$ is the observed number of g-dropout galaxies in protocluster regions defined in Section 2.2.5 in each magnitude bin. $\Phi_{\rm field}(M_{\rm UV})$ is the field UVLF without the contamination correction (see Section 2.3.2). In order to determine $\Phi_{\rm PC}(M_{\rm UV})$, we estimate the completeness function of g-dropout galaxies $C(M_{\rm UV}, z)$ and

the field UVLF without contamination treatment in the following section.

2.3.2 Formulation of field luminosity function

The field UVLF is derived from the observed number of g-dropout galaxies in the entire HSC-SSP field and the completeness function, as described in Equation 2.10.

$$\Phi_{\rm field}(M_{\rm UV}) = \frac{n_{\rm obs,field}(M_{\rm UV})}{V_{\rm eff}(M_{\rm UV})}. \tag{2.10}$$

Here, $n_{\rm obs,\,field}(M)$ is the observed number of field galaxies and contaminants of $M_{\rm UV} = M$. Before deriving $n_{\rm obs,\,field}(M)$, we remove all known low-z galaxies, stars, or QSOs from the available spectroscopic survey archives, such as SDSS DR12 (Alam et al., 2015), HectoMAP cluster survey (Sohn et al., 2018), and VIPERS DR1 (Garilli et al., 2014). The majority of matched objects are galaxies at $0.3 < z < 0.6$ and QSOs at the same redshift distribution of g-dropout galaxies.

Again, we note that we do not statistically exclude the contamination of g-dropout galaxies. This is because the observed protocluster galaxies also contain contaminants and our aim of deriving the protocluster luminosity function without contaminants is achieved the excluding the field luminosity function with contaminants.

2.3.3 Completeness estimation

As in the previous studies of UVLFs of the field LBGs (e.g., Ono et al., 2018; van der Burg et al., 2010; Yoshida et al., 2006), we insert mock galaxies into the actual images and estimate a completeness function as a function of the redshift and magnitude.

The method of estimation is as follows. Mock galaxies are firstly inserted into the coadd images of the g, r, i band images of HSC-SSP products. We generate mock images through the `Balrog`[1] (Suchyta et al., 2016), which inserts mock galaxies with the help of the `galsim`[2] (Rowe et al., 2015) followed by their detection and measurement through `SourceExtractor`. However, the HSC-SSP source catalog is constructed based on `hscpipe`; therefore, we do not use the result of detection of `SourceExtractor` and measure the photometry of the mock galaxies through

[1] https://github.com/emhuff/Balrog
[2] https://github.com/GalSim-developers/GalSim

`hscpipe`, instead. We assume that the surface brightness profile follows the Sérsic profile (Sérsic, 1963) with a fixed Sérsic index of 1.5 for mock galaxies. In addition, the effective size distribution is assumed to be consistent with that of Shibuya et al. (2015). The real profile of mock galaxies are considered with the point spread function (PSF) of that field by convolving it taken from PSFEx[3] (Bertin, 2011). The SED of mock galaxies are generated using the CIGALE[4] (Boquien et al., 2019). We assume a constant star formation and use the single stellar population models of Bruzual & Charlot (2003). We adopt the Salpeter initial mass function (IMF) (Salpeter, 1955) with an age of 100 Myr and metallicity of $Z/Z_{\odot} = 0.2$. The dust extinction follows Calzetti et al. (2000) with $E(B-V) = 0.0 - 0.4$ mag. The IGM absorption is accounted for according to Meiksin (2006). We change their redshift from 3.0 to 5.0 with interval of $\delta z \sim 0.1$. From the detected catalogs, we select mock g-dropout galaxies by the same criteria as used in Toshikawa et al. (2018), including color, magnitude, and flag selection.

In estimating the completeness function of WIDE g-dropout galaxies, we use `hscpipe` version 4, which is the same software used for the HSC-SSP S16A data release. We estimate the completeness function for each five fields and the same completeness function is used for protoclusters in the same field. The WIDE layer has the uniform depth, so this assumption is well justified. We select one region called `tract`, with an area of 2.3 deg^2, for each field to execute the procedure. The number of inserted galaxies is about 35 per arcmin^2.

For each field, we calculate the completeness as the number ratio of selected mock g-dropout galaxies to all inserted objects in each magnitude and redshift bin. Figure 2.1 shows the completeness function of each field in the case of WIDE layer, demonstrating that the five fields have almost the same completeness.

2.3.4 Protocluster luminosity function

We first derive the field UVLF. For galaxies in the wide layer, we use the 2.0" aperture for calculating the total magnitude. To apply the aperture correction, we compare the input total magnitude and the measured 2.0" aperture magnitude of mock galaxies

[3] https://www.astromatic.net/software/psfex
[4] https://cigale.lam.fr/

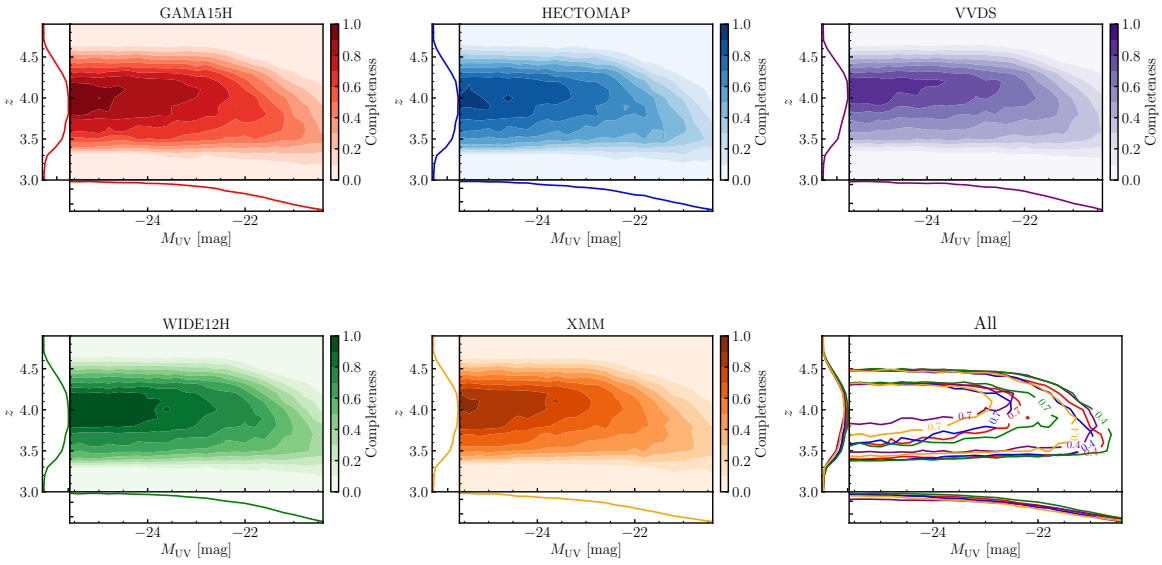

Figure 2.1: Completeness functions of g-dropout galaxies for each target field of WIDE layer. The bottom right panel shows their comparison. Colors match those shown in each panel of single field. Values written in the contour in the right bottom panel represent the completeness.

used in Section 2.3.3, and find that 2.0” aperture magnitude has a +0.08 mag offset on average from the input magnitude. Therefore, we apply a 0.08 mag aperture correction to our measured 2.0” magnitude to derive the total magnitude. We confirm that the derived total magnitudes are consistent with the measured aperture magnitudes, with larger apertures, such as 3.0”, 4.0”. We also correct the galactic extinction by using the extinction map from Schlegel et al. (1998).

Based on Equation 2.10 and the completeness function derived in Section 2.3.3, the field UVLF in the WIDE layer is derived. We derive the field UVLFs for each five fields. This UVLF is not necessarily the same as the field UVLF derived in previous studies (e.g., Ono et al., 2018; Bouwens et al., 2015) since our function includes contaminants, as seen in Figure 2.2. The bottom panel of Figure 2.2 shows the difference between the average of the UVLFs and that of Ono et al. (2018) normalized by this UVLF. Since the UVLF of Ono et al. (2018) exclude contaminants, this represents the expected fraction of contaminants among our g-dropout galaxies. We can find that this ratio is consistent with that estimated for the WIDE layer in Ono et al. (2018), overplotted in the bottom panel of Figure 2.2. We conclude that our completeness function is consistent with

previous studies. Hereafter, we will use these UVLFs and the completeness function to estimate the PC UVLF.

The PC UVLF of the WIDE layer is estimated according to Equation 2.9. Two protoclusters are excluded since they are located in low-quality regions with quite shallow limiting magnitudes ($m \sim 25.6$ mag for 5σ i-band limiting magnitude); thus 177 protocluster regions are used for estimating the PC UVLF. Since the completeness function and $\Phi_{\rm field}(M_{\rm UV})$ have been determined for each field, the PC UVLF is also estimated for each field separately, and we take the average weighted by the total area for each field as our final PC UVLF. We note that all PC UVLFs for each field are overall consistent within the uncertainty.

We show the average PC UVLF of the HSC-SSP protocluster candidates in the WIDE layer in Figure 2.3. Our PC UVLF has apparent differences from the field UVLF in the literature (e.g., Ono et al., 2018). First, the amplitude is much higher than the field UVLF, with the integrated value of the PC UVLF at $M_{\rm UV} \leq -20.3$ is about 230 times higher than that of the field UVLF of Ono et al. (2018). Second, its shape is remarkably different from the field UVLF. The amplitude-matched field UVLF is also shown in the top panel of Figure 2.3 for reference, and compared with that, the PC UVLF has a significant excess towards the bright-end ($M_{\rm UV} \leq -20.8$). The trend can also be seen on the bottom panel of Figure 2.3, which shows the ratio of the PC and the field UVLF. We see that the excess gets larger towards the brighter bin. If the shapes are identical between them, this ratio should stay constant at any brightness.

Since the number density of galaxies decreases towards the bright-end, the photometric error of each galaxy might enhance the amplitude of the bright-end of UVLF, which is known as “Eddington Bias" (Eddington, 1913). We estimate the effect of this bias by convolving the error distribution of magnitude to the field UVLF of Ono et al. (2018). The detail of this analysis is described in Appendix A.1. We confirm that the Eddington bias is not significant to generate the shape of our PC UVLF. Since the contribution from low-z contaminants are distributed homogeneously and subtracted from the sample as mentioned in Section 2.3.1, the bright-end excess is not likely due to low-z galaxy contaminants. We note that its slightly decreasing trend toward the faint-end is not likely due to the incompleteness since we consider the completeness in the estimation and there is no additional incompleteness due to the overdense region (see Section 2.7.1).

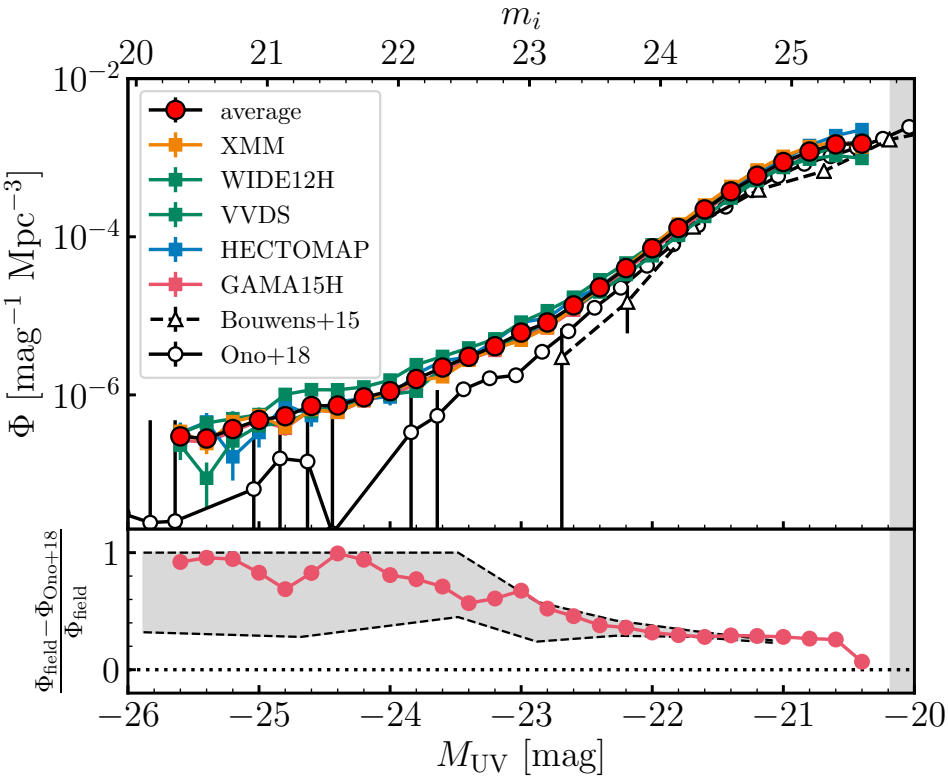

Figure 2.2: Top panel: Field UVLF of the WIDE layer at $z \sim 4$ for each field (squares) and their average (red circles). Black open circles and triangles are UVLFs in the literature (Ono et al., 2018; Bouwens et al., 2015). Note that we do not correct for contaminants. Bottom panel: The red circles show the difference between the average of this work UVLFs, which is not corrected for contaminants, and the UVLF from Ono et al. (2018) normalized by this work's UVLF. Gray shaded region shows the contamination rate of g-dropout galaxies estimated in Ono et al. (2018). The red circles correspond to a contamination fraction of our g-dropout galaxies, which is in good agreement with that in Ono et al. (2018).

The rest-frame UV luminosity of galaxies represents their SFR. Therefore, this result indicates that the overdense regions at $z \sim 4$ have not only a high SFRD caused by the excess of the number of galaxies, but also a higher fraction of galaxies with high SFR compared to those in the blank field. This trend is also seen in some protoclusters at lower redshifts. Therefore, this study, for the first time, shows that the enhancement of star formation of UV-bright galaxies in overdense regions is already seen as early as from $z \sim 4$. We have to note that some bright ($M_{\rm UV} < -23.0$) LBGs can be AGNs, whose UV emission cannot be a proxy of SFR of their host galaxies (e.g., Adams et al., 2020; Ono et al., 2018). We discuss a possible contribution from AGN in Section 2.5.

2.3.5 Functional fitting

To compare the shape of the derived PC UVLF with the field UVLF more quantitatively, we fit the Schechter function (Schechter & Press, 1976), which is defined as follows;

$$\phi(L)dL = \phi^* \left(\frac{L}{L^*}\right)^{\alpha} \exp\left(-\frac{L}{L^*}\right) d\left(\frac{L}{L^*}\right), \tag{2.11}$$

where α is the faint-end slope, L^* is the characteristic luminosity, and ϕ^* is the overall normalization. This function can be also expressed as a function of the absolute magnitude $M_{\rm UV}$,

$$\begin{aligned}\Phi(M_{\rm UV}) = \frac{\ln 10}{2.5}\phi^* 10^{-0.4(M_{\rm UV}-M^*_{\rm UV})(\alpha+1)} \\ \times \exp(-10^{-0.4(M_{\rm UV}-M^*_{\rm UV})}).\end{aligned} \tag{2.12}$$

We fit the Schechter function in terms of absolute magnitude to the PC UVLF using the χ^2 minimization method. We show the best-fit Schechter function in Figure 2.4 and the parameters in Table 2.2. Compared to the best-fit parameters of the field UVLF in previous studies (Ono et al., 2018; Bouwens et al., 2015; van der Burg et al., 2010; Yoshida et al., 2006), our PC UVLF has a less steep faint-end slope, as shown in Figure 2.5. Our best-fit $M^*_{\rm UV}$ is consistent with that of the field UVLFs at the 68/95% confidence level. This implies that the PC UVLF has a different shape compared to the field UVLF, although the discrepancy between our PC UVLF and the best-fit Schechter function is large, particularly at the bright-end ($M_{\rm UV} < -23$).

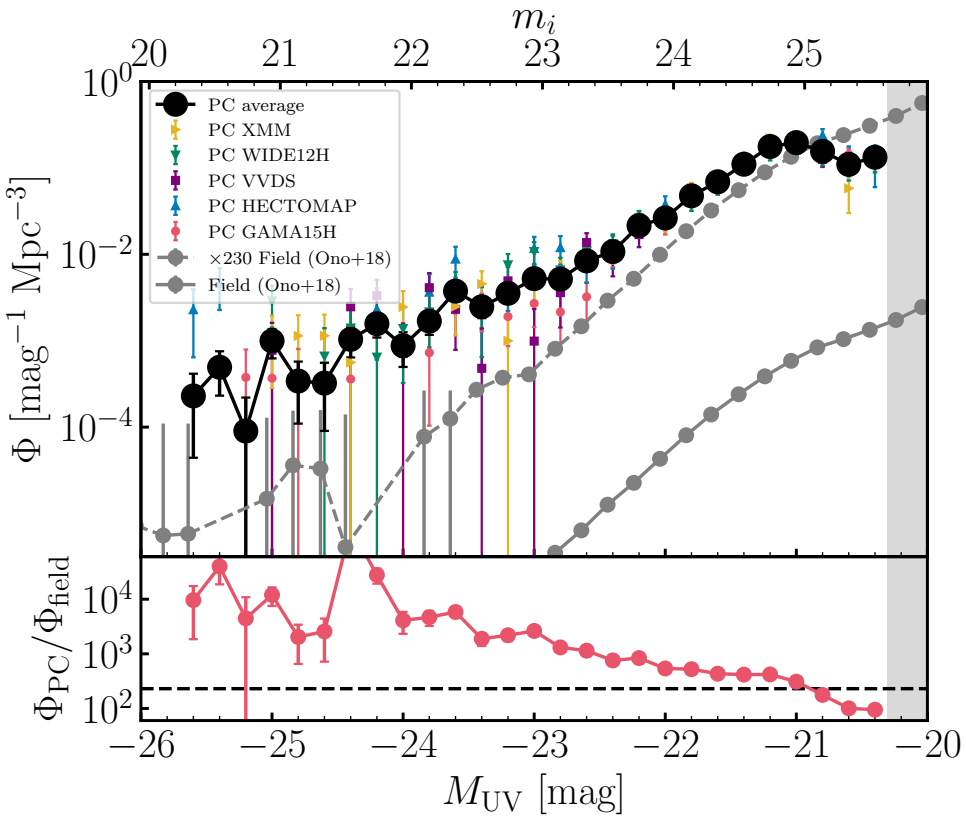

Figure 2.3: Luminosity function of galaxies in protocluster candidates in the HSC-SSP WIDE layer at $z \sim 4$. The color-coded markers represent the PC UVLF for each survey field. The black circles show the average of all fields. For reference, we show the field UVLF of Ono et al. (2018) (gray solid line with circles) and shifted upward to match the PC UVLF (gray dashed line with circles). The bottom panel shows the ratio of the PC UVLF and the field UVLF (red circles). The black dashed line shows the value of the ratio of the sum of each UVLF. For both panels, the magnitude range that is fainter than the depth is shaded in gray.

The large reduced χ^2 shown in Table 2.2 implies this failure of fitting at the bright-end. This can be because the PC UVLF does not seem to have a clear exponential decrease at the bright-end. Therefore, we try to fit another functional form. Recent UVLF studies of field galaxies at higher redshift ($z \geq 4$) have suggested that the galaxy UVLF can be well described by a double power-law (DPL) function (e.g., Bowler et al., 2020; Bouwens et al., 2015; Ono et al., 2018). The DPL function is defined as follows;

$$\phi(L)dL = \phi^* \left[\left(\frac{L}{L^*} \right)^{-\alpha} + \left(\frac{L}{L^*} \right)^{-\beta} \right]^{-1} \frac{dL}{L*}, \tag{2.13}$$

where β represents the power-law slope at the bright-end ($M_{\rm UV} < M^*_{\rm UV}$). We fit this function in terms of absolute magnitude, same as in fitting with the Schechter function. We fix the faint-end slope α to be the same as that of the best-fit Schechter function. We also show the best-fit DPL function in Figure 2.4, and their parameters in Table 2.2. The DPL function fits better than the Schechter function, even though the best-fit DPL function still has some deviation from the observed PC UVLF at $M_{\rm UV} < 23$.

The deviation from the best-fit Schechter/DPL function of UVLFs of field galaxies is often explained by AGNs. Ono et al. (2018) claim that the gap of UVLFs of field galaxies from their best-fit Schechter function at $z \sim 4 - 7$ is explained by the contribution of AGN UVLFs at the same redshift. Also, Konno et al. (2016) construct the Lyα luminosity function of LAEs at $z = 2.2$ and argue that the gap at the brightest-end from its best fit is due to AGNs. We discuss the possible contribution from AGNs in Section 2.5 and do not reject the possibility of the gap in both best-fit results due to AGNs. However, we can not conclude which functions represent the galaxy UVLF more precisely. Therefore, we use both fitting functions in the following sections.

2.4 Implications of Protocluster Luminosity Function

In this section, we will discuss the stellar mass function, diversity of protocluster luminosity function, and SFRD from the derived PC UVLF.

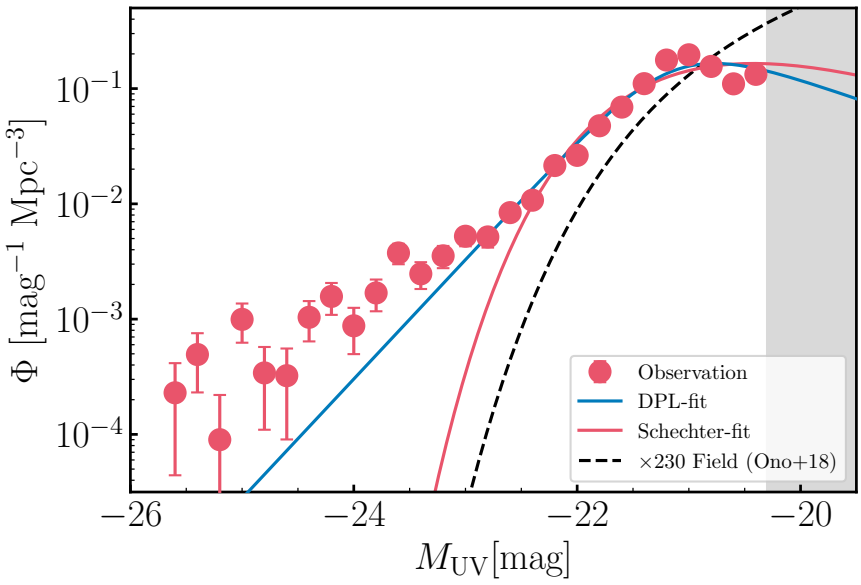

Figure 2.4: Result of the fitting of the Schechter/DPL function to PC UVLF. Circles show the derived PC UVLF. The red (blue) lines represent the best-fit of the Schechter (DPL) function. As a reference, the black dashed line is the best-fit Schechter function of the field UVLF in Ono et al. (2018). Same as Figure 2.3, the gray shade represents the magnitude range which is not discussed.

$M^*_{\rm UV}$ (mag)	ϕ^* (Mpc^{-3})	α	β	χ^2_ν
Schechter function				
$-20.61^{+0.12}_{-0.14}$	$0.48^{+0.02}_{-0.02}$	$-0.16^{+0.25}_{-0.25}$	-	11.2
Double power-law function				
$-21.13^{+0.04}_{-0.04}$	$0.31^{+0.01}_{-0.01}$	(-0.16)	$-3.59^{+0.08}_{-0.11}$	5.5

Table 2.2: Best-fit parameters and the reduced χ^2 of the Schechter and DPL functions fitted to the PC UVLF in the WIDE layer. We fix the faint-end slope in the case of the DPL to the best-fit value in the case of the Schechter function.

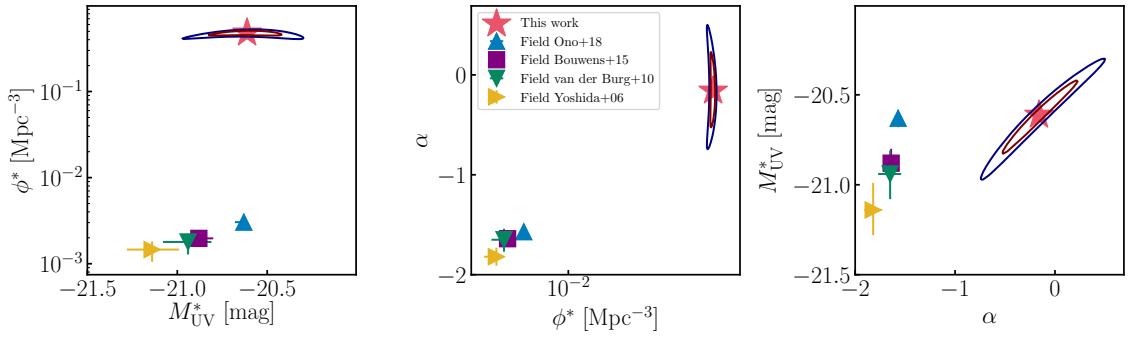

Figure 2.5: Comparison of best-fit parameters of our PC UVLF with those of the field UVLFs from the literature. Red stars represent this work, and blue, purple, green and yellow markers represent Ono et al. (2018), Bouwens et al. (2015), van der Burg et al. (2010), and Yoshida et al. (2006), respectively. Red and Blue contours represent the 68.3%, and 95.5% confidence levels of the best-fit parameters of our PC UVLF, respectively.

2.4.1 Stellar mass function

We estimate the SMF based on the measured PC UVLF, assuming that all protocluster g-dropout galaxies are located on the star formation main-sequence of field galaxies at the same redshift. We utilize the main sequence estimated by Song et al. (2016), which determine the main-sequence by applying SED-fitting analysis to field photo-z selected galaxies from Finkelstein et al. (2015). We assume the main sequence is equivalent between protoclusters and the field, which is supported by observational studies (e.g., Long et al., 2020; Shi et al., 2019b; Koyama et al., 2013) and a theoretical study (e.g., Lovell et al., 2020), while some studies report a large contribution from star burst galaxies in protoclusters (e.g., Miller et al., 2018), leading to the possibility of different main sequences from those of field galaxies.

We use the “constant-scatter galaxy SMF" method, which is conducted in some previous studies (e.g., Song et al., 2016). First, $M_{\rm UV}$ is randomly assigned. Its probability distribution for each $M_{\rm UV}$ is approximated by the PC UVLF, in which Gaussian random errors for each bin are assigned, whose 1σ is equivalent to that of the observed PC UVLF. The $M_{\rm UV}$ is converted into the stellar mass M_* according to the M_*-$M_{\rm UV}$ relation of Song et al. (2016) with a constant scatter of 0.4 dex, and finally, the stellar mass distribution is obtained. This procedure is repeated for 1000 times, and the SMF of

protocluster galaxies (PC SMF) is obtained by taking their average. The uncertainty of the SMF is taken from the variation among 1000 results. The SMF of field galaxies (field SMF) is also estimated from the field UVLF of Ono et al. (2018) in the same manner. We find that the estimation of SMFs has only a negligible change within the uncertainty when we use the main sequence of Tomczak et al. (2016), which has a flatter massive end ($\log(M_*/\mathrm{M}_\odot) > 10.5$), compared to the main sequence of Song et al. (2016) as shown in Figure 2.6.

Figure 2.6 shows our SMF estimate. We normalize them to fix the value at $\log(M_*/\mathrm{M}_\odot) = 10$ for the easy comparison. The gray shaded region ($\log(M_*/\mathrm{M}_\odot) < 9.72$) in Figure 2.6 shows the incomplete mass range due to the limiting magnitude ($M_{\mathrm{UV}} > -20.3$). We hereafter discuss the SMF in the stellar mass range of $\log(M_\star/\mathrm{M}_\odot) > 9.72$. The PC SMF shows a clear excess from that of field galaxies towards the massive end, suggesting that protoclusters contain a relatively high fraction of massive galaxies compared to the field. Here, we mention three notes. First, this SMF only includes g-dropout galaxies, which are typically star-forming, and we do not consider quiescent galaxies. Recent studies report the existence of massive quiescent galaxies even at $z \sim 4$ in the blank field (e.g., Valentino et al., 2020; Tanaka et al., 2019, see Section 1.3 for more detailed review), but the fraction of them are expected to be small ($< 5\%$) according to field SMFs (e.g., Davidzon et al., 2017), though the value in overdense environments has uncertainty. Therefore, we ignore the effect of quiescent galaxies. Second, the bend of the PC UVLF around $M_{\mathrm{UV}} < -23$ is not seen in PC SMF. This is because the SMF is estimated from the main-sequence with the constant scatter, which is so called "Eddington Bias". Third, the most massive-end ($\log(M_\star/\mathrm{M}_\odot) > 11.15$) is dominated by objects with $M_{\mathrm{UV}} \leq -23$. As we mention in Section 2.5, objects in such magnitude range can be AGNs; therefore, the values of the SMF in this mass range can have uncertainty.

We fit the Schechter function to the measured PC SMF as well as to the field SMF at $z \sim 4$. We can see that the PC SMF has a higher characteristic stellar mass and faint-end slope than the field SMF as seen in Figure 2.7. Protocluster galaxies have about 2.8 times higher characteristic stellar mass than field galaxies. This also supports the result that protocluster galaxies are more massive than field galaxies.

The difference of the PC SMF and the field SMF is also seen in simulations at $z \sim 4$ (Lovell et al., 2018; Muldrew et al., 2015). In Figure 2.6, we compare our PC SMF and

the field SMF with those predicted in Lovell et al. (2018). Lovell et al. (2018) use the semi-analytical model (SAM) from Henriques et al. (2015) and trace the evolutionary track of halos with $M_{200}/\mathrm{M}_\odot > 10^{14}$ at $z \sim 0$ to higher redshift. M_{200} is the mass within $r < r_{200}$, where the density is 200 times the critical density. We use their predicted SMFs constructed from galaxies with SFR > 5 $\mathrm{M}_\odot$ yr^{-1} at $z = 3.10$ and 3.95. The average redshift of our protocluster sample is between redshifts of these predicted SMFs. Our SMF is found to be almost consistent with the theoretical predictions and located between the predicted SMF at $z = 3.95$ and that at $z = 3.10$. Though the PC SMF has higher amplitude than the theoretical prediction at the most massive-end ($\log(M_*/\mathrm{M}_\odot) > 11.15$), this can be explained by the contribution of AGNs mentioned above.

We compare our PC SMF with those of (proto)cluster galaxies at lower redshifts. Shimakawa et al. (2018) estimate a SMF of HAEs in a protocluster called USS1558-003 at $z \sim 2.5$. Nantais et al. (2016) focus on four galaxy clusters at $z \sim 1.5$ from the Spitzer Adaptation of the Red-sequence Cluster Survey (SpARCS) (Muzzin et al., 2009; Wilson et al., 2009; Demarco et al., 2010). van der Burg et al. (2013) present a SMF of galaxies of ten rich clusters in the Gemini Cluster Astrophysics Spectroscopic Survey (GCLASS) at $0.86 < z < 1.34$. The SMF of galaxies in 21 clusters detected with the Plank satellite at $0.5 < z < 0.7$ is also presented in van der Burg et al. (2018). Calvi et al. (2013) estimate a SMF of cluster galaxies from the WIde-field Nearby Galaxy-cluster Survey (WINGS) at $0.04 \leq z \leq 0.07$ (Fasano et al., 2006), and compare with that of field galaxies at the same redshift. Figure 2.8 shows our PC SMF with other SMFs and the field SMF. Same as in Figure 2.6, we normalize the amplitude of all SMFs at $\log(M_*/\mathrm{M}_\odot) = 10$. This is because the definition of the (proto)clusters' volume depends on studies, leading to the difficulty of the amplitude comparison. Therefore, we only focus on the shape difference of these SMFs. We also convert their assumed IMF to Salpeter IMF, which is used in Song et al. (2016).

We can see that there is a dearth of massive galaxies in the SMF of our protoclusters at $z \sim 4$ compared to those at lower-z. This suggests that our protoclusters at $z \sim 4$ are still in the process of mass growth. Particularly, from $z \sim 4$ (HSC-SSP protoclusters) to $z \sim 1$ (van der Burg et al., 2013), SMFs shows a monotonic growth at the massive end. At $z \sim 0 - 1$, the ratio of SMFs at massive-end to those at the low mass-end decreases towards a lower redshift. This may be due to the significant contribution of

less massive infalling galaxies. We discuss it in more detail in Section 2.7.3.

We note that these SMFs are based on galaxy clusters selected by different methods. They might be at different stages of the evolution of clusters (Toshikawa et al., 2020), which may make it difficult to compare them with each other. Moreover, protocluster sample of this study and Shimakawa et al. (2018) only focus on star-forming galaxies, while others contain quiescent galaxies. The fraction of quiescent galaxies at $z > 2$ is known to be smaller than that at lower redshift, so we ignore the effects of this difference. Also as mentioned in Section 2.2.3, our protocluster candidates are overdense regions expected to evolve into clusters with $\langle M_{\rm halo} \rangle = 4.1^{+0.7}_{-0.7} \times 10^{14} h^{-1} {\rm M}_\odot$ at $z \sim 0$. The majority of clusters from WINGS is as massive as $M_{200} \sim (1-10) \times 10^{14} {\rm M}_\odot$ (Biviano et al., 2017), which is same mass range as the expected halo mass of our protoclusters. On the other hand, the cluster halo mass of other studies is $M_{200} \sim 3 \times 10^{14} {\rm M}_\odot$ for SpARCS (Lidman et al., 2012) and GCLASS (van der Burg et al., 2013), and $M_{200} \sim (3-13) \times 10^{14} {\rm M}_\odot$ in van der Burg et al. (2018). These clusters are already as massive as WINGS clusters, even at $z \sim 1$, so they may grow more by $z \sim 0$, leading them to have difficulty for comparing with WINGS clusters and our sample. In addition, the halo mass of USS1558-003 is not estimated; therefore, it is still under debate whether HSC-SSP protoclusters at $z \sim 4$ are progenitors of protoclusters such as USS1558-003.

2.4.2 Diversity of protocluster luminosity functions

Our protocluster sample has some variation in terms of overdensity. As shown in Figure 1 of Uchiyama et al. (2018), the overdensity of protoclusters ranges from 4σ to 9.5σ, and overdensity and descendant halo mass are broadly positively correlated (Toshikawa et al., 2016). Here, we make subsamples of protoclusters according to the overdensity and construct UVLFs for each subsample.

We divide protocluster samples into four groups according to their overdensity δ; 1). $4\sigma \leq \delta < 5\sigma$, 2). $5\sigma \leq \delta < 6\sigma$, 3). $6\sigma \leq \delta < 7\sigma$, 4). $7\sigma \leq \delta$. The numbers of protoclusters in each subgroup are 120, 37, 13, and 7, respectively. In Figure 2.9, we show the PC UVLF for each subsample. The amplitude of the faint-end ($M_{\rm UV} > -21.2$) is almost the same among subsamples, while the bright-end ($M_{\rm UV} < -21.2$) depends on the overdensity of protoclusters. More overdense protoclusters tend to have a higher bright-end amplitude compared to less massive protoclusters. These protoclusters can

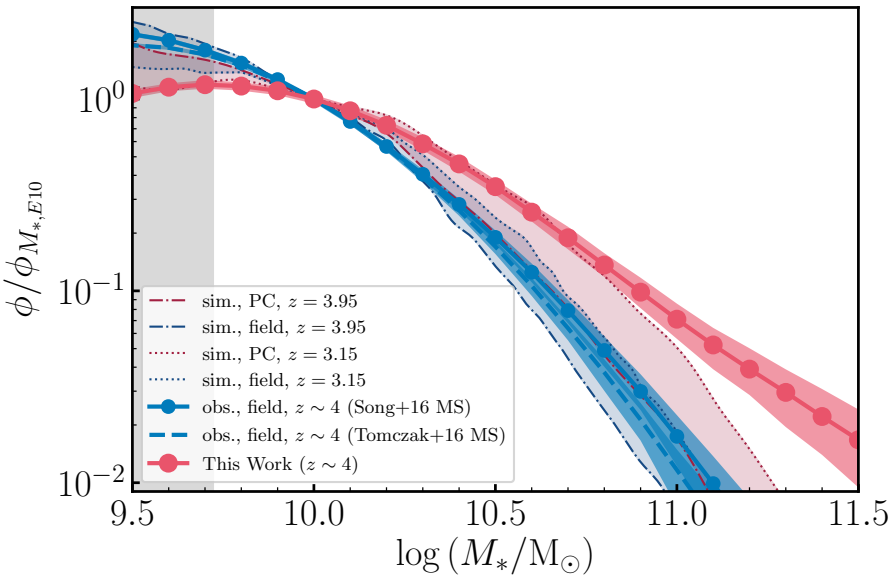

Figure 2.6: The comparison between our SMFs and SMFs predicted in Lovell et al. (2018). Red and blue circles are SMFs of protocluster and field galaxies estimated in this study. Their 1σ uncertainty are shown in shaded regions with each color. Blue dashed line is the SMF of field galaxies from Tomczak et al. (2016). Red and blue dash-dotted (dotted) lines are predicted SMFs of galaxies in protocluster and those in the field at z=3.95 (z=3.10), respectively. We normalize SMFs at $\log(M_*/\mathrm{M}_\odot) = 10.0$.

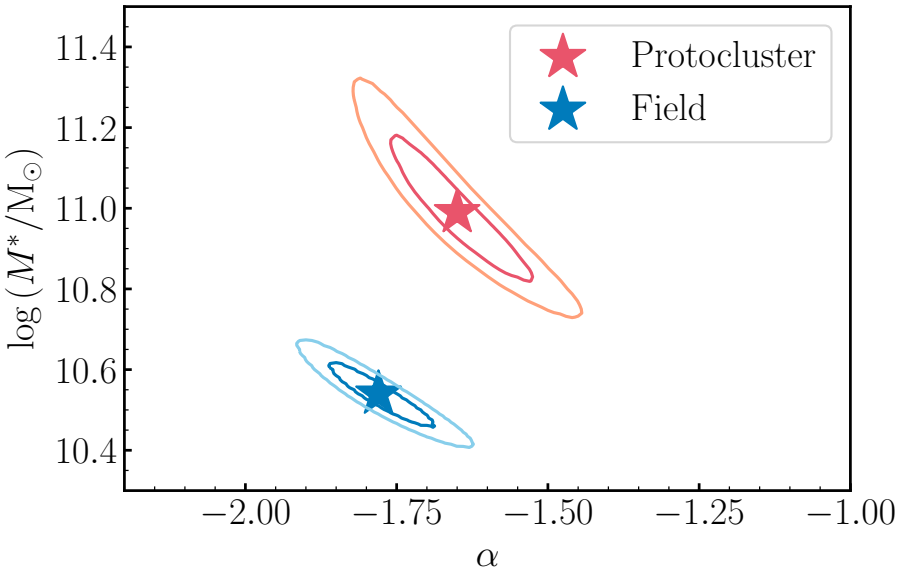

Figure 2.7: The best-fit parameters of the Schechter function to the PC SMF (Red star) and the field SMF (Blue star). The contours represent their 68/95% confidence interval.

be more spatially extended, which could cause such a dependency on overdensity; however, we find that this is unlikely as discussed in Section 2.7.2.

The dependency of the bright-end excess on overdensity can be seen even for each protocluster separately. Figure 2.10 shows the cumulative UVLF of galaxies in each protocluster. The bright-end amplitude of more overdense protoclusters tends to be higher than those of less massive protoclusters, suggesting that protoclusters with higher overdensity significance have brighter objects. More interestingly, almost all of protoclusters at $z \sim 4$ have this excess at the bright-end compared to those of field galaxies, although the variation is seen even if we focus on only protoclusters with the same overdensity. Therefore, we conclude that the bright-end excess is ubiquitously seen for protoclusters at $z \sim 4$.

2.4.3 Star formation rate density

We estimate the SFRD of protocluster galaxies, based on a combination of the PC UVLF and the far IR (FIR) luminosity density. The PC UVLF is approximated by the best-fit Schechter/DPL function. Parameter spaces with a 68% confidence level estimated in

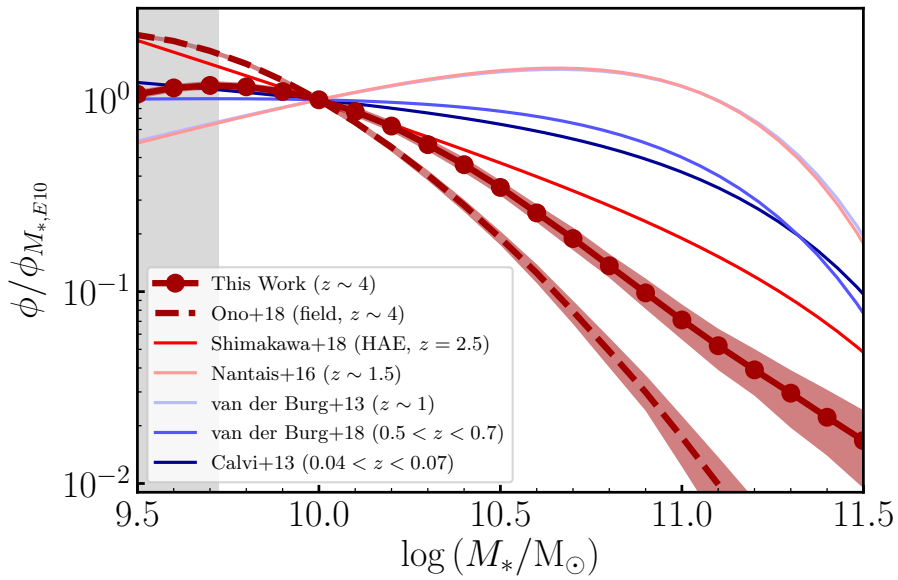

Figure 2.8: SMFs of (proto)cluster galaxies at different redshift. Their amplitudes are normalized at $\log(M_*/\mathrm{M}_\odot) = 10.0$. A red line with circles show that of protocluster galaxies at $z \sim 4$ (this work). For reference, the SMF of field galaxies estimated from the field UVLF of Ono et al. (2018) is plotted in a red dashed line. Their shaded region shows the 1σ uncertainty of them. Other red lines show SMFs of $z \geq 1.5$ (proto)clusters from other studies (Shimakawa et al., 2018; Nantais et al., 2016), and blue lines show SMFs of $z \leq 1$ clusters (van der Burg et al., 2013, 2018; Calvi et al., 2013).

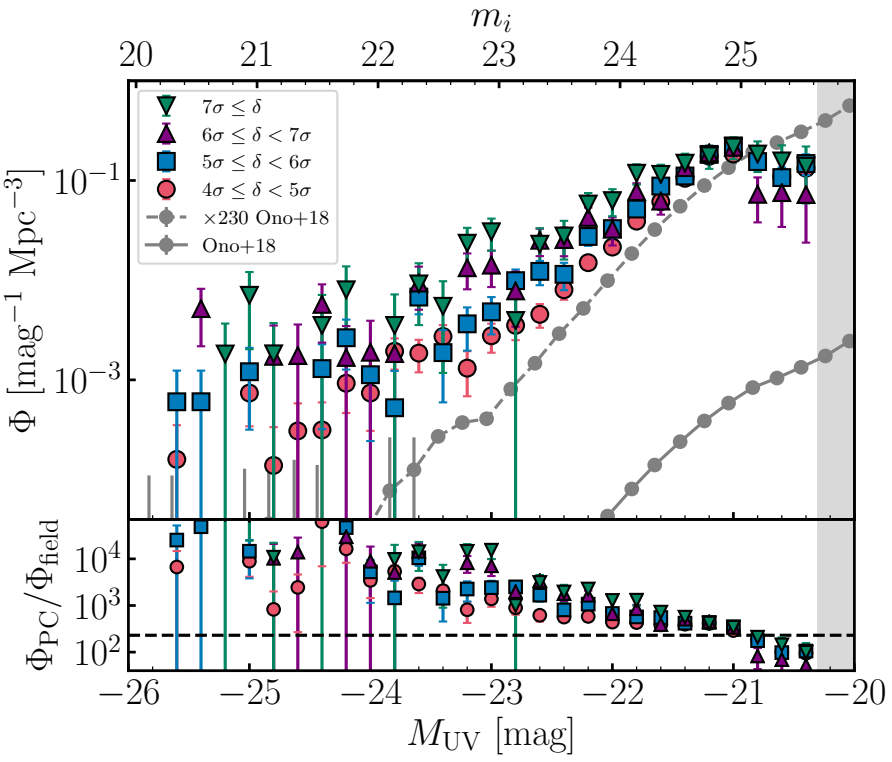

Figure 2.9: The UVLFs of members of protoclusters grouped according to their overdensities. Red, blue, purple, and green markers show those whose host protoclusters' overdensity are $4\sigma \leq \delta < 5\sigma$, $5\sigma \leq \delta < 6\sigma$, $6\sigma \leq \delta < 7\sigma$, $7\sigma \leq \delta$, respectively. The gray lines are same as in Figure 2.3.

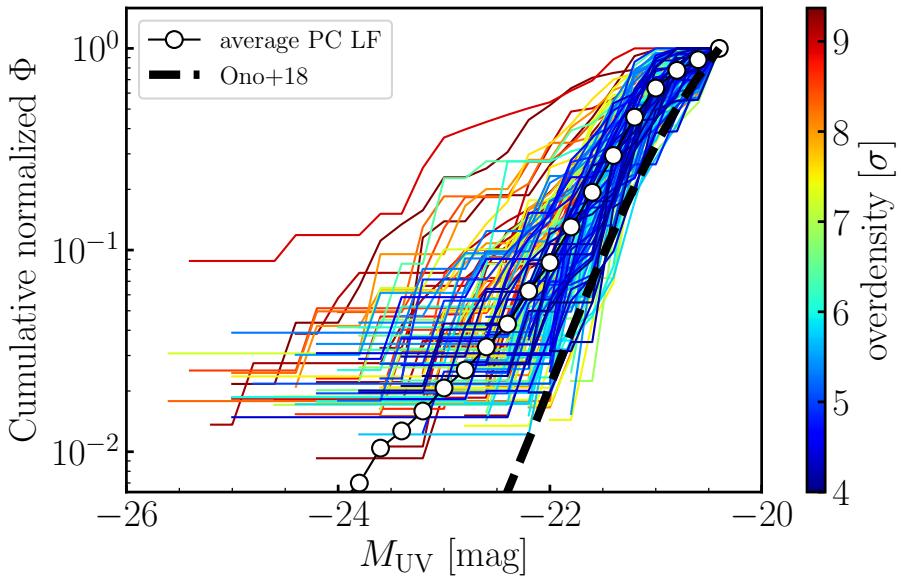

Figure 2.10: The cumulative UVLFs of galaxies in each protocluster candidates. Colors represent their overdensity significance. For reference, the average cumulative luminosity function of protocluster galaxies (black open circles) and the cumulative luminosity function of field galaxies (dashed line) are also plotted.

Section 2.3.5 are employed for the PC UVLF.

We first estimate the UV luminosity density $\rho_{\rm UV}$ from the PC UVLF as $\rho_{\rm UV} = \int_{L_{\rm faint}}^{L_{\rm bright}} L_{\rm UV}\phi(L_{\rm UV})dL_{\rm UV}$. We set $L_{\rm faint} = 2.7 \times 10^{27}$erg s^{-1} Hz^{-1}, corresponding to $M_{\rm UV} = -17$ mag, which is the same as applied in Bouwens et al. (2015), and $L_{\rm bright} = 1.1 \times 10^{31}$erg s^{-1} Hz^{-1}, corresponding to $M_{\rm UV} = -26$ mag.

The FIR ($8-1000\mu m$) luminosity density $\rho_{\rm FIR}$ is estimated as $\rho_{\rm FIR} = \int_{L_{\rm faint}}^{L_{\rm bright}} L_{\rm FIR}\phi(L_{\rm UV})dL_{\rm UV}$ with the use of the IRX-β-M_* relation of $z \sim 3$ LBGs (Álvarez-Márquez et al., 2019). The $\beta - M_{\rm UV}$ relation is known to exist even in protocluster galaxies at $z \sim 4$ (Overzier et al., 2008). The β distribution is determined by using the conversion equation from $i - y$ color to β in Bouwens et al. (2012a). We linearly fit the median value of β distribution in each 0.2 mag magnitude bin of $M_{\rm UV} \leq -20.3$. We use its best-fit parameters with their 1σ error for $\beta - M_{\rm UV}$ relation. We also estimate the $\beta - M_{\rm UV}$ relation of our field galaxies in the same manner and compare it with the literature in Appendix A.2. Our estimation is consistent with literature within the uncertainty, suggesting that our measurement and the sample selection is robust. The stellar mass M_* is estimated from the UV absolute magnitude in the same method in Section 2.4.1 with the correction of IMF from Salpeter IMF to that of what Álvarez-Márquez et al. (2019) use (Chabrier, 2003) by dividing stellar mass by 1.74. From the $\beta - M_{\rm UV}$ relation and the estimated stellar mass, $L_{\rm UV}$ is converted into $L_{\rm FIR}$.

We derive average $\rho_{\rm UV}$ and $\rho_{\rm FIR}$ weighted by the likelihood obtained in the fitting. We employ their minimum and maximum value to estimate the error by varying the parameters of the UVLF/$\beta - M_{\rm UV}$ relation in the range of their 16th and 84th percentiles, respectively. As a result, we estimate the UV/FIR luminosity density of HSC-SSP protocluster galaxies as $\rho_{\rm UV} = 3.46^{+0.35}_{-0.29} \times 10^{28}$ ($3.53^{+0.17}_{-0.16} \times 10^{28}$) erg s^{-1} Hz^{-1} Mpc^{-3}, and $\rho_{\rm FIR} = 1.7^{+0.9}_{-0.9} \times 10^{11}$ ($2.5^{+1.8}_{-1.0} \times 10^{11}$) $L_\odot$ Mpc^{-3} in the case of the Schechter (DPL) function, respectively.

Kubo et al. (2019) conduct stacking analysis of FIR images taken from Planck, AKARI, IRAS, and Herschel at the position of the same HSC-SSP protoclusters. Based on their best fit of the SED model composed of star, dust, and AGN flux components, the total FIR luminosity of all galaxies per protocluster is inferred as $L_{\rm FIR} = 1.3^{+1.6}_{-1.0} \times 10^{13} L_\odot$. In the case of the SED model without the AGN component, it is estimated as $L_{\rm FIR} = 19.3^{+0.6}_{-4.2} \times 10^{13} L_\odot$. As mentioned in Kubo et al. (2019), the best-fit $L_{\rm FIR}$ has degeneracy between two cases, so the uncertainty is quite large. Considering

this point and the effective volume of our protoclusters, our estimation of $\rho_{\rm FIR}$ is consistent with these estimations.

For deriving SFRD, We apply the conversion equation from Kennicutt (1998) to $\rho_{\rm UV}$ and $\rho_{\rm FIR}$, as described below;

$$\mathrm{SFRD} = 1.73 \times 10^{-10} \rho_{\rm FIR} + 1.4 \times 10^{-28} \rho_{\rm UV}. \tag{2.14}$$

As a result, our protocluster galaxies are estimated to have the SFRD corresponding to $\log_{10} \mathrm{SFRD}/(\mathrm{M}_\odot\ \mathrm{yr}^{-1}\ \mathrm{Mpc}^{-3}) = 1.54^{+0.16}_{-0.20}$ $(1.68^{+0.16}_{-0.17})$ in the case of the Schechter (DPL) function. This value is roughly ~ 2.5 dex higher than that of field galaxies (e.g., $\log_{10} \mathrm{SFRD}/(\mathrm{M}_\odot\ \mathrm{yr}^{-1}\ \mathrm{Mpc}^{-3}) = -1.00 \pm 0.06$ in Bouwens et al. (2015)), suggesting that our protocluster regions have active star formation.

Previous studies estimate the SFRD of field LBGs by assuming the IRX $-$ β relation of local starburst galaxies in Meurer et al. (1999). For reference, the SFRD of our protocluster members estimated with this IRX-β relation is $\log_{10} \mathrm{SFRD}/(\mathrm{M}_\odot\ \mathrm{yr}^{-1}\ \mathrm{Mpc}^{-3}) = 1.61^{+0.33}_{-0.45}$ $(1.71^{+0.26}_{-0.31})$ in the case of the Schechter (DPL) function, which is consistent with the original result.

Next, we estimate the fraction of the cosmic SFRD from progenitors of massive halos ($M_{\rm halo} > 10^{14} \mathrm{M}_\odot$). We convert the estimated SFRD, which is per unit volume of protocluster, to that per unit of cosmic volume, and divide it by the field SFRD. The field SFRD is taken from Bouwens et al. (2015) ($\log_{10} \mathrm{SFRD}/(\mathrm{M}_\odot\ \mathrm{yr}^{-1}\ \mathrm{Mpc}^{-3}) = -1.00 \pm 0.06$). Using other estimates (e.g., van der Burg et al., 2010; Bouwens et al., 2009) changes the result by only ~ 0.1 dex.

In addition, our protocluster sample is not complete for all progenitors of dark matter halos of $M_{\rm halo} > 10^{14} \mathrm{M}_\odot$ at $z \sim 0$. Some fraction of dark matter halos with overdensity below 4σ at $z \sim 4$ will also evolve into such halos. We can identify such progenitor halos in the simulation of Toshikawa et al. (2018, 2016). The fraction of halos that can be observed by our protocluster selection with a galaxy overdensity significance greater than 4σ at $z \sim 4$ is about $6.2 \pm 1.0\%$, suggesting that our sample has a very high purity but low completeness. The fraction of halos can be translated to the fraction of member galaxies based on the overdensity distribution of progenitor halos, which is equivalent to $9.67 \pm 0.41\%$. Most of the non-observed member galaxies should be hosted by progenitor halos whose overdensity significance is less than

4σ. With a simple assumption that the UVLF of these galaxies is the same as our PC UVLF, we can derive the intrinsic contribution of progenitor of massive halos to the cosmic SFRD by dividing by this completeness. We mention that the shape of PC UVLF depends on the overdensity, but the main difference of the shape is at $M_{\rm UV} < -22$, which does not significantly affect the SFRD measurement.

Moreover, 76% of our protocluster sample are expected to evolve into $M_{\rm halo} > 10^{14}{\rm M}_\odot$ at $z \sim 0$ (Toshikawa et al. (2018)), so we correct the purity by multiplying this ratio. Finally, we estimate that the $9.4^{+4.7}_{-3.4}$% ($13.9^{+6.5}_{-4.9}$%) of the cosmic SFRD occurs in progenitors of massive halos in the case when we use the best fit of the Schechter function (the DPL function).

We compare this measurement with the prediction from the SAM in Chiang et al. (2017). They focus on galaxies with $\log(M_*/{\rm M}_\odot) > 8.5$ in progenitors of cluster of $M_{200} > 10^{14}{\rm M}_\odot$ at $z \sim 0$, and estimate that the contribution of protocluster galaxies is about 24 (19)% at $z \sim 4$ when they use Henriques et al. (2015) (Guo et al., 2013) SAM. The comparison between the observed and predicted fraction of protocluster galaxies in the cosmic SFRD is shown in Figure 2.11. Our result is close to the theoretical prediction but slightly lower.

Assuming that the theoretical prediction is correct, there are two possible explanations for the discrepancy between it and this study. The first possibility is that the study includes only UV-bright galaxies, and although their star formation rates are dust-corrected, it misses other galaxy populations, such as SMGs, that would not be selected by LBG selection. However, the contribution of galaxy populations other than LBGs to CSFRD can be considered not significant for the following reasons. According to Bouwens et al. (2015), the SFR obtained from rest-UV of LBG and the SFR obtained from FIR are comparable in the general field. In addition, according to Zavala et al. (2021), the SFRs obtained from FIR and rest-UV are approximately equal for all galaxies at $z \sim 4$. Since the SFR obtained from rest-frame UV for galaxy populations other than LBGs should not be large, their SFR obtained from FIR should also not be large, considering the above two observational results. A recent result of Bouwens et al. (2020) suggests the insignificant contribution of Ultra-Luminous Infrared Galaxies (ULIRG, $L_{\rm IR} > 10^{12}L_\odot$), which can not be selected from LBG selection, to the CSFRD based on the ALMA observation of LBGs. These observational results support the above expectation. Therefore, if this is the same for protocluster, we can assume that

LBGs are responsible for most of the contribution to the SFRD.

On the other hand, recent studies report highly overdense regions of SMGs (e.g., Oteo et al., 2018; Miller et al., 2018; Daddi et al., 2021; Mitsuhashi et al., 2021). Also, Marrone et al. (2018) report two SMGs are located in a small separation, implying that they are located in a massive halo. These dusty star-forming galaxies have quite high SFR, which can impact the value even if their number is small. If such an overdense region of SMGs, which is not found in the general field, ubiquitously exists in the protoclusters, they may explain the discrepancy between our results and those of Chiang et al. (2017). The FIR luminosity of the stacked SED of the HSC-SSP protocluster naively supports this (Kubo et al., 2019). Although it has a large degeneracy dependent on the SED model, the SFRD combined with the UV luminosity density estimated in this work and the stacked FIR luminosity is consistent with the theoretical prediction within the uncertainty. This FIR luminosity, estimated from the stacking, includes the contribution of UV-undetected SMGs, so this does not reject that SMG may be one of the reasons.

Second, we may miss some members located at the outskirts of massive protoclusters. This is because we define the protocluster members according to the predicted size of the progenitor of “Fornax-type" clusters, which should be smaller than the progenitors of more massive clusters, like “Coma-type" clusters.

We can compare our observational result with the prediction of the hydro-dynamical simulation. Yajima et al. (2021) conduct a cosmological hydrodynamical simulation of the ten most massive halos, which are likely to be protocluster regions, at $z \sim 2$ with each volume of $(28.6\mathrm{cMpc})^3$. They estimate these protoclusters at $z \sim 3$ possess the integrated SFR as $3400 - 6200\mathrm{M}_\odot/\mathrm{yr}$ for each (Figure 4 of Yajima et al., 2021) when assuming the same Salpeter IMF as ours. Based on our observed SFRD in protoclusters, our protocluster regions have $5600 - 17000\mathrm{M}_\odot/\mathrm{yr}$ within the same volume for each. This value is broadly consistent with their prediction within the uncertainty of the measurement, though it is slightly higher. This trend is opposite to the situation of what we saw when we compare our result with Chiang et al. (2017). This is probably because the model does not sample such extremely dense regions due to the limitation of the simulation box, while the observation focuses only on galaxy-dense regions with extremely high overdensities as 4σ at $z \sim 4$, which leads to higher SFR. The observational criterion of overdensity $> 4\sigma$ is intended to securely select protoclusters,

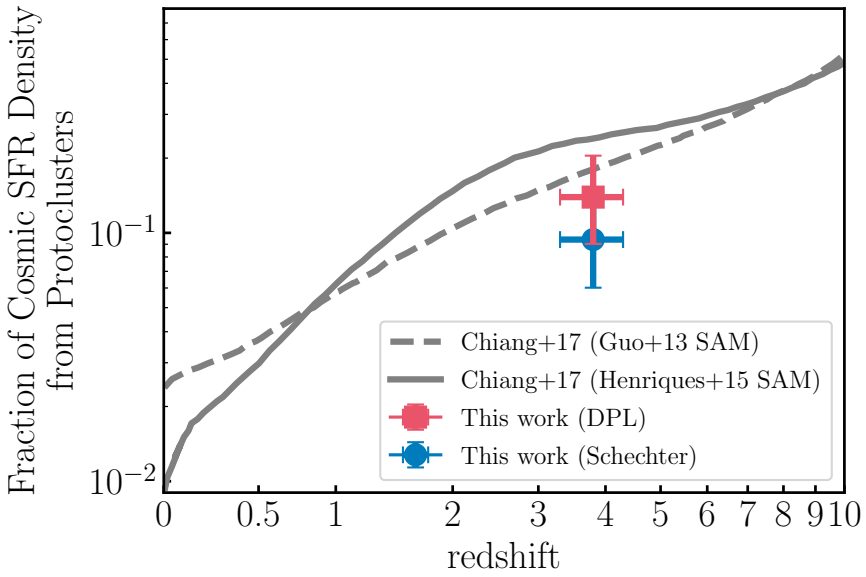

Figure 2.11: The fraction of the cosmic SFRD in protoclusters. Blue circle and red square represent our estimated value for HSC-SSP protoclusters at $z \sim 4$ assuming that PC UVLF follows Schechter function and DPL function, respectively. Gray solid and dashed lines are its predicted evolution in Chiang et al. (2017) with the use of the semi-analytical model of Henriques et al. (2015) and Guo et al. (2013), respectively.

whereas, of course, there are far more protoclusters with overdensity less than 4σ. It should be noted that the difference in overdensity criterion between the two samples was corrected in comparison with Chiang et al. (2017). This is likely to be why we do not see such a feature in that comparison.

2.5 Possible AGN Contribution to Bright-end Excess

Several studies have argued that the bright-end ($M_{\rm UV} \leq -23.0$) of the UVLF at $z \sim 4$ is mainly dominated by AGNs (e.g., Adams et al., 2020; Ono et al., 2018). Here, we discuss how well the contribution due to the AGNs can explain the bright-end excess that we found in the PC UVLF for $M_{\rm UV} \leq -20.8$. We conduct three discussions, i.e., comparison with the literature, the AGN fraction of the sample based on the morphological information, and the SED fitting analysis.

2.5.1 Comparison with literature

As in Section 2.4, the WIDE protoclusters and its PC UVLF are used for the discussion in this subsection.

First of all, we compare our PC UVLF to the field quasar UVLF. Akiyama et al. (2018) construct the quasar UVLF at $z \sim 4$. The number density of quasars based on the best-fit DPL function for the magnitude range of $-25.8 < M_{\rm UV} < -20.8$, which is the range where our PC UVLF has an excess, is about $(0.9 - 10) \times 10^{-7}$ Mpc^{-3} mag^{-1}. This value is $(1 - 240) \times 10^3$ times lower than the excess at the bright-end that we found in the study. In addition, we have found that UV-luminous quasars scarcely exist in the protoclusters at $z \sim 4$ (Uchiyama et al., 2018, 2020), suggesting that the number density of luminous quasars in protoclusters should not be larger than that in the field.

The difference between PC UVLF and the field UVLF in the magnitude range of $M_{\rm UV} \leq -20.8$ corresponds to 16 objects per protocluster. The expected total number of members in a protocluster is about 50, indicating that the bright-end excess corresponds to about 32% of the total protocluster members. If we assume that all of the excess at the bright-end is due to the AGN, such a high AGN fraction in protoclusters is inconsistent with previous studies. For example, Toshikawa et al. (2016) make follow-up spectroscopy for protocluster member candidates, and they do not find any AGN in 11 members in a protocluster at $z \sim 3$, suggesting that the AGN fraction is less than 9%. Assuming that the same upper limit for the AGN fraction, the expected number of AGNs in a protocluster is less than five out of 50 members. Other studies show similar AGN fractions for protoclusters from X-ray counterparts. Lehmer et al. (2009) estimate AGN fraction ($9.5^{+12.7}_{-6.1}$ percent) for LBGs in the SSA22 protocluster at $z = 3.09$. Macuga et al. (2019) estimate AGN fraction as $2.0^{+2.6}_{-1.3}$ percent for HAEs in the USS1558-003 protocluster at $z = 2.53$. Krishnan et al. (2017) investigate AGNs in a protocluster called Cl 0218.3 − 0510 at $z = 1.62$ and estimate that AGN fraction of massive ($\log(M_*/{\rm M}_\odot) > 10$) protocluster galaxies is 17^{+6}_{-5} percent. Though they argue that this value is high compared to that of the blank field at the same redshift, it is not enough to explain the bright-end excess of our PC UVLF. It should be mentioned that the AGN fraction estimated from the X-ray detection can be sensitive to its depth, but these comparison implies that protoclusters at $z \sim 4$ are less likely to host such amount of UV-bright AGNs.

We note that residuals at $M_{\rm UV} < -23.0$ of PC UVLF from the best fit of the Schechter (DPL) correspond to 1.5/0.5 objects per protocluster. This seems to be reasonable for the AGN fraction in a protocluster; therefore, a part of the bright-end excess can be contributed by the AGN.

2.5.2 AGN fraction from morphological properties

Based on the recent studies, the size in the rest-frame UV light indicates the transition from the star-formation dominated system (i.e., galaxies) to the AGN dominated systems. Bowler et al. (2021) show that the number of sources with point source morphology ($r_{1/2} < 0.1$ arcsec) continues to increase towards the bright-end of the UVLF, and together with evidence from spectral features, the AGN fraction increase rapidly. Here, $r_{1/2}$ is the half-light radius of the source. If the enhancement of AGNs primarily causes the bright-end excess, the AGN fraction estimated from the number of point source objects should be higher for protocluster galaxies than for field galaxies. Here, we derive the AGN fraction of protocluster galaxies and field galaxies from their morphology and discuss its possible excess due to the environment.

The effective radius is derived from the i band image of the HSC-SSP S21A data, which is the latest imaging product of the HSC-SSP. We use the GALFIT (Peng et al., 2010a) for the size measurement. The input images are cut to 100pixels×100pixels, which corresponds to 16.8arcsec × 16.8arcsec. Surrounding objects are masked out. The sky, which is the standard deviation of the source-masked images with 200pixels × 200pixels, is subtracted from the images. We use the "coadd PSF" (Bosch et al., 2018) as an input PSF image, which is needed to decompose the observed light profile. In GALFIT, we fit galaxy images with a single-component Sérsic profile. The HSC-SSP images do not have the image quality to constrain the Sérsic index precisely; therefore, we run GALFIT with eight different Sérsic indexes from $n = 0$ to $n = 4$ and derive the effective radius for the case with the smallest chi-square in the fitting. The standard deviation of these cases is employed as the size measurement error. In the fitting, sources near target galaxies are masked to minimize confusion. The effective radius is derived in the range of 0.1pixel $< r_e <$ 20pixel under the condition that the offset of the center position from the HSC-SSP coordinate and the offset of the i band magnitude from the HSC-SSP coordinate are within three pixels, and within one magnitude,

respectively. We estimate the quality of the size measurement in Section A.4 and find that the HSC-SSP images in the DEEP/UltraDEEP layer provide the accurate size of galaxies with $m_i < 25$, where the bright-end excess is seen in the PC UVLF (Figure 2.3). A possible systematic bias of the HSC-SSP size measurement is negligible (≤ 0.05 dex), and its scatter is ≤ 0.2 dex, but it depends on the magnitude, the size, and the image quality. Therefore, we correct the bias as a function of the magnitude and sizes for each region (tract/patches). In addition, there are regions in which the size measurement has a larger scatter than other fields, possibly due to the bad seeing and the shorter integration time (Figure A.7). We remove objects in such regions. For a more detailed analysis method and discussion, please refer to Section A.4.

Here, we focus on g-dropout galaxies in DEEP/UltraDEEP layers of the S20A data release, where the depth is deeper than the WIDE layer. Protocluster galaxies are defined in the same way as in Section 2.2.5, as objects within 1.8′ around the $\geq 4\sigma$ overdensity peak. Field galaxies are also used as a reference, defined as other g-dropout galaxies apart from protoclusters in the entire field of DEEP/UltraDEEP layers. The total number of protocluster and field galaxies is 225 and 19441, respectively.

In Figure 2.12, we show the size-luminosity relation of protocluster galaxies and field galaxies. The absolute magnitude is calculated in the same way as described in Section 2.3.1. Our measurements are consistent with the size-luminosity relation at $z \sim 4$ of Bowler et al. (2021). According to the definition of Bowler et al. (2021), we classify objects with $r_e < 0.1$ arcsec (brown hatched region in Figure 2.12) as AGNs.

In Figure 2.13, we show the AGN fraction of protocluster galaxies and field galaxies. Though our protocluster sample only constrains a few bins due to the small sample size, there is no significant difference between protocluster and field galaxies. If all bright-end excess is contributed from AGNs, not galaxies, this AGN fraction should be higher in protocluster galaxies than field galaxies. Therefore, this result does not support particularly the enhancement of the AGNs in the bright-end of the PC UVLF. We note that the AGN fraction might be overestimated in the faintest bin since the outskirt of size-luminosity relation enters the AGN selection criteria at $M_{\rm UV} < -22$ (c.f., Shibuya et al., 2015; Bowler et al., 2021), but this applies to both protocluster and field sample and does not change the conclusion.

We note that the low-z contaminants, which should have larger sizes than AGNs at high redshift, can decrease the amplitude of this relation. Especially, the bending of

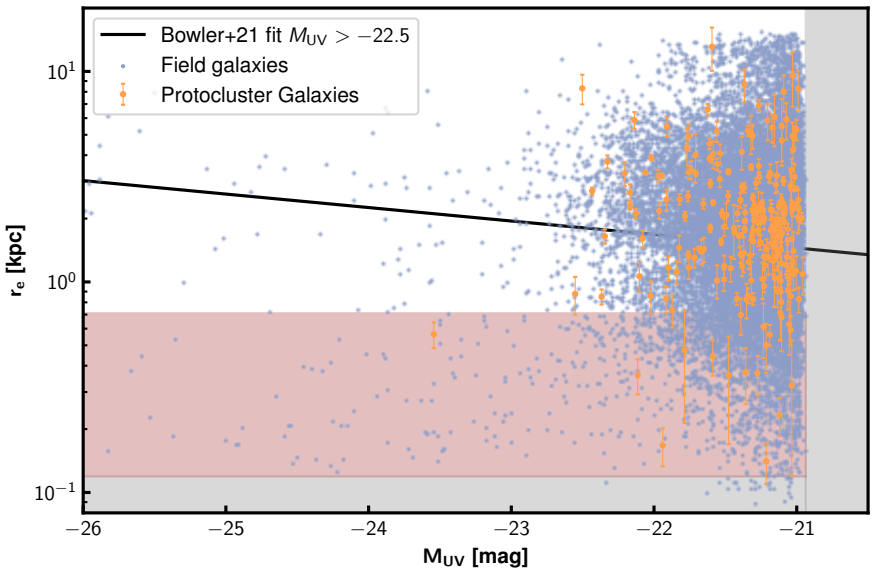

Figure 2.12: Size-luminosity relation of protocluster galaxies (orange) and field galaxies (blue). The black solid line shows the best-fit of the size-luminosity relation in Bowler et al. (2021). The brown hatched region shows the selection criteria of AGNs. The gray hatched region is not focused due to the large uncertainty of the size measurement.

the AGN fraction of field galaxies at the brightest magnitude might be due to this contaminant. To exclude this effect, we examine the AGN fraction of galaxies with $z_{\rm phot} > 3$ by using the result of Section 2.5.3. The trend of the insignificant difference of the AGN fraction between protocluster galaxies and field galaxies is the same, but the bending of field galaxies without being seen (the right-color marker of Figure 2.13). Therefore, our conclusion does not change if we consider them. It should also be noted that this protocluster sample is selected in the projection, so it includes field LBGs outside the protoclusters. On the other hand, the number of real protocluster galaxies is much larger than the field LBGs. Therefore, if all of the bright-end excesses are due to AGNs, the AGN fraction still should be higher in protoclusters.

2.5.3 AGN properties from SED fitting analysis

We conduct the SED fitting analysis for protocluster galaxies by using the multi-color dataset of the HSC-SSP joint catalog. In the SED fitting, protocluster galaxies are

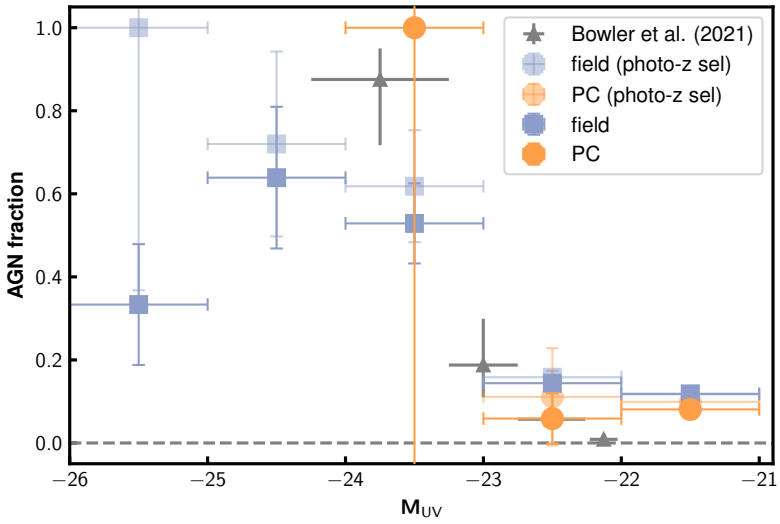

Figure 2.13: AGN fraction of protocluster (orange) and field (blue). The right color markers show those estimated only focusing on objects with high redshift solution of photo-z. The gray triangles are the AGN fraction estimated in Bowler et al. (2021). We note that the AGN fraction might be overestimated in the faintest bin since the outskirt of size-luminosity relation of galaxies enters the AGN selection criteria at $M_{\rm UV} < -22$ (c.f., Shibuya et al., 2015; Bowler et al., 2021).

divided into two groups. One is objects with VIRCAM photometry, and the other is those with WFCAM photometry. Protocluster members with counterparts of the joint-catalog within one arcsec are further discussed. A small fraction of the former groups also have photometry of WFCAM, and these photometries are also used in the SED fitting. This classification is motivated by the possibility that such filter configuration differences might induce the quality difference of the SED fitting. Other than this NIR photometry, the broadband photometry of $UgrizY$ is used (see Section 2.2.1 for more details of the data information). In these groups, protocluster galaxies with $i < 25$ are focused on investigating the bright-end excess property, the same as in Section 2.5.2, which leads to the sample number of sources with VIRCAM and WFCAM photometry of 109 and 152, respectively.

We use the SED fitting software CIGALE (Boquien et al., 2019). We use the single stellar population model of Bruzual & Charlot (2003) with the initial mass function (IMF) of Chabrier (2003) and the solar metallicity. The star formation history is followed by the delayed SFR, i.e., SFR $\propto \frac{t}{\tau^2} \exp(-t/\tau)$, where t is time from since the onset of star formation. The τ is assumed to be 0.1Gyr $< \tau <$ 11Gyr in addition to $\tau = 0, \infty$. The nebular emission is included based on Inoue (2011). The dust attenuation is modeled based on Calzetti et al. (2000) (see Boquien et al., 2019, for more detail). Inter galactic absorption is considered by using the model of Meiksin (2006). These model assumption is set to be similar to MIZUKI code Tanaka (2015), which will be used in Chapter 3 and Chapter 4. Lastly, the AGN models of Fritz et al. (2006) is included.

Protocluster galaxies are defined based on the projected distance from the overdensity peak. Therefore, this sample might have some fraction of contamination of the low-z galaxies. The contamination fraction, which is defined as the fraction of objects with best-fit photo-z outside of $3.3 < z < 4.3$, is 19(22)% in the VIRCAM (WFCAM) sample, respectively. Hereafter, we exclude these objects and compare the properties of protocluster galaxies with those of field galaxies. It should be noted that field galaxy subtraction is not conducted in the analysis, same as in Section 2.5.2.

The brightness of objects is correlated with their properties. To minimize the bias due to the brightness differences and only focus on the property difference due to their living environment, we randomly select field galaxies and construct a field sample with the same rest-frame UV magnitude distribution. The field sample number is set to be twice of the protocluster galaxy sample to reduce the effect of the sample variance on

the result. In addition, galaxies located at lower redshift are excluded similarly to protocluster galaxies.

Figure 2.14 and Figure 2.15 show the distribution and the correlation among derived parameters, i.e., the AGN fraction, SFR, stellar age, τ, and stellar mass. The leftmost panels compare the AGN fraction of protocluster galaxies, the ratio of the AGN flux to the total flux, with that of field galaxies. The Kolmogorov-Smirnov (KS) test does not reject the null hypothesis that the two distributions of the AGN fraction are the same. Therefore, this result does not provide clear evidence that bright protocluster galaxies have higher AGN activity than field galaxies. In addition, we do not find any differences between protocluster galaxies and field galaxies by conducting the KS test for other parameters. This implies that protocluster galaxies may have similar properties with field galaxies at the same rest-frame UV brightness (i.e., SFR), which is roughly consistent with reports of the environmental-independent star formation main sequence (e.g., Long et al., 2020; Shi et al., 2019b; Koyama et al., 2013). We note that such indifferent properties might be partly due to the uncertainty of the derived information of the SED fitting analysis, including the photometric redshift. In the near future, the Spitzer photometry will be included in the HSC-SSP joint catalog (SHIRAZ), which will significantly improve the accuracy of the SED fitting.

Based on these three discussions in Section 2.5.1, 2.5.2 and 2.5.3, we conclude that AGNs are unlikely to explain all of bright-end excess in the PC UVLF. It should be noted that we here discuss the UV-bright AGNs, and we do not include obscured AGNs. As mentioned in Section 2.4.3, Kubo et al. (2019) stack various IR images and estimate the total FIR luminosity of the protocluster sample used in this study. Their results imply that HSC-SSP protoclusters can include a population of UV-dim AGNs. However, they are unlikely to contribute to the bright-end excess of UVLF, since they are UV-dim.

2.6 Properties of Brightest Protocluster Galaxies

We show that more rest-frame UV bright objects exist in the protocluster regions from the shape of the rest-frame UV luminosity function, and all of them are not likely to be AGNs according to the AGN fraction of protocluster galaxies in the literature, their morphology, and the best-fit of the SED fitting. Here, we briefly introduce the

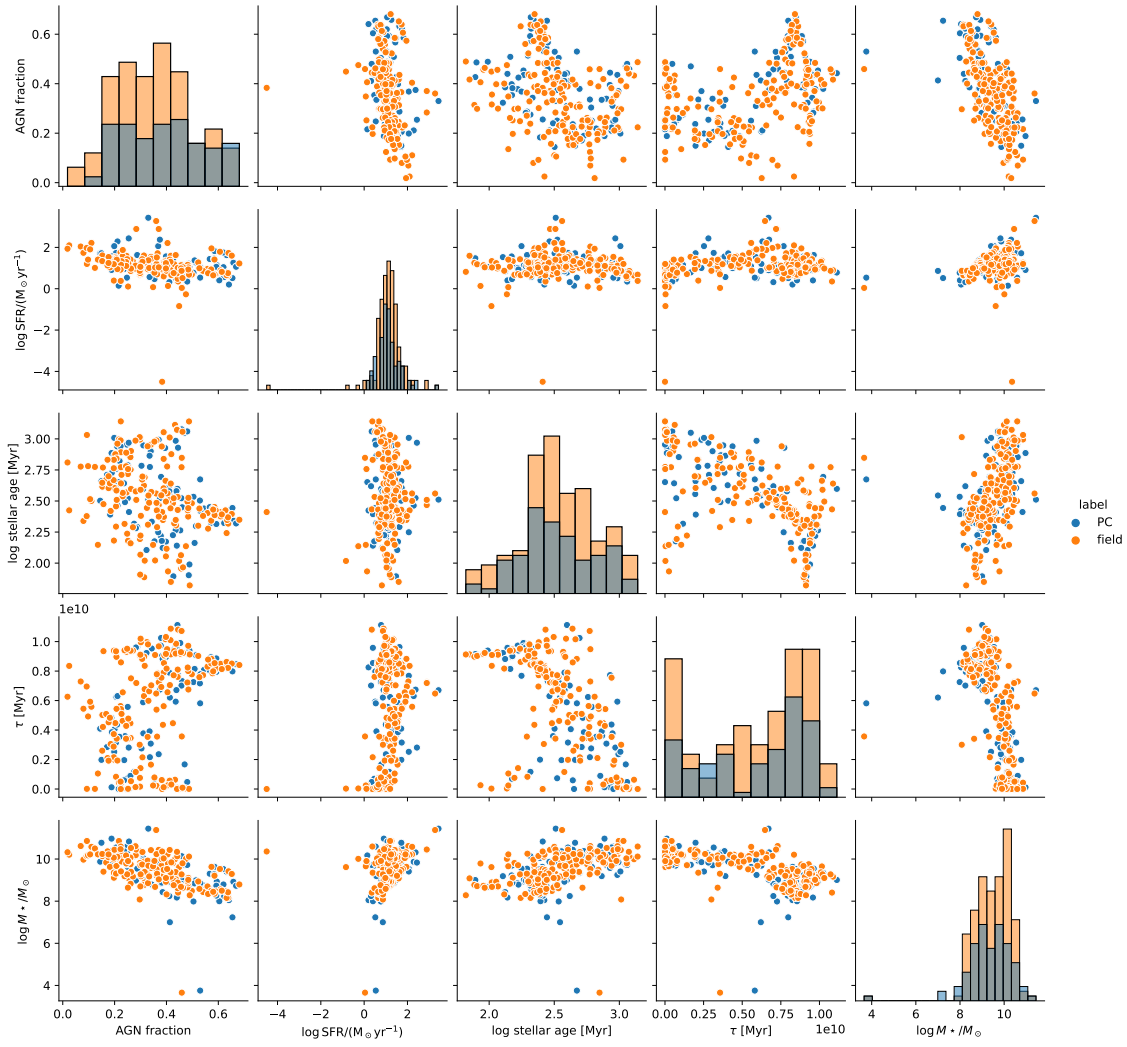

Figure 2.14: Distribution and correlation among the derived parameters of protoclusters (blues) and field galaxies (oranges) observed in the VIRCAM.

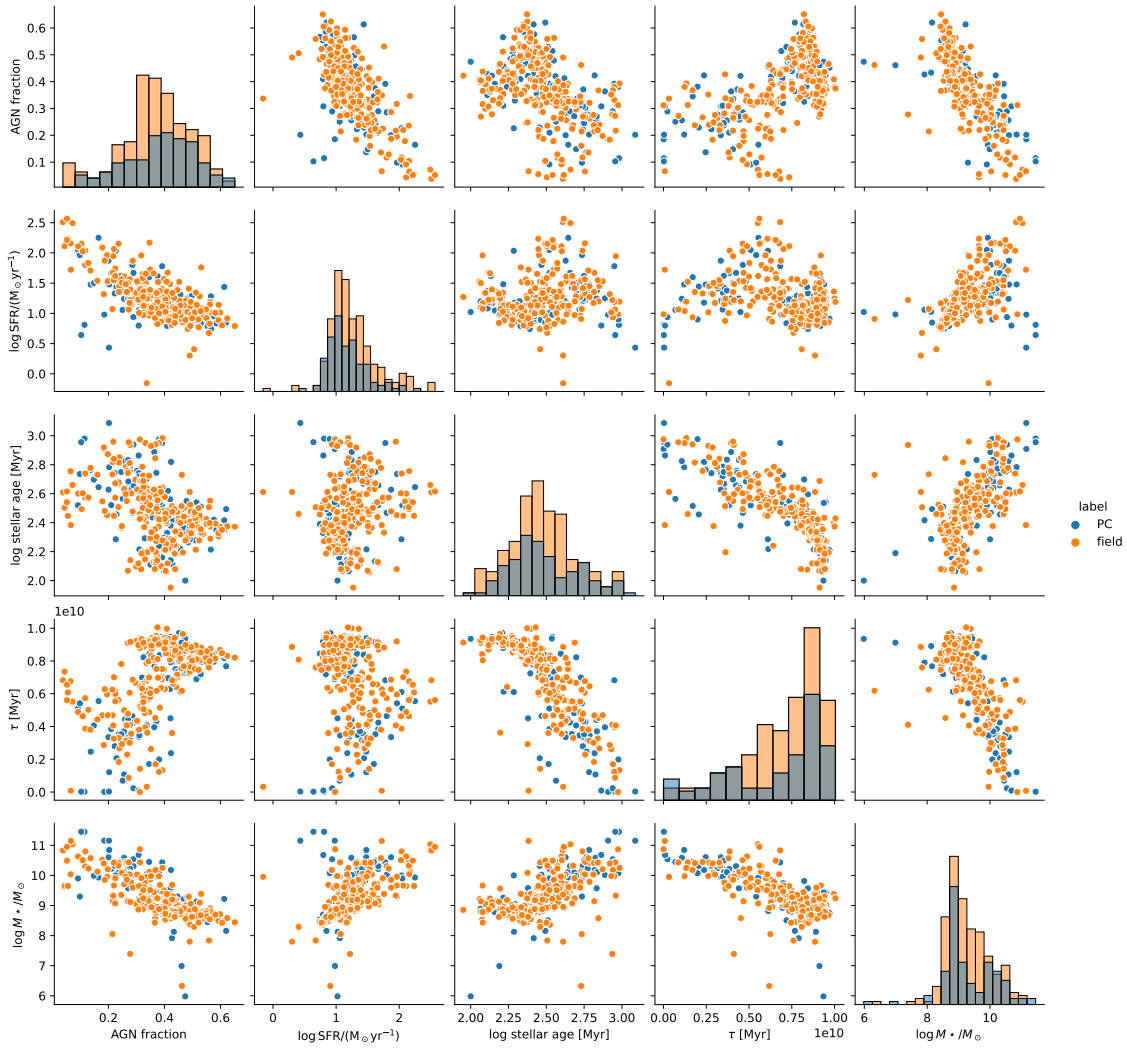

Figure 2.15: Distribution and correlation among the derived parameters of protoclusters (blues) and field galaxies (oranges) observed only in the WFCAM.

properties of the uniquely brightest galaxies in protoclusters, located in the magnitude range of the bright-end excess of the PC UVLF. This result is taken from Ito et al. (2019).

2.6.1 Sample selection

We only focus on uniquely brightest galaxies in protoclusters, defined as the brightest galaxies whose magnitude is more than one magnitude brighter than the fifth brightest protocluster galaxies. Here, we use the slightly larger protocluster scale as 3′ (1.3 physical Mpc at $z \sim 3.8$) than in the rest-UV luminosity function analysis. In total, we select the 63 brightest protocluster galaxies for this analysis. Their magnitude ranges in $21.34 < m_i < 23.68$, which are overlapped with the magnitude range where the bright-end excess of the PC UVLF is seen. They do not always live in the peak of the overdensity but are located in various place of protoclusters. This might be due to the uncertainty of peak location of overdensity map or the fact that they will move through dynamical interaction with other galaxies.

2.6.2 Comparison of properties

We first compare the rest-frame UV colors of the 63 brightest protocluster galaxies with those of field galaxies. The rest-UV color, equivalent to the rest-frame UV continuum slope, depends on the rest-frame UV brightness (e.g., Bouwens et al., 2009). Therefore, we compare them after matching the rest-frame UV magnitude of both samples. We here take the average magnitude at the middle wavelength between the i-band and z-band, as mag=$(i + z)/2$. To obtain the average color distribution of field galaxies, we randomly select objects in each bin. We choose field galaxies as many the brightest protocluster galaxies whose magnitude distribution is to be matched and repeat this procedure 100 times. The color distribution is shown in Figure 2.16. The magnitude distributions of both samples are shown in their insets. Their average $i - z$ color is (0.1771 ± 0.0254) mag and (0.1423 ± 0.001) mag for the brightest protocluster galaxies and field galaxies, respectively. This result shows that the brightest protocluster galaxies are redder ($\Delta(i - z) \sim 0.03$) than field galaxies. The result of the Anderson-Darling test suggests that the p-value $p = 1.1 \times 10^{-2}$, so we reject the null hypothesis that these two color distributions are drawn from the same parent population at the 2σ level.

Next, we compare their rest-frame UV size with that of field galaxies. Since these brightest protocluster galaxies are in the Wide layer, it is not easy to measure the size of individual objects due to the shallowness of the image. Therefore, we conduct the stacking analysis of images and derived the average effective radius. The stacking procedure is conducted with the following four steps. We first generate postage stamps in the i-band with a size of 8" × 8", which corresponds to 3.35×10^3 physical kpc^2 at $z \sim 3.8$. Secondly, we smooth all of the images to 0.806", which is the worst full width at half the maximum of their point spread function. To avoid weighting brighter objects, we thirdly normalize each image to the peak count of objects. We finally stack the images using the `Imcombine` task in the IRAF package and apply the average stacking. Following Momose et al. (2014), we applied 3σ clipping to remove unusually bright pixels. The central position of each object was based on the HSC catalog.

We measure the effective radius of the stacked images to compare our results with those of a previous study. We use GALFIT to fit the two-dimensional surface brightness profile, the same as in Section 2.5.2. For simplicity, we fix Sérsic index as $n = 1.5$ and fit the Sérsic index profile. We calculate the effective radius r_e, by converting the effective radius along the semi-major axis $r_{e,\mathrm{major}}$ through $r_e \equiv r_{e,\mathrm{major}}\sqrt{q}$, where q is the axis ratio of the object. We estimate the errors in the effective radii of these stacked images using the following procedure. First, we make an image of Gaussian random noise equivalent to a 1σ error in the radial profile and then repeat this procedure 1,000 times. Second, we apply GALFIT to each image and obtain the effective radius distribution. Finally, we use that the average value of this distribution as the typical value of the effective radius and its $16^{\mathrm{th}}/84^{\mathrm{th}}$ percentile as the error of the effective radius due to the uncertainty of the stacked image. We obtain an effective proto-BCG radius of $r_{e,\,\mathrm{BCG}} = 2.042^{+0.012}_{-0.013}$ kpc and that of field galaxies of $r_{e,\,\mathrm{Field}} = 1.597^{+0.003}_{-0.003}$ kpc. We find that the effective radius of the brightest protocluster galaxies is slightly larger than that of the field galaxies. These estimated values are compared to the rest-UV size-luminosity relationships of the dropout galaxies at $z \sim 4$ from Shibuya et al. (2015) in Figure 2.17. Our measurement of the effective radius of the field galaxies is consistent with Shibuya et al. (2015), and the size of the brightest protocluster galaxies is slightly larger ($\sim 28\%$).

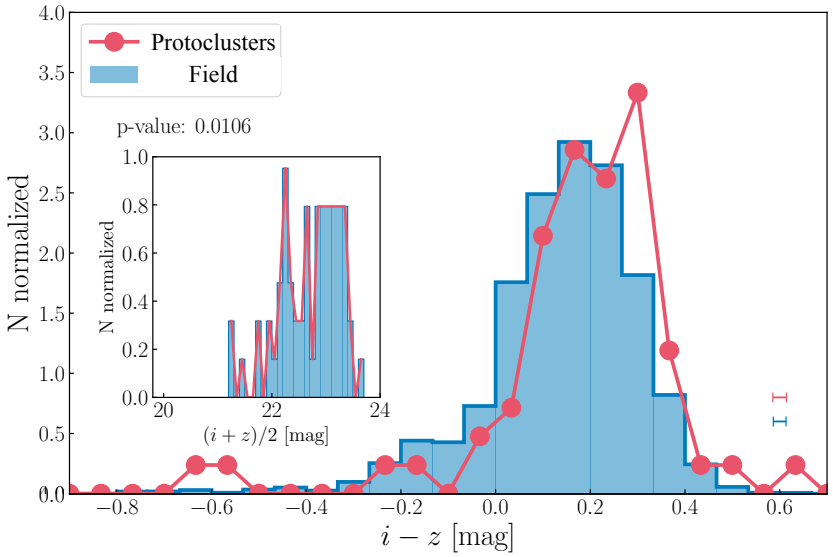

Figure 2.16: The color distribution between magnitude-matched field galaxies and the other samples. The red line in each panel shows the color distribution of the brightest protocluster galaxies. The blue histogram in each panel represents the $i-z$ distribution of magnitude-matched field galaxies. In each inset, $(i+z)/2$ distributions of field galaxy sample (blue) and its comparison samples (red). The error bars at the lower-right corner in each panel illustrate mean uncertainties in $i-z$.

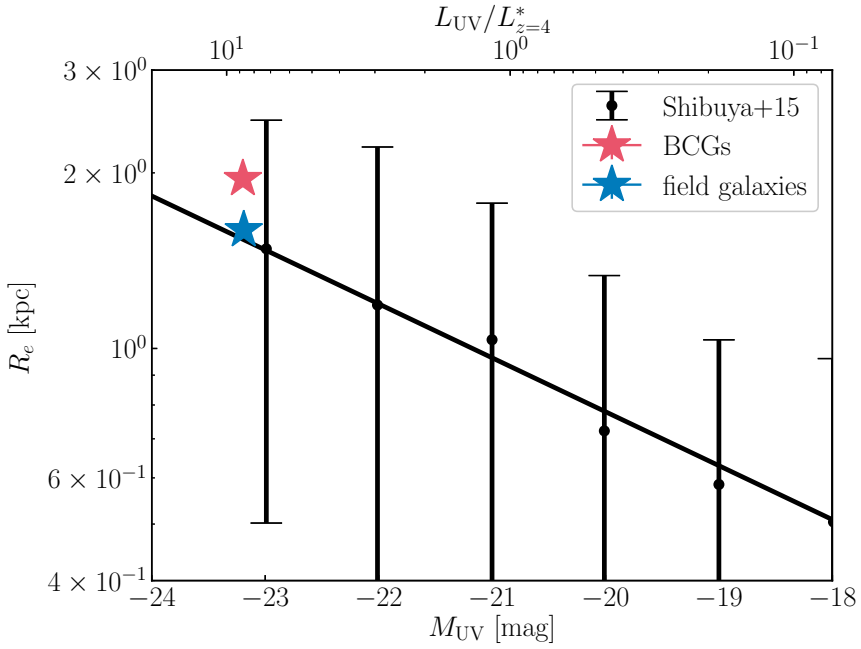

Figure 2.17: The comparison of effective radii of the stacked image of proto-BCG candidates and field galaxies to Shibuya et al. (2015). The red star represents the effective radius of proto-BCG candidates, while the blue star represents that of field galaxies sample. The solid black line and the points with error bars is the size-luminosity relation of the distribution of dropout galaxies at $z \sim 4$ from Shibuya et al. (2015). The error bars is the 16^{th} and 84^{th} percentiles of the effective radius of galaxies.

2.6.3 Implication of property differences

These results suggest that brightest galaxies have distinguished properties from field galaxies even at $z \sim 4$. The redder rest-frame UV color can be occurred by dust enrichment, older age, or the enhancement of the metallicity. Bouwens et al. (2009) use the SED model of U-dropout galaxies at $z \sim 2.5$ assuming Saltpeter IMF, and they investigate the effect of several properties of galaxies to the value of its rest-frame UV slope β (see their Figure 7). They argue that the amount of dust is the most effective to the change of β. Our brightest protocluster galaxies are ~ 0.03 mag redder than other field galaxies, and it corresponds to $\Delta\beta \sim 0.3$ according to the conversion equation between $i - z$ and β in Overzier et al. (2008). Assuming the relationship between the change of β and that of other properties is the same for $z \sim 3.8$ g-dropout galaxies, brightest protocluster galaxies have to be ~ 0.9 dex older than field galaxies on average if the age difference is the only cause for the color difference. Our brightest protocluster galaxies and field galaxies are LBGs, generally young galaxies, so it is unlikely that the only brightest protocluster galaxies have such older ages. In addition, the difference of the metallicity needs to be greater than that of the case of age to explain such UV color difference. Therefore, We can interpret the dust enrichment causes the redder color in the rest-frame UV.

The brightest protocluster galaxies are the most massive objects among LBGs in protoclusters. By using M_*-M_{UV} (SFR) relations Song et al. (2016), which derived a M_*-M_{UV} relation, their average stellar mass is derived from the average absolute magnitude of $M_{\rm UV} = -23.20$ as $\log(M_\star/M_\odot) = 10.87$. These objects can evolve into the most massive galaxies in local clusters, called “brightest cluster galaxies (BCGs)." With the assumption of this hypothesis, by comparing the average size of our brightest protocluster galaxies with those of BCGs, we can discuss their evolution track. Figure 2.18 shows a comparison between the size-stellar mass growth of BCGs and massive galaxies reported in previous papers. Compared to the evolution tracks of massive quiescent galaxies (Kubo et al., 2018), BCGs are shifted towards larger sizes. Also, according to a simple toy model, the mass and size growth by the major merger is followed by $r_e \propto M_*$, while the growth by the minor merger is followed by $r_e \propto M_*^2$ (Bezanson et al., 2009; Naab et al., 2009). We move both models track in order to overlap our data and find the fit line of the minor-merger schema to be in good agreement with

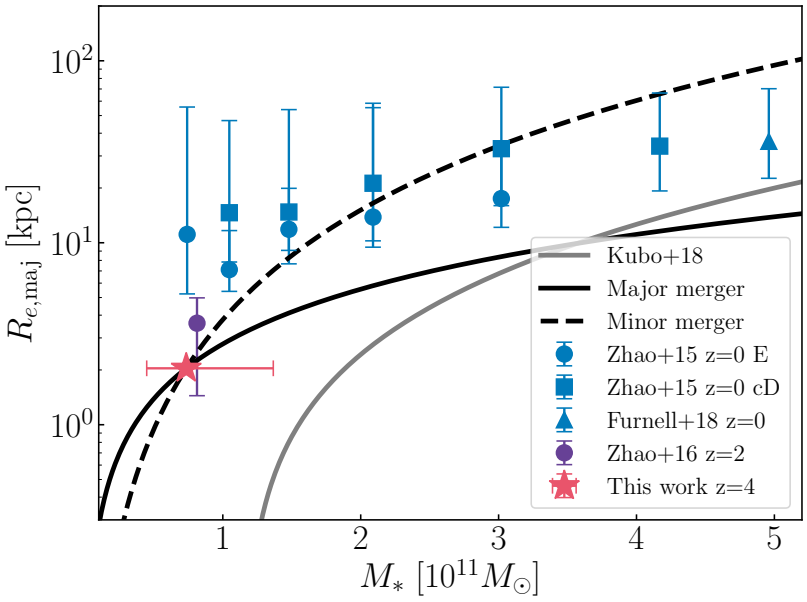

Figure 2.18: Size-mass relation. The red star represents the size of the median stacked images of the rest-frame UV brightest protocluster galaxies. To compare previous study, we plot BCGs at $z \sim 2$ (A purple circle, Zhao et al., 2015), $0.05 < z < 0.3$ (Blue triangles, Furnell et al., 2018), $0.05 < z < 0.1$ (Blue circles and squares, Zhao et al., 2015). The solid black line and the dashed line represents the mass growth trend by major merger and minor merger from this work, respectively (Bezanson et al., 2009; Naab et al., 2009). The solid gray line represents the massive quiescent galaxies obtained in Kubo et al. (2018).

the results reported by Zhao et al. (2015); Furnell et al. (2018). If our proto-BCGs evolve exclusively by minor mergers with local BCGs, we expect that our proto-BCG will evolve into local BCGs with $\sim 3 - 4 \times 10^{11}\ M_\odot$ in Zhao et al. (2015).

2.7 Discussion of Chapter 2

2.7.1 Possible confusion limit

We have evaluated the sample incompleteness in the same manner as most of the other studies of field LBGs (Section 2.3.3), and find that it is consistent with previous studies

by comparing it with the field UVLF. However, another possible incompleteness could be caused by object confusion in crowded regions, such as in protoclusters. In some overdense regions, some fraction of galaxies will be mixed with nearby objects, which could lower the completeness. Our finding of a flatter UVLF in protoclusters than in the field UVLF could be due to this confusion effect, which might more significantly affect fainter galaxies. The luminosity function shape could change, as seen in this study.

We check this effect by inserting mock galaxies into an overdense region to compare the completeness function in the overdense region with that in the blank field, as estimated in Section 2.3.3. We summarize the detailed procedure in Appendix A.3 and find that there is no additional incompleteness due to the object confusion in regions with an overdensity significance up to $\sim 8\sigma$. We now see that the completeness function of g-dropout galaxies estimated in this study is consistent with that of previous studies and that the blending due to focusing on overdense regions like HSC-SSP protoclusters does not lower the completeness. These results imply that the deficit is at least not due to incompleteness.

2.7.2 Effect of spatial extension of protoclusters

We have selected protocluster members from galaxies located within 1.8′ from each overdensity peak. Since protoclusters with more significant overdensity tend to be more extended, we may miss some protocluster members on the outskirts of protoclusters, and this could lead to the bright-end excess. To examine this possibility, we redefine protocluster members as galaxies which are located within 4.′2 from the overdensity peak, which corresponds to the size of progenitors of only the most massive halos ($M_{\rm halo} > 10^{15} {\rm M}_{\odot}$) like the Coma cluster at $z \sim 4$. We find that the shape of PC UVLF does not change from the case of 1.′8, suggesting that the trend is not caused by the differences in the typical spatial dimensions of protoclusters of different masses. We also check the case of a smaller protocluster radius ($\sim 1'$) and find that the trend does not change.

2.7.3 Galaxy formation in overdense regions

As introduced in Section 1.5, some protocluster galaxies at $z \sim 2$ are known to have higher SFR than field galaxies. In addition, Shi et al. (2019a) report a tentative evidence

of higher SFR for Lyα emitting galaxies in protoclusters at $z = 3.13$. On the other hand, local galaxy clusters show the opposite trend. For example, cluster galaxies at $0.18 < z < 0.55$ have SFRs about from $0.00 \pm 0.11\ h^{-2} \mathrm{M}_\odot\ \mathrm{yr}^{-1}$ to $0.17 \pm 0.02\ h^{-2}\ \mathrm{M}_\odot\ \mathrm{yr}^{-1}$, which are always lower than those of field galaxies (Balogh et al., 1998). Similarly, the low star formation activity in a cluster is also reported at $z = 1.6$ (Kriek et al., 2009). Combining our results with those from the literature, the enhancement of SFR in overdense environments has already started at $z \sim 4$.

Focusing on the stellar mass, there are several reports that there are more massive galaxies in protoclusters at $z \sim 2 - 3$ (Shimakawa et al., 2018; Koyama et al., 2013; Cooke et al., 2014; Hatch et al., 2011b), similar to our results at $z \sim 4$. At lower redshift ($z < 1.5$), the situation is controversial. Many studies report that the shape of the SMFs of star-forming and quiescent galaxies in clusters are similar (e.g., Lin et al., 2017; van der Burg et al., 2013; Calvi et al., 2013), while for those of all cluster galaxies, it is argued that there are significant differences not only in the normalization but also in shape at $z \sim 1$ in van der Burg et al. (2013), at $z \sim 0.5 - 0.7$ in van der Burg et al. (2018) and at $z \sim 0$ in Balogh et al. (2001). In addition, Kovač et al. (2010) report a difference between the SMFs of galaxies in a group environment and those in the blank field. On the other hand, Calvi et al. (2013) suggest that the shape of the SMF is independent of the environment for $z \sim 0$, likewise Nantais et al. (2016) support it for $z \sim 1.5$.

It should be noted that some studies report almost no difference from field galaxies in terms of the SFR and stellar mass of protocluster galaxies at $z = 2.9$ (Cucciati et al., 2014), and at $z = 4.57$ (Lemaux et al., 2018). These studies are based on only spectroscopically confirmed members, which are free from contamination, however the sample of members is small (~ 10 objects), which may not reveal the differences that we find based on the statistical sample.

These comparisons suggest that galaxies in overdense regions are more massive and have more active star formation compared to galaxies in the blank field at $z > 1.5$. Whereas at lower redshift, these trends change; galaxies in overdense regions have lower SFR, and the SMF can be identical to that of the field at least when focusing on the same galaxy population. In addition, star-forming galaxies in protoclusters tend to locate on the main sequence at $z \sim 4$ (Long et al., 2020; Shi et al., 2019b), and $z \sim 2 - 2.5$ (Shimakawa et al., 2018; Koyama et al., 2013). This means that the majority of protocluster members are normal galaxies, and the starburst activity

is not significant. Therefore, these results may imply the earlier star formation in protoclusters.

This early formation scenario is consistent with theoretical predictions. Chiang et al. (2017) suggest three phases for the evolution of (proto)clusters (c.f., Section1.4). At $z \leq 1.5$, star formation in galaxies is finished, and infalling galaxies into (proto)clusters dominate the main stellar mass growth in protoclusters. Such infalling galaxies are one of the possible reasons that the differences of SMFs of galaxies in local clusters disappear (Vulcani et al., 2013). Steeper SMFs for cluster galaxies at lower-z seen in Section 2.4.1 can also be explained by this infalling galaxy effect. In addition, they also imply that $\sim 20\%$ of the cosmic SFRD is contributed by protocluster galaxies at $z \sim 4$, which is roughly consistent with our estimation, as discussed in Section 2.4.3.

The shape difference of the PC UVLF and the PC SMF seen in this study can also be related to frequent mergers or an increase in gas supply towards the center of the connection of several connected filaments in an overdense region, as suggested in Shimakawa et al. (2018). Indeed, Tomczak et al. (2017) show that “top-heavy" SMFs may originate from the enhancement of mergers in the overdense region. They first construct SMFs for star-forming galaxies and quiescent galaxies at $z \sim 1$ subdivided by their local environment. They find that shapes of SMFs in more overdense regions tend to be more top-heavy. They try to explain this trend by a simple semiempirical model. This model first generates $\sim 10^6$ galaxies at $z = 5$. For each redshift slice, some fractions of galaxy pairs are selected for the merger, and some fractions of galaxies are selected for quenching. The only free parameter is the merged galaxy fraction. The model shows that the observed SMF in overdense regions can be explained by high-merger rate ($80 - 90\%$). In addition, the increase of gas supply can keep galaxies, which are too massive to be star-forming galaxies in the blank field, to have star formation. This effect also makes the SMF of protocluster galaxies, which consist only of star-forming ones, to be top-heavy.

Differences of the rest-frame UV brightest protocluster galaxies (Section 2.6) can be consistent with the above scenarios. If the bright-end excess of the PC UVLF represents the early galaxy formation in overdense regions, protocluster galaxies should have the same characteristics with field galaxies with the fixed brightness. In this case, different properties of the brightest protocluster galaxies from field galaxies might trace the distinguished evolution of BCGs as suggested from the different luminosity profile of

local BCGs (e.g., Schombert, 1986). If the frequent mergers induce the bright-end excess of the PC UVLF, this might also induce the redder color of the brightest protocluster galaxies with the increased amount of dust from the star-burst activity. To constrain the origin of the bright-end excess and the distinguished properties of the brightest protocluster galaxies, we need more detailed and precise analyses.

We find in Section 2.4.2 that all protoclusters follow the same trend that galaxies in more massive overdense regions tend to have a flatter UVLF, though the diversity exists even if we focus on protoclusters with the same overdensity. The trend implies that more massive regions have generally experienced the distinguished formation, but their evolutionary stage has a significant variation even at the same epoch. This indicates that a large sample at each redshift is critically essential for tracing the general evolutionary sequence of protoclusters within this diversity.

2.8 Summary of Chapter 2

In this chapter, we derive the rest-UV luminosity function of g-dropout galaxies in 177 protocluster candidates (PC UVLF) at $z \sim 4$ detected in the HSC-SSP data S16A data and discuss properties of the rest-frame UV bright galaxies with the use of the recent deeper S20A data and multi-band photometry, called HSC joint catalog. Main results are as follows:

1. Compared to the UVLF of galaxies in the blank field, the PC UVLF has a significant excess towards the bright-end in addition to a higher normalization. The best-fit parameters of both the Schechter functions and DPL functions for the PC UVLF also reveal the shape differences from that of the field. The excess towards the bright-end implies that the SFR of galaxies in overdense regions must have accelerated at $z \geq 4$.

2. Assuming that all protocluster galaxies follow the “main sequence" of star-forming galaxies, we convert the PC UVLF to the SMF. Protocluster galaxies are inferred to have 2.8 times more massive characteristic stellar mass than their field counterparts at the same epoch. We show that protocluster galaxies have to continue their stellar mass growth to match SMFs of (proto)cluster galaxies at lower redshift.

3. More massive protoclusters tend to have a higher bright-end amplitude in the UVLF, although the variation is seen even if we only focus on protoclusters with the same overdensity. The bright-end excess is ubiquitously seen in most of protoclusters at $z \sim 4$.

4. Protoclusters have the enhanced SFRD as $\log_{10} \mathrm{SFRD}/(\mathrm{M}_\odot\ \mathrm{yr}^{-1}\ \mathrm{Mpc}^{-3}) = 1.54^{+0.16}_{-0.20}$ ($1.68^{+0.16}_{-0.17}$) using the best-fit of Schechter (DPL) function. This corresponds to the $6-20\%$ of the cosmic SFRD, being close to the theoretical prediction of Chiang et al. (2017), but somewhat smaller. This difference from the prediction might be due to the ignorance of SMG in this study and the missed protocluster members located at the edges of protoclusters.

5. The bright-end excess is not only due to the enhancement of AGNs. The AGN fraction of known protoclusters estimated from X-ray observation can not explain the all of bright-end excess, which corresponds to 32% of the total protocluster members. In addition, the AGN fraction of bright protocluster members in DEEP/UltraDEEP layers is estimated from their morphology following the method of Bowler et al. (2021), and it is consistent with the field value, suggesting that we do not have any signature of the enhancement of the AGN fraction in protoclusters. The SED fitting analysis also naively supports this.

6. The rest-frame UV brightest protocluster galaxies are redder and larger in the rest-frame UV than field galaxies at the same magnitude. This can suggest their different formation history due to their living environment.

Highly star forming and more massive galaxies in protoclusters are reported in protoclusters at lower redshift. This chapter shows that protocluster galaxies are affected by their living environment even at $z \sim 4$. We interpret this trend as a signature of the fact that protoclusters at $z \sim 4$ are regions in the cosmic web where galaxies and structures form earlier and galaxies therein are in the active star formation mode.

3

Environment of Multiple Galaxy Populations at $2 < z < 4.5$

- Based on Ito et al. (2021)

3.1 Background of Chapter 3

In Chapter 2, we have shown that SFR is enhanced for galaxies in protoclusters, which have been selected through the overdensity of LBGs. On the other hand, as introduced in Chapter 1, several protoclusters are known to have different spatial distribution for different galaxy populations. In this chapter, we discuss the differences of the spatial distribution among different galaxy population in order to examine its general trend. For quantifying this, the cross-correlation is an effective tool. It has been measured for different galaxy populations (e.g., Béthermin et al., 2014; Hatfield & Jarvis, 2017) and used to determine the connections between galaxies and intergalactic media (IGM) (e.g., Tejos et al., 2014; Momose et al., 2021c; Liang et al., 2021). The overdensity, which is

defined as the excess of the surface number density over the average value, is another tool for quantifying the environment. The overdensity is measured using a variety of methods. Some methods fix the scale in which the density is estimated, whereas others calculate the density based on the number of nearby galaxies. Recent studies have proposed a density measurement technique, called the Voronoi Monte Carlo Mapping, that does not assume any density scale (e.g., Tomczak et al., 2017; Lemaux et al., 2020). These methods are based on different assumptions, so it is essential to systematically apply a unified method to all populations to see the difference of their environments.

In this chapter, three galaxy populations are focused: massive SFGs, massive QGs, and LAEs in the Cosmic Evolution Survey (COSMOS) field. SFGs and QGs are selected based on the multi-photometry catalog constructed in Laigle et al. (2016), whereas LAEs are taken from the extensive narrow- and medium-band based survey in SC4K (Sobral et al., 2018). The large amount of data in the COSMOS field enables us to investigate the differences in their distributions up to $z \sim 4.5$, based on the clustering analysis and the overdensity distribution.

3.2 Dataset

3.2.1 Star-forming galaxies and quiescent galaxies

Sample construction

We use the COSMOS multi-band catalog constructed in Laigle et al. (2016). This catalog consists of photometries of $\sim$ 30 bands, i.e., near-UV of GALEX (Galaxy Evolution Explorer, Zamojski et al., 2007), u^*-band of CFHT, $BVri^+z^{++}$ and several intermediate/narrow bands of Suprime-Cam (Taniguchi et al., 2007, 2015) and Y-band of Hyper Suprime-Cam of Subaru Telescope, $YJHK_s$ of VIRCAM of the VISTA telescope (McCracken et al., 2012), HK_s of Wide-field InfraRed Camera (WIRCam) from CFHT (McCracken et al., 2010), and Channels 1, 2, 3, and 4 of the Infrared Array Camera (IRAC) of the Spitzer telescope from the SPLASH survey. This catalog is based on detection in the χ^2 sum of the $YJHK_s$ and z^{++} images. For more details, please refer to Laigle et al. (2016).

In this study, SFGs and QGs samples are constructed to be magnitude-limited

based on the 3σ limiting magnitude of K_s band ($K_s < 24$), where K_s is the 3" aperture magnitude of K_s band. Objects are further selected with flags (FLAG_COSMOS and FLAG_PETER) to only focus on objects with the clean photometry. We then estimate the photometric redshift using MIZUKI code (Tanaka, 2015). One advantage of this code is that we are able to simultaneously derive the photometric redshifts and physical properties (e.g., $M_\star$, SFR, and dust extinction) with their Bayesian priors. This allows us to include the uncertainty of the photometric redshift in the estimate of the physical properties. It should be noted that the photo-z between MIZUKI and Laigle et al. (2016) is consistent with each other with $\delta z/(1+z) = 0.003$, after excluding objects with the bad chi-squares ($\chi^2_\nu > 4$) at $2 < z < 4.5$.

MIZUKI conducts the fitting based on spectral templates from Bruzual & Charlot (2003), Chabrier IMF (Chabrier, 2003), and Calzetti dust attenuation curve (Calzetti et al., 2000). We use an exponentially declining SFR, i.e., SFR $\propto \exp(-t/\tau)$, where t is time. The τ is assumed to be 0.1 Gyr $< \tau <$ 11 Gyr in addition to $\tau = 0,\ \infty$, which is equivalent to the single stellar population model and the constant SFR model. The age is assumed to be between 0.05 and 14 Gyr. Also, the optical depth in the V band (τ_V) is between 0 and 2 with a step of 0.1, in addition to $\tau_V = 2.5,\ 3,$ and 4. Because the templates mentioned above include only stellar emissions, the nebular emissions are included according to Inoue (2011). Similar to Kubo et al. (2018), which select QGs at $3.5 < z < 4.5$ in the ultradeep survey (UDS) region using MIZUKI code, galaxies with bad chi-squares ($\chi^2_\nu > 4$) in the SED fitting are excluded ($\sim 4\%$ of the total sample in the target redshift). Objects with large reduced chi-squares have generally poor-photometry due to the affection by nearby bright stars or blending. Also, apparent AGNs can be excluded from this criteria since any AGN template is not included in the fitting. The typical uncertainty of the estimated redshift, $M_\star$, and SFR of objects at $2 < z < 4.5$ are $\delta z/(1+z) \sim 0.05$, $\delta M_\star/M_\star \sim 0.2$, and δSFR/SFR ~ 0.4, respectively.

SFGs and QGs are distinguished based on the specific star formation rate (sSFR) derived by the SED fitting, as in our other studies (Kubo et al., 2018, Chapter 4). We define galaxies with $\mathrm{sSFR}_{1\sigma,\mathrm{upper}} < 10^{-9.5}$ yr^{-1} as QGs, and classify the others as SFGs. Here, $\mathrm{sSFR}_{1\sigma,\mathrm{upper}}$ is the upper limit of sSFR, which is defined as the ratio of the 1σ upper limit of SFR to the 1σ lower limit of stellar mass, derived from the SED fitting. We note that our result does not change even if we modify this classification, for example, by considering the redshift evolution of the star formation main sequence (i.e., a stricter

threshold for lower-z objects) or by defining SFGs with $\mathrm{sSFR}_{1\sigma,\mathrm{lower}} > 10^{-9.5}$ yr^{-1} to exclude overlapped region with QGs in $M_\star$–SFR plane.

We focus on sources at $2 < z < 4.5$, where the number of sources is sufficient to quantify the average spatial distributions. The relationship between the stellar mass and SFR of SFGs and QGs are shown in Figure 3.1. The threshold is located in ~ 1 dex lower than the main sequence. Also, we see that QGs are mainly selected from the outer envelope of the main sequence of galaxies. It should be noted that this threshold does not select only passive galaxies, which are completely quenched, but post-starburst galaxies as well. The stellar mass of LAEs of SC4K used in this study is reported to have a median value of $\log(M_\star/M_\odot) = 9.0 - 9.5$ (Santos et al., 2020), so our photo-z-selected galaxies tend to be much more massive than them.

In addition, powerful AGNs, which are detected in X-ray, are not included in this study because the SED fitting may incorrectly estimate their host galaxy properties. We use the X-ray image of Chandra COSMOS Legacy Survey (Civano et al., 2016), which reaches 8.9×10^{-16} erg s^{-1} cm^{-2} in $0.5 - 10$ keV band. We cross-match with the multi-photometric catalog of this survey (Marchesi et al., 2016a) by using coordinates from optical and NIR images and exclude objects with counterparts with a separation of ≤ 1". The fraction of excluded objects is $2 - 7\%$ and depends on the stellar mass and the redshift. Some AGNs that are not bright enough to be detected in this catalog may be included in our sample, but their emission is expected to hardly affect the outcome of the SED fitting.

Stellar mass completeness

We estimate the stellar mass completeness of our SFG and QG sample from the method employed in the previous studies (e.g., Pozzetti et al., 2010; Laigle et al., 2016; Davidzon et al., 2017). First, the rescaled stellar mass (M_{resc}) expected at the magnitude limit ($K_{s,\mathrm{lim}}$) is estimated from the $M_\star$ and K_s band magnitude of galaxies. Here, we focus on objects brighter than the limiting magnitude. The M_{resc} is derived as follows:

$$\log M_{\mathrm{resc}} = \log M_\star + 0.4(K_s - K_{s,\mathrm{lim}}). \tag{3.1}$$

The stellar mass completeness limit is defined as the bottom 90th percentile of the M_{resc} distribution in each redshift bin. We see the evolution of the stellar mass completeness

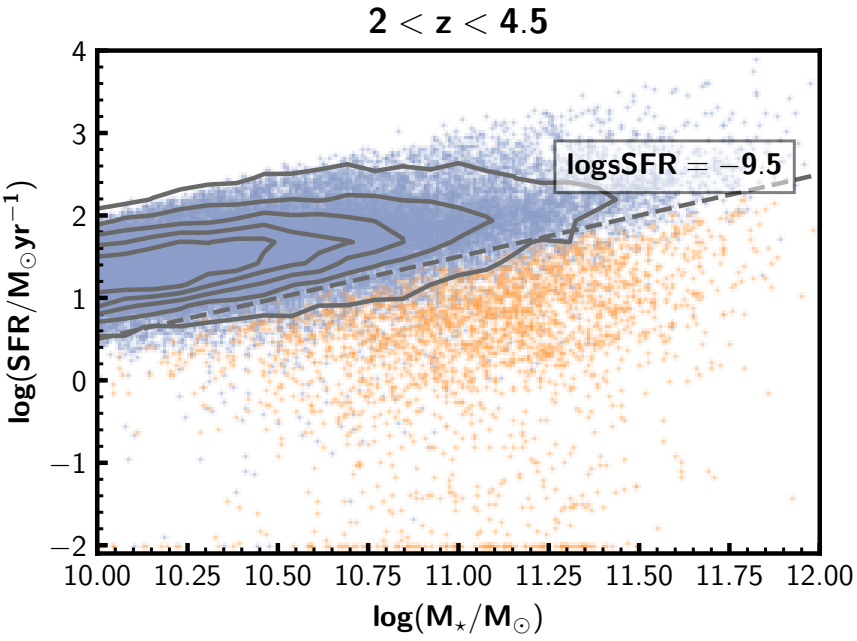

Figure 3.1: $M_\star$–SFR relation of target galaxies. The blue dots show SFGs, and the orange dots show QGs. Objects with SFR lower than $0.01 M_\odot \mathrm{yr}^{-1}$ are shown at $0.01 M_\odot \mathrm{yr}^{-1}$ for the illustrative purposes. For reference, the contour estimated from all objects in figure is shown. The dashed line shows the location of $\log(\mathrm{sSFR}/\mathrm{yr}^{-1}) = -9.5$.

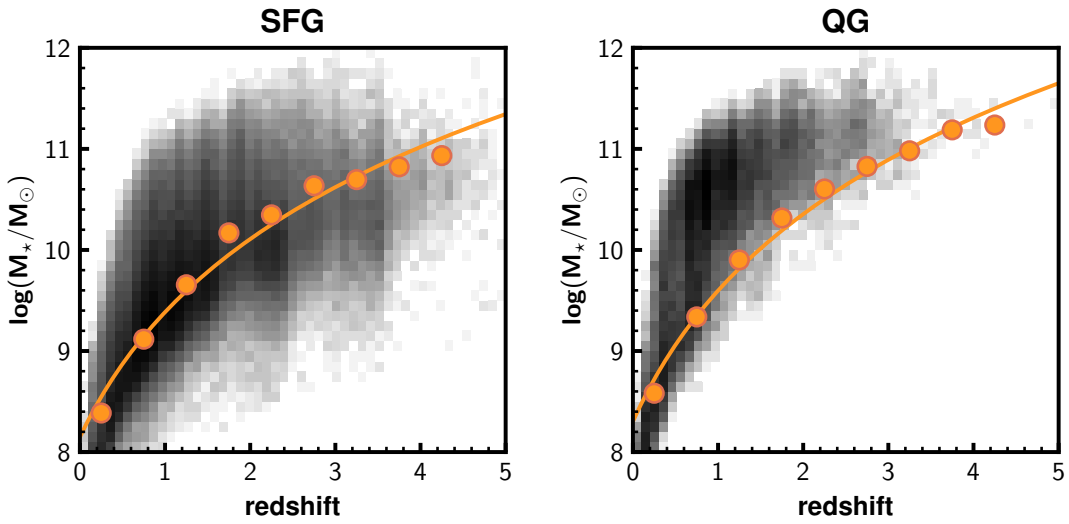

Figure 3.2: Stellar mass completeness evolution (orange circles) for SFGs (left) and QGs (right). The orange lines show the best power-law fits of observed value in every $\delta z = 0.5$. The background color map shows the distribution of observed galaxies with $K_s < 24$ mag.

limit of SFGs and QGs in Figure 3.2, which shows those in every $\delta z = 0.5$. The stellar mass limit is often fitted by the power-law function (e.g., Davidzon et al., 2017). The best-fits are described as $M_\star = 10^{8.15} \times (1+z)^{4.11}\ M_\odot$ for SFGs, and $M_\star = 10^{8.30} \times (1+z)^{4.30}\ M_\odot$ for QGs. The stellar mass completeness limit is generally higher for QGs than for SFGs because the mass-to-light ratios of QGs are higher than those of SFGs. In the following sections, we estimate the stellar mass completeness limit for each group following by the above procedure, and employ their value.

3.2.2 Lyα emitters

We use the LAE catalog of Sobral et al. (2018), who construct a systematic LAE sample at $z \sim 2-6$, referred to as the SC4K sample. This catalog is based on the intermediate band (IB) data of Suprime-Cam and narrow band (NB) data of the Wide Field Camera (WFC) of the Isaac Newton Telescope and Suprime-Cam. They select LAEs using an observed equivalent width (EW) threshold and by imposing the color selection and non-detection of broadband blue-ward Lyα emissions at the target redshift. Spurious

objects are excluded from the sample via visual inspection. Contaminants found by previous spectroscopic surveys are also excluded. They finally select 3908 sources as LAEs in 16 redshift slices.

The target redshift range ($2 < z < 4.5$) corresponds to LAEs selected from NB392, IA427, IA464, IA484, IA505, IA527, IA574, and IA624 bands at $2.20 < z < 2.24$, $2.42 < z < 2.59$, $2.72 < z < 2.90$, $2.89 < z < 3.08$, $3.07 < z < 3.26$, $3.23 < z < 3.43$, $3.63 < z < 3.85$, and $4.00 < z < 4.25$, respectively. In this study, we construct a Lyα luminosity ($L_{\mathrm{Ly}\alpha}$) complete sample by imposing a 3σ Lyα luminosity limit cut for each selection band. The 3σ limiting luminosity of the sample is $\log(L_{\mathrm{Ly}\alpha}/\mathrm{erg\ s^{-1}}) = 42.3 - 42.8$, dependent on the selection filter (see Sobral et al., 2018, for details). We note that NB392 LAEs are selected with a loose threshold (EW $> 5 \times (1+z)$ Å) compared to other IB LAEs (EW $> 50 \times (1+z)$ Å).

The spatial coverage of the LAE survey is slightly different from the surveys from which SFGs and QGs are selected. Thus, this study focuses on the region where all of SFGs, QGs, and LAEs exist. We note that the survey fields for most of the selection filters are larger than the field of photo-z galaxies, but that of NB392 is 22% smaller.

It is known that bright LAEs can be AGNs (e.g., Konno et al., 2016; Sobral et al., 2018). Such objects can have different properties from those of typical LAEs described in Section 1.3. Therefore, LAEs with high Lyα luminosity ($\log(L_{\mathrm{Ly}\alpha}/\mathrm{erg\ s^{-1}}) > 43.3$) are excluded from the sample. The fraction of these objects is quite small ($\sim 3\%$ of the total), and if they are included, the following results do not change. We also exclude objects with counterparts in the Chandra COSMOS Legacy Survey catalog in the same manner as that for photo-z galaxies.

3.3 Clustering Analysis

In this section, we estimate auto- and cross-correlation function signals among SFGs, QGs, and LAEs and discuss the difference in spatial distributions of these galaxy populations.

3.3.1 Group construction

LAEs are constructed in discrete redshifts, as summarized in Section 3.2.2. By comparison, the samples of SFGs and QGs have continuous redshift distributions. To increase the signal to noise ratio of cross-correlation functions, we construct four redshift groups at $2 < z < 4.5$ by combining LAEs selected from eight IBs/NB. These four redshift groups are $2.05 < z < 2.39$, $2.40 < z < 2.95$, $2.85 < z < 3.50$, and $3.50 < z < 4.50$. Hereafter, we refer to these groups as z-group1, z-group2, z-group3, and z-group4, respectively. The redshift range is determined to include possible photo-z galaxies located in the same redshift of LAEs. The redshift range of the lowest redshift bin is defined to match that of NB392 LAEs ($2.20 < z < 2.24$), including the photo-z uncertainty ($\delta z/(1+z) \sim 0.05$), which leads to a narrower range than those of other bins. For the highest redshift group, we select objects within a broader redshift range ($\delta z = 1$) to enhance the signal to noise ratio of cross-correlation. Noticeably, a slight duplication exists between the second and the third subgroup, but this does not affect our overall result.

Also, we divide SFGs and QGs sample into four subgroups in terms of their stellar mass, which includes only objects whose stellar masses are $\log(M_\star/M_\odot) \geq 10.4$, 10.6, 10.8, and 11.0, respectively. Hereafter, we refer to these groups as $M_\star$-group1, $M_\star$-group2, $M_\star$-group3, and $M_\star$-group4, respectively. From the method summarized in Section 3.2.1, the stellar mass completeness limit of each z-group1, 2, 3, and 4 is estimated as $\log(M_\star/M_\odot) = 10.3$, 10.6, 10.7, and 10.8 for SFGs and $\log(M_\star/M_\odot) = 10.6$, 10.8, 11.0, and 11.1 for QGs, respectively. Some $M_\star$-group whose threshold is below the stellar mass completeness limit are not discussed furthermore. The total numbers of the samples for each of the redshifts and each of the stellar mass thresholds are summarized in Table 3.1.

The redshift distributions of each group of SFGs and QGs are estimated using the summation of the probability distribution function (PDF) of the photo-z of galaxies in each group, similar to the method used in Coupon et al. (2012). The photo-z PDF often has a complex shape, but for simplicity, we choose to represent each PDF with normalized Gaussian centered at the median PDF and its 68% confidence interval as $\pm 1\sigma$. We sum up these Gaussian functions of all objects in a group and construct the average redshift distribution of a group. Meanwhile, the redshift distribution of LAEs

is assumed to be number-weighted sum of the Lyα detection rate predicted from each NB/IB transmission curve. The redshift distribution of each sample is summarized in Figure 3.3.

If the same object exists in two groups wherein the cross-correlation function is measured, the clustering amplitude is artificially increased. Therefore, objects that are also selected as LAEs are excluded from the SFG sample. The fraction of duplication is $0.05 - 1\%$ for all groups. There are no QGs classified as LAEs in our sample.

Table 3.1: Summary of numbers of samples for clustering analysis

$M_\star$-group ($\log(M_\star/M_\odot)$)	z-group1 $2.05 < z < 2.39$	z-group2 $2.40 < z < 2.95$	z-group3 $2.85 < z < 3.50$	z-group4 $3.50 < z < 4.50$
		SFG		
$M_\star$-group1 (> 10.4)	3077	-	-	-
$M_\star$-group2 (> 10.6)	1940	2817	-	-
$M_\star$-group3 (> 10.8)	1128	1670	1464	736
$M_\star$-group4 (> 11.0)	561	909	736	371
		QG		
$M_\star$-group1 (> 10.4)	-	-	-	-
$M_\star$-group2 (> 10.6)	513	-	-	-
$M_\star$-group3 (> 10.8)	421	745	-	-
$M_\star$-group4 (> 11.0)	303	587	198	-
		LAE		
-	93	725	1195	161

3.3.2 Autocorrelation function

We calculate the autocorrelation function (ACF) using the method from Landy & Szalay (1993), who propose an estimator as follows:

$$\omega_{\mathrm{ACF,obs}}(\theta) = \frac{DD(\theta) - 2DR(\theta) + RR(\theta)}{RR(\theta)}, \tag{3.2}$$

where, DD, DR, and RR are the normalized numbers of galaxy–galaxy, galaxy–random, and random–random pairs, respectively.

The ACF is often expressed in the power-law form:

$$\omega_{\mathrm{ACF}} = A_\omega \theta^{1-\gamma}. \tag{3.3}$$

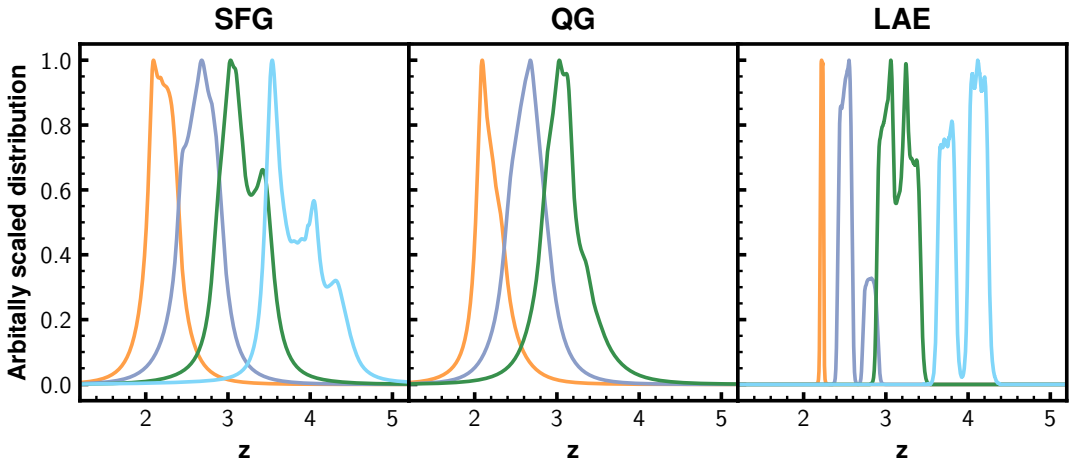

Figure 3.3: Redshift distributions for each galaxy populations in the four redshift bins. The distributions are normalized at the peak. We show cases of the minimum stellar mass threshold of each redshift groups for photo-z galaxies.

In this study, we fix γ to a fiducial value ($\gamma = 1.8$), following previous studies of LAEs (e.g., Kusakabe et al., 2018; Ouchi et al., 2018) and photo-z galaxies (e.g., Coupon et al., 2012).

Random objects are generated with a number density of ~ 200 arcmin^{-2}, which is more than 200 times higher than those of photo-z galaxies and LAE. Random objects are distributed in the same region as that of galaxies, including flags.

It is known that the observed ACF based on Equation 3.2 is underestimated because of the finite observation field, referred to as “integral constraint". To correct this bias, the integral constraint C is derived using the following equation:

$$C = \frac{\Sigma_i \theta_i^{1-\gamma} RR(\theta_i)}{\Sigma_i RR(\theta_i)}. \tag{3.4}$$

In this study, the C is estimated to be $C = 1.46$ for z-group1, and $C = 1.36$ for the others. Because the survey field is smaller in NB392 (see Section 3.2.2), the C is higher in z-group1 than in other bins. The C provides a corrected ACF $\omega_{\rm ACF}$ according to the following equation:

$$\omega_{\rm ACF} = \omega_{\rm ACF,obs} \frac{\theta^{1-\gamma}}{\theta^{1-\gamma} - C}. \tag{3.5}$$

The error of the ACFs is estimated based on the Jackknife re-sampling. We divide the observed field into 5×5 regions, and removing one region at a time, we estimate $\omega_{i,k}$ in k-th trial. This procedure repeats in 25-times trails and compute the variance of $\omega_{\rm ACF}(\theta_i)$ for each bin:

$$Var_i = \frac{N-1}{N} \sum_{k=1}^{N} (\omega_{i,k} - \bar{\omega}_i)^2, \tag{3.6}$$

where N is the number of re-sampling trials, and $\bar{\omega}_i$ is the mean of $\omega_{i,k}$. For calculating the variance, we do not consider the trial when the subtracted region is overlapped by over 50% mask region.

We fit a power-law function (Equation 3.3) to ACFs via the `Python` module `lmfit` by the least-square method. The distribution of satellite galaxies around the central galaxy is not within the scope of this study, and we are only interested in the larger scale outside of the single halo. Therefore, the angular scale corresponding to within a halo, referred to as the "one-halo term", are excluded from the ACF fitting range. Specifically, we do not consider $\theta < 40$" for photo-z galaxies and $\theta < 10$" for LAEs, where the one-halo term dominates as implied by previous studies (e.g., Ishikawa et al., 2015; Ouchi et al., 2018).

We note that the amplitude can decrease due to contaminants. Low-z galaxies whose Balmer breaks can be misclassified as Lyman breaks at the target redshifts in the case of photo-z galaxies. [OII], Hβ, [OIII] emitters are contaminant candidates for LAEs (see Sobral et al., 2018, for more concrete discussion). Nonetheless, as will be discussed in Section 3.3.7, these contaminants do not affect our overall results related to the distribution difference. Therefore, we do not correct these contaminants for the value of the amplitude.

Figure 3.4 shows the estimated ACFs with the best-fit power-law functions. The observed ACFs are well described in the power-law form in the large scale. Focusing on smaller scale correlation, QGs have a significant deviation from the power-law, especially in z-group1 and 2. Such enhancement of the one-halo term for QGs are seen in other studies (e.g., Cowley et al., 2019) and can be related to the higher satellite fraction. The best-fit values of A_ω are summarized in Table 3.2.

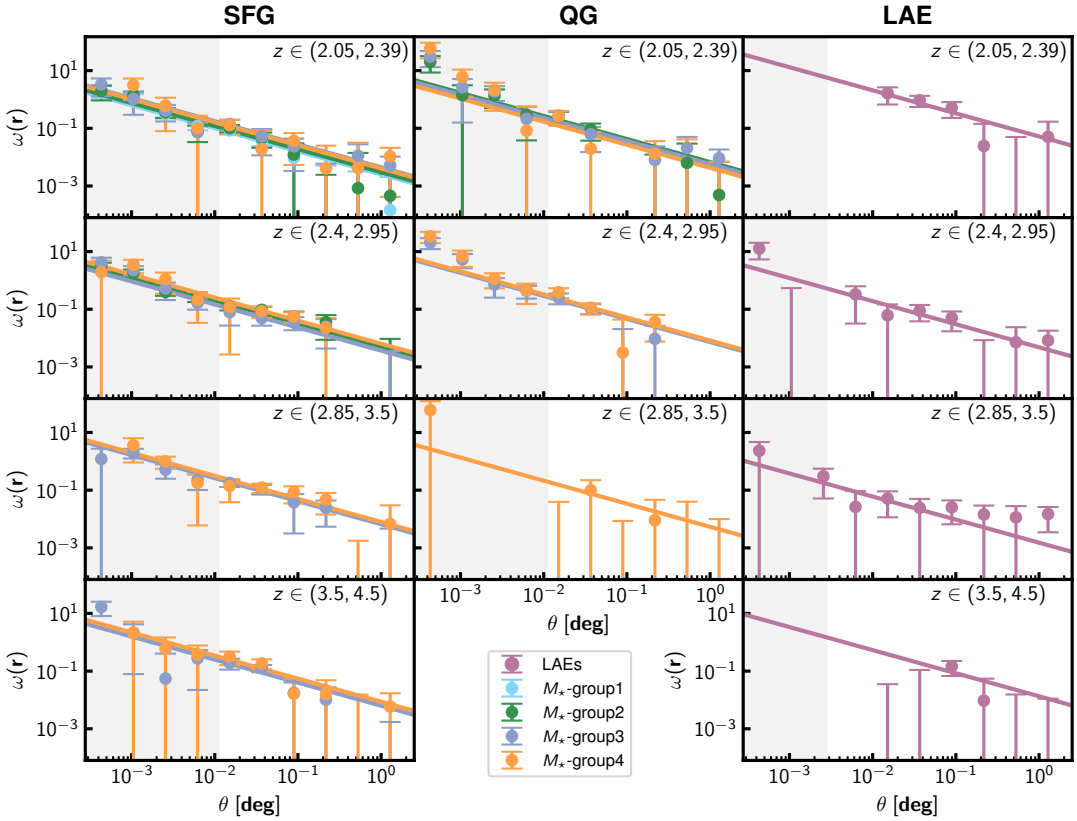

Figure 3.4: ACFs of SFGs (left), QGs (center), and LAEs (right) at each redshift. Circles show the estimated points, and error bars are derived via Jack-knife re-sampling. Colors among SFGs and QGs represent stellar mass groups. Solid lines correspond to the best fit of identical colors. Gray-shaded regions show ranges not used for deriving the amplitude A_ω of the power-law.

3.3.3 Cross-correlation function

The cross-correlation function (CCF) of samples 1 and 2 is estimated as follows:

$$\omega_{\mathrm{CCF,obs}}(\theta) = \frac{D_1D_2(\theta) - D_1R(\theta) - D_2R(\theta) + RR(\theta)}{RR(\theta)}, \tag{3.7}$$

where D_1D_2, D_1R, and D_2R are the normalized numbers of pair of samples 1 and 2, sample 1 and random, and sample 2 and random, respectively. The integral constraint correction and the error estimation are performed in the same manner as for the ACF.

In this study, we measure the difference in the clustering of each population with respect to SFGs. Therefore, we estimate CCFs between SFGs and LAEs and those between SFGs and QGs. The latter cases are determined for the same stellar mass thresholds for both populations. We do not discuss CCFs between QGs and LAEs because we do not obtain any meaningful constraints about the distribution differences due to the poor statistics. The estimated CCFs are shown in Figure 3.5. As with ACFs, we fit using the power-law with the fixed $\gamma = 1.8$. The CCFs of $\theta > 40$" are used to avoid the one-halo term for photo-z galaxies. The results are summarized in Table 3.3. There is no clear stellar mass dependence of the amplitude of CCF of photo-z galaxies.

3.3.4 Correlation length and halo mass

The ACFs and CCFs are evaluated based on projected separations on the sky. The spatial correlation function $\xi(r)$ can be estimated from ACFs and CCFs. The galaxy spatial correlation function is often approximated as follows:

$$\xi(r) = \left(\frac{r}{r_0}\right)^{-\gamma}, \tag{3.8}$$

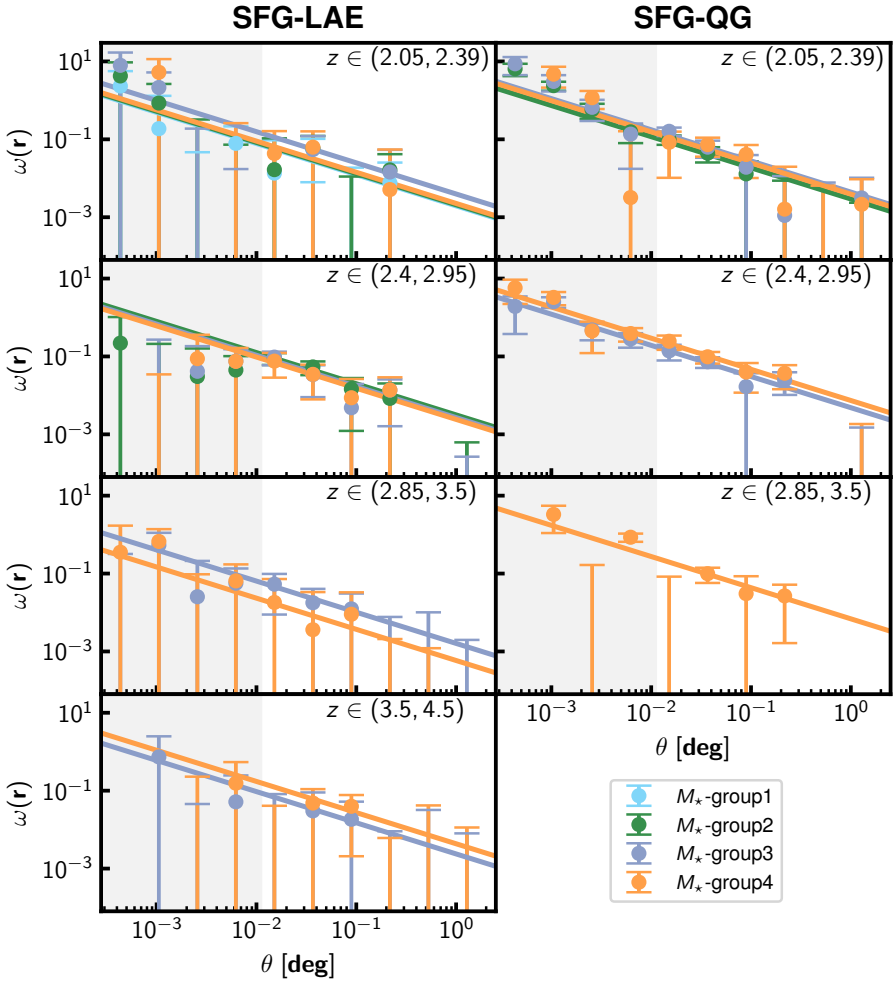

Figure 3.5: CCFs between SFGs and LAEs (left) and between SFGs and QGs (right) at each redshift. We estimate CCFs between the entire LAE sample and SFGs in each stellar mass bin and those between SFGs and QGs in the same stellar mass bins. Colors show the stellar mass groups of SFGs and QGs, which are identical to those used in Figure 3.4.

where r_0 is the correlation length. To derive the r_0 from ACFs, we employ the Limber equation (Peebles, 1980; Efstathiou et al., 1991),

$$A_\omega = C r_0^\gamma \frac{\int_0^\infty F(z) D_\theta(z)^{1-\gamma} N(z)^2 g(z) dz}{[\int_0^\infty N(z) dz]^2}, \tag{3.9}$$

$$g(z) = \frac{H_0}{c}(1+z)^2 \left\{1 + \Omega_m z + \Omega_\Lambda \left[(1+z)^{-2} - 1\right]\right\}^{1/2}, \tag{3.10}$$

$$C = \frac{\sqrt{\pi}\Gamma[(\gamma-1)/2]}{\Gamma(\gamma/2)}, \tag{3.11}$$

where $D_\theta(z)$ is the angular diameter distance, and $N(z)$ is the redshift distribution of the sample. $F(z)$ describes the redshift evolution of $\xi(z)$, which is modeled as $F(z) = [(1+z)/(1+\bar{z})]^{-3+\epsilon}$ with $\epsilon = -1.2$ (Roche & Eales, 1999). The $\bar{z}$ is the average redshift of the sample. c and Γ are the light speed and the Gamma function, respectively. The derived correlation lengths are summarized in Table 3.2.

In Figure 3.6, the correlation lengths are compared with those in previous studies. We see that our correlation measurement is consistent with previous results within the uncertainty. The correlation length of SFGs at the lowest redshift bin is located in a similar range as that of Hα emitters (HAEs) with $\log(M_\star/M_\odot) > 10.1$ reported in Cochrane et al. (2018). HAEs are typical star-forming galaxies and expected to have the same correlation length as our SFGs at fixed stellar mass. Those of LAEs at $z \geq 2.4$ are also consistent with those in Khostovan et al. (2019), which also use SC4K LAEs. Though LAEs of z-group1 are higher than those at similar redshift in Kusakabe et al. (2018), their LAEs reach fainter luminosity than ours. Such a difference can cause the different value.

In addition, Figure 3.6 shows that more massive SFGs have slightly higher amplitudes at fixed redshift, also consistent with previous studies (e.g., McCracken et al., 2015). For QGs, we do not see such a trend due to a large uncertainty.

The correlation lengths of the spatial CCF are also derived from the amplitude of its CCFs via the following equation, which is a slightly modified version of Equation 3.9 (Croom & Shanks, 1999):

$$A_\omega = C r_0^\gamma \frac{\int_0^\infty F(z) D_\theta(z)^{1-\gamma} N_1(z) N_2(z) g(z) dz}{\int_0^\infty N_1(z) dz \int_0^\infty N_2(z) dz}, \tag{3.12}$$

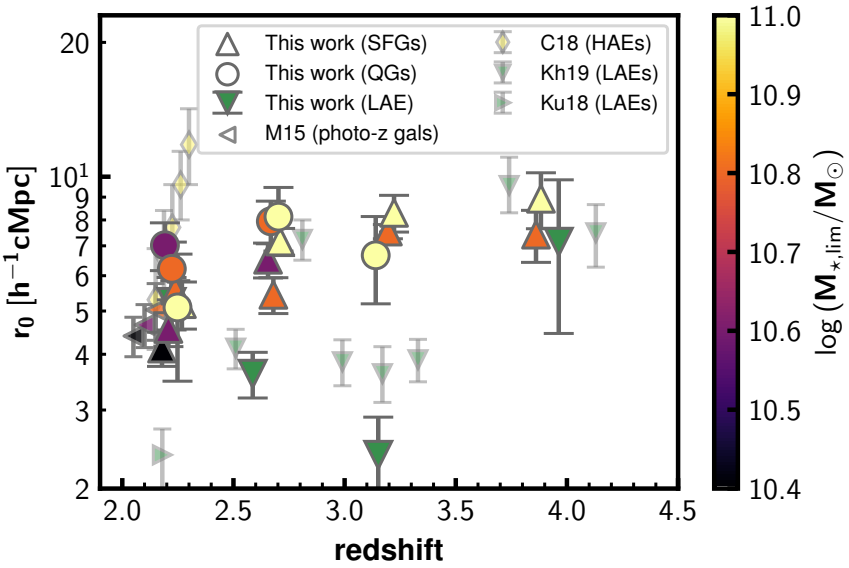

Figure 3.6: Correlation lengths of different galaxy populations. Colored triangles, circles, and green inverted triangles are correlation lengths of stellar mass groups of QGs, SFGs, and LAEs in this study. Colored left-pointing triangles are those of photo-z galaxies at $2.0 < z < 2.5$ from McCracken et al. (2015). Their redshift is slightly shifted for the illustrative purpose. Small green markers are those of LAEs from Khostovan et al. (2019) (inverse triangles) and from Kusakabe et al. (2018) (right-pointing triangle). Small yellow diamonds are those of HAEs with $\log(M_\star/M_\odot) > 10.1$ (Cochrane et al., 2018). The colors of markers for circles, triangles, and left-pointing triangles show the stellar mass limit of each bins.

where $N_1(z)$ and $N_2(z)$ are the redshift distribution functions of samples 1 and 2, respectively. The best-fit correlation lengths are summarized in Table 3.3. We note that though the redshift distribution is different among LAE, SFG, and QG, as seen in Figure 3.3, this formulation consider this by using the appropriate N_1 and N_2.

From the derived correlation length of the spatial ACFs, we also calculate the mean dark-matter halo mass. Firstly, the galaxy-matter bias b_g is estimated as follows:

$$b_g(r) = \sqrt{\frac{\xi(8\ h^{-1}\mathrm{cMpc})}{\xi_{\mathrm{DM}}(8\ h^{-1}\mathrm{cMpc}, z)}}, \tag{3.13}$$

where $\xi_{\mathrm{DM}}(8\ h^{-1}\mathrm{Mpc}, z)$ is the correlation function for the dark matter, estimated from the dark-matter power spectrum computed using the transfer function approximation reported in Eisenstein & Hu (1998). Secondly, the mean dark-matter halo mass $\langle M_h \rangle$ is estimated based on an assumption that the mean dark matter halo mass has a galaxy bias equal to the measured value:

$$b_g = b(\langle M_h \rangle). \tag{3.14}$$

In this study, $b(\langle M_h \rangle)$ is based on Tinker et al. (2010). The uncertainty of $\langle M_h \rangle$ corresponds to a possible range from the 1σ uncertainty of b_g. The derived bias and the mean dark-matter halo mass are also summarized in Table 3.2.

Figure 3.7 shows the redshift evolution of the mean dark-matter halo masses of SFGs, QGs, and LAEs. First of all, LAEs tend to reside in less massive halos than SFGs and QGs. Moreover, for SFGs, higher stellar mass galaxies tend to have higher halo masses. This is also inferred from the higher amplitude of ACFs and the findings of previous studies, such as McCracken et al. (2015) at $z \sim 2$. For QGs, we do not see such a clear trend due to the large uncertainty compared to that of SFGs, as seen in Table 3.2.

Table 3.2: Summary of autocorrelation function measurements

	$\log(M_{\star,\mathrm{lim}}/M_\odot)^a$	A_ω^b $[\times 10^{-3}\mathrm{deg}^{0.8}]$	r_0^c $[h^{-1}\mathrm{cMpc}]$	b_g^d	$\langle M_h \rangle^e$ $[\times 10^{12} h^{-1} M_\odot]$
			SFG		
z-group1	10.4	2.53 ± 0.40	4.12 ± 0.36	2.01 ± 0.16	$0.45^{+0.17}_{-0.14}$
	10.6	3.01 ± 0.47	4.56 ± 0.40	2.20 ± 0.17	$0.66^{+0.24}_{-0.19}$
	10.8	4.44 ± 0.42	5.56 ± 0.29	2.63 ± 0.12	$1.33^{+0.24}_{-0.22}$
	11.0	4.07 ± 0.89	5.18 ± 0.63	2.47 ± 0.27	$1.05^{+0.49}_{-0.38}$
z-group2	10.6	5.07 ± 0.82	6.52 ± 0.58	3.45 ± 0.28	$1.53^{+0.46}_{-0.39}$
	10.8	3.67 ± 0.61	5.44 ± 0.50	2.92 ± 0.24	$0.86^{+0.29}_{-0.24}$
	11.0	6.38 ± 0.80	7.16 ± 0.50	3.75 ± 0.24	$2.05^{+0.45}_{-0.40}$
z-group3	10.8	6.58 ± 0.43	7.54 ± 0.28	4.46 ± 0.15	$1.61^{+0.18}_{-0.17}$
	11.0	7.91 ± 1.35	8.30 ± 0.78	4.87 ± 0.41	$2.12^{+0.61}_{-0.52}$
z-group4	10.8	6.30 ± 1.51	7.42 ± 0.99	5.09 ± 0.61	$0.96^{+0.43}_{-0.34}$
	11.0	8.69 ± 2.24	8.92 ± 1.28	6.01 ± 0.78	$1.64^{+0.73}_{-0.59}$
			QG		
z-group1	10.6	6.72 ± 1.48	7.02 ± 0.86	3.23 ± 0.36	$2.81^{+1.13}_{-0.92}$
	10.8	5.76 ± 1.53	6.22 ± 0.92	2.90 ± 0.39	$1.93^{+1.02}_{-0.78}$
	11.0	4.26 ± 2.43	5.09 ± 1.61	2.42 ± 0.69	$1.00^{+1.48}_{-0.77}$
z-group2	10.8	7.28 ± 1.44	7.94 ± 0.87	4.10 ± 0.40	$2.79^{+0.94}_{-0.80}$
	11.0	8.21 ± 2.40	8.14 ± 1.32	4.20 ± 0.61	$2.98^{+1.54}_{-1.20}$
z-group3	11.0	5.37 ± 2.14	6.67 ± 1.48	3.92 ± 0.78	$1.19^{+0.96}_{-0.65}$
			LAE		
z-group1	-	52.18 ± 12.64	5.24 ± 0.71	2.51 ± 0.30	$1.08^{+0.56}_{-0.43}$
z-group2	-	4.79 ± 1.01	3.62 ± 0.42	1.99 ± 0.21	$0.20^{+0.11}_{-0.08}$
z-group3	-	1.51 ± 0.58	2.38 ± 0.51	1.58 ± 0.31	$0.02^{+0.03}_{-0.01}$
z-group4	-	13.41 ± 9.10	7.15 ± 2.69	5.06 ± 1.72	$0.78^{+1.20}_{-0.61}$

[a] The stellar mass threshold of the sample.
[b] Best-fit amplitude of power-law (Equation 3.3) with $\gamma = 1.8$.
[c] Correlation length derived from the Limber equation (Equation 3.9).
[d] Galaxy matter bias.
[e] Mean halo mass.

Table 3.3: Summary of cross-correlation function measurements

	$\log(M_{\star,\mathrm{lim}}/M_\odot)^a$	A_ω^b $[\times 10^{-3}\mathrm{deg}^{0.8}]$	r_0^c $[h^{-1}\mathrm{cMpc}]$
		SFG-LAE	
z-group1	10.4	1.96 ± 1.12	3.00 ± 0.95
	10.6	2.09 ± 1.31	3.14 ± 1.10
	10.8	3.95 ± 0.12	4.40 ± 0.08
	11.0	2.26 ± 0.91	3.13 ± 0.70
z-group2	10.6	3.15 ± 0.33	4.64 ± 0.27
	10.8	2.69 ± 0.60	4.23 ± 0.52
	11.0	2.42 ± 0.37	3.92 ± 0.34
z-group3	10.8	1.61 ± 0.20	3.10 ± 0.22
	11.0	0.59 ± 0.24	1.77 ± 0.40
z-group4	10.8	2.38 ± 0.26	4.48 ± 0.27
	11.0	4.33 ± 1.13	6.26 ± 0.91
		SFG-QG	
z-group1	10.6	2.94 ± 0.55	4.50 ± 0.47
	10.8	4.42 ± 0.86	5.50 ± 0.59
	11.0	3.91 ± 0.81	5.00 ± 0.57
z-group2	10.8	4.84 ± 0.67	6.34 ± 0.49
	11.0	7.39 ± 0.75	7.73 ± 0.43
z-group3	11.0	6.88 ± 0.63	7.83 ± 0.40

[a]The stellar mass threshold of photo-z galaxies.
[b]Best-fit amplitude of power law (Equation 3.3) with $\gamma = 1.8$.
[c]Correlation length derived from the Limber equation (Equation 3.12).

3.3.5 Distribution differences inferred from correlation functions

We discuss the difference of distributions of three galaxy populations by comparing spatial correlation functions estimated from ACFs and CCFs. As reported in Tejos et al. (2014), the following relation among spatial ACFs and CCFs exists according to the Cauchy–Schwarz inequality:

$$\xi_{D1D2}^2 \leq \xi_{D1D1}\xi_{D2D2}, \tag{3.15}$$

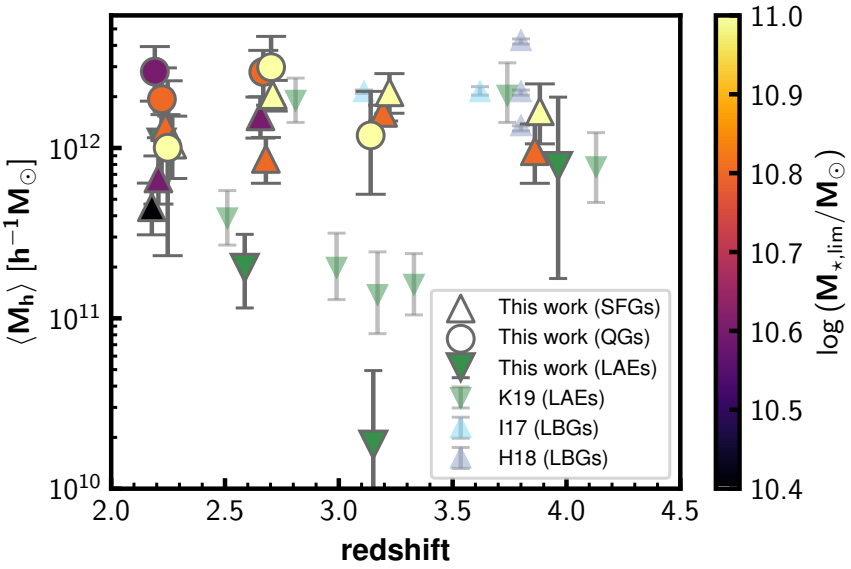

Figure 3.7: Mean halo mass at $2 < z < 4.5$. Colored triangles, colored circles, and green inverted triangles are identical to those in Figure 3.6. Small markers are those of LBGs (Ishikawa et al., 2017; Harikane et al., 2018) and LAEs (Khostovan et al., 2019).

where ξ_{D1D2} is the spatial CCF between samples 1 and 2, and ξ_{D1D1} and ξ_{D2D2} are the spatial ACFs of sample 1 and sample 2, respectively. When the equality is valid, the distributions of two populations are determined based only on by their dark matter halo masses, whereas an inequality sign implies the spatial CCF is not determined by the halo mass alone and that some additional physics affects their distributions. Therefore, we derive the spatial correlation function ratio $\xi^2_{\mathrm{D1D2}}/(\xi_{\mathrm{D1D1}}\xi_{\mathrm{D2D2}})$ and examine whether or not their distribution is explained only by the dark-matter halo mass. With the assumption of power-law forms of spatial ACFs and CCFs with the same γ, the ratio is expressed by the correlation lengths:

$$\frac{\xi^2_{\mathrm{D1D2}}}{\xi_{\mathrm{D1D1}}\xi_{\mathrm{D2D2}}} = \left(\frac{r^2_{0,\mathrm{D1D2}}}{r_{0,\mathrm{D1D1}}r_{0,\mathrm{D2D2}}}\right)^{\gamma}, \tag{3.16}$$

where $r_{0,\mathrm{D1D2}}$, $r_{0,\mathrm{D1D1}}$, and $r_{0,\mathrm{D2D2}}$ are the correlation lengths of the spatial CCF between samples 1 and 2 and their each spatial ACFs, respectively. We use the correlation lengths derived in Section 3.3.4.

Figure 3.8 is the main result of this chapter. The top panel shows the spatial correlation function ratio for SFGs and LAEs. We find that the ratios are below unity for most of the bins, implying that the spatial CCFs between SFGs and LAEs are not determined by the halo mass alone, and that some additional physics segregate the spatial distributions of SFGs and LAEs. This trend is independent of the stellar mass threshold of SFGs.

In the second lowest redshift ($z \sim 2.7$) bin, the spatial correlation function ratio for SFGs and LAEs in $M_\star$-group2 and 3 is consistent with unity if we consider the uncertainty. We do not know the exact origin of the peculiar behavior in this redshift bin, but we show several possibilities. In this redshift bin, LAEs are selected mainly from IA427, leading to a focus on smaller volumes in terms of line of sight compared to those of other bins at higher redshifts. This may induce to trace a peculiar structure by chance. Also, Cucciati et al. (2018) report a “proto-supercluster" at $z = 2.45$ in COSMOS field, within the scope of this bin. This may cause a different behavior in that bin.

The limiting luminosity for LAEs is different depending on the selection filter, as mentioned in Section 3.2.2. In particular, the limiting magnitude of higher redshift LAEs is shallower. This may cause a bias in the value of each bin. To check this possible bias, we derive the spatial correlation function ratios between SFGs and LAEs brighter than $\log (L_{\mathrm{Ly}\alpha}/\mathrm{erg\ s^{-1}}) > 42.8$ in z-group1. This threshold corresponds to the maximum 3σ limiting luminosity of our LAE sample. The ratios are 0.21 ± 0.38, 0.12 ± 0.18, 0.43 ± 0.76, and 1.54 ± 2.56 for SFGs of $M_\star$-group1, 2, 3, and 4, respectively. Though the last two cases have too large uncertainty to state any trend, possibly due to the small sample number of LAEs, these values imply that the limiting Lyα luminosity difference does not impact our results.

The bottom panel of Figure 3.8 shows the spatial correlation function ratios for SFGs and QGs. Unlike the spatial correlation function ratios for SFGs and LAEs, most of those for SFGs and QGs maintain unity, suggesting that only their dark-matter halo masses can account for the distributions for SFGs and QGs. If we derive the CCFs of SFGs and QGs adopting the different stellar mass threshold to each population and estimate the ratio, we find that the result generally does not change.

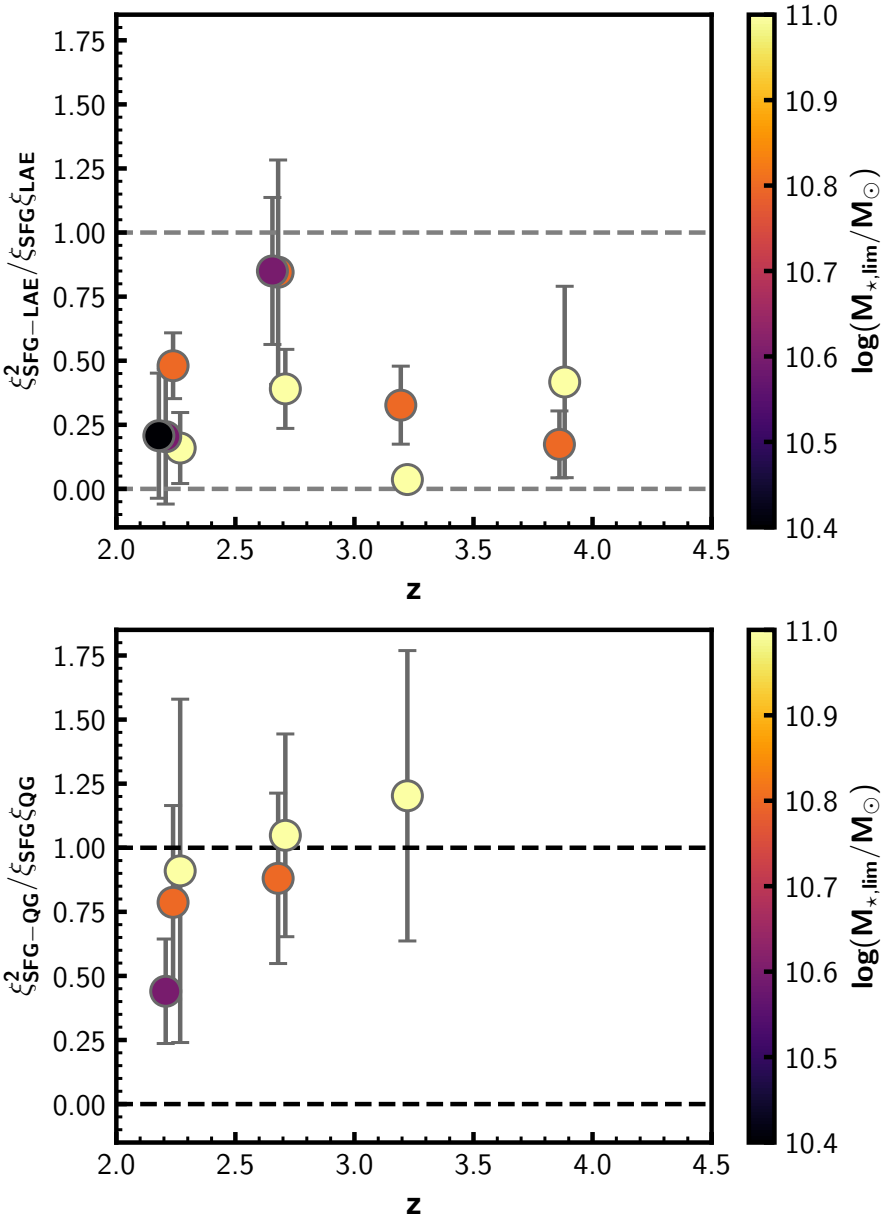

Figure 3.8: Spatial correlation function ratio $\xi^2_{\mathrm{D1D2}}/(\xi_{\mathrm{D1D1}}\xi_{\mathrm{D2D2}})$. The top panel shows cases for SFGs and LAEs, whereas the bottom panel shows cases for SFGs and QGs. Colors of markers correspond to stellar mass thresholds for SFGs/QGs. The same stellar mass thresholds are imposed for both samples in the case of the correlation function ratio for SFGs and QGs. The redshift is slightly shifted for the illustrative purpose.

3.3.6 Dependence of correlation function ratio on rest-frame UV magnitude of LAE

To investigate the effect of the stellar mass of LAEs on the results, we divide LAEs in terms of their rest-frame UV absolute magnitude. The absolute magnitude of SC4K LAEs is calculated based on i^+ band photometry summarized in Laigle et al. (2016), under the assumption of a flat continuum. With the assumption of LAEs locating in the main sequence and with small dust attenuation, the rest-UV luminosity is proportional to SFR and thus to stellar mass. The LAE sample is divided into two subsamples: one with an $M_{\rm UV}$ greater than -20, i.e., "UV-faint LAEs" and the other with an $M_{\rm UV}$ less than -20, i.e., "UV-bright LAEs". LAEs undetected in the i^+ band are classified under the former subsample. The 3σ limiting magnitude of this i^+ band photometry is 26.2 mag in 3" aperture (Laigle et al., 2016), which corresponds to $M_{\rm UV} \sim -20.0$ mag at $z = 4.5$. This ensures that we completely select UV-bright LAEs at all redshift bins. Moreover, this threshold corresponds to $\log(M_\star/M_\odot) \sim 9.5 - 10$ according to the star-formation main sequence and UV magnitude - UV slope relation of SC4K LAEs (Santos et al., 2020). Therefore, in terms of the stellar mass, the UV-bright LAE sample is more similar to QG and SFG than the total LAE sample.

We derive ACFs and CCFs for these subsamples and estimate the spatial correlation function ratios from the correlation lengths in the same manner as in Section 3.3.5. Figure 3.9 shows the ratio $\xi^2_{\rm SFG-LAE}/(\xi_{\rm SFG}\xi_{\rm LAE})$ as a function of the redshift for the cases of UV-bright LAEs and UV-faint LAEs. Interestingly, the ratios for UV-bright LAEs tend to be higher than those for UV-faint LAEs or have at least the same values for some bins within the uncertainty. Moreover, some bins for UV-bright LAEs have ratios equal to unity, suggesting that a distribution difference does not exist, whereas those bins for UV-faint LAEs exhibit ratios less than one. For z-group2 cases, this trend may be related to the unity value of the correlation function ratio between the total LAEs and SFGs, but this overall trend implies that the distribution difference between SFGs and LAEs depends on the UV-magnitude of LAEs.

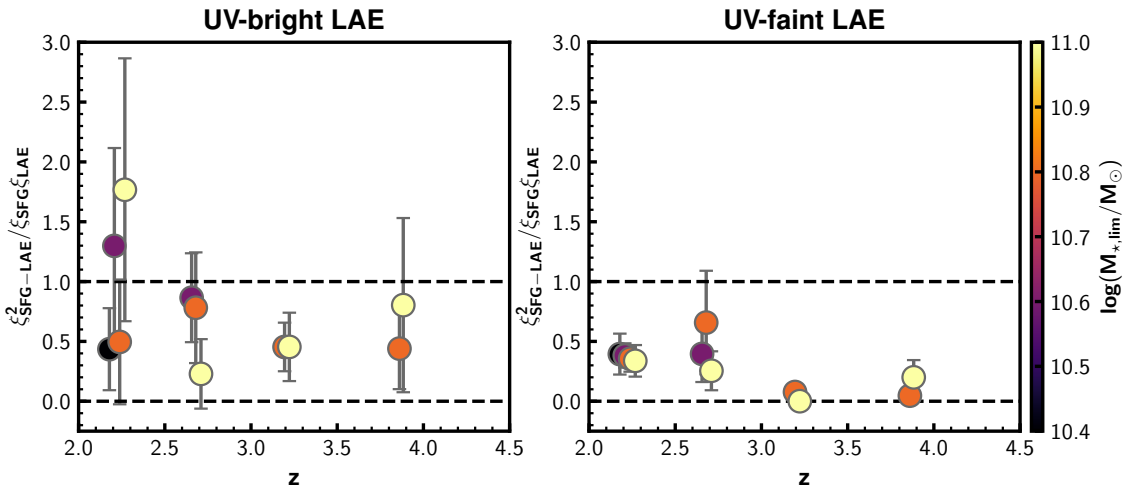

Figure 3.9: Left panel: Spatial correlation function ratio $\xi^2_{\rm SFG-LAE}/(\xi_{\rm SFG}\xi_{\rm LAE})$ only for UV-bright ($M_{\rm UV} < -20.0$) LAEs. The marker colors correspond to the stellar mass group of SFGs. Right panel: Same as the left panel, but for UV-faint ($M_{\rm UV} > -20.0$) LAEs.

3.3.7 Impact of catastrophic photo-z error

We have evaluated the impact of the catastrophic error of photo-z on the results. The correlation for $M_\star$-group3 SFGs and LAEs in z-group3 bin is used as an example because these have the largest numbers of LAEs, and their Poisson errors do not govern the uncertainty. Galaxies at $0.2 < z < 0.4$, whose Balmer breaks can be misclassified as Lyman breaks at $z \sim 3$, are possible interlopers to our SFG sample at that redshift.

We randomly select galaxies in our sample and replace them with randomly selected galaxies at $0.2 < z < 0.4$ from our photo-z catalog. The fraction of the replaced sample corresponds to the contamination fraction of the sample. Although its precise value is not certainly determined, we tentatively assume 10% of our sample. This is of the same order as the fraction of the catastrophic errors of photo-z summarized in Laigle et al. (2016). We derive ACFs and a CCF between the SFGs and LAEs and a spatial correlation function ratio. We conduct this procedure 50 times in the same manner as in Section 3.3. Figure 3.10 shows the results in terms of the correlation function ratios. The average of the 50-times procedures is consistent with the original value, and the value of individual trials is always below unity. This trend implies that the catastrophic error of photo-z does not change the spatial correlation function ratio.

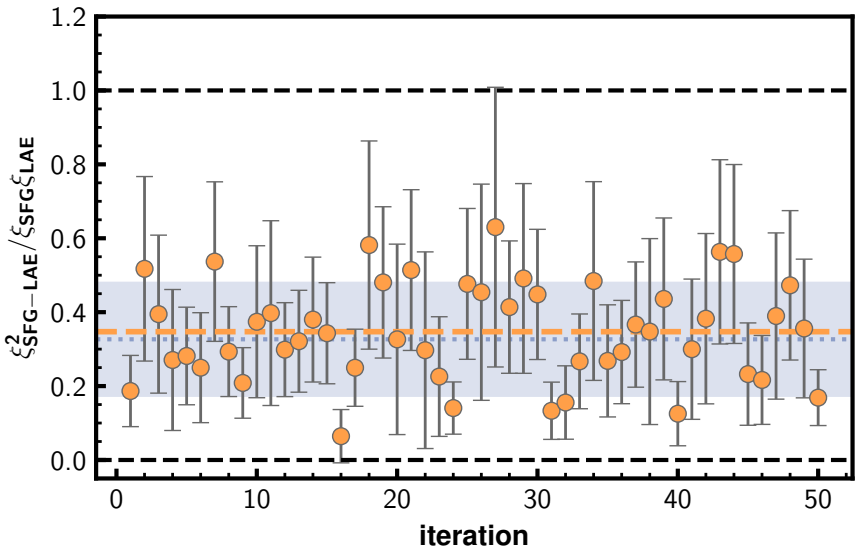

Figure 3.10: A test of the effect of the catastrophic photo-z error on the trend of the correlation function ratio of SFGs and LAEs. Values of the ratio $\xi^2_{\mathrm{SFG-LAE}}/(\xi_{\mathrm{SFG}}\xi_{\mathrm{LAE}})$ is shown, when 10% of galaxies are replaced with galaxies at $0.2 < z < 0.4$, are shown in orange circles. The orange dashed line indicates their average. The blue dotted line and the hatch show the original value and their 1σ uncertainty range derived in Section 3.3.5.

This trend can be explained by the dependence of the contamination fraction f on the correlation length inferred from the Limber equation (Equation 3.9 and 3.12). The correlation lengths of spatial ACFs decrease by a factor of $(1-f)^{2/\gamma}$, whereas those of spatial CCFs decrease by a factor of $(1-f)^{1/\gamma}$. These factors are compensated in the ratio $\xi^2_{\mathrm{SFG-LAE}}/(\xi_{\mathrm{SFG}}\xi_{\mathrm{LAE}})$ and the ratio equals to the original value.

The same can be applied to the low-z contaminants of LAEs. By matching the spectroscopic redshift in the literature, Sobral et al. (2018) estimate the contamination fraction of SC4K LAEs to be $10-20$%, which is a similar value to the assumption in the above test. We admit that this is derived from a limited sample; nonetheless, this information supports its insignificant impact on our result.

3.4 Overdensity Distribution Comparison

Galaxy overdensity is another often used quantity for characterizing the galaxy environment. (e.g., Peng et al., 2010b; Kawinwanichakij et al., 2017). We estimate the overdensity at the positions of SFGs, QGs, and LAEs to examine whether the spatial distribution difference suggested from the clustering analysis can be seen. Because we discuss the spatial distribution difference with reference to SFGs in the clustering analysis, the surface number density of SFGs is used as an index of overdensity.

The overdensity at the position of the i-th galaxy is defined as follows (Chartab et al., 2020):

$$\delta(\boldsymbol{X}_i) = \frac{\sum_j \omega_j^i \sigma_j(\boldsymbol{X}_i)}{\sum_j \omega_j^i \bar{\sigma}_j} - 1, \tag{3.17}$$

where $\boldsymbol{X}_i$ is the position of the i-th galaxy, and ω_j^i is its probability of residing in the j-th redshift slice. $\sigma_j(\boldsymbol{X}_i)$ is the surface number density of galaxies at that position, and $\bar{\sigma}_j$ is the average surface number density in the entire field in the j-th redshift slice. The redshift slice is generated with an interval of $\delta z/(1+z) = 0.01$, which is of the same order as the typical photo-z uncertainty of photo-z galaxies. The ω_j^i is determined via integration of the PDF distribution of the redshift for the range of each redshift slice. The PDF of photo-z galaxies is assumed to be Gaussian centered at the median PDF and its 68% confidence interval as $\pm 1\sigma$. For LAEs, we derive their PDF from the expected Lyα detection rate based on the IB transmission curve.

The surface number density map at each redshift slice is estimated using the weighted Gaussian kernel density method. The surface number density at the position of $\boldsymbol{X}_i$ is derived as :

$$\sigma_{j,\mathrm{obs}}(\boldsymbol{X}_i) = \frac{\sum_k \omega_j^k K(\boldsymbol{X}_k, \boldsymbol{X}_i)}{\sum_k \omega_j^k}. \tag{3.18}$$

This method sums the contributions of all galaxies with the weight ω_j^k of the probability of k-th galaxy being located at j-th redshift slice. We consider the 2D Gaussian kernel $K(\boldsymbol{X}_k, \boldsymbol{X}_i)$ to be:

$$K(\boldsymbol{X}_k, \boldsymbol{X}_i) = \frac{1}{2\pi a^2} \exp\left[-\frac{r(\boldsymbol{X}_k, \boldsymbol{X}_i)^2}{2a^2}\right], \tag{3.19}$$

where $r(\boldsymbol{X}_k, \boldsymbol{X}_i)$ is the projected distance between two positions, and a is the bandwidth parameter. It is important to carefully select the bandwidth for estimating the adequate

scale of the density. Several previous studies determine the bandwidth to minimize the variance of the density map (e.g., Chartab et al., 2020; Bădescu et al., 2017), but this leads to bandwidth sizes that differ with redshift. Therefore, we apply a constant bandwidth of 5 cMpc, which is the typical correlation length of SFGs. It is noted that the surface number density at an SFG is systematically higher than the density elsewhere because there is always one galaxy, making it impractical to compare the number density distributions for several populations. Therefore, the contribution from itself is subtracted from $\sigma_{j,\mathrm{obs}}(\boldsymbol{X}_i)$ when the surface number density at an SFG is calculated.

Given the finite observed field, it is essential to correct the boundary effect and the masked region. The intrinsic surface number density can be expressed as follows (Jones, 1993):

$$\sigma_j(\boldsymbol{X}_i) = \frac{\sigma_{j,\mathrm{obs}}(\boldsymbol{X}_i)}{\int_S K(\boldsymbol{X}, \boldsymbol{X}_i) dS}, \tag{3.20}$$

where S is the area of the observed field with the masking. The denominator in Equation 3.20 is equal to unity if the position $\boldsymbol{X}_i$ is near the center of the observed field and free from the masked region, whereas it becomes smaller if the position $\boldsymbol{X}_i$ is at the edge of the field or covered by the mask. We apply the correction for each galaxy.

We compare the overdensity distributions of galaxies in z-group2 and 3. We focus on this redshift range because it has enough sample numbers for all galaxy populations. We do not consider z-group1, because LAEs exist only in a smaller survey field than other samples (see Section 3.2.2), which will make it difficult to calculate the density continuously at all redshift range. Furthermore, we assign the same stellar mass threshold to SFGs and QGs, which means that photo-z galaxies with $\log(M_\star/M_\odot) > 10.8$ in z-group2 and those with $\log(M_\star/M_\odot) > 11.0$ in z-group3 are discussed. There is an overlap between the redshift range of these groups, and we conservatively impose the latter threshold for galaxies in that overlapped range.

The overdensity distributions at the position of three galaxy populations are shown in Figure 3.11. The overdensity at LAEs tends to be lower than those at SFGs and QGs. We test whether this distribution difference is significant using two statistical tests, the Anderson–Darling (AD) test and the Kolmogorov–Smirnov (KS) test. The AD test is sensitive to the difference at the edge of the distribution, whereas the KS test is sensitive to the difference at the center. The P-value from both the AD test and

the KS test is less than 0.01, so we reject the null hypothesis that the overdensity distributions of LAEs and SFGs are the same, suggesting that this distribution difference is significant. On the other hand, the overdensity distributions of SFGs and QGs appear to be consistent, suggesting that the QGs are located in a similar environment to SFGs. The statistical tests do not suggest a significant difference between these two overdensity distributions, according to $P = 0.10$ from the AD test and $P = 0.23$ from the KS test. The median values of the overdensity also support these trends. These suggest that we see the distribution difference between SFGs and LAEs not only from the clustering but also from the overdensity distribution, whereas we do not see it between SFGs and QGs.

We note that this analysis does not consider dark matter halo mass difference among galaxy populations, different from the clustering analysis in Section 3.3. The overdensity is one of the most often-used index for evaluating the environment, and this has been used to discuss the distribution difference among different galaxy populations in protoclusters (e.g., Shimakawa et al., 2017; Shi et al., 2019b, 2020). However, this might induce a some fraction of the difference between LAEs and other massive galaxies.

3.5 Discussion of Chapter 3

3.5.1 Test of clustering among HAEs, LAEs, and SFGs at $z = 2.22$

Thus far, we report that massive SFGs and LAEs are distributed differently beyond the difference of their halo masses. We confirm that the correlation function ratio $\xi^2_{\mathrm{SFG-LAE}}/(\xi_{\mathrm{SFG}}\xi_{\mathrm{LAE}})$ is less than unity, and this is not affected by the catastrophic failure of the photo-z estimation of some objects. Here, we conduct the same clustering analysis for Hα emitters (HAEs) instead of photo-z selected SFGs. HAEs are typical star-forming galaxies more massive than LAEs and have smaller redshift uncertainty than photo-z selected galaxies. Therefore, this test can be used to examine whether or not the trend in Section 3.3 is caused by the large redshift uncertainty of photo-z selected SFGs. Here, an HAE sample at $z = 2.22$ constructed as a part of the HiZELs survey (Sobral et al., 2013) is used. This sample was constructed based on the flux excess of $\mathrm{NB_K}$ at 2.121μm compared to the K band and the color selection on the

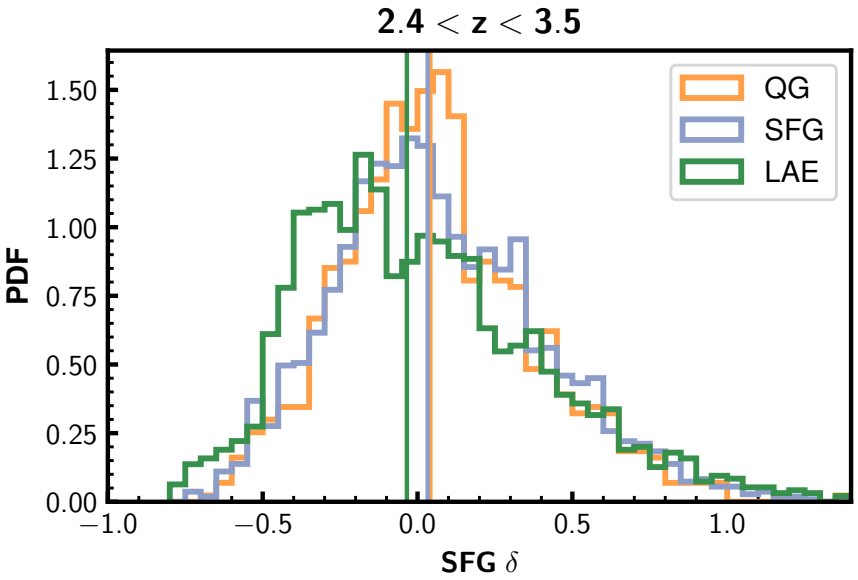

Figure 3.11: The overdensity distribution of SFGs at the position of QGs (orange), SFGs (blue), and LAEs (green). The median values are shown in vertical lines in colors same as the distribution.

BzK diagram. Their redshift uncertainty is as small as that of LAEs, and the survey covers 2.34 deg^2 in the COSMOS field. Objects with higher fluxes than the average limiting flux $\log(F_{\mathrm{H}\alpha}/\mathrm{erg\ s^{-1}\ cm^{-2}}) \sim -16.5$ (Figure 7 in Sobral et al., 2013), at which the completeness of the sample is $\sim 50\%$, are used in the study. We use LAEs selected from NB392 from SC4K, which are identical to the sample used in Section 3.3, because the selection redshift range is almost the same (Figure 1 in Sobral et al., 2017).

The survey area of LAEs is slightly different from that of HAEs. We focus only on regions where LAEs and HAEs coexist and are not affected by any masks of Laigle et al. (2016). There are three duplications between LAEs and HAEs. For the same reason mentioned in Section 3.3.1, we exclude two duplications from HAE sample. The total numbers of HAEs and LAEs are 406 and 87, respectively.

The ACFs and the CCF are estimated in the same manner as in Section 3.3. We fit the power-law at $\theta > 10$" for the ACF of the LAEs and $\theta > 40$" for the ACF of the HAEs and the CCF. The measured correlation function is shown in Figure 3.12. The amplitude of CCF is lower than those of ACFs of HAEs and LAEs. The correlation length of the

ACFs and the CCF are estimated in the same manner as in Section 3.3, and the spatial correlation function ratio $\xi^2_{\mathrm{HAE-LAE}}/(\xi_{\mathrm{HAE}}\xi_{\mathrm{LAE}})$ is estimated to be 0.27 ± 0.12, which is less than unity. This value suggests that the spatial CCF signal cannot be explained by only their halo mass difference, which is the same as in photo-z SFGs.

We also derive the CCFs between HAEs and SFGs. We use SFGs which are in the lowest redshift bin constructed in Section 3.3 and located in the same survey region as HAEs. In the same way as in Section 3.3, four stellar mass thresholds are employed, and ACFs and CCFs are estimated for each. Because both HAEs and SFGs are thought to be similar galaxy populations, many of them are duplicated. Here, we do not exclude these duplications to make the HAE sample analysis consistent with that performed for the LAEs. The values for the ratio $\xi^2_{\mathrm{HAE-SFG}}/(\xi_{\mathrm{HAE}}\xi_{\mathrm{SFG}})$ are calculated to be 0.70 ± 0.34, 0.68 ± 0.42, 0.37 ± 0.33, and 1.35 ± 0.84 for SFGs' stellar mass thresholds of $\log(M_\star/M_\odot) > 10.4,\ 10.6,\ 10.8,$ and 11.0, respectively. These values are higher than the case of HAEs and LAEs, and most of the bins equal unity. This implies that, unlike the clustering between HAEs and LAEs, the clustering between HAEs and SFGs is explainable only by their halo mass.

These tests support the trends shown in Section 3.3. Thanks to the smaller redshift uncertainty of HAEs, the spatial correlation function ratio between HAEs and LAEs implies that uncertainties in the photo-z estimates do not cause the trend. The fact that the spatial correlation function ratios for HAEs and SFGs are equal to unity also supports the hypothesis that these differences in distribution do not occur for all line emitters, but only for LAEs. Moreover, these results imply that trends are seen even for less massive SFGs. The Hα flux limit corresponds to SFR of $\sim 24 M_\odot \mathrm{yr}^{-1}$, based on an assumption of 1 magnitude dust extinction and the standard calibration method by Kennicutt (1998). Such SFR corresponds to a stellar mass of $\log(M_\star/M_\odot) \sim 9.8$, according to the relation between SFR and $M_\star$ of HAEs reported in Oteo et al. (2015), which is ~ 0.6 dex smaller than the minimum stellar mass threshold of photo-z selected SFGs.

It should be noted that the depth of Hα flux of this HAE sample has a variation from field to field (Sobral et al., 2013; Cochrane et al., 2017). In order to reduce the effect from the depth variance, we verify whether the result with brighter HAEs ($\log(F_{\mathrm{H}\alpha}/\mathrm{erg\ s^{-1}\ cm^{-2}}) > -16.0$) is consistent with the original result. The value of the spatial correlation function ratio is consistent within the 1σ uncertainty both for

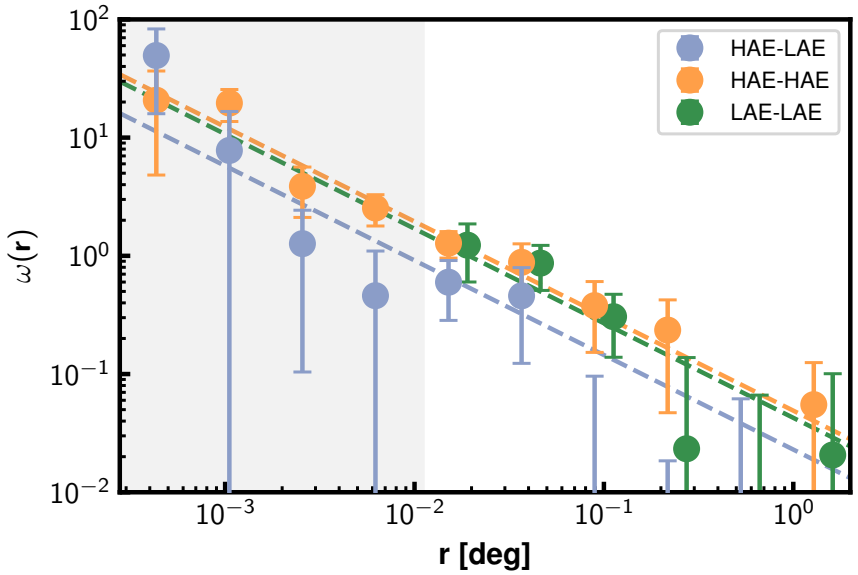

Figure 3.12: The ACFs and the CCF of HAEs and LAEs at $z = 2.22$. Oranges and green circles are ACFs of HAEs and LAEs, respectively, whereas blue circles show their CCF. Best-fit of the power-law (Equation 3.3) is shown in dashed lines. The CCF signal is significantly lower than those of ACFs.

the correlation function of HAE-LAE and those of HAE-SFG. This suggests that the field variance does not significantly affect our result.

3.5.2 Why are LAEs located in a different environment?

We have investigated the spatial distribution difference among SFGs with $\log(M_\star/M_\odot) > 10.4$, QGs with $\log(M_\star/M_\odot) > 10.6$, and LAEs by two methods, i.e., the clustering analysis and the overdensity analysis. The small signal of CCFs between SFGs and LAEs requires some additional physics to account for it, whereas CCFs between SFGs and QGs can be perfectly explained by their halo mass differences. The CCFs among HAEs, SFGs, and LAEs support the existence of that distribution difference in the case of the stellar mass of SFGs down to $\log(M_\star/M_\odot) \sim 9.8$ and suggest that the trend is unlikely to be due to the photo-z uncertainty. The overdensity distribution also reveals that LAEs are statistically located in less dense regions than SFGs on the scale of $\sim$ 5cMpc, whereas SFGs and QGs are located in the same density field. These trends

suggest that LAEs are somehow distributed differently compared to SFGs and QGs.

Several previous studies report hints of this distribution difference, indirectly or in peculiar environments. For example, Momose et al. (2021c) measure CCFs between HI IGM tomography data and several galaxy populations and find that the CCF of LAEs is flat up to $r \sim 3h^{-1}$ cMpc, which is different from the behavior of other SFGs. This trend indirectly suggests a potential distribution difference between LAEs and SFGs. In addition, the segregation of LAEs and SFGs is found in protoclusters. Shi et al. (2019a) measure the LAE distribution in a known LBG protocluster at $z = 3.13$ (Toshikawa et al., 2016) and find that LAEs are segregated from the overdensity of LBGs in a few ten cMpc scales. Shimakawa et al. (2017) also report the segregation of LAEs and HAEs in a protocluster core region at $z = 2.5$ (please refer to Hough et al. (2020) for perspectives from semi-analytic simulations). This study directly suggests that such distribution segregation between SFGs and LAEs is ubiquitously seen at $z \sim 2 - 4.5$.

On the other hand, Bielby et al. (2016) calculate the CCFs between LAEs and spectroscopically confirmed LBGs at $z = 3.1$ and demonstrated the ratio $\xi^2_{\mathrm{LBG-LAE}}/(\xi_{\mathrm{LBG}}\xi_{\mathrm{LAE}}) = 1.28 \pm 0.46$, which is consistent with unity. The result seems to be inconsistent with ours. However, their spectroscopic confirmation of LBGs is mainly based on Lyα emission or absorption, and the dominant fraction of LBGs seems to have Lyα emission, as seen from their stacked spectra (see Figure 15 in Bielby et al., 2013). This may have lead to tracing similar populations from both samples, which may have caused a higher amplitude in the CCF.

The distribution difference between LAEs and SFGs can be explained by the assembly bias (e.g. Gao & White, 2007), which is similar to a scenario suggested in Shi et al. (2019a). LAEs are typically younger in terms of the luminosity weighted age (e.g. approximately 10 Myr in Nakajima et al., 2012; Hagen et al., 2014) than massive galaxies, such as the SFGs (e.g. approximately 100 Myr in Hathi et al., 2013) or QGs (e.g. approximately 1 Gyr in Belli et al., 2019; Gobat et al., 2012). Such differences in age can be related to the different formation time of galaxies and eventually that of their host halos. The different formation epoch of halos is known to cause an impact on the signal of the correlation function. Zehavi et al. (2018) suggest that, even at similar halo mass, the clustering signal can change depending on their formation epoch. The assembly bias tends to increase the clustering signal. If this trend exists in our case, the CCFs between later formed halos and earlier formed halos (i.e., LAEs and

SFGs) are expected to be weaker than that expected from each ACFs. We find that UV-brighter LAEs tend to have a higher ratio $\xi^2_{\mathrm{SFG-LAE}}/(\xi_{\mathrm{SFG}}\xi_{\mathrm{LAE}})$ than UV-fainter LAEs. The UV-brighter LAEs are expected to reside in more evolved halos, or in other words, in earlier forming halos, thus reducing such an effect.

The large amount of HI gas in their circumgalactic media or surrounding intergalactic media associated with massive halos is another possible explanation. This gas absorbs the Lyα photons and prevents us from detecting the Lyα emission of galaxies in massive halos, i.e., galaxies around or in massive halos are preferentially observed as non-LAEs. This makes the distribution of LAEs different from others. Other studies indirectly argue a similar hypothesis. Toshikawa et al. (2016) demonstrate a smaller Lyα equivalent width in an LBG-selected protocluster at $z = 3.67$ than in field galaxies. Shimakawa et al. (2017) infer that the accretion of cold streams, which provide pristine HI gas to the protocluster core, could prevent Lyα photons from escaping from the dense regions. Meanwhile, Momose et al. (2021c) have shown that LAEs tend to avoid HI overdensity peaks, whereas Liang et al. (2021) present a similar trend from the correlation of the optical depth of the sightlines of quasi-stellar objects (QSOs) and the spatial distribution of LAEs. In addition, Momose et al. (2021a) shows that LAEs are more likely to be selected in front of the HI density peak in the line of sight direction. We note that these results are on different scales. Shimakawa et al. (2017) show the distribution segregation on a scale of a few hundred pkpc, whereas other studies have focused on a few pMpc. Regardless, the typical scale of this effect and the amount of HI gas around massive galaxies remain unclear.

It is possible that both effects contribute to the distribution difference. Although a conclusive origin for the distribution difference between SFGs and LAEs remains under debate, our result reinforces the importance of investigating multiple galaxy populations to reveal their environment.

3.5.3 Quenching and environment

Our sample is large enough to investigate a possible correlation between SFR and the overdensity for different galaxy populations. From the overdensity values for the SFGs and QGs estimated in Section 3.4, we check the existence of that correlation at $2.4 < z < 3.5$. The top panel of Figure 3.13 shows the relationship between SFR and

overdensity. SFGs and QGs are distinguished with their medians and their uncertainties estimated based on the normalized medians of the absolute deviations. The median values may seem to slightly increase towards higher overdensities for SFGs and QGs, especially at $\log(1+\delta) > 0$, but the Spearman's rank correlation test does not indicate any significant correlations (the correlation coefficient $\rho \sim 0.03$ with $P = 0.3$ for both populations). Therefore, we conclude that a significant correlation between the number density and SFR is not seen in our sample. Clear trends are also not identified for sSFR, as shown in the bottom panel of Figure 3.13.

This result is in contrast to what we observe in the local universe, where there is a clear anti-correlation between SFR and the number density (e.g., Lewis et al., 2002). Furthermore, at $z > 1$, the reversal of the relation has been reported (e.g., Elbaz et al., 2007; Lemaux et al., 2020). In particular, Lemaux et al. (2020) argue the existence of a weak but significant positive correlation between the SFR and the overdensity of star-forming galaxies at $2 < z < 5$, based on density measurement via Voronoi Monte Carlo mapping. The difference in trends between our results and those of Lemaux et al. (2020), as shown in Figure 3.13, may be due to the different density estimation methods and/or sample difference. Their targets have a lower stellar mass completeness limit (80% complete to $\log(M_\star/M_\odot) \sim 9.2 - 9.5$) than that in our study ($\log(M_\star/M_\odot) > 10.8$). Moreover, they use a spectroscopically confirmed sample with more accurate redshifts. This can lead to a clearer contrast for the density map and a larger dynamic range for the overdensity.

One may think that this looks contradictory to what we show in Chapter 2, i.e., galaxies in overdense regions have higher SFR than field galaxies. Mainly two differences between them are likely to cause this. Firstly, HSC protocluster trace more overdense regions than the overdensity range of this analysis. According to the average number density and its standard deviation, the overdensity of protoclusters ranges 2-5, where there is almost no data-point in Figure 3.13. This overdensity difference might imply that the correlation can be seen only when we focus on the extremely dense regions. Secondly, the scale for the density measurement is different between the two studies. Chapter 2 is based on the overdensity map measured with 1.8' (3.6 cMpc) aperture, which is smaller than this analysis. Such different scales induce a different trend.

We also check the trend at lower redshift in the same manner and examine the

existence of redshift evolution. We use SFGs and QGs in $M_\star$-group2 of z-group1 ($2.05 < z < 2.39$) in Section 3.3. Figure 3.14 shows their SFR-δ relation. Even a weak increasing trend in median values is not found. The correlation coefficient from Spearman's rank correlation test also does not indicate a significant correlation. The disappearance of the apparently increasing median value trend could be due to the redshift evolution of the relation, which has been reported by Lemaux et al. (2020) at a similar redshift.

Based on the previously presented results, including those from the clustering analysis and the overdensity distribution, our results possibly imply that the environment is not likely to impact significantly on the star-formation quenching of such massive galaxies at $z \geq 2$. Several studies support our trends. Hatfield & Jarvis (2017) estimate the CCF signal of SFGs and QGs and argue that the environment does not play a significant role in quenching at $z \sim 2$, based on their model for the environmental quenching within the halo occupation distribution scheme. Lin et al. (2016) also report only little dependency on the local density for the quiescent fraction at $1.5 < z < 2.5$. Also, Kawinwanichakij et al. (2017) argue that mass and environmental quenching are comparable for massive galaxies at $0.5 < z < 2.0$ with stellar masses similar to those of photo-z galaxies in this study. Their target redshift is lower than ours, so our results may suggest that environmental quenching at $z > 2$ is not significant compared to at lower redshift. On the other hand, Chartab et al. (2020) argue that the average SFR of galaxies with stellar masses similar to ours decreases if they are located in more overdense regions, even at $2.2 < z < 3.5$, suggesting that the galaxy environment does affect quenching at $z > 2$. This result may contrast with ours, but this can be related to the different number of the sample or the quality of the SED modeling.

Moreover, it should be emphasized that the methods used to measure the environments in previous studies and in this study have large variations in terms of techniques and target scales. For example, Kawinwanichakij et al. (2017) quantify environments based on the 3rd nearest neighbor, which tends to represent a much smaller scale environment than what we explore. Chartab et al. (2020) estimate the number density distribution based on a bandwidth of less than $1h^{-1}$cMpc. Such scale differences may make it difficult to compare the results among different studies.

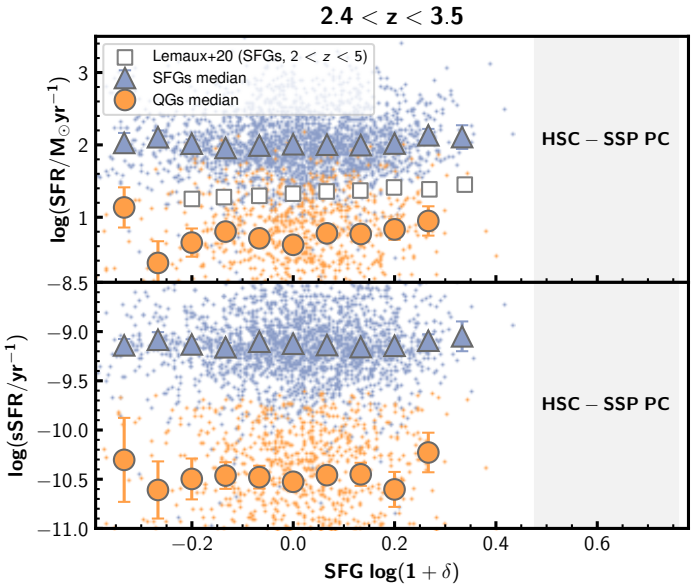

Figure 3.13: Top panel: Relation of SFR and overdensity for SFGs (blue) and QGs (orange) at $2.4 < z < 3.5$. Their median values of bins which contain more than ten objects are shown in blue triangles and orange circles. The median trend at $2 < z < 5$ reported in Lemaux et al. (2020) is shown in white circles for reference. Their median amplitude of SFR is different from ours because of slight difference in their redshift and stellar mass range. Bottom panel: Relation of sSFR and the overdensity. Colors and markers are identical to those of top panel. For reference, we show the peak overdensity range of $z \sim 4$ HSC-SSP protoclusters, discussed in Chapter 2. We note that this overdensity is measured by the different galaxy tracers (LBGs), and the estimation method is also different.

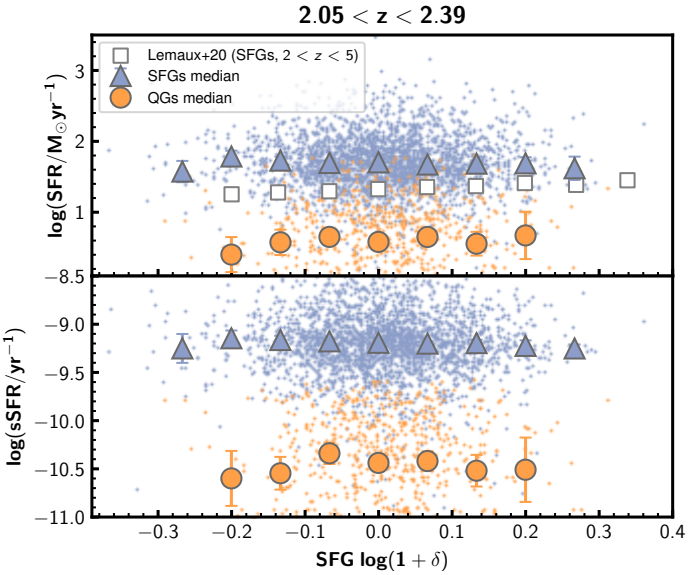

Figure 3.14: The same as Figure 3.13, but for objects in z-group1.

3.6 Summary of Chapter 3

In this chapter, we have investigated the spatial distribution differences among massive ($\log(M_\star/M_\odot) \geq 10.4$) SFGs and QGs selected by photometric redshift, and LAEs selected by narrow/intermediate bands in the COSMOS field. Through the use of deep and multiband photometry, a systematic study has been performed for $2 < z < 4.5$. Our main results are summarized as follows:

1. We first derive the autocorrelation function and cross-correlation function of three populations. The spatial correlation function ratio $\xi^2_{\rm D1D2}/(\xi_{\rm D1D1}\xi_{\rm D2D2})$ of SFGs and QGs is equal to unity, suggesting that their distribution can be explained only by their host halo mass. On the other hand, the ratios of SFGs and LAEs are significantly below unity, implying that some additional physical processes spatially segregate these two populations in general.

2. The same analysis is conducted among HAEs at $z = 2.22$ from HiZELs survey, LAEs, and photo-z selected SFGs. The spatial correlation function ratio of HAEs and LAEs is significantly lower than unity, supporting the segregation of LAEs from other galaxy populations.

3. We also derive the overdensity at the position of three populations with the use of the surface number density of SFGs. LAEs are found to be located in less dense regions than SFGs and QGs at $2.4 < z < 3.5$. On the other hand, QGs are confirmed to be located in the same environments as SFGs.

4. With the use of overdensity distribution, we explore the relation between the star forming activity and overdensity. Neither SFGs nor QGs exhibit significant correlations between SFR (sSFR) and the overdensity. The results mentioned above and this results suggest that the environment does not significantly impact the star-formation quenching in our dynamic range of the overdensity and the scale of the environment.

There are several possible origins of LAEs exhibiting different spatial distributions to other galaxy populations. One is assembly bias, which is supported by the higher spatial correlation function ratios of UV-brighter LAEs and SFGs than those of UV-fainter LAEs. The other is a large amount of HI gas associated with massive halos in their circumgalactic media or surrounding intergalactic media. Our results highlight the importance of exploring the galaxy environment through multiple populations.

4

X-ray and Radio Stacking for Quiescent Galaxies at $0 < z < 5$

- Based on Ito et al. (submitted)

4.1 Background of Chapter 4

It is not well understood what physical processes are responsible for the rapid quenching and suppressing subsequent star formation activities, although the cold streams are expected to supply gas at the high redshift (e.g., Dekel et al., 2009). One of the preferred mechanisms is feedback from AGNs. The radiation, wind, or radio jet from AGNs can eject the gas from galaxies or heat the gas in/around galaxies, thereby suppressing star formation activity, although the detailed mechanism still remains unclear. In the local universe, there are multiple lines of observational evidence for the AGN feedback (see Fabian, 2012, for review).

Investigating the AGN activity of QGs is essential to explore the relation between

quenching and AGNs. In that sense, the stacking of the X-ray and radio images is a powerful tool to reveal the average picture of the AGN activity, reaching low luminosities even at high redshift. So far, Olsen et al. (2013) show that the stacked X-ray luminosity of individually undetected QGs at $z \sim 2$ cannot be explained by the X-ray luminosity originated from the star formation, lending support to the presence of AGNs. The radio stacking of QGs at $z < 2$ also suggests a high radio luminosity for their star formation rate (Man et al., 2016; Gobat et al., 2018; Magdis et al., 2021), which is in line with the X-ray picture. On the other hand, X-ray and radio properties of typical QGs are almost unexplored at higher redshifts ($z > 2$). Indeed, several studies have discussed the X-ray property focusing on the only limited sample. At $3 < z < 4$, Schreiber et al. (2018) focus only on X-ray detected sources. Carraro et al. (2020) and D'Eugenio et al. (2021) include individually detected sources in their statistical analysis at $z < 3.5$, but this is potentially a problem. Powerful AGNs, which are detected individually, may not sample the entire AGN population (see the X-ray luminosity function work such as Ueda et al., 2014; Miyaji et al., 2015) and might make the average trend of the sample skewed owing to their high luminosity. This limitation toward the higher redshift is primarily due to the rapid decrease of the number of QGs toward higher redshift (e.g., Merlin et al., 2019) and the lack of deep X-ray and radio imaging which can detect the faint signal of the stacked high-z objects. In addition, if we want to discuss AGN activity in the context of quenching, we should compare the properties of QGs to those of star-forming galaxies (SFGs).

In this chapter, we perform a systematic stacking analysis for the X-ray and radio images of QGs at $0 < z < 5$ which are individually undetected in the X-ray. QGs are selected using the latest photometric catalog of the COSMOS field (COSMOS2020, Weaver et al., 2021). The COSMOS field covers $\sim 2\,\mathrm{deg}^2$, and in addition to the deep multiband optical and infrared data, the deep X-ray and the radio data exist (Schinnerer et al., 2007; Civano et al., 2016; Marchesi et al., 2016a; Smolčić et al., 2017), enabling us to unveil the average properties of typical QGs with the largest sample out to the highest redshift ever. By comparing with SFGs selected from the same catalog, we examine the difference in AGN activity between these two different populations.

4.2 Sample Selection

4.2.1 Photometric redshift measurement

We use the latest photometric catalog from Cosmic Evolution Survey (COSMOS, Scoville et al., 2007), called COSMOS2020 (Weaver et al., 2021), covering a $\sim 2\,\mathrm{deg}^2$ field. This catalog consists of multi-band photometry from FUV band of GALEX to IRAC photometry of Spitzer Space telescope, which leads to the wavelength coverage of $0.1 - 10\mu$m. This is an updated version of the previous COSMOS multi-photometry catalog of Laigle et al. (2016) (COSMOS2015) and includes the latest imaging data of this field, such as U-band data of CLAUDS survey (Sawicki et al., 2019) by CFHT MegaCam, $grizy$-band data of HSC-SSP PDR2 (Aihara et al., 2019) by Subaru HSC, $YJHKs$-band data of UltraVISTA DR4 (McCracken et al., 2012) by VISTA VIRCAM, and Spitzer/IRAC channel 1,2,3, and 4 data of the Cosmic Dawn Survey (Moneti et al., 2021). In this study, we use photometry of the "classic catalog". In the classic catalog, the aperture photometry is used for all bands except for the IRAC bands. For the IRAC bands, where the source confusion makes the aperture photometry difficult, we use the photometry measured by the IRACLEAN software (Hsieh et al., 2012). We construct the magnitude-limited sample with $Ks < 25$ mag from the catalog. In addition, sources in the vicinity of bright stars are removed from the sample based on the bright star mask of HSC-SSP PDR2 (Coupon et al., 2018), which results in the final area of $\sim 1.4\,\mathrm{deg}^2$. Same as in Chapter 3, we utilize photometric redshifts estimated from the `MIZUKI` code (Tanaka, 2015). The configuration is also same in Chapter 3. We exclude sources with unreliable photo-z by applying a reduced chi-square cut of $\chi^2_\nu < 50$ and a photo-z $(z_{\mathrm{upper},95} - z_{\mathrm{lower},95})/(1+z) < 0.7$, where the term in the brackets is the 95% confidence range. Finally, we have 322,743 objects at $0 < z < 5$ in total.

In Figure 4.1, our photometric redshifts are compared with spectroscopic redshifts available in the COSMOS field (Ilbert et al. in prep.). To infer the photometric redshift accuracy, we estimate the outlier rate η, which is defined as the fraction of objects with $|z_{\mathrm{phot}} - z_{\mathrm{spec}}|/(1+z_{\mathrm{spec}}) > 0.15$, the precision measured with the normalized median absolute deviation $\sigma_{\mathrm{NMAD}} = 1.48 \times \mathrm{median}\left(|(z_{\mathrm{phot}} - z_{\mathrm{spec}}) - \mathrm{median}(z_{\mathrm{phot}} - z_{\mathrm{spec}})|/(1+z_{\mathrm{spec}})\right)$, and the bias $b = \mathrm{median}(z_{\mathrm{phot}} - z_{\mathrm{spec}})$, where z_{phot}, z_{spec} are the photometric redshift and spectroscopic redshift, respectively. This comparison shows that our photometric

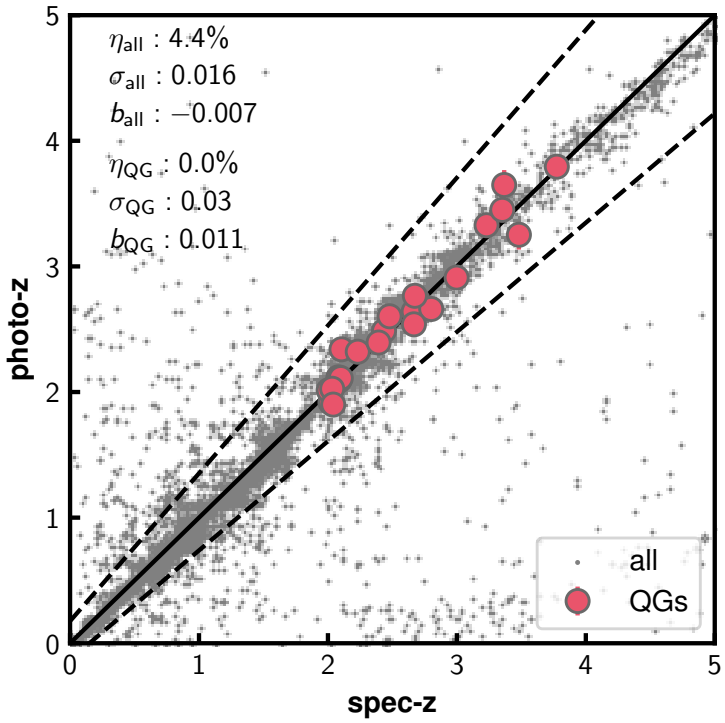

Figure 4.1: Comparison of the photometric redshift with the spectroscopic redshift of all spectroscopic confirmed objects (gray) and spectroscopic confirmed QGs at $z > 2$ (red, Belli et al., 2017; Schreiber et al., 2018; Saracco et al., 2020; Stockmann et al., 2020; Valentino et al., 2020; D'Eugenio et al., 2021). The outlier rate η, precision measured with the normalized median absolute deviation σ, and bias b are shown.

redshift have $\eta = 4.35\%$, $\sigma_{\rm NMAD} = 0.016$ and $b = 0.007$. In addition, MIZUKI also predicts the redshift of high redshift QGs with the good accuracy. The spectroscopically confirmed QG sample is collected from the literature (Belli et al., 2017; Schreiber et al., 2018; Saracco et al., 2020; Stockmann et al., 2020; Valentino et al., 2020; D'Eugenio et al., 2021), which confirm galaxies at $z > 2$ with the quiescent features in the NIR spectrum (e.g., Balmer absorption lines, Balmer break). The outlier rate, precision, and bias of the redshift for the spec-z QG sample are estimated as $\eta = 0.0\%$, $\sigma_{\rm NMAD} = 0.029$ and $b = -0.01$, respectively.

4.2.2 Quiescent galaxy selection

Here, we select QGs based on the latter method following our previous works (Kubo et al., 2018; Tanaka et al., 2019; Ito et al., 2021). We select galaxies with $\log(\mathrm{sSFR}_{1\sigma,\mathrm{upper}}/\mathrm{yr}^{-1}) < -11,\ -10.5,\ -10.0,\ -9.5$ as QGs at $0 < z < 0.5$, $0.5 < z < 1.0$, $1.0 < z < 2.0$, $2 < z < 5$, respectively. Here, $\mathrm{sSFR}_{1\sigma,\mathrm{upper}}$ is the upper limit of sSFR, which is defined as the ratio of the 1σ upper limit of SFR to the 1σ lower limit of stellar mass, derived from the SED fitting. This threshold roughly corresponds to ~ 1 dex below the star formation main sequence in each redshift bin. We note that Tanaka (2015) shows that MIZUKI provides the stellar mass consistent with ones from other photo-z code (FAST, Kriek et al., 2009) and SFR consistent with those from the rest-frame UV and IR luminosity. We classify the other galaxies as SFGs.

It is possible that dusty star-forming galaxies contaminate the QG sample. D'Eugenio et al. (2021) try to remove them using the Spitzer/MIPS 24μm from their QG sample at $z \sim 3$. We have confirmed that our main results do not change, even if we remove objects with $S/N > 4$ detection in MIPS 24μm (Le Floc'h et al., 2009) (Appendix B.1). On the other hand, we note that 24μm is sensitive not only to star formation but also to AGNs at that redshift. Therefore, we chose not to remove objects detected at 24μm.

4.2.3 Stacking subsamples

We define subsamples of QGs and SFGs based on their stellar mass and redshift. We divide galaxies into three stellar mass bins at $\log(M_\star/M_\odot) \geq 10.0$ and seven redshift bins at $0 < z < 5$, as shown in Figure 4.2. In order to increase the signal-to-noise ratio in the stacking, the bin size is larger at the most massive bin and the highest redshift bin. Our main sequence is slightly lower than that of Leslie et al. (2020). On the other hand, the main sequence of Leslie et al. (2020) is also higher than those of the literature (e.g., Speagle et al., 2014; Schreiber et al., 2015; Tomczak et al., 2016; Iyer et al., 2018). These difference might be the sample selection or the SFR estimation method, since we derive the SFR through the SED fitting, whereas Leslie et al. (2020) derive it from the stacked radio luminosity. We summarize the number of sources in each subsample in Figure 4.3.

The stellar mass completeness due to the magnitude limit cut can be calculated from the method in Pozzetti et al. (2010); Laigle et al. (2016); Davidzon et al. (2017). The

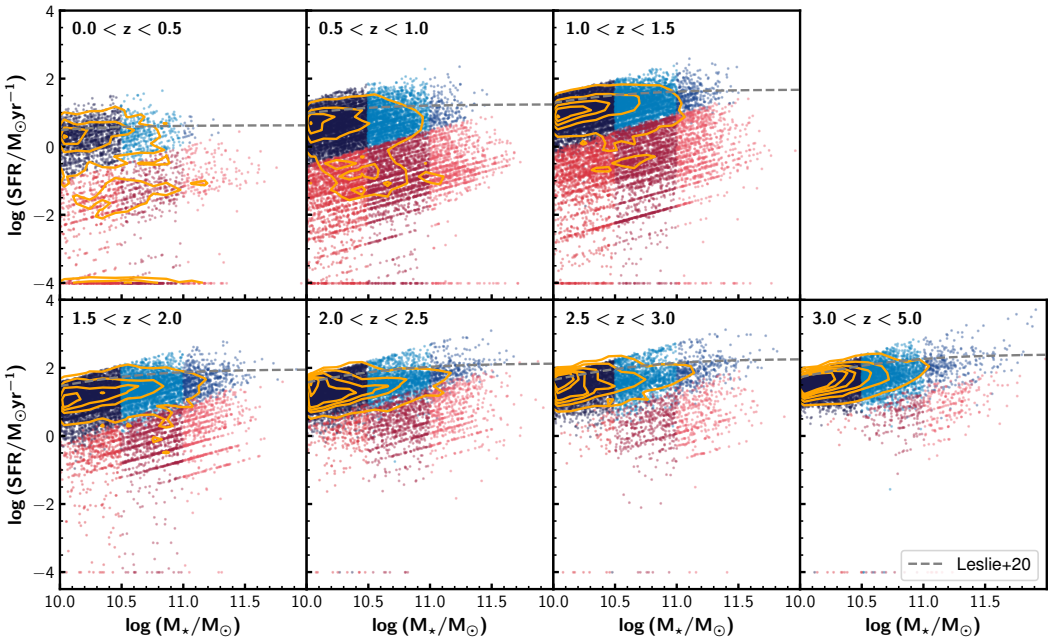

Figure 4.2: Relation of stellar mass and star formation rate of our sample. The red-colored objects are classified as quiescent galaxies and the others as star-forming galaxies. Different colors in each panel show different stellar mass bins. Objects with SFRs lower than 10^{-4} $M_\odot$ yr^{-1} are arbitrarily located at SFR of 10^{-4} $M_\odot$ yr^{-1} only for illustrative purpose. Orange contours show the distribution of all galaxies at that redshift. The slight stripe of data points is due to the model grid of the SED fitting. The gray dashed line shows the best-fit main sequence of star-forming galaxies from Leslie et al. (2020).

magnitude cut of $Ks < 25$ mag corresponds to the 90% completeness limit of QGs at $\log(M_\star/M_\odot) = 10.2,\ 10.4$ at $2.5 < z < 3.0$ and $3.0 < z < 5.0$, respectively. The least massive bins of these redshift bins are thus complete less than 90%, but the derived flux does not change even if we remove the magnitude cut. We note that other bins are more than 90% complete for both QGs and SFGs.

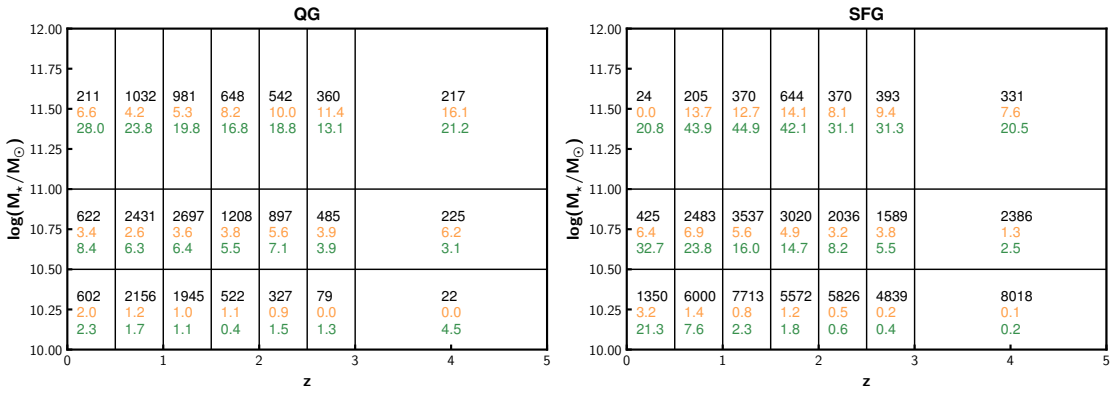

Figure 4.3: Total number of galaxies (black) in each redshift and stellar mass bin for QGs (left) and SFGs (right). Orange and green numbers show the fraction of sources detected in the X-ray and radio in the percent notation, respectively.

4.3 X-ray Stacking Analysis

4.3.1 Stacking procedure

In this work, we use the Chandra COSMOS-Legacy survey data (Civano et al., 2016) for the X-ray stacking. This survey is 4.6 Ms Chandra GO Program covering 2.2 deg^2 of the COSMOS field. The limiting depths are 2.2×10^{-16}, 1.5×10^{-15} erg cm^{-2} s^{-1} in the 0.5-2 keV, and 2-10 keV bands, respectively. For more detail, refer to Civano et al. (2016).

In the stacking of X-ray images, we utilize the Chandra stacking tool (CSTACK v.4.32[1], Miyaji et al., 2008). CSTACK creates the stacked images at $0.5 - 2$ keV (soft band) and $2 - 8$ keV (hard band), separately. It first checks whether each object is located within 8.0′ from the optical axis and not affected by resolved sources. Next, it generates a 30” $\times$ 30” cutout image of each object in the sample and sums up counts within the radius corresponding to 90% of encircled counts fraction of the point spread function at each off-axis angle. In addition to the source count, it also estimates the background count from the outer region of images $>$ 7” apart from the objects. From the estimated source and background counts, it derives a source count rate of each object. Finally, it derives the exposure time-weighted mean count rate of the stacked sample. This procedure is conducted for both soft and hard bands. Hereafter, we use

[1] http://lambic.astrosen.unam.mx/cstack/

these values as the typical count rates of each subsample. We note that the physical scale is slightly different depending on the redshift. However, the source radius is larger than the typical size of galaxies. In addition, the hot gas emission of galaxy groups or clusters is negligible due to the rarity of massive halo.

The uncertainty of the mean count rate is derived via bootstrapping. CSTACK reselects the sample from the original sample allowing duplication and reestimate the sample's mean count rate. This procedure is conducted 500 times, and the standard deviation of the mean count rate distribution is employed as 1σ uncertainty of the count rate.

In this chapter, we are focusing on the properties of typical QGs. Due to their high luminosity, the X-ray detected sources might affect the overall trend even though they are a small fraction in the entire sample. Therefore, all individually X-ray detected sources are removed from the sample. The galaxy catalog is cross-matched with the Chandra COSMOS-Legacy Survey source catalog, allowing the separation of 2.0". The fraction of the X-ray detected sources in each bin is summarized in Figure 4.3. It varies from 0% to 16% dependent on the redshift and galaxy populations. In particular, galaxies with higher stellar mass tend to have a more significant fraction of X-ray detected sources for both QGs and SFGs at any redshift. All removed sources are point sources. Overall, we remove 668 and 1,261 X-ray-detected sources from our QG and SFG samples, respectively.

The stacked image is summarized in Figure 4.4. We can see the signal of the soft band for both QGs and SFGs in any redshift, at least for the $\log(M_\star/M_\odot) > 10.5$ bins. The signal-to-noise ratio is weaker in the hard band, but you can see the clear detection in some bins for both QGs and SFGs even at $z \sim 3-5$. The derived count rate for each sample is summarized in Table 4.1.

4.3.2 Hardness ratio and spectral evolution

The hardness ratio (hereafter, referred to as HR), defined as $\mathrm{HR} = (H-S)/(H+S)$, is an indicator of the X-ray spectral shape, i.e., a combination of the photon index Γ and the hydrogen column density (N_H). Here, S, and H is the count rate of the soft and hard band, respectively. To discuss the spectral shape of our sample, we estimate the HR from the observed stacked count rates.

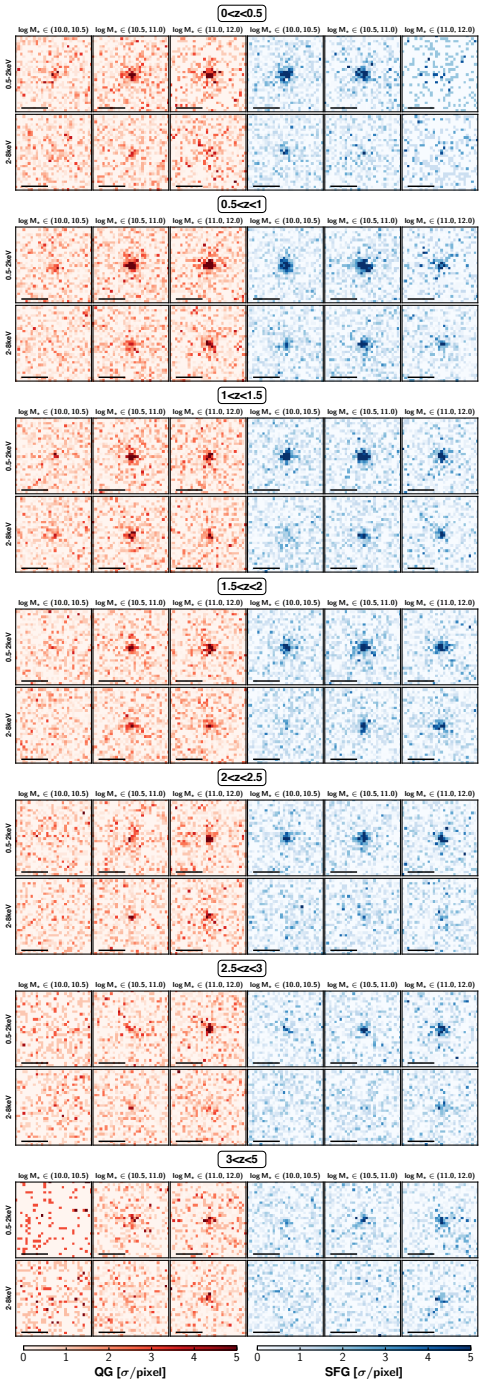

Figure 4.4: 0.5-2 keV and 2-8 keV stacked images for QGs (red) and SFGs (blue) in each stellar mass and redshift bin. All images are 15” × 15” and shown with the same relative flux scale. The horizontal line corresponds to the scale of 5”.

Figure 4.5 shows the HR as a function of the redshift of our stacked sample. Although their uncertainty is large, mainly due to the low sensitivity in the hard band, we can see a tentative trend that the HR increases with increasing redshift for both QGs and SFGs, whereas there is no significant dependency of the stellar mass. This trend is consistent with results in the literature (e.g., Fornasini et al., 2018; Carraro et al., 2020).

In order to derive the absorption corrected X-ray luminosity, estimating the best column density value is essential. Here, we compare the observed HR value to the model power-law spectrum absorbed by different neutral column densities derived by PIMMS[2] tool (Mukai, 1993) and the auxiliary response file of Cycle 14. In the model spectra, the photon index is fixed to be $\Gamma = 1.8$, which is typical value of the AGN X-ray photon index (e.g., Ricci et al., 2017; Marchesi et al., 2016b). Its column density varies over $\log(N_H/\mathrm{cm}^{-2}) = 21 - 24$ with 0.1dex interval. The galactic absorption is also considered by assuming the column density as $N_H = 2.6 \times 10^{20}$ cm^{-2} (Kalberla et al., 2005). In Figure 4.5, we overplot the expected hardness ratio in the case of the column densities of $\log(N_H/\mathrm{cm}^{-2}) = 21,\ 22,\ 23,$ and 24. We conduct the least-squares fitting to derive the best column density for QGs and SFGs in three redshift cases ($0 < z < 1$, $1 < z < 2$, and $2 < z < 5$) by using all stellar mass and redshift bins with the significant detection of either bands.

The estimated column densities are $\log(N_H/\mathrm{cm}^{-2}) = 22.3\ (22.3),\ 23.1\ (23.0)$, and $23.5\ (23.3)$ for $0 < z < 1$, $1 < z < 2$, and $2 < z < 5$ of QGs (SFGs), respectively. The column density of QGs is higher than those of SFGs. Such dependency of the column density on the quiescence (i.e., sSFR) is similar to that reported in Fornasini et al. (2018). They stack X-ray images of SFGs at $0.1 < z < 5$ selected from UVJ diagram in COSMOS and report that the best column density is $\log(N_H/\mathrm{cm}^{-2}) = 22.2$ for galaxies with $\log(\mathrm{sSFR}/\mathrm{yr}^{-1}) > -8.5$ and $\log(N_H/\mathrm{cm}^{-2}) = 22.0\ (23.0)$ for galaxies with $\log(\mathrm{sSFR}/\mathrm{yr}^{-1}) \leq -8.5$ at $z < 1.3$ ($z > 1.3$) with the photon index of $\Gamma = 1.4$. Hereafter, we employ our column densities to estimate the absorption corrected X-ray luminosities.

[2] https://cxc.harvard.edu/toolkit/pimms.jsp

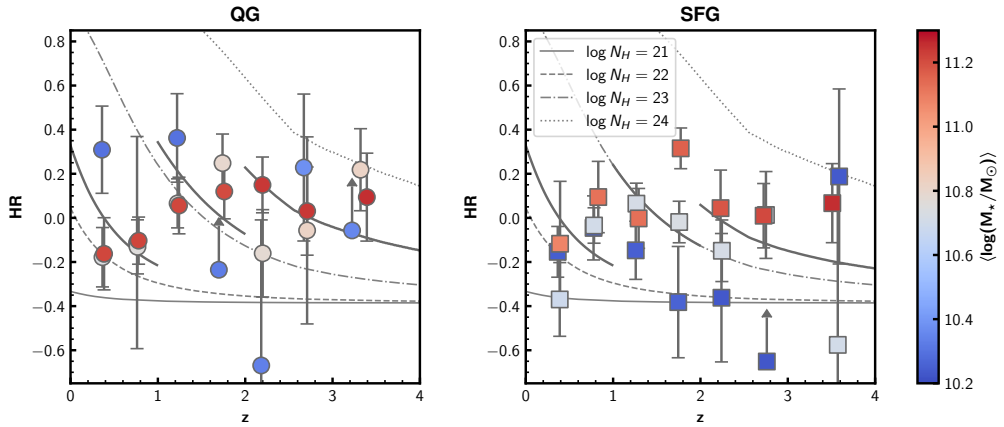

Figure 4.5: Hardness ratio of the stacked sample as a function of redshift. The left and right panels represent the hardness ratios of QGs and those of SFGs, respectively. The color of symbols indicates the average stellar mass of each sample. Bins of soft band flux with $S/N < 2$ are shown in the 2σ lower limit (arrows). The black lines show the expected HR value in the cases of the best-fit column densities. The gray solid, dashed, chain, and dotted lines show the hardness ratios of the power-law spectra with $\Gamma = 1.8$ with the column densities of $\log N_H/\mathrm{cm}^{-2} = 21,\ 22,\ 23$, and 24, respectively.

4.3.3 Luminosity estimation

The source count rate is converted to the absorption-corrected flux via the conversion factor, which is estimated by the PIMMS tool with the auxiliary response file of Cycle 14. Here, we assume the model spectrum of the power law with the slope with $\Gamma = 1.8$ and correct for the galactic absorption and intrinsic absorption. The best column density value estimated in Section 4.3.2 is used in correcting the intrinsic absorption.

The absorption-corrected X-ray luminosity in the rest frame 2-10 keV is derived from the following equation.

$$L_{2-10\mathrm{keV}} = \frac{4\pi d_L^2 (10^{2-\Gamma} - 2^{2-\Gamma})}{(1+\bar{z})^{2-\Gamma}(E_2^{2-\Gamma} - E_1^{2-\Gamma})} F_X, \tag{4.1}$$

where F_X is the absorption-corrected flux in the observed $E_1 - E_2$ keV band and the d_L is the luminosity distance at the average redshift ($\bar{z}$) of the sample. Here, we use the soft band flux as F_X (i.e., $E_1 = 0.5$ keV, $E_2 = 2$ keV) since the Chandra effective area is larger in this band. Same as before, $\Gamma = 1.8$ is assumed.

Figure 4.6 shows the luminosity as a function of stellar mass and redshift. From this figure, we make four points. Firstly, we successfully detect the signals of both QGs and SFGs and constrain their X-ray luminosity in all redshift bins. The most distant X-ray detection of individually it non-detected QGs has been at $z \sim 2$ (Olsen et al., 2013). Thus, this study extends the X-ray detection of typical QGs up to $z \sim 5$ for the first time. There are a few least massive bins ($10.0 < \log(M_\star/M_\odot) < 10.5$) at $z > 1.5$ that do not yield a significant signal for both QGs and SFGs. These low mass QGs may be suffered from small number statistics as expected from the galaxy stellar mass functions (e.g., Muzzin et al., 2013; Ilbert et al., 2013; Davidzon et al., 2017). On the other hand, SFGs have a large sample number in that bin ($\sim$ 5000 objects), so this is likely to reflect the intrinsically small X-ray luminosity of SFGs.

Secondly, the luminosity increases with increasing stellar mass at the fixed redshift in both populations. Carraro et al. (2020) reports a similar trend for both QGs and SFGs with the average X-ray AGN luminosity of the sample including individually detected objects at $z < 3.5$.

Thirdly, we do not see any significant luminosity difference between QGs and SFGs at fixed redshift and stellar mass for most bins. However, the same luminosity between QGs and SFGs does not necessarily mean that the X-ray is due to the same mechanism since X-ray binaries (XRBs) contribute to the X-ray luminosity at different levels for different SFR and stellar masses. We discuss this point in Section 4.3.4.

Lastly, the luminosity generally increases towards higher redshift for both QGs and SFGs. This trend can be the redshift evolution, but it can also be due to the selection bias because we focus on undetected objects in the source catalog, as mentioned in Section 4.3.1. The limiting luminosity increases with increasing redshift, and thus the stacked sample covers a wider luminosity range for higher redshift bins. This can make the average luminosity possibly higher for higher redshift bins. For this reason, we hereafter do not discuss the redshift evolution of the value itself but only focus on the trend difference between QGs and SFGs at the same redshift.

4.3.4 Contribution of XRBs and AGNs to luminosity

The X-ray emission in a galaxy comes from two main sources: XRBs and AGNs. The X-ray luminosity of the low-mass XRBs is correlated to the stellar mass, and that of the

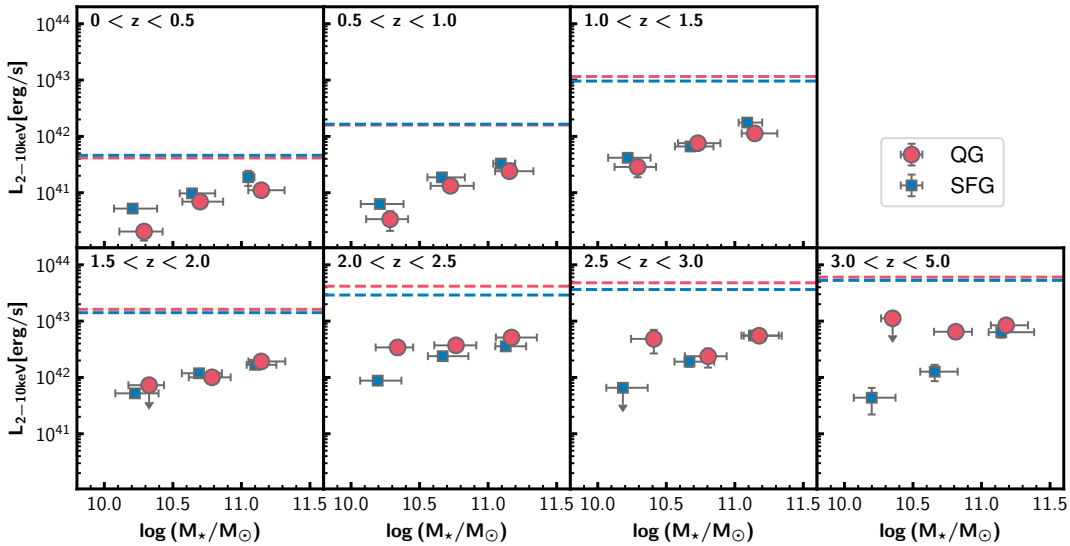

Figure 4.6: Stacked X-ray luminosity of QGs (red circles) and SFGs (blue squares) as a function of redshift and stellar mass. Data points represent the median of the stellar mass and the average-stacked rest-frame 2-10keV luminosity. Their error bars on the vertical axis represent the 1σ uncertainty and those on the horizontal axis represent the 16th and 84th percentiles of the stellar mass distribution of each bin. The error bars of some bins are smaller than the size of the symbol. If the soft band flux has a signal-to-noise ratio of smaller than two, the 2σ upper limit is plotted with the arrow. The limiting luminosity of the individual detection calculated from the limiting soft band flux and the best column density value for each redshift is shown in red and blue horizontal dashed lines in QGs and SFGs, respectively.

high-mass XRBs is correlated to the star formation activity (e.g., Lehmer et al., 2010, 2016; Aird et al., 2017). We estimate the contribution of XRBs to the observed X-ray luminosity to derive the AGN luminosity.

In this study, we use an empirical XRB scaling relation of galaxies at $z < 4$ in the Chandra Deep Field South found in Lehmer et al. (2016). This relation is estimated in a similar way as ours and covers most of the redshift range that we are interested in this chpater. There are other functional forms of the relation in the literature, and we show that there is only little effect of this assumption on our conclusions in Appendix B.2. The XRB luminosity, $L_{X,\mathrm{XRB}}$, is estimated from the average redshift, stellar mass, and SFR by the following relation:

$$L_{X,\mathrm{XRB}}\ [\mathrm{erg/s}] = 10^{29.37\pm0.15}(1+z)^{2.0\pm0.6}M_{\star}\ [\mathrm{M_{\odot}}]+10^{39.28\pm0.05}(1+z)^{1.3\pm0.1}\mathrm{SFR}\ [\mathrm{M_{\odot}yr^{-1}}]. \tag{4.2}$$

Figure 4.7 shows the ratio of the XRB luminosity and observed luminosity. The observed X-ray luminosity of SFGs is typically ≤ 3 times of the XRB luminosity at all redshift, which means that XRBs explain most of the observed X-ray luminosity of SFGs. On the other hand, the observed luminosity of QGs is higher than the expected XRB luminosity. Especially, it is higher by a factor of 5-50 at $z > 1$, indicating that the observed X-ray luminosity of QGs cannot be explained only by XRBs. This implies that AGNs are the dominant source of the X-ray emission for QGs.

The excess of the observed X-ray luminosity to the expected XRB luminosity is interpreted as the AGN luminosity. Figure 4.8 shows the AGN luminosity in each redshift bin. Interestingly, at $z > 1.5$, the AGN luminosity of QGs is higher than that of SFGs at any stellar mass bins. If we focus on bins at $z > 2$ having the positive AGN luminosity for both populations, QGs have ~ 2.9 times higher AGN luminosity than SFGs on average. Moreover, the difference between QGs and SFGs is the largest in the highest redshift bin, where QGs have $L_{X,\mathrm{AGN}} \sim (6-7)\times10^{42}$ erg/s, whereas the AGN luminosity of SFGs is lower than QGs, and it is consistent with zero at some subsample. It appears that QGs harbor more active AGNs than SFGs at these high redshifts, suggesting that AGNs may have played a role in quenching. On the other hand, at $z < 1.5$, such enhancement of the AGN luminosity of QGs is not seen.

Moreover, at the lowest redshift bin, SFGs have higher AGN luminosity than QGs.

This trend along the redshift is clearly seen in Figure 4.9, which shows the excess of the X-ray AGN luminosity of QGs over that of SFGs. All bins at $z > 1.5$ have positive values, whereas values of most of the bins at $z < 1.5$ are consistent with zero or even negative. The observed trend has a significant implication for the quenching process. Before we discuss it, we examine another useful probe of AGN activity; radio emission.

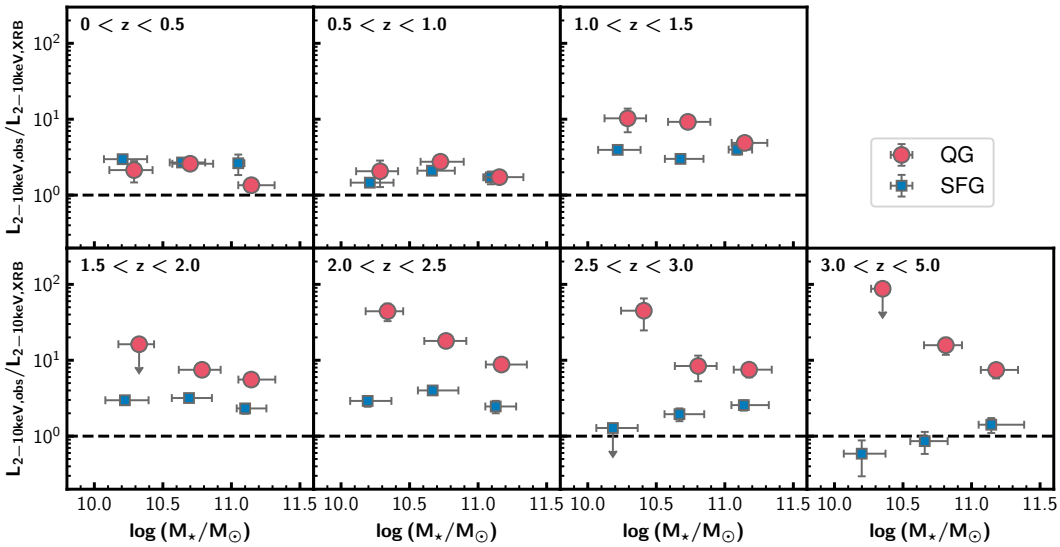

Figure 4.7: Ratio of the expected luminosity from XRBs and the observed luminosity as a function of redshift and stellar mass. The meanings of the symbols and the horizontal axis value of the data points are the same as in Figure 4.6. We show the 2σ upper limit when the signal to noise ratio is less than two in the soft band.

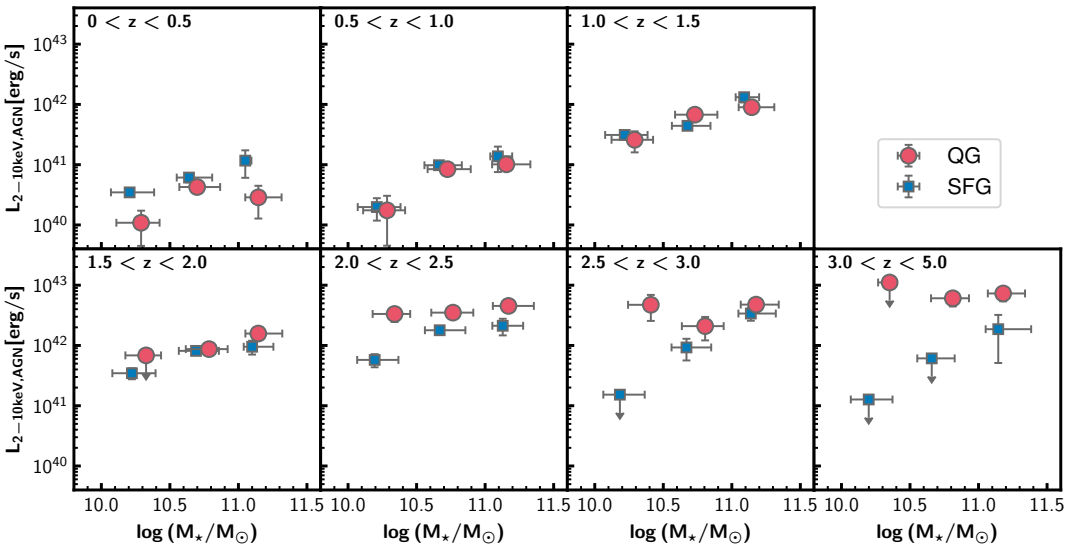

Figure 4.8: X-ray AGN luminosity as a function of redshift and stellar mass. The meanings of the symbols and the horizontal axis value of the data points are the same as in Figure 4.6. If the luminosity has a signal to noise ratio less than two or the AGN luminosity is negative, the 2σ upper limit of AGN luminosity is shown. If these upper limits are negative, it is replaced by 1.5×10^{40} erg/s only for illustrative purposes (shown in light color).

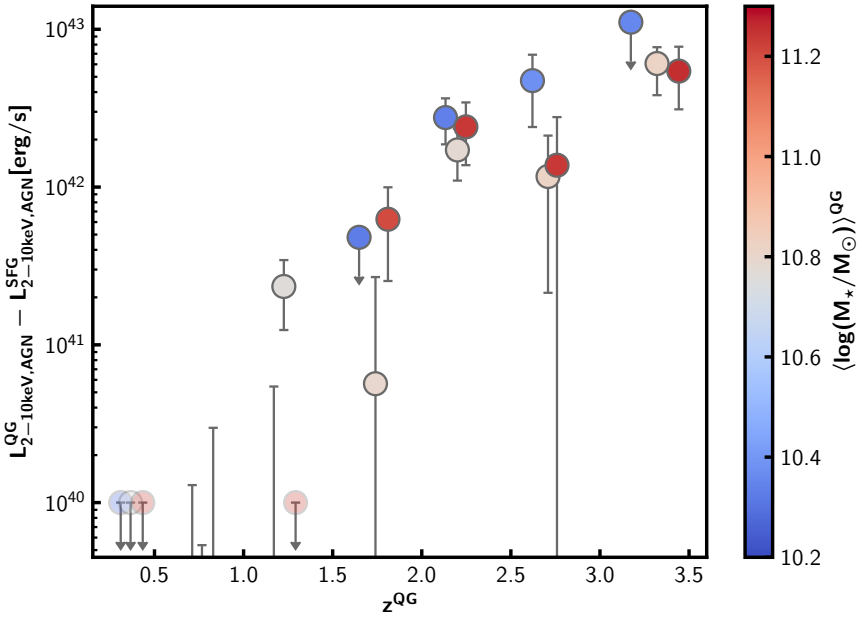

Figure 4.9: X-ray AGN luminosity excess of QGs over SFGs as a function of the redshift. The color of the marker shows the average stellar mass. If the AGN luminosity of QGs have only 2σ upper limit, 2σ upper limit of the excess is also shown in this figure. Also, if the 2σ upper limit of the X-ray AGN luminosity of SFGs is negative, we show the X-ray AGN luminosity of QGs, assuming SFGs do not have AGN luminosity. If the X-ray AGN luminosity difference is negative even considering the 1σ uncertainty, it is replaced by 1×10^{40} erg/s only for illustrative purposes (shown in light color).

Table 4.1: Stacked X-ray properties of QGs and SFGs

ID	z bin	$\log M_\star$ bin ($\log M_\odot$)	$\langle z \rangle^a$	$\langle \log M_\star \rangle^b$ ($\log M_\odot$)	$\langle \mathrm{SFR} \rangle^c$ ($M_\odot\ \mathrm{yr}^{-1}$)	soft CR ($\times 10^{-6}$ cts/s)	hard CR ($\times 10^{-6}$ cts/s)	HR^d	L_X^e ($\times 10^{41}$ erg/s)	$L_{X,\mathrm{AGN}}^e$ ($\times 10^{41}$ erg/s)
					QG					
0	(0.0,0.5)	(10.0,10.5)	0.36	10.295 ± 0.006	0.032 ± 0.002	1.81 ± 0.57	3.4 ± 1.1	0.31 ± 0.20	0.204 ± 0.064	0.109 ± 0.064
1	(0.0,0.5)	(10.5,11.0)	0.37	10.739 ± 0.006	0.088 ± 0.006	5.98 ± 0.64	4.2 ± 1.1	-0.18 ± 0.13	0.694 ± 0.074	0.426 ± 0.074
2	(0.0,0.5)	(11.0,12.0)	0.38	11.214 ± 0.014	0.224 ± 0.025	8.8 ± 1.2	6.3 ± 1.9	-0.16 ± 0.16	1.11 ± 0.16	0.29 ± 0.16
3	(0.5,1.0)	(10.0,10.5)	0.76	10.292 ± 0.003	0.128 ± 0.003	0.77 ± 0.29	0.62 ± 0.55	-0.11 ± 0.48	0.34 ± 0.13	0.17 ± 0.13
4	(0.5,1.0)	(10.5,11.0)	0.77	10.757 ± 0.003	0.340 ± 0.010	2.97 ± 0.29	2.28 ± 0.52	-0.13 ± 0.12	1.32 ± 0.13	0.84 ± 0.13
5	(0.5,1.0)	(11.0,12.0)	0.78	11.218 ± 0.006	0.650 ± 0.032	5.24 ± 0.49	4.26 ± 0.83	-0.10 ± 0.11	2.41 ± 0.22	1.01 ± 0.22
6	(1.0,1.5)	(10.0,10.5)	1.22	10.299 ± 0.003	0.359 ± 0.010	0.89 ± 0.31	1.90 ± 0.59	0.36 ± 0.20	2.87 ± 0.99	2.59 ± 0.99
7	(1.0,1.5)	(10.5,11.0)	1.23	10.761 ± 0.003	1.157 ± 0.031	2.34 ± 0.28	2.67 ± 0.51	0.07 ± 0.11	7.58 ± 0.89	6.76 ± 0.89
8	(1.0,1.5)	(11.0,12.0)	1.24	11.212 ± 0.007	2.688 ± 0.119	3.45 ± 0.47	3.86 ± 0.84	0.06 ± 0.13	11.3 ± 1.5	9.0 ± 1.5
9	(1.5,2.0)	(10.0,10.5)	1.70	10.327 ± 0.005	0.500 ± 0.022	0.51 ± 0.57	2.2 ± 1.1	> -0.24	< 7.3	< 6.8
10	(1.5,2.0)	(10.5,11.0)	1.74	10.794 ± 0.004	1.333 ± 0.044	2.21 ± 0.41	3.67 ± 0.78	0.25 ± 0.13	10.0 ± 1.9	8.7 ± 1.9
11	(1.5,2.0)	(11.0,12.0)	1.76	11.202 ± 0.007	3.090 ± 0.158	4.18 ± 0.60	5.3 ± 1.1	0.12 ± 0.12	19.2 ± 2.8	15.8 ± 2.8
12	(2.0,2.5)	(10.0,10.5)	2.18	10.335 ± 0.007	1.976 ± 0.095	2.93 ± 0.76	0.6 ± 1.4	-0.67 ± 0.66	34.1 ± 8.8	33.3 ± 8.8
13	(2.0,2.5)	(10.5,11.0)	2.20	10.783 ± 0.005	4.300 ± 0.154	3.18 ± 0.48	2.30 ± 0.87	-0.16 ± 0.20	37.1 ± 5.6	35.1 ± 5.6
14	(2.0,2.5)	(11.0,12.0)	2.20	11.236 ± 0.010	11.825 ± 0.617	4.38 ± 0.69	5.9 ± 1.2	0.15 ± 0.13	51.1 ± 8.0	45.3 ± 8.0
15	(2.5,3.0)	(10.0,10.5)	2.67	10.378 ± 0.012	1.875 ± 0.176	3.7 ± 1.6	5.8 ± 3.1	0.23 ± 0.33	48 ± 22	47 ± 22
16	(2.5,3.0)	(10.5,11.0)	2.71	10.815 ± 0.006	3.722 ± 0.198	1.77 ± 0.66	1.6 ± 1.2	-0.06 ± 0.42	23.8 ± 8.8	20.9 ± 8.8
17	(2.5,3.0)	(11.0,12.0)	2.71	11.236 ± 0.011	8.423 ± 0.660	4.09 ± 0.85	4.4 ± 1.5	0.03 ± 0.20	55 ± 11	48 ± 11
18	(3.0,5.0)	(10.0,10.5)	3.22	10.351 ± 0.018	1.507 ± 0.327	1.4 ± 2.8	11.8 ± 5.7	> -0.06	< 112	< 111
19	(3.0,5.0)	(10.5,11.0)	3.32	10.816 ± 0.009	5.800 ± 0.311	3.83 ± 0.97	6.0 ± 1.8	0.22 ± 0.19	65 ± 16	61 ± 16
20	(3.0,5.0)	(11.0,12.0)	3.39	11.253 ± 0.018	13.819 ± 1.350	4.9 ± 1.1	5.9 ± 2.0	0.09 ± 0.20	84 ± 19	73 ± 19

						SFG				
0	(0.0,0.5)	(10.0,10.5)	0.37	10.244 ± 0.004	2.89 ± 0.09	4.50 ± 0.41	3.30 ± 0.72	−0.15 ± 0.12	0.523 ± 0.047	0.35 ± 0.048
1	(0.0,0.5)	(10.5,11.0)	0.39	10.686 ± 0.007	3.70 ± 0.24	7.52 ± 0.78	3.5 ± 1.3	−0.37 ± 0.17	0.97 ± 0.10	0.61 ± 0.10
2	(0.0,0.5)	(11.0,12.0)	0.39	11.079 ± 0.018	3.52 ± 0.37	14.3 ± 4.3	11.3 ± 5.5	−0.12 ± 0.28	1.89 ± 0.56	1.17 ± 0.56
3	(0.5,1.0)	(10.0,10.5)	0.78	10.246 ± 0.002	6.46 ± 0.09	1.38 ± 0.18	1.26 ± 0.33	−0.05 ± 0.15	0.630 ± 0.080	0.198 ± 0.080
4	(0.5,1.0)	(10.5,11.0)	0.78	10.707 ± 0.003	10.56 ± 0.26	4.05 ± 0.30	3.78 ± 0.54	−0.03 ± 0.08	1.87 ± 0.14	0.98 ± 0.14
5	(0.5,1.0)	(11.0,12.0)	0.83	11.121 ± 0.008	16.56 ± 1.54	6.4 ± 1.2	7.7 ± 2.1	0.09 ± 0.16	3.30 ± 0.62	1.37 ± 0.62
6	(1.0,1.5)	(10.0,10.5)	1.26	10.251 ± 0.002	13.47 ± 0.13	1.56 ± 0.16	1.16 ± 0.29	−0.15 ± 0.13	4.17 ± 0.42	3.11 ± 0.42
7	(1.0,1.5)	(10.5,11.0)	1.27	10.718 ± 0.003	24.58 ± 0.38	2.46 ± 0.24	2.80 ± 0.44	0.06 ± 0.09	6.62 ± 0.65	4.41 ± 0.65
8	(1.0,1.5)	(11.0,12.0)	1.29	11.126 ± 0.007	41.58 ± 2.49	6.40 ± 0.87	6.4 ± 1.5	−0.00 ± 0.14	17.6 ± 2.4	13.2 ± 2.4
9	(1.5,2.0)	(10.0,10.5)	1.75	10.258 ± 0.002	17.78 ± 0.21	1.33 ± 0.18	0.60 ± 0.34	−0.38 ± 0.25	5.22 ± 0.71	3.46 ± 0.71
10	(1.5,2.0)	(10.5,11.0)	1.76	10.730 ± 0.003	33.61 ± 0.62	3.00 ± 0.26	2.89 ± 0.48	−0.02 ± 0.09	11.9 ± 1.0	8.1 ± 1.0
11	(1.5,2.0)	(11.0,12.0)	1.77	11.160 ± 0.007	53.85 ± 2.33	4.18 ± 0.61	8.0 ± 1.2	0.32 ± 0.09	16.7 ± 2.5	9.5 ± 2.5
12	(2.0,2.5)	(10.0,10.5)	2.24	10.234 ± 0.002	26.02 ± 0.28	1.08 ± 0.17	0.51 ± 0.33	−0.36 ± 0.29	8.8 ± 1.4	5.8 ± 1.4
13	(2.0,2.5)	(10.5,11.0)	2.24	10.719 ± 0.003	46.00 ± 1.04	2.93 ± 0.32	2.17 ± 0.57	−0.15 ± 0.14	23.8 ± 2.6	17.9 ± 2.6
14	(2.0,2.5)	(11.0,12.0)	2.23	11.183 ± 0.009	106.21 ± 6.20	4.42 ± 0.80	4.8 ± 1.4	0.04 ± 0.17	35.8 ± 6.5	21.2 ± 6.5
15	(2.5,3.0)	(10.0,10.5)	2.76	10.229 ± 0.002	37.83 ± 0.39	0.26 ± 0.19	0.50 ± 0.37	> -0.65	< 6.6	< 1.5
16	(2.5,3.0)	(10.5,11.0)	2.75	10.718 ± 0.004	66.34 ± 1.72	1.87 ± 0.36	1.92 ± 0.66	0.01 ± 0.20	19.1 ± 3.6	9.3 ± 3.6
17	(2.5,3.0)	(11.0,12.0)	2.72	11.208 ± 0.010	134.00 ± 8.46	5.51 ± 0.81	5.6 ± 1.4	0.01 ± 0.15	55.5 ± 8.1	34.0 ± 8.2
18	(3.0,5.0)	(10.0,10.5)	3.59	10.238 ± 0.002	41.98 ± 0.30	0.29 ± 0.14	0.43 ± 0.28	0.19 ± 0.40	4.4 ± 2.2	−3.1 ± 2.2
19	(3.0,5.0)	(10.5,11.0)	3.57	10.703 ± 0.003	77.70 ± 1.40	0.85 ± 0.28	0.23 ± 0.52	−0.58 ± 0.76	12.7 ± 4.1	−2.1 ± 4.1
20	(3.0,5.0)	(11.0,12.0)	3.51	11.256 ± 0.016	233.22 ± 28.10	4.40 ± 0.89	5.0 ± 1.5	0.07 ± 0.18	64 ± 13	19 ± 14

[a]Average redshift of the sample
[b]Average stellar mass of the sample
[c]Average SFR of the sample
[d]If the sample is detected with $S/N \leq 2$ in the soft band, we show the 2σ lower limit.
[e]If the sample is detected with $S/N \leq 2$ in the soft band, we show the 2σ upper limit of the estimated luminosity.

4.4 Radio Stacking Analysis

4.4.1 Stacking procedure, flux estimation

We use the imaging data at 3 GHz (Smolčić et al., 2017) and 1.4 GHz (Schinnerer et al., 2007) taken by Karl G. Jansky Very Large Array (VLA) to derive the average rest-frame 1.4 GHz luminosity of the sample. The 3 GHz data is taken from VLA-COSMOS 3 GHz Large Project, and the total observation time is 384 hours, which leads to a median 1σ flux uncertainty of 2.3 μJy beam^{-1}. It covers 2 deg^2 of the COSMOS field with the angular resolution of 0.75" $\times$ 0.75". The 1.4 GHz data is taken from VLA-COSMOS Large project, and the total observation time is 275 hours, which leads to a median 1σ flux uncertainty of 10.5(15) μJy beam^{-1} for 1(2)deg^2 of the COSMOS field. The angular resolution of 1.4 GHz data is 1.5" $\times$ 1.4".

The radio emission of all objects does not correlate with the X-ray emission, so some objects without X-ray detection can be detected in either 3 GHz or 1.4 GHz. Here, we aim to compare radio properties with X-ray properties. Therefore, we chose to use the same sample in the X-ray stacking, although a small fraction of the galaxies is individually detected in radio. The number of the radio-detected objects is obtained by cross-matching our galaxy sample with 1.4GHz (Schinnerer et al., 2007) and 3GHz (Smolčić et al., 2017) catalog, where the separation of 1"/0.8" is allowed, respectively. As seen in Figure 4.3, the fraction of the detected sources in the total sample ranges from 0% to 45% dependent on redshift, stellar mass, and QGs/SFGs. In particular, this fraction is higher for SFGs with higher stellar mass. This trend can be due to their high SFR. It is noted that the 1.4 GHz data does not cover a small part of the COSMOS field, and the objects there are removed. The fraction of removed objects is smaller than 1% of the whole parent sample (186 objects), which is negligible enough not to alter our conclusions.

A similar method to the X-ray stacking is applied to the 3 GHz and 1.4 GHz images. We first generate cutout images of all galaxies with a size of 15" $\times$ 15". The systematic offset of the position in the radio image is corrected by using the best-fit linear relation in Smolčić et al. (2017). We then derive the average of these images, which is referred to as the stacked image. In order to reduce the impact of nearby interlopers, 5σ-clipping is applied when averaging.

The stacked image radio flux is estimated by fitting a 2D Gaussian profile to the central 8" × 8" of the images. Free parameters are its center position, sigma, and its amplitude. We use the integration of the best-fit 2D Gaussian profile as the total flux. The uncertainty of the flux is estimated using bootstrapping. It first re-selects the same number of galaxies in the bin allowing for duplication. Averaging of the images is then applied, and the flux is estimated by fitting the 2D Gaussian with the same center as the best fit of original images. This trial is repeated 1000 times, and we take their standard deviation as the flux uncertainty. We show the stacked images of QGs and SFGs in Figure 4.10 and summarize the estimated fluxes in Table 4.2. The 1.4GHz band signal is seen in the figure for bins with $\log(M_\star/M_\odot) > 10.5$ of both QGs and SFGs at any redshift.

4.4.2 Luminosity estimation

The spectral shape is assumed to be $S_\nu \propto \nu^\alpha$. The spectral index α is determined from the flux ratio of the observed 1.4 GHz and 3 GHz as follows:

$$\alpha = \frac{\log\left(\frac{F_{3\mathrm{GHz}}}{F_{1.4\mathrm{GHz}}}\right)}{\log\left(\frac{3}{1.4}\right)}, \tag{4.3}$$

where $F_{3\mathrm{GHz}}$, $F_{1.4\mathrm{GHz}}$ is the observed flux at 3 GHz and 1.4 GHz. Because the estimated flux at 1.4 GHz in many bins of QGs has large uncertainty ($S/N < 2$), we assume that $\alpha = -0.75$ for all bins, which is an empirical value used for SFGs in the literature (e.g., Delvecchio et al., 2021). We note that the spectral slope does not significantly evolve with the redshift at least up to $z \sim 2$, at least for SFGs (Magnelli et al., 2015). In order not to cause any systematic difference, we use the same value for both SFGs and QGs.

In this study, we discuss the radio luminosity at rest-frame 1.4 GHz, which is determined as follows:

$$L_{1.4\mathrm{GHz}} = \frac{4\pi d_\mathrm{L}^2}{(1+z)^{\alpha+1}} \left(\frac{1.4}{3}\right)^\alpha F_{3\mathrm{GHz}}, \tag{4.4}$$

where d_L is the luminosity distance at that redshift and $F_{3\mathrm{GHz}}$ is the observed flux at 3 GHz. The average redshift of galaxies in each bin is used in deriving the luminosity.

Figure 4.11 shows the rest-frame 1.4 GHz luminosity of QGs and SFGs in each

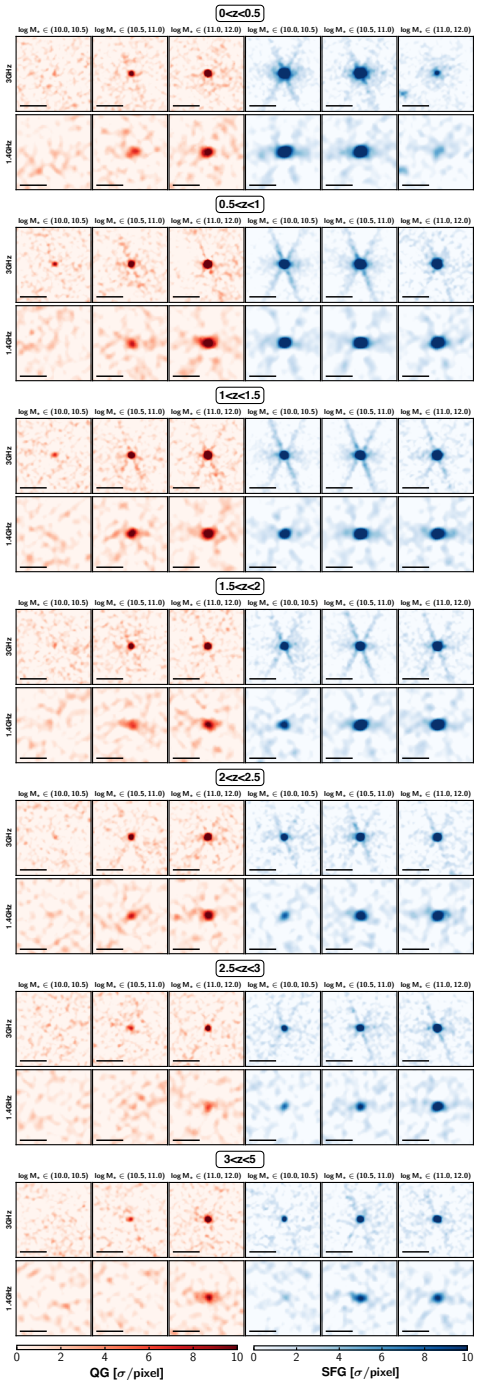

Figure 4.10: The 3 GHz and 1.4 GHz stacked image for QGs (red) and SFGs (blue) in each stellar mass and redshift bins. All images are 15" × 15" and shown with the same relative flux scale. The horizontal line corresponds to the scale of 5".

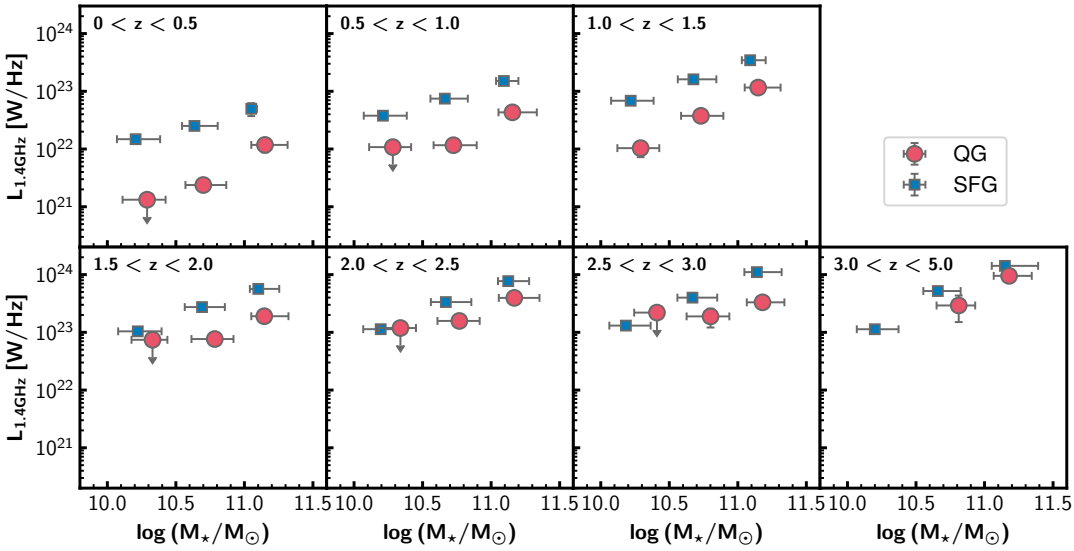

Figure 4.11: Stacked radio luminosity of QGs (red circles) and SFGs (blue squares) as a function of redshift and stellar mass. Data points represent the median of the stellar mass and the average-stacked rest-frame 1.4GHz luminosity. Their error bar on the vertical axis represent the 1σ uncertainty and those on the horizontal axis represent the 16th and 84th percentiles of the stellar mass distribution of each bin. The error bars of some bins are smaller than the size of the symbol. If the sample is detected at the 3 GHz with the signal to noise ratio less than two, we show the 2σ upper limit. The least massive subsample of QGs at the highest redshift is missing due to the poor statistics.

redshift bin. We successfully detect radio signals of QGs up to $z \sim 5$ at least for the most massive bin. We find that SFGs have a higher rest-frame 1.4 GHz luminosity than QGs at fixed stellar mass at all redshift, which is a different trend from X-ray analysis. In addition, the luminosity increases as the stellar mass increases for each galaxy population. As in the X-ray analysis, there are several origins of radio emission. In order to characterize the AGN activity, we need to account for the other origin, which is the subject of the following subsection.

4.4.3 Rest-frame 1.4 GHz AGN luminosity of QGs and SFGs

The radio continuum of galaxies has mainly two origins. One is related to star formation activity, which is the synchrotron emission from supernovae and their remnants or the free-free emission from warm HII regions. The other is from AGNs. To investigate

the contribution of AGN, we compare the observed luminosity and the expected contribution from star formation.

Similar to the X-ray analysis, we examine the contribution from star formation with the use of a known correlation between the total SFR and the rest-frame 1.4 GHz luminosity of SFGs. Here, we use an empirical relation suggested in Delvecchio et al. (2021), which is based on the stacking analysis of IR and radio images for $NUVrJ$ selected SFGs at $0 < z < 4.5$:

$$q_{SFR}(M_\star, z) = (2.743 \pm 0.034) \times (1+z)^{(-0.025\pm0.012)} - (0.234 \pm 0.017) \times (\log(M_\star/M_\odot) - 10), \quad (4.5)$$

where $q_{SFR}(M_\star, z) = \log(L_{SFR}[\mathrm{W}]/(3.75 \times 10^{12}\mathrm{Hz})) - \log(L_{1.4\mathrm{GHz}}\ [\mathrm{W\ Hz^{-1}}])$, and L_{SFR} is the luminosity equivalent to their SFR from the SED-fitting based on the correction factor in Kennicutt (1998).

There is a slight offset between the SED-fitting based star formation main sequence of this work and those of Delvecchio et al. (2021). We scale our SED-fitting based SFR to match that of Delvecchio et al. (2021) in estimating the expected luminosity from SFR from Equation 4.5. To deal with the redshift bin difference of our study and Delvecchio et al. (2021), we use the formulation of the redshift-dependent main sequence of Schreiber et al. (2015), which is argued to be in good agreement with that of Delvecchio et al. (2021). The ratio between our SFR and their expected SFR at fixed stellar mass and redshift is employed as the correction factor for SFR, which is in the range of $1.5 - 2.5$. We note that the results of the X-ray analysis do not significantly change whether or not these correction factors are applied.

In Figure 4.12, we compare the observed rest-frame 1.4 GHz luminosity and the luminosity from the star formation. QGs have 3-10 times higher luminosity than expected from SFR at any redshift and stellar mass bins, whereas the observed 1.4 GHz luminosity of SFGs is comparable to those expected from their SFR. This high value suggests that the luminosity of QGs is mainly due to AGNs. This is fully consistent with our findings in Section 4.3. Previous studies also report the enhancement of radio luminosity for color-selected QGs at $z < 2$ (e.g., Man et al., 2016; Gobat et al., 2018; Magdis et al., 2021), which lend further support to our results.

We next estimate the AGN luminosity at rest-frame 1.4 GHz. Similar to the discussion of X-ray stacking, the rest-frame 1.4 GHz AGN luminosity is defined to be the excess of the observed luminosity to the expected luminosity from star formation. Figure 4.13 shows the evolution of the AGN luminosity of QGs and SFGs. Similar to the result in X-ray stacking, the radio AGN luminosity of QGs is higher at $z > 1.5$ than those of SFGs and comparable at $z < 1.5$. Figure 4.14, which shows the excess of the radio AGN luminosity of QGs over that of SFGs, supports this observed trend. Once again, our findings here are entirely consistent with the X-ray analysis, demonstrating the robustness of our result. Now, we are in a position to discuss them in the context of galaxy quenching.

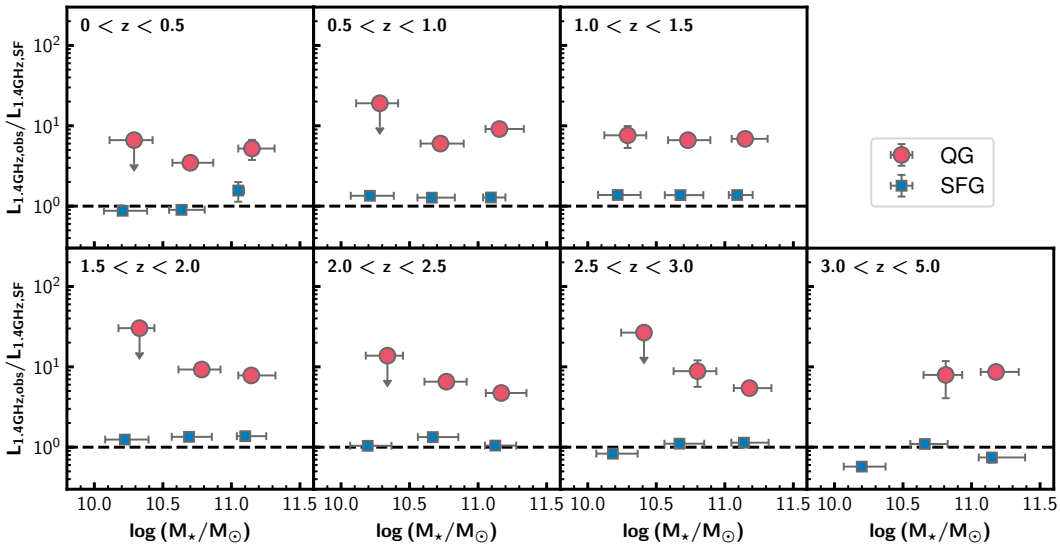

Figure 4.12: Ratio of observed radio luminosity and expected luminosity due to star formation for QGs and SFGs. The meanings of the symbols and the horizontal axis value of the data points are the same as in Figure 4.11. The least massive subsample of QGs at the highest redshift is missing due to the poor statistics.

Table 4.2: Stacked radio properties of QGs and SFGs

ID	3GHz Flux (μJy)	1.4GHz Flux (μJy)	$L^a_{1.4\mathrm{GHz}}$ ($\times 10^{22}$ W/Hz)	$L^a_{1.4\mathrm{GHz,\ AGN}}$ ($\times 10^{22}$ W/Hz)
		QG		
0	0.81 ± 0.51	11 ± 1564	< 0.13	< 0.11

1	3.17 ± 0.43	8.7 ± 2.1	0.24 ± 0.03	0.17 ± 0.03
2	13.7 ± 3.5	25.3 ± 6.5	1.18 ± 0.30	0.95 ± 0.30
3	1.01 ± 0.81	2.4 ± 2.9	< 1.1	< 1.0
4	2.79 ± 0.27	8.6 ± 2.6	1.16 ± 0.11	0.97 ± 0.11
5	9.9 ± 1.0	26.7 ± 2.7	4.32 ± 0.43	3.84 ± 0.44
6	0.84 ± 0.25	6 ± 934	1.04 ± 0.31	0.90 ± 0.31
7	3.00 ± 0.19	7.1 ± 1.5	3.76 ± 0.24	3.19 ± 0.24
8	8.94 ± 0.62	19.2 ± 2.1	11.60 ± 0.81	9.92 ± 0.81
9	0.85 ± 0.96	16.0 ± 6.2	< 7.4	< 7.2
10	2.71 ± 0.46	7.9 ± 1.7	7.7 ± 1.3	6.8 ± 1.3
11	6.57 ± 0.56	13.8 ± 2.4	19.0 ± 1.6	16.6 ± 1.6
12	1.17 ± 0.67	2.7 ± 1.8	< 12	< 11
13	3.26 ± 0.36	6.7 ± 2.4	15.8 ± 1.8	13.4 ± 1.8
14	8.19 ± 0.64	16.4 ± 2.4	39.5 ± 3.1	31.2 ± 3.1
15	0.6 ± 1.2	0 ± 817	< 22	< 21
16	2.45 ± 0.88	11.8 ± 6.6	18.9 ± 6.8	16.8 ± 6.8
17	4.30 ± 0.58	11.3 ± 4.2	33.1 ± 4.5	27.0 ± 4.5
18	2 ± 4726	15 ± 495	< 107349	< 107349
19	2.4 ± 1.2	2 ± 108	29 ± 14	26 ± 14
20	7.6 ± 1.2	26.4 ± 6.1	95 ± 15	84 ± 15
		SFG		
0	19.69 ± 0.77	36.6 ± 1.9	1.480 ± 0.055	−0.211 ± 0.076
1	29.0 ± 1.3	57.7 ± 3.9	2.51 ± 0.12	−0.28 ± 0.21
2	57 ± 14	92 ± 21	5.0 ± 1.3	1.8 ± 1.3
3	8.80 ± 0.18	13.01 ± 0.60	3.777 ± 0.078	0.970 ± 0.086
4	17.10 ± 0.34	30.1 ± 1.0	7.46 ± 0.14	1.61 ± 0.20
5	30.0 ± 1.9	68.0 ± 6.6	15.09 ± 0.97	3.3 ± 1.4
6	5.14 ± 0.14	7.51 ± 0.54	6.86 ± 0.19	1.88 ± 0.19
7	11.91 ± 0.22	20.93 ± 0.95	16.12 ± 0.29	4.37 ± 0.35
8	24.2 ± 1.0	52.4 ± 4.1	34.5 ± 1.4	9.4 ± 2.0
9	3.66 ± 0.17	4.24 ± 0.49	10.41 ± 0.49	2.04 ± 0.50
10	9.50 ± 0.22	17.28 ± 0.92	27.40 ± 0.62	7.03 ± 0.73
11	19.17 ± 0.71	39.1 ± 2.3	56.6 ± 2.1	15.3 ± 2.7
12	2.25 ± 0.16	2.81 ± 0.44	11.34 ± 0.81	0.44 ± 0.82
13	6.62 ± 0.25	12.5 ± 1.2	33.5 ± 1.2	8.4 ± 1.4
14	15.49 ± 0.74	35.8 ± 3.8	77.2 ± 3.7	3.5 ± 5.6
15	1.63 ± 0.17	1.90 ± 0.37	13.1 ± 1.4	−2.7 ± 1.4
16	5.01 ± 0.32	9.0 ± 1.7	39.9 ± 2.6	3.8 ± 2.8
17	14.15 ± 0.75	23.6 ± 2.6	110.5 ± 5.8	13.4 ± 8.3

18	0.791 ± 0.087	1.27 ± 0.59	11.3 ± 1.2	−8.4 ± 1.3
19	3.66 ± 0.27	6.94 ± 0.98	52.0 ± 3.9	4.6 ± 4.0
20	10.42 ± 0.76	18.9 ± 3.0	142 ± 10	−49 ± 25

[a]If the sample whose 3GHz flux is detected with $S/N < 2$, we show the upper limit of the estimated luminosity.

4.5 Discussion of Chapter 4

So far, we find QGs have X-ray and radio emissions which are dominantly from AGNs, and their luminosity is higher than SFGs with the same stellar mass at $z > 1.5$. Here, we will discuss implications for the galaxy quenching.

4.5.1 AGN activity and galaxy populations

We first compare the X-ray and radio AGN luminosity in Figure 4.15. The AGN luminosity estimated in two different wavelengths is correlated well with the same relation for both QGs and SFGs. We calculate Spearman's rank correlation coefficients ρ between the X-ray and radio AGN luminosity bins which have significant positive detection in both wavelengths. The Spearman's ρ value is estimated to as $\rho = 0.94$ with $P = 2 \times 10^{-7}$ and $\rho = 0.77$ with $P = 0.001$ for QGs and SFGs, respectively. These values support the strong correlation between the X-ray and radio luminosity. Given the redshift and the stellar mass, the relation of the X-ray and the radio luminosity for the star formation is derived from Equation 4.2 and Equation 4.5. Our result has lower radio luminosity than the star formation relation at the fixed X-ray luminosity, again reinforcing that the emission does not originate from star formation. Moreover, the slope of the relation is similar to that of "fundamental plane of the black hole activity" with $L_{\rm radio} \propto L_X^{0.6}$ in the local universe (Merloni et al., 2003). In particular, the observed relation has a similar amplitude to their local relation with the black hole mass of $\log(M_{\rm BH}/M_\odot) = 8 - 9$, after converting the rest-frame 5GHz luminosity to the rest-frame 1.4 GHz luminosity with $\alpha = -0.75$. This suggests that this emission is likely from AGN, and we show for the first time that the low luminosity AGNs of QGs are located along with the local relation even up to $z \sim 5$.

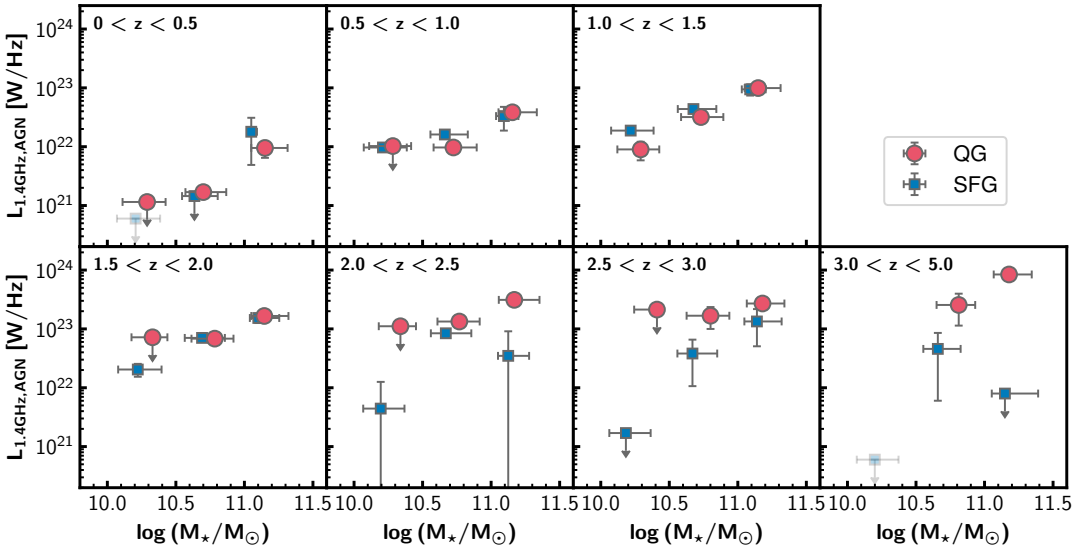

Figure 4.13: Radio AGN luminosity for QGs and SFGs as a function of redshift and stellar mass. The meanings of the symbols and the horizontal axis value of the data points are the same as in Figure 4.11. The least massive subsample of QGs at the highest redshift is missing due to the poor statistics. If the luminosity has a signal to noise ratio less than two or the radio AGN luminosity is negative, the 2σ upper limit of the AGN luminosity is shown. If the upper limit is negative, it is replaced by 6×10^{20} W/Hz only for illustrative purposes (shown in light color).

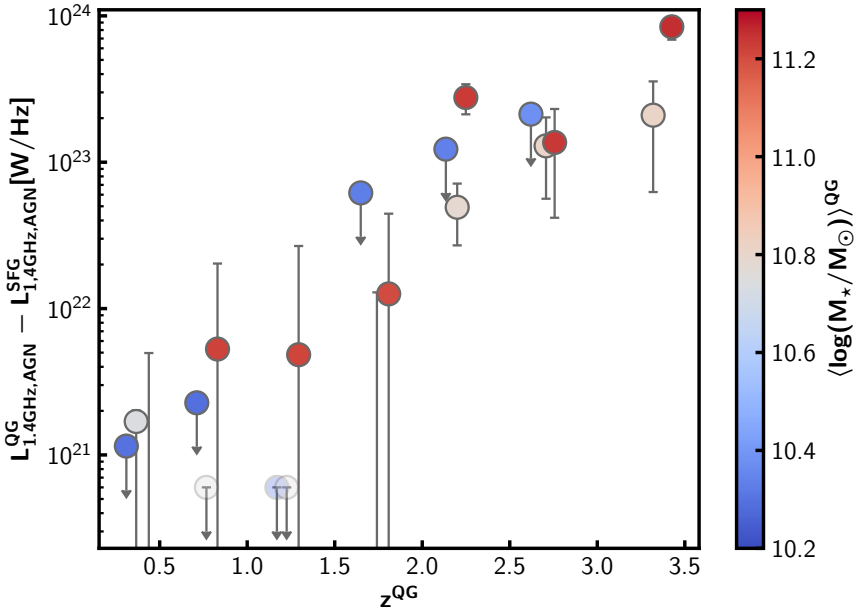

Figure 4.14: Radio AGN luminosity excess of QGs over SFGs as a function of the redshift. The color of the marker shows the average stellar mass. The least massive bin of QGs at the highest redshift is missing due to the poor statistics. If the radio AGN luminosity of QGs have only 2σ upper limit, 2σ upper limit is also shown in this figure. Also, if the 2σ upper limit of the radio AGN luminosity of SFGs is negative, we here show the radio AGN luminosity of QGs, assuming SFGs do not have AGN luminosity. If the radio AGN luminosity difference is negative even considering the 1σ uncertainty, it is replaced by 7×10^{20} W/Hz only for illustrative purposes (shown in light color).

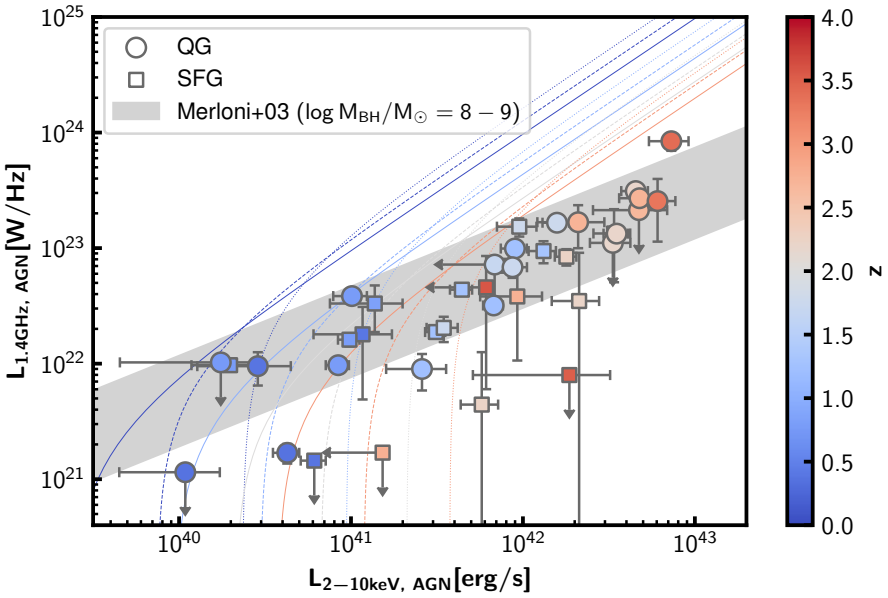

Figure 4.15: Comparison between the X-ray and radio AGN luminosity of QGs (circles) and SFGs (squares). The color of each marker shows the average redshift of each bin. Same as in Figure 4.8 and Figure 4.13, if the observed luminosity has a signal to noise ratio of less than two or the AGN luminosity is negative, the 2σ upper limit is shown. Negative upper limits in either X-ray or radio are not shown, assuming that they do not contain AGNs. Following the Figure 4.13, the least massive bin at $3.0 < z < 5.0$ is not shown due to the poor statistics in the radio stacking. An expected relation of the X-ray and radio luminosity for star formation can be derived from Equation 4.2 and 4.5 for bins with $\log(M_\star/M_\odot) = 10.0,\ 10.5,$ and 11.0 in solid, dashed, and dotted lines, at $z = 0,\ 1,\ 2,$ and 3, following the same color map as symbols. The local relation with black hole mass of $\log(M_{BH}/M_\odot) = 8-9$ from Merloni et al. (2003) after correcting to the unit in this study is shown in gray hatched region.

In addition, the X-ray AGN luminosity can be converted to the black hole accretion rate (BHAR) via a bolometric correction and an assumption of the accretion efficiency. The average bolometric luminosity is derived from the average X-ray AGN luminosity by using the conversion factor $k_{\rm bol}$ ($k_{\rm bol} \equiv L_{\rm bol}/L_X$) used in Yang et al. (2018), which is a modified version of Lusso et al. (2012) for subsample with $\log L_X[{\rm erg/s}] > 42.4$. For subsample with $\log L_X[{\rm erg/s}] < 42.4$, $k_{\rm bol} = 16$ is used as in She et al. (2017). The average BHAR, $\langle {\rm BHAR} \rangle$, is then derived from the average bolometric luminosity as follows:

$$\langle {\rm BHAR} \rangle (M_\star, z) = \frac{(1-\epsilon) \times \langle L_{\rm bol} \rangle (M_\star, z)}{\epsilon c^2}, \tag{4.6}$$

where, c is the speed of the light and ϵ is the efficiency of the mass conversion. Following previous studies (e.g., Carraro et al., 2020; D'Eugenio et al., 2021), we assume $\epsilon = 0.1$.

The left panel of Figure 4.16 shows the average BHAR evolution of QGs and SFGs. We estimate BHARs of QGs at $z > 3$ for the first time. As suggested from the X-ray AGN luminosity, BHARs of QGs are higher than those of SFGs at least at $z > 1.5$. The BHAR from Carraro et al. (2020) is also overplotted and is larger than ours. This is likely because Carraro et al. (2020) included individually detected X-ray sources. Interestingly, the higher BHAR for QGs is not seen in their study, which is different from our observed trend. This may indicate that such enhanced AGN activity of QGs only occurs at relatively low flux levels, and the inclusion of individually detected sources may hide this trend. It can also be due to the different classification methods of QGs ($NUVrJ$ diagram) from this study.

The right panel of Figure 4.16 shows the ratio of BHAR and SFR of this study and those from the literature. We find that QGs have larger ratios than SFGs. This is because the BHAR of QGs is higher than those of SFGs and the SFR of QGs is lower than those of SFGs. This trend implies that QGs do not only have higher AGN activity than SFGs but also have a higher rate of gas accretion towards the nuclei compared to the gas consumption by star formation than SFGs. In addition, the $\langle {\rm BHAR} \rangle / \langle {\rm SFR} \rangle$ ratio of QGs is almost constant ($\langle {\rm BHAR} \rangle / \langle {\rm SFR} \rangle \sim 10^{-3}$) regardless of redshift. This might suggest that the growth rate of stellar and black hole mass ratio does not have significant redshift evolution. We note that our work only focuses on

non-detected objects, and thus this ratio is lower than other studies at similar redshift (e.g., D'Eugenio et al., 2021).

The AGN component in the observed optical/NIR can be estimated from the bolometric luminosity. By using the optical bolometric correction factor $K_O \equiv L_{bol}/L_O$ of Duras et al. (2020), here L_O is the rest-frame B-band luminosity value, the rest-frame optical luminosity of AGNs is derived. The value is significantly lower than the luminosity of the corresponding observed optical/NIR. For example, the observed average rest-frame B-band luminosity of QGs in the highest redshift bin, derived from the average K band luminosity and the k-correction with the typical SED model of QGs (e.g., Valentino et al., 2020), is about ~ 30 times higher than the expected rest-frame optical AGN luminosity. This suggests that the AGN component is much smaller than the stellar component in the optical/NIR, and our SED-fitting assuming only stellar components is well justified.

4.5.2 Implication to galaxy quenching

We have systematically investigated the AGN activity of typical QGs based on the X-ray and radio stacking analyses. As shown in Sections 4.3 and 4.4, their X-ray and radio luminosities cannot be explained only by XRBs or SFR, and QGs are found to generally host AGNs with X-ray luminosity of $L_{2-10keV,AGN} \sim 10^{41-43}$ erg/s at any redshift up to $z \sim 5$. The connection between QGs and AGNs has been discussed in the literature by only focusing on X-ray undetected objects at $z \sim 2$ (Olsen et al., 2013), including the individually detected objects in X-ray at $z < 3.5$ (e.g., Carraro et al., 2020; D'Eugenio et al., 2021) and in radio at $z < 2$ (e.g., Magdis et al., 2021; Gobat et al., 2018; Man et al., 2016). This study only focuses on the X-ray undetected objects to unveil the average AGN activity and perform both X-ray and radio analysis consistently out to a previously unreached redshift of $z \sim 5$.

One of our primary findings is that QGs have higher AGN luminosity than SFGs at $z > 1.5$ both in the X-ray and radio. This implies that the quenching tends to occur with more active AGNs, supporting the AGN feedback for quenching massive galaxies at high redshifts. Simulations show the necessity of the AGN feedback to reproduce the observed steep bent of the rest-optical luminosity/stellar mass functions (e.g., Benson et al., 2003; Bower et al., 2006; Croton et al., 2006; Beckmann et al., 2017). In

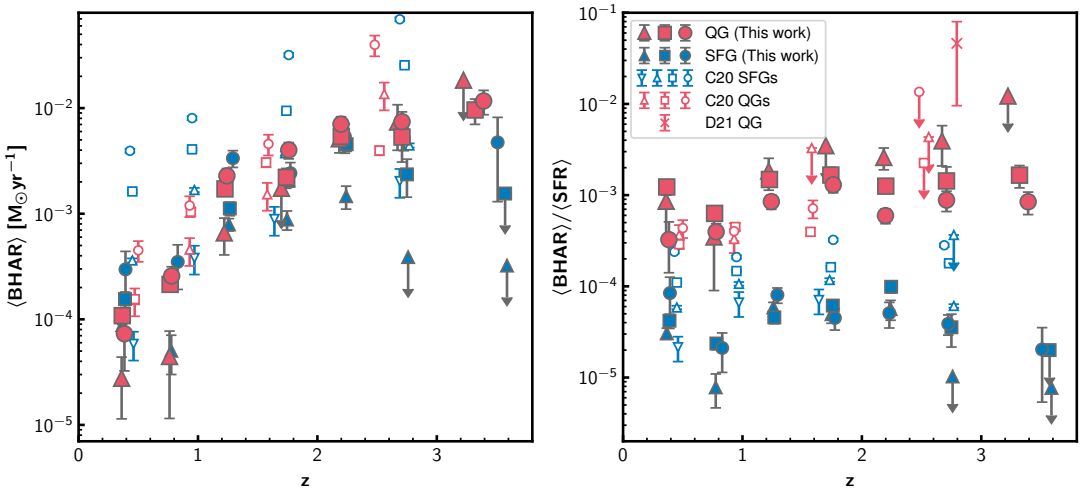

Figure 4.16: **Left panel:** Redshift evolution of BHAR. The red and blue filled symbols show the QGs and SFGs, respectively. The triangles, squares, and circles represent bins of $10.0 < \log(M_\star/M_\odot) < 10.5$, $10.5 < \log(M_\star/M_\odot) < 11.0$, and $11.0 < \log(M_\star/M_\odot) < 12.0$ for each population, respectively. The red and blue open symbols show the BHARs of Carraro et al. (2020). Their stellar mass bins are shown in different symbols. If the X-ray AGN luminosity is negative, BHAR is replaced by $2 \times 10^{-5} M_\odot \mathrm{yr}^{-1}$ only for illustrative purposes (shown in light color). **Right panel:** Ratio of BHAR and SFR. The triangles, squares, and circles represent same as in the left panel. The red cross shows the ratio of individually detected QGs in D'Eugenio et al. (2021). The data points with negative X-ray AGN luminosity are not shown.

fact, Beckmann et al. (2017) argue that AGN feedback at higher redshift affects the quenching of even less massive galaxies. According to their best-fit relation, galaxies with $\log(M_\star/M_\odot) \geq 9.9$ are expected to be largely affected by AGN feedback at $z > 1.5$, which is fully consistent with our findings.

The AGN feedback is thought to occur mainly through two processes. One is called "quasar-mode feedback" (e.g., Silk & Rees, 1998). In this mode, the wind from AGNs expels gases from galaxies and suppress the star formation. This is thought to occur in high-luminosity AGNs such as QSOs, close to the Eddington limit. The other mode is called "radio-mode feedback" (also known as kinetic-mode feedback, Fabian, 1994). In this mode, low-luminosity AGNs, such as less than one percent of the Eddington luminosity, heats the circumgalactic and halo gas by their radio jets, preventing the gas from cooling. Compared to the quasar-mode feedback, the radio-mode feedback is expected to keep the quiescence rather than stopping the star formation. Considering that AGNs seen in this study are low-luminosity AGNs and their star formation is already suppressed, we may be witnessing the radio-mode feedback from AGNs in action, which keep the star formation of our quiescent galaxies suppressed.

Low-luminosity AGNs are also observed in spectroscopically confirmed massive QGs at $z > 1.5$ by other features. Some studies found QGs with broad emission lines (Kriek et al., 2009; Marsan et al., 2015) or report a high [NII]/Hα ratio (Belli et al., 2019), which are likely from low luminosity AGNs. In addition, there are Spitzer/MIPS detections which cannot be explained by star formation (e.g., D'Eugenio et al., 2021). All these results are consistent with our findings. Together with the theoretical support (e.g., Beckmann et al., 2017), we might probe that AGN activity is a key phenomenon to make massive galaxies in the quiescent phase at $z \geq 1.5$.

At $z < 1.5$, we do not see such an enhancement of the AGN luminosity of QGs. Their AGN activity is comparable to or even weaker than SFGs. This difference between the high and low redshifts might be due to other quenching mechanisms operating at lower redshifts, such as environment quenching. There is clear observational evidence that the quiescent fraction at $z < 1.5$ is higher in denser regions, such as in galaxy clusters or groups, than in the general field (e.g., Peng et al., 2010b; Wetzel et al., 2012; van der Burg et al., 2013; Kawinwanichakij et al., 2017; Nantais et al., 2017; Reeves et al., 2021). Several mechanisms, such as ram-pressure stripping, are expected to quench galaxies in high-dense regions more effectively and keep the star formation stopped.

At $z > 2$, several studies argue that such a trend is not significant (e.g., Lin et al., 2016; Ito et al., 2021) or even reversed in terms of SFR (Lemaux et al., 2020, but also see Chartab et al. 2020), supporting this hypothesis for explaining the different trend. It seems that $z \sim 1.5 - 2$ is the epoch when the significant environmental dependence of galaxy properties emerges in the history of the Universe, and the environment quenching can be the dominant quenching process at lower redshifts. Because they do not necessarily trigger AGN activity, QGs may not exhibit enhanced AGN luminosity. On the other hand, environmental quenching is less dominant at higher redshifts, and instead, the AGN quenching has the primary role for the quenching, as suggested in this study. Thus, the combination of the AGN and the environmental quenching may be able to explain our observations.

We note that lower redshift bins can tend to have lower X-ray luminosities because we remove X-ray detection, but this would not introduce the redshift evolution of the AGN luminosity difference between QGs and SFGs. We construct the QG and SFG samples in the same way in each redshift bin. Thus, comparisons between them are fair comparisons. In addition, the typical stellar age of QGs might be different among the different redshift bins, i.e., QGs at lower redshift are older than those at high redshift. On the other hand, since we see objects which are already in the quenching phase, the mechanism keeping their star formation suppressed is necessary regardless of their quenching epoch. Therefore, the different ages among the different redshift bins are unlikely to affect the results. In addition, here we discuss the AGN luminosity difference between QG and SFG as an implication for quenching, but there is a possibility that SFG have lower black hole activity than expected.

4.6 Summary of Chapter 4

In this chapter, we systematically investigate the X-ray and radio properties of typical quiescent galaxies (QGs) with $\log(M_\star/M_\odot) > 10$ at $0 < z < 5$ for the first time. The QG sample is constructed based on the latest COSMOS2020 catalog with the sSFR criteria. The X-ray and radio stacking analyses are conducted for both QGs and SFGs, and we compare their properties. Our main results are summarized as follows:

1. The stacked X-ray flux is detected up to $z \sim 5$ for individually non-detected QGs

in the most stellar mass bins with the signal-to-noise ratio of more than two. The hardness ratios of QGs are tentatively higher than those of SFGs, suggesting higher obscurations.

2. The absorption-corrected rest-frame 2-10keV luminosity of QGs is comparable to that of SFGs. The luminosity increases with increasing stellar mass for both populations.

3. The observed X-ray luminosity is compared with the expected XRB luminosity from the SED-based stellar mass and SFR by using the empirical relation of Lehmer et al. (2016). The X-ray luminosity of QGs is significantly higher than the XRB luminosity, especially 5-50 times higher at $z > 1$. On the other hand, the X-ray luminosity of SFGs is comparable or slightly higher (≤ 3) than the expected XRB luminosity. This trend suggests the existence of the additional radiation source in QGs, i.e., AGN.

4. The X-ray AGN luminosity, defined as the excess of the observed luminosity to the expected XRB luminosity, is estimated. The AGN luminosity of QGs is higher than that of SFGs at fixed stellar mass at $z > 1.5$. This high luminosity implies the possible relationship between the galaxy quenching and the AGN activity. On the other hand, we do not see such enhanced luminosity of QGs at $z < 1.5$.

5. The rest-frame 1.4 GHz radio luminosity is also estimated for the same sample. For massive ($\log(M_\star/M_\odot) > 10.5$) QGs, the stacked radio flux is significantly detected with the signal-to-noise ratio more than 2σ up to $z \sim 5$.

6. Similar to the X-ray analysis, the radio AGN luminosity is derived by subtracting the luminosity related to their star formation estimated from the stellar mass and the SFR by the empirical relation of Delvecchio et al. (2021) from the observed luminosity. Similar to the X-ray luminosity, the only star formation can hardly explain the radio luminosity of QGs, and their radio AGN luminosity is higher than those of SFGs at $z > 1.5$.

7. The X-ray and radio AGN luminosity are well correlated for both QGs and SFGs. The slope of its relation is quite similar to the local relation in Merloni et al.

(2003). This study is the first time to show that QGs are located at the same scaling relation even up to $z \sim 5$.

8. As suggested from the high X-ray AGN luminosity, BHARs of QGs are higher than those of SFGs at $z > 1.5$. Moreover, the $\langle \mathrm{BHAR} \rangle / \langle \mathrm{SFR} \rangle$ of QGs is higher than those of SFGs and constant as $\langle \mathrm{BHAR} \rangle / \langle \mathrm{SFR} \rangle \sim 10^{-3}$ regardless of the redshift.

This chapter unveils typical properties of AGNs in QGs at $z \sim 3-5$ for the first time. The enhanced AGN luminosity at $z > 1.5$, revealed independently and consistently from the X-ray and radio, indicates a crucial role of AGNs in star formation quenching of massive galaxies, especially through the radio-mode feedback. This is further supported by recent spectroscopic observations of massive QGs, many of which turn out to host AGNs. Less pronounced AGN activity in QGs at $z < 1.5$ might be due to the increasing role of environmental quenching at lower redshifts. Our work hints at the evolving role of AGN feedback for galaxy quenching toward higher redshift, and future observations of QGs may shed further light on the detailed physics.

5 Discussion & Future prospects

5.1 Star Formation Activity and its Connection to Environment

This thesis has conducted three studies and tried to answer questions: the rest-frame UV luminosity function at $z \sim 4$ (“How star formation rate is different depending on the environment?"), the clustering and overdensity analysis among different galaxy populations at $2 < z < 4.5$ (“Do the different galaxy populations trace different spatial distribution?", “Does the environmental quenching exist at $z > 2$?"), and the X-ray and radio stacking analysis of quiescent galaxies at $0 < z < 5$ (“Can AGNs be a mechanism for quenching?"). The main results of these studies are as follows:

1. Galaxies in protoclusters are brighter than field galaxies in rest-frame UV, suggesting that they have more active star formation than field galaxies even at $z \sim 4$. Previous studies have shown the similar trend at $z \sim 2$, so we prove that it exists at earlier universe (Chapter 2).

2. The rest-frame UV luminosity function implies that protocluster at $z \sim 4$ contribute $\simeq 6-20\%$ of the total star formation occurring in the universe (Chapter 2).

3. According to the clustering and overdensity analyses, LAEs are generally segregated from massive star-forming/quiescent galaxies at $z \sim 2-4.5$. We show that the distinguished distribution of LAE, which has been reported in several protoclusters (e.g., Shimakawa et al., 2017; Shi et al., 2019a), are seen even in the general field (Chapter 3).

4. Quenching is not significantly related to the environment at $z \sim 2-3.5$, as seen from the spatial correlation function ratio and overdensity distribution between SFGs and QGs (Chapter 3).

5. We successfully detect the X-ray and radio signal of QGs at the highest redshift so far. QGs have higher X-ray/radio AGN luminosity than SFGs at $z > 1.5$, suggesting the contribution of the radio-mode feedback to the quenching. At $z < 1.5$, there is no difference in the luminosity between them (Chapter 4).

I here summarize the implications of these studies to the connection between star formation activity and the environment, dividing into three redshift bins, i.e., $2 < z < 4$, $1.5 < z < 2$, and $z < 1.5$, which are the epochs we observationally investigated (Figure 5.1).

Before the Cosmic Noon ($2 < z < 4$):

At this epoch, the dense environment increases the star formation rates (c.f., Chapter 2), and the environmental quenching is not significant (c.f., Section 3.4). This enhanced star formation activity is likely to result from the early formation of galaxies in massive halos and not likely due to the unique physics, which increases sSFR. This scenario is supported by the insignificant difference in the star formation main sequence of protocluster galaxies in the literature (see discussion in Section 2.7.3). In addition, our SED fitting analysis showed no difference in stellar population properties between protocluster galaxies and field galaxies at the same brightness (Section 2.5.3).

Recent studies report protoclusters with a number of dusty star-forming galaxies, which is a galaxy population not selected in this thesis (e.g., Miller et al., 2018; Oteo

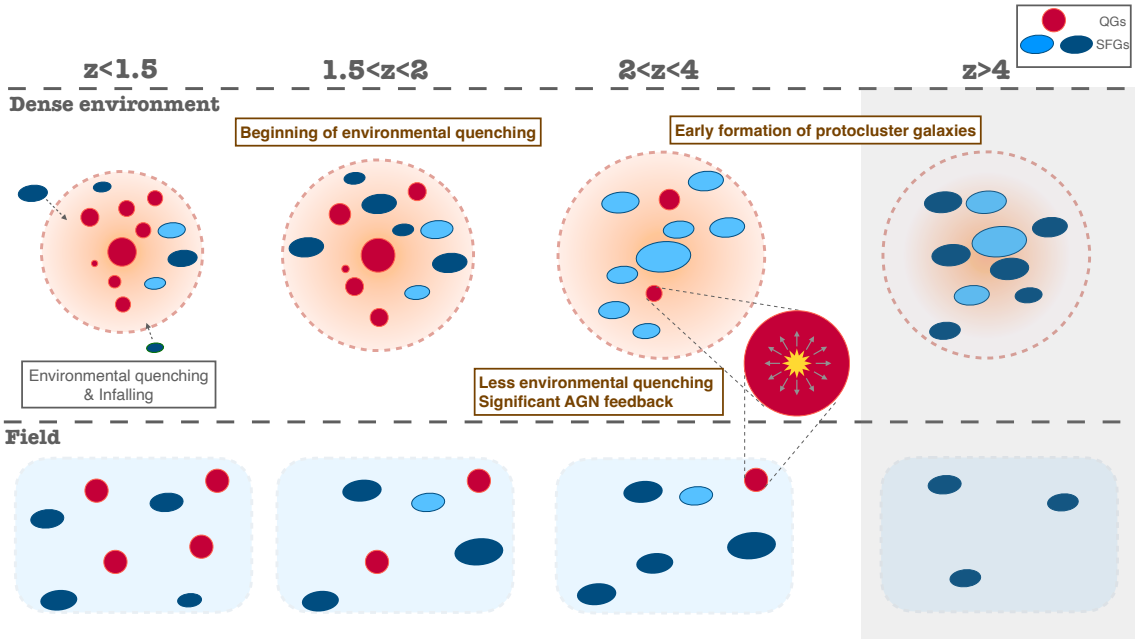

Figure 5.1: Schematic view of the evolution of the star formation activity and quenching in overdense regions and the field suggested from results of this thesis and other observational studies. The main implications of this thesis are shown with the bold faces and brown color. We here classify galaxies into two populations, QGs (red), SFGs (blue). Right-blue SFGs are meant to have higher SFR than dark-blue SFGs. The gray-shaded region ($z > 4$) is not observationally investigated in detail, and we show the prediction from this thesis.

et al., 2018; Umehata et al., 2019; Mitsuhashi et al., 2021; Koyama et al., 2021). Kubo et al. (2019) also suggest that HSC-SSP protoclusters also possess the dust-obscured star formation from the stacked IR spectra. These also imply that the overdense regions are in the active star-forming phase at this epoch.

Our X-ray and radio stacking implies that QGs have low-luminosity AGNs in general. QGs at z>2, which are now confirmed by the latest NIR spectrograph, are likely to be quenched through the feedback from AGNs. Therefore, quenching seems to be independent of the environment on average at this epoch.

The fact that the higher SFR of protocluster galaxies at $z \sim 2-3$ (e.g. Koyama et al., 2013; Shimakawa et al., 2018) is also seen at higher redshift ($z \sim 4$, this study) naively supports a “nature"-like environmental effect, i.e., the galaxy evolution is related to the living environment from their birth. In addition, our estimated SFRD in protoclusters suggests that they contributed to the high fraction of the star formation in the universe at that time, despite their small volume. Therefore, this thesis observationally proves that protoclusters at $2 < z < 4$ follow the “extended star formation" epoch in the prediction of Chiang et al. (2017) (see Figure 1.2) when protoclusters have active star formation in the entire region, and they are the main driver of cosmic star formation at that epoch.

Around the Cosmic Noon ($1.5 < z < 2$):

At this epoch, the dense environment begins to quench galaxies. The higher fraction of quiescent galaxies (see studies referred in Chapter 1) and the emergence of quiescent dominated clusters (e.g., Strazzullo et al., 2013; Newman et al., 2014) support this picture. Moreover, the average X-ray and radio properties of QGs suggest that the trend of higher AGN luminosity gets less significant, implying that the transition of the quenching mechanism from the AGN feedback to others. If the latter mechanism is related to the environment, we can explain both observational results.

The accelerated quenching might be the natural consequence of the “early formation of galaxies in massive halos", if their star formation duration is the same as that of field galaxies. This epoch corresponds to the transition from “extended star formation" phase to “infalling and quenching" phase according to Chiang et al. (2017).

After the Cosmic Noon ($z < 1.5$):

At this epoch, the environment tends to quench galaxies, i.e., the environmental quenching is significant. As many other studies show (see Chapter 1 for the detailed introduction), the dense environment has a higher quiescent fraction. The indifferent AGN luminosity of QGs and SFGs supports that the quenching is dominantly occurred by other different mechanisms, not the AGN feedback (Chapter 4).

In addition, Section 2.7.3 discusses infalling galaxies is important to explain the redshift evolution of the stellar mass function from $z \sim 4$ to $z \sim 0$. Such external contribution might also be important on the average picture of star-formation activity and stellar mass growth of (proto)cluster galaxies.

One important caveat of this thesis is that, in general, the distribution of only one galaxy population can extract biased environmental features that cannot be explained by the halo mass distribution alone (Chapter 3). The discussion on the environment in this thesis is based on LBGs or photo-z selected galaxies, which are considered typical galaxies selected from the general spectroscopic features of the spectra at that epoch. Therefore, we expect that our environment measurement traces the typical one in the universe. However, We must carefully compare these results with properties of other protoclusters selected from other populations, such as LAEs.

5.2 Future Prospects

We here discuss the next steps to extend our results. Based on the current data set and the construction plan of future telescopes, we propose six studies described below. The first four topics are to understand or examine the picture obtained in this thesis in detail, and the latter two are to explore new populations, based on their implication:

5.2.1 Examining evolutionary picture of protoclusters: Towards higher redshift and precise spatial measurement

As discussed in Section 5.1, our observational results are consistent with the theoretical prediction of the protocluster evolution suggested by Chiang et al. (2017). It is crucial to conduct the following two studies to examine the picture further.

The first is a protocluster survey at higher-z. In this study, we only focus on $z \leq 4$ universe, i.e., “extended star formation" phase in Chiang et al. (2017). The observation studies beyond this redshift are still few. It has been challenging to discuss whether the real universe at $z > 5$ is following the “inside-out growth" phase suggested by Chiang et al. (2017). In particular, they predict that protoclusters at $z > 5$ contribute more significantly to the star formation in the universe than those $z < 4$, therefore they are expected to show more significant difference than what we see at $z \sim 4$. To examine this, we need systematically selected protoclusters at higher redshift. With the upcoming data set and telescope, we can significantly improve the situation. Currently, we are selecting protocluster candidates at $z \sim 2 - 6$ by using LBGs selected based on optical colors of HSC-SSP, which is the identical method used in this thesis (Toshikawa et al., 2018). This new high-z protocluster sample will enable us to determine the UVLF and SFRD of protocluster galaxies even at $z > 5$. In addition, the James Webb Space Telescope (JWST), the Nancy Grace Roman Space Telescope (RST), and the 30m-class telescope (e.g., TMT) will provide us a sample of overdense regions at $z > 6$. For example, JWST can find line emitters, such as O[III] emitters and HAEs, at $z < 9$, and RST will provide LBG samples at $z \sim 9$ from the extensive survey area. TMT will easily reveal the spectroscopic feature of protocluster members. These newly found protoclusters will be an ideal laboratory to explore their picture at a higher redshift than this thesis.

Secondly, the precise spatial distribution measurement is also critical to disentangle the “extended star formation" and “inside-out growth" phases. The most significant difference between these two is the location where the active star formation occurs. In the former phase, the active star formation occurs in the entire protocluster region, while it only occurs in the only core regions in the latter phase. Therefore, exploring the structure of active star formation in and around protoclusters is critical to constrain the phase. Our UVLF is based on all protocluster galaxies in the typical protocluster scale, likely to support the former phase. On the other hand, identifying the core regions of protoclusters was difficult due to the poor accuracy of the center position. The spectroscopic redshift is essential to increase the position accuracy. The upcoming Prime Focus Spectrograph (PFS) of the Subaru Telescope and the Multi-Object Optical and Near-infrared Spectrograph (MOONS) on the Very Large Telescope are expected to provide a large number of the deep spectra of high redshift galaxies. These will

determine the exact spatial distribution of member galaxies in protoclusters and are helpful to understand the exact location where the active star formation occurs.

5.2.2 Investigating origin of distribution differences of LAEs

The main result of Chapter 3 is that LAEs are generally distributed differently from other massive galaxies at $2 < z < 4.5$. We argue that this trend can be caused by plenty of surrounding HI gas absorbing the Lyα emission or assembly bias. In the former scenario, investigating the distribution of galaxies and IGM HI gas is essential. Supporting results are now reported (e.g., Momose et al., 2021b), which argue that LAEs at $z \sim 2.3$ tend to be hardly observed behind the dense region of HI gas along with the light of sight direction. On the other hand, this study includes only a limited sample (19 LAEs), so enlarging the number of samples and expanding the redshift range will be essential to constrain the scenario. The Subaru telescope's PFS will conduct a sizeable Lyα tomography. Combining the obtained IGM HI gas distribution and the spectroscopically confirmed galaxy sample at the same redshift, we will be able to see the three-dimensional picture of galaxies and HI gas. Comparing their interrelations, including LAEs, we will understand how HI gas affects the observed distribution of LAEs and massive galaxies.

The latter scenario is challenging to assess since the halo formation epoch cannot be constrained observationally. It will be necessary to compare our results with the theoretical studies in this situation. As mentioned in Section 3.5.2, some studies predict the existence of the assembly bias from simulations. However, these studies focus on all galaxies, and they do not distinguish galaxies based on the observational properties, such as Lyα equivalent width, which is used to select LAEs. To directly compare our results with them, we should impose the same criteria on the simulation as on observation. Hydrodynamical radiative simulations, which take into account the Lyα emission (e.g., Inoue et al., 2018), will be pretty valuable. With the similar information, which we now have observationally, and the information of the halo formation epoch, which we cannot obtain from the observation, we can indirectly discuss how the assembly bias affects the observed distribution difference among different galaxy populations.

5.2.3 Connecting AGN activity with living environment

Chapter 4 shows the effectiveness of the X-ray/radio stacking analysis to reveal the average AGN activity of galaxies. A more detailed investigation will be valuable to understand the origin of our findings. In particular, revealing the effect of galaxies' living environment is a highly needed step. The trend difference of the AGN luminosity at different redshifts can be due to the transition of quenching mechanisms from the AGN feedback to the environmental quenching. This additional analysis will examine this hypothesis.

Future telescopes will be expected to help to achieve this. In terms of X-ray observation, the planned Advanced X-ray Imaging Satellite (AXIS) probe and the forthcoming Advanced Telescope for High Energy Astrophysics (ATHENA) will provide an ideal dataset. According to Marchesi et al. (2020), 0.3Ms AXIS and 14Ms ATHENA observation will detect the soft-band individual signal of QGs even at the high redshift over $\sim 1\,\mathrm{deg}^2$ and $\sim 4\,\mathrm{deg}^2$, respectively. These new facilities will push us to connect the AGN activity and their large-scale environment and constrain their role in galaxy quenching.

5.2.4 Unveiling mechanisms reducing star formation

In Chapter 4, we argue that AGNs are essential to keep the star formation suppressed in massive quiescent galaxies at high redshift. In addition to the mechanism that keeps the star formation suppressed, the mechanism that reduces star formation is also critical to understanding the galaxy evolution. There can be several pathways to constrain it.

Firstly, the detailed characterization of the X-ray/radio luminosity will be important. We will prove the exact phase of the peak AGN activity by subdividing the quiescent galaxies into the different specific star formation rate (i.e., the quenching phase). Suppose the AGN has an essential role in reducing star formation, possibly through the quasar-mode feedback. In that case, galaxies with the declining SFR should have higher AGN luminosity than completely quenched ones. Thus, this detailed analysis can constrain the possible physical mechanism. However, it might be currently challenging, especially at $z > 2$, due to the lack of enough sensitivity of the X-ray/radio observations. As mentioned above, the upcoming facilities will enable us to achieve

high sensitivity. In addition, ngVLA will also have the power to improve this situation in the radio wavelength. Recent observations of quasar host galaxies show the existence of quasar-driven outflows, which can quench galaxies even at $z \sim 6-7$ (e.g. Maiolino et al., 2012; Izumi et al., 2021), which are in line with quasar-mode feedback. This detailed X-ray/radio stacking analysis will assess whether such a quasar-driven outflow generally affects the quenching associated with the AGN activity.

Subdividing based on their morphology might be also useful to discuss the contribution of the morphological quenching scenario (e.g., Martig et al., 2009). In addition, the ALMA observation will help us determine the molecular gas mass. Some studies show that QGs have a lower amount of molecular gas than that of SFGs (e.g., Magdis et al., 2021; Gobat et al., 2018; Zavala et al., 2019; Whitaker et al., 2021). This follow-up observation will examine whether the quenching has occurred with the decreasing gas mass.

5.2.5 Exploring multiple galaxy populations in HSC-SSP protoclusters

This thesis shows the significant power of the HSC-SSP protocluster sample thanks to its large sample size. On the other hand, as shown in Chapter 3, we need to survey various galaxy populations, not only LBGs in protocluster regions, in order to understand the intrinsic living environment. Galaxy populations described below should be surveyed in our current protocluster sample.

Firstly, an extensive LAE survey is interesting to connect our protoclusters to Lyα-selected protoclusters at higher redshift (e.g., Shimasaku et al., 2003; Chiang et al., 2015; Jiang et al., 2018; Higuchi et al., 2019; Harikane et al., 2019). The spectroscopy of HSC-SSP protocluster galaxies aiming at their Lyα emission has been conducted (Toshikawa et al., S17A-105, S19A-080). However, it has been expensive since it needs to target many objects with a long integration time. Therefore, the extensive spectroscopy campaign by the upcoming PFS will accelerate to achieve it.

Surveying massive QGs is another pathway to understanding star-forming activity and quenching in HSC-SSP protoclusters. This will lead to a more precise measurement of the protocluster stellar mass function (Section 2.4.1) and a discussion of the environmental quenching in more extreme environments than in Section 3.4. This will

be achieved by the large-field multi-photometric data of the HSC-SSP joint catalog. In addition, the extensive medium band survey with Subaru/SWIMS is now conducted, which will select massive galaxies with the significant Balmer break in the NIR (Ruby-Rush, Kodama, et al., S21A-013).

The sub-millimeter follow-up is also essential to reveal the hidden galaxies in the rest-frame UV wavelength (e.g., SMGs). We are now conducting this for several targets using the ALMA and will broadly expand its survey volume in the future.

5.2.6 Exploring new types of protoclusters of galaxies with suppressed star formation

The HSC-SSP protocluster sample has provided many insights not only as described in this thesis but also in other published papers (Uchiyama et al., 2018; Onoue et al., 2018; Kubo et al., 2019). On the other hand, this is not a complete protocluster sample at that redshift. In particular we expect that there are other protocluster populations dominated by quiescent galaxies, which had not been selected from the only HSC-SSP. According to observations for protoclusters of dusty star-forming galaxies at $z > 4$ identified with ALMA (e.g., Oteo et al., 2018), their gas depletion time ranges from 70 Myr to 1 Gyr (Long et al., 2020). This short time implies that most members therein will be quenched and form overdense structures of QGs at $z \sim 3$ unless they are replenished with fresh gas. To comprehensively understand the star formation activity and the quenching, we should survey these populations, too. Indeed, recent extensive multi-photometric surveys and the latest NIR spectroscopic follow-up show the hints of their existence, which find that massive quiescent galaxies coexist with star-forming galaxies in protoclusters at $z \sim 3$ (Kubo et al., 2021; Kalita et al., 2021; McConachie et al., 2021).

The COSMOS2020 catalog, which is one of the deepest and largest multi-photometric catalogs so far used in Chapter 4, will provide several protoclusters mainly consisting of quiescent galaxies at $z \sim 3$. Indeed, we are beginning this survey and proposing a NIR spectroscopy by Keck/MOSFIRE and HST/WFC3 for several plausible candidates. These unique targets enable us to explore the connection between the environment and quenching in the extreme regions, which is complementary to the result of Chapter 3, where its average picture is discussed.

6 Summary

In this thesis, I present observational studies which focus on galaxies and their connection to their living environment based on the wide-field survey data of the Hyper Suprime-Cam Subaru Strategic Program (HSC-SSP) and the Cosmic Evolution Survey (COSMOS). I conducted three statistical studies mainly focusing on the star formation activity at high redshift. The main results are summarized as follows:

1. Rest-frame UV luminosity function of protocluster galaxies at $z \sim 4$:
We derived the rest-frame UV luminosity function of protocluster at $z \sim 4$. The protocluster sample used in this study is selected from the HSC-SSP in Toshikawa et al. (2018) and Toshikawa in (prep.). After the statistical subtraction of field galaxies and low-redshift contaminants and the completeness correction for protocluster galaxies, we find that protocluster galaxies tend to be brighter in the rest-frame UV than field galaxies at the same epoch. The AGN fraction in the literature, the morphological properties, and the SED fitting suggest that the all of the bright-end excess is not likely due to AGNs. This suggests that protocluster galaxies tend to be more active in star

formation. The star formation rate density occurring in protoclusters is estimated from this rest-frame UV luminosity function. After correcting the sample completeness and purity of the protocluster sample, we find that the protoclusters contribute to $\simeq 6-20\%$ of the total star formation in the universe at $z \sim 4$. These suggest that the environment has already affected the galaxy evolution at $z \sim 4$, and protocluster galaxies may evolve earlier than field galaxies.

2. Evaluation of environment of multiple galaxy populations at $2 < z < 4.5$:
We discussed differences in the spatial distribution of photo-z selected massive star-forming and quiescent galaxies (SFGs and QGs) and that of LAEs at $2 < z < 4.5$ in the COSMOS field. SFGs and QGs are selected based on the SED fitting with the multi-band photometry of Laigle et al. (2016), and the LAE sample is taken from the SC4K survey (Sobral et al., 2018). We conduct the clustering analysis among these three populations and derive the overdensity distribution around them. The cross-correlation signals of SFGs and QGs are explained solely by their halo mass differences (i.e., the strength of the autocorrelation signal). However, those of SFGs and LAEs are significantly lower than those expected from their autocorrelation signals, suggesting that some other physical processes segregate these two populations. From the overdensity distributions, LAEs are located in less dense regions than SFGs and QGs, whereas SFGs and QGs tend to be in the same overdensity distributions. These results imply that only LAEs are segregated from other galaxy populations by some physics, and they reinforce the importance of exploring multiple galaxy populations in quantifying the intrinsic galaxy environment of the high-z universe. In addition, we discuss the connection between SFR and the living environment from the derived overdensity, and we do not find any correlation. Based on the clustering analysis and the overdensity, this work suggests that the environmental quenching is insignificant at $z > 2$.

3. X-ray and Radio Stacking for Quiescent Galaxies at $0 < z < 5$:
We conduct the X-ray and radio stacking analysis for QGs with $\log(M_\star/M_\odot) > 10$ at $0 < z < 5$. QGs are photometrically selected from the latest COSMOS2020 catalog. We conduct the stacking analysis of X-ray images of the Chandra COSMOS Legacy Survey for individually undetected QGs. Thanks to the large sample and deep images, the stacked X-ray signal is significantly detected up to $z \sim 5$ for the first time. The average

X-ray luminosity can not be explained by the X-ray luminosity of X-ray binaries, suggesting that the low-luminosity active galactic nuclei (AGNs) ubiquitously exist in QGs. Moreover, the X-ray AGN luminosity of QGs at $z > 1.5$ is higher than that of SFGs, derived in the same manner as QGs. The stacking analysis of the VLA-COSMOS images is conducted for the identical sample, and the signal for QGs is detected up to $z \sim 5$. We find that the radio AGN luminosity of QGs at $z > 1.5$ is also higher than SFGs, which is in good agreement with the X-ray analysis. The enhanced activity of AGNs in QGs suggested by the individual analysis in the X-ray and radio indicates an important role of the AGN activity for quenching at high redshift.

This thesis shows the primordial environment effect even at $z \sim 4$, which induces the active structure formation in dense regions. In contrast, quenching is likely to primarily occur not by environmental quenching but by the AGN feedback. At the same time, this thesis shows the importance of mapping the various galaxy populations to characterize the real environment. In particular, we should survey LAEs, QGs, and dusty star-forming galaxies in HSC-SSP protoclusters, which might be missed in the current member sample. This will provide a more multi-faced view of protoclusters and a precise evaluation of the enhanced star formation activity in overdense regions. In addition, we should explore a new population of protoclusters consisting of QGs. These researches will be achieved in future analysis and follow-up observations.

Bibliography

Adams, N. J., Bowler, R. A. A., Jarvis, M. J., et al. 2020, Monthly Notices of the Royal Astronomical Society, 494, 1771, doi: 10.1093/mnras/staa687

Aihara, H., Arimoto, N., Armstrong, R., et al. 2018, Publications of the Astronomical Society of Japan, 70, 1, doi: 10.1093/pasj/psx066

Aihara, H., Alsayyad, Y., Ando, M., et al. 2019, Publications of the Astronomical Society of Japan, 71, 1, doi: 10.1093/pasj/psz103

Aird, J., Coil, A. L., & Georgakakis, A. 2017, Monthly Notices of the Royal Astronomical Society, 465, 3390, doi: 10.1093/mnras/stw2932

Akiyama, M., He, W., Ikeda, H., et al. 2018, Publications of the Astronomical Society of Japan, 70, 1, doi: 10.1093/pasj/psx091

Alam, S., Albareti, F. D., Prieto, C. A., et al. 2015, The Astrophysical Journal Supplement Series, 219, 12, doi: 10.1088/0067-0049/219/1/12

Álvarez-Márquez, J., Burgarella, D., Buat, V., Ilbert, O., & Pérez-González, P. G. 2019, Astronomy and Astrophysics, 630, A153, doi: 10.1051/0004-6361/201935719

Axelrod, T., Kantor, J., Lupton, R. H., & Pierfederici, F. 2010, Software and Cyberinfrastructure for Astronomy, 7740, 774015, doi: 10.1117/12.857297

Balogh, M., Eke, V., Miller, C., et al. 2004, Monthly Notices of the Royal Astronomical Society, 348, 1355, doi: 10.1111/j.1365-2966.2004.07453.x

Balogh, M. L., Christlein, D., Zabludoff, A. I., & Zaritsky, D. 2001, The Astrophysical Journal, 557, 117, doi: 10.1086/321670

Balogh, M. L., Schade, D., Morris, S. L., et al. 1998, The Astrophysical Journal, 504, L75, doi: 10.1086/311576

Bamford, S. P., Nichol, R. C., Baldry, I. K., et al. 2009, Monthly Notices of the Royal Astronomical Society, 393, 1324, doi: 10.1111/j.1365-2966.2008.14252.x

Beckmann, R. S., Devriendt, J., Slyz, A., et al. 2017, Monthly Notices of the Royal Astronomical Society, 472, 949, doi: 10.1093/mnras/stx1831

Belli, S., Newman, A. B., & Ellis, R. S. 2017, The Astrophysical Journal, 834, 18, doi: 10.3847/1538-4357/834/1/18

—. 2019, The Astrophysical Journal, 874, 17, doi: 10.3847/1538-4357/ab07af

Benson, A. J., Bower, R. G., Frenk, C. S., et al. 2003, The Astrophysical Journal, 599, 38, doi: 10.1086/379160

Bertin, E. 2011, Analysis, 442, 435. http://adsabs.harvard.edu/abs/2011ASPC..442..435B

Béthermin, M., Kilbinger, M., Daddi, E., et al. 2014, Astronomy and Astrophysics, 567, A103, doi: 10.1051/0004-6361/201423451

Bezanson, R., van Dokkum, P. G., Tal, T., et al. 2009, The Astrophysical Journal, 697, 1290, doi: 10.1088/0004-637X/697/2/1290

Bielby, R., Hill, M. D., Shanks, T., et al. 2013, Monthly Notices of the Royal Astronomical Society, 430, 425, doi: 10.1093/mnras/sts639

Bielby, R. M., Tummuangpak, P., Shanks, T., et al. 2016, Monthly Notices of the Royal Astronomical Society, 456, 4061, doi: 10.1093/mnras/stv2914

Biviano, A., Moretti, A., Paccagnella, A., et al. 2017, Astronomy and Astrophysics, 607, A81, doi: 10.1051/0004-6361/201731289

Bleem, L. E., Stalder, B., de Haan, T., et al. 2015, The Astrophysical Journal Supplement Series, 216, 27, doi: 10.1088/0067-0049/216/2/27

Boquien, M., Burgarella, D., Roehlly, Y., et al. 2019, Astronomy and Astrophysics, 622, A103, doi: 10.1051/0004-6361/201834156

Bosch, J., Armstrong, R., Bickerton, S., et al. 2018, Publications of the Astronomical Society of Japan, 70, 1, doi: 10.1093/pasj/psx080

Bouwens, R., González-López, J., Aravena, M., et al. 2020, The Astrophysical Journal, 902, 112, doi: 10.3847/1538-4357/abb830

Bouwens, R. J., Illingworth, G. D., Franx, M., et al. 2009, The Astrophysical Journal, 705, 936, doi: 10.1088/0004-637X/705/1/936

Bouwens, R. J., Illingworth, G. D., Oesch, P. A., et al. 2012a, The Astrophysical Journal, 752, L5, doi: 10.1088/2041-8205/752/1/L5

—. 2012b, The Astrophysical Journal, 754, 83, doi: 10.1088/0004-637X/754/2/83

—. 2014, The Astrophysical Journal, 793, 115, doi: 10.1088/0004-637X/793/2/115

—. 2015, The Astrophysical Journal, 803, 34, doi: 10.1088/0004-637X/803/1/34

Bower, R. G., Benson, A. J., Malbon, R., et al. 2006, Monthly Notices of the Royal Astronomical Society, 370, 645, doi: 10.1111/j.1365-2966.2006.10519.x

Bowler, R. A. A., Adams, N. J., Jarvis, M. J., & Häußler, B. 2021, Monthly Notices of the Royal Astronomical Society, 502, 662, doi: 10.1093/mnras/stab038

Bowler, R. A. A., Jarvis, M. J., Dunlop, J. S., et al. 2020, Monthly Notices of the Royal Astronomical Society, 493, 2059, doi: 10.1093/mnras/staa313

Bruzual, G., & Charlot, S. 2003, Monthly Notices of the Royal Astronomical Society, 344, 1000, doi: 10.1046/j.1365-8711.2003.06897.x

Butcher, H., & Oemler, A., J. 1978, The Astrophysical Journal, 219, 18, doi: 10.1086/155751

Bădescu, T., Yang, Y., Bertoldi, F., et al. 2017, The Astrophysical Journal, 845, 172, doi: 10.3847/1538-4357/aa8220

Cai, Z., Fan, X., Peirani, S., et al. 2016, The Astrophysical Journal, 833, 135, doi: 10.3847/1538-4357/833/2/135

Calvi, R., Poggianti, B. M., Vulcani, B., & Fasano, G. 2013, Monthly Notices of the Royal Astronomical Society, 432, 3141, doi: 10.1093/mnras/stt667

Calzetti, D., Armus, L., Bohlin, R. C., et al. 2000, The Astrophysical Journal, 533, 682, doi: 10.1086/308692

Carraro, R., Rodighiero, G., Cassata, P., et al. 2020, Astronomy and Astrophysics, 642, A65, doi: 10.1051/0004-6361/201936649

Chabrier, G. 2003, The Astrophysical Journal, 586, L133, doi: 10.1086/374879

Chartab, N., Mobasher, B., Darvish, B., et al. 2020, The Astrophysical Journal, 890, 7, doi: 10.3847/1538-4357/ab61fd

Chiang, Y.-K., Overzier, R., & Gebhardt, K. 2013, The Astrophysical Journal, 779, 127, doi: 10.1088/0004-637X/779/2/127

—. 2014, The Astrophysical Journal, 782, L3, doi: 10.1088/2041-8205/782/1/L3

Chiang, Y.-K., Overzier, R. A., Gebhardt, K., & Henriques, B. 2017, The Astrophysical Journal, 844, L23, doi: 10.3847/2041-8213/aa7e7b

Chiang, Y.-K., Overzier, R. A., Gebhardt, K., et al. 2015, The Astrophysical Journal, 808, 37, doi: 10.1088/0004-637X/808/1/37

Civano, F., Marchesi, S., Comastri, A., et al. 2016, The Astrophysical Journal, 819, 62, doi: 10.3847/0004-637x/819/1/62

Cochrane, R. K., Best, P. N., Sobral, D., et al. 2018, Monthly Notices of the Royal Astronomical Society, 475, 3730, doi: 10.1093/mnras/stx3345

—. 2017, Monthly Notices of the Royal Astronomical Society, 469, 2913, doi: 10.1093/mnras/stx957

Cooke, E. A., Hatch, N. A., Muldrew, S. I., Rigby, E. E., & Kurk, J. D. 2014, Monthly Notices of the Royal Astronomical Society, 440, 3262, doi: 10.1093/mnras/stu522

Coupon, J., Czakon, N., Bosch, J., et al. 2018, Publications of the Astronomical Society of Japan, 70, 7, doi: 10.1093/pasj/psx047

Coupon, J., Kilbinger, M., McCracken, H. J., et al. 2012, Astronomy and Astrophysics, 542, A5, doi: 10.1051/0004-6361/201117625

Cowley, W. I., Caputi, K. I., Deshmukh, S., et al. 2019, The Astrophysical Journal, 874, 114, doi: 10.3847/1538-4357/ab089b

Croom, S. M., & Shanks, T. 1999, Monthly Notices of the Royal Astronomical Society, 303, 411, doi: 10.1046/j.1365-8711.1999.02232.x

Croton, D. J., Springel, V., White, S. D., et al. 2006, Monthly Notices of the Royal Astronomical Society, 365, 11, doi: 10.1111/j.1365-2966.2005.09675.x

Cucciati, O., Tresse, L., Ilbert, O., et al. 2012, Astronomy and Astrophysics, 539, A31, doi: 10.1051/0004-6361/201118010

Cucciati, O., Zamorani, G., Lemaux, B. C., et al. 2014, Astronomy and Astrophysics, 570, A16, doi: 10.1051/0004-6361/201423811

Cucciati, O., Lemaux, B. C., Zamorani, G., et al. 2018, Astronomy and Astrophysics, 619, A49, doi: 10.1051/0004-6361/201833655

Daddi, E., Valentino, F., Rich, R. M., et al. 2021, Astronomy and Astrophysics, 649, 1, doi: 10.1051/0004-6361/202038700

Darvish, B., Scoville, N. Z., Martin, C., et al. 2020, The Astrophysical Journal, 892, 8, doi: 10.3847/1538-4357/ab75c3

Davidzon, I., Ilbert, O., Laigle, C., et al. 2017, Astronomy and Astrophysics, 605, A70, doi: 10.1051/0004-6361/201730419

De Lucia, G. 2006, 379, 257. https://arxiv.org/abs/0611350

Dekel, A., Birnboim, Y., Engel, G., et al. 2009, Nature, 457, 451, doi: 10.1038/nature07648

Delvecchio, I., Daddi, E., Sargent, M. T., et al. 2021, Astronomy and Astrophysics, 647, A123, doi: 10.1051/0004-6361/202039647

Demarco, R., Wilson, G., Muzzin, A., et al. 2010, The Astrophysical Journal, 711, 1185, doi: 10.1088/0004-637X/711/2/1185

D'Eugenio, C., Daddi, E., Gobat, R., et al. 2021, Astronomy and Astrophysics, 653, A32, doi: 10.1051/0004-6361/202040067

Dressler, A. 1980, The Astrophysical Journal, 236, 351, doi: 10.1086/157753

Duras, F., Bongiorno, A., Ricci, F., et al. 2020, Astronomy and Astrophysics, 636, A73, doi: 10.1051/0004-6361/201936817

Eddington, A. S. 1913, Monthly Notices of the Royal Astronomical Society, 73, 359, doi: 10.1093/mnras/73.5.359

Efstathiou, G., Bernstein, G., Katz, N., Tyson, J. A., & Guhathakurta, P. 1991, The Astrophysical Journal Letters, 380, L47, doi: 10.1086/186170

Eisenstein, D. J., & Hu, W. 1998, The Astrophysical Journal, 496, 605, doi: 10.1086/305424

Elbaz, D., Daddi, E., Le Borgne, D., et al. 2007, Astronomy and Astrophysics, 468, 33, doi: 10.1051/0004-6361:20077525

Fabian, A. 2012, Annual Review of Astronomy and Astrophysics, 50, 455, doi: 10.1146/annurev-astro-081811-125521

Fabian, A. C. 1994, Annual Review of Astronomy and Astrophysics, 32, 277

Fasano, G., Marmo, C., Varela, J., et al. 2006, Astronomy and Astrophysics, 445, 805, doi: 10.1051/0004-6361:20053816

Finkelstein, S. L., Ryan, R. E., Papovich, C., et al. 2015, The Astrophysical Journal, 810, 71, doi: 10.1088/0004-637X/810/1/71

Fornasini, F. M., Civano, F., Fabbiano, G., et al. 2018, The Astrophysical Journal, 865, 43, doi: 10.3847/1538-4357/aada4e

Forrest, B., Annunziatella, M., Wilson, G., et al. 2020, The Astrophysical Journal, 890, L1, doi: 10.3847/2041-8213/ab5b9f

Fritz, J., Franceschini, A., & Hatziminaoglou, E. 2006, Monthly Notices of the Royal Astronomical Society, 366, 767, doi: 10.1111/j.1365-2966.2006.09866.x

Furnell, K. E., Collins, C. A., Kelvin, L. S., et al. 2018, Monthly Notices of the Royal Astronomical Society, 478, 4952, doi: 10.1093/mnras/sty991

Furusawa, H., Koike, M., Takata, T., et al. 2018, Publications of the Astronomical Society of Japan, 70, 1, doi: 10.1093/pasj/psx079

Gao, L., & White, S. D. 2007, Monthly Notices of the Royal Astronomical Society: Letters, 377, 5, doi: 10.1111/j.1745-3933.2007.00292.x

Garilli, B., Guzzo, L., Scodeggio, M., et al. 2014, Astronomy and Astrophysics, 562, A23, doi: 10.1051/0004-6361/201322790

Gawiser, E., van Dokkum, P. G., Gronwall, C., et al. 2006, The Astrophysical Journal, 642, L13, doi: 10.1086/504467

Gawiser, E., Francke, H., Lai, K., et al. 2007, The Astrophysical Journal, 671, 278, doi: 10.1086/522955

Geach, J. E., Smail, I., Best, P. N., et al. 2008, Monthly Notices of the Royal Astronomical Society, 388, 1473, doi: 10.1111/j.1365-2966.2008.13481.x

Glazebrook, K., Schreiber, C., Labbé, I., et al. 2017, Nature, 544, 71, doi: 10.1038/nature21680

Gobat, R., Strazzullo, V., Daddi, E., et al. 2012, The Astrophysical Journal, 759, L44, doi: 10.1088/2041-8205/759/2/L44

Gobat, R., Daddi, E., Magdis, G., et al. 2018, Nature Astronomy, 2, 239, doi: 10.1038/s41550-017-0352-5

Griffith, R. L., Cooper, M. C., Newman, J. A., et al. 2012, The Astrophysical Journal Supplement Series, 200, 9, doi: 10.1088/0067-0049/200/1/9

Gunn, J. E., & Gott, J. Richard, I. 1972, The Astrophysical Journal, 176, 1, doi: 10.1086/151605

Guo, Y., Ferguson, H. C., Giavalisco, M., et al. 2013, The Astrophysical Journal Supplement Series, 207, 24, doi: 10.1088/0067-0049/207/2/24

Hagen, A., Ciardullo, R., Gronwall, C., et al. 2014, The Astrophysical Journal, 786, 59, doi: 10.1088/0004-637X/786/1/59

Harikane, Y., Ouchi, M., Ono, Y., et al. 2018, Publications of the Astronomical Society of Japan, 70, 1, doi: 10.1093/pasj/psx097

—. 2019, The Astrophysical Journal, 883, 142, doi: 10.3847/1538-4357/ab2cd5

Harikane, Y., Ono, Y., Ouchi, M., et al. 2021. https://arxiv.org/abs/2108.01090

Hatch, N. A., Kurk, J. D., Pentericci, L., et al. 2011a, Monthly Notices of the Royal Astronomical Society, 415, 2993, doi: 10.1111/j.1365-2966.2011.18735.x

Hatch, N. A., De Breuck, C., Galametz, A., et al. 2011b, Monthly Notices of the Royal Astronomical Society, 410, 1537, doi: 10.1111/j.1365-2966.2010.17538.x

Hatfield, P. W., & Jarvis, M. J. 2017, Monthly Notices of the Royal Astronomical Society, 472, 3570, doi: 10.1093/mnras/stx2155

Hathi, N. P., Cohen, S. H., Ryan, R. E., et al. 2013, The Astrophysical Journal, 765, 88, doi: 10.1088/0004-637X/765/2/88

Hayashi, M., Kodama, T., Tadaki, K.-i., Koyama, Y., & Tanaka, I. 2012, The Astrophysical Journal, 757, 15, doi: 10.1088/0004-637X/757/1/15

Hayashino, T., Matsuda, Y., Tamura, H., et al. 2004, The Astronomical Journal, 128, 2073, doi: 10.1086/424935

Henriques, B. M., White, S. D., Thomas, P. A., et al. 2015, Monthly Notices of the Royal Astronomical Society, 451, 2663, doi: 10.1093/mnras/stv705

Higuchi, R., Ouchi, M., Ono, Y., et al. 2019, The Astrophysical Journal, 879, 28, doi: 10.3847/1538-4357/ab2192

Hildebrandt, H., Pielorz, J., Erben, T., et al. 2009, Astronomy and Astrophysics, 498, 725, doi: 10.1051/0004-6361/200811042

Hogg, D. W. 1999, 1, 1. https://arxiv.org/abs/9905116

Hopkins, P. F., Hernquist, L., Cox, T. J., & Kereš, D. 2008, The Astrophysical Journal Supplement Series, 175, 356, doi: 10.1086/524362

Hough, T., Gurung-López, S., Orsi, Á., et al. 2020, Monthly Notices of the Royal Astronomical Society, 499, 2104, doi: 10.1093/mnras/staa3027

Hsieh, B.-C., Wang, W.-H., Hsieh, C.-C., et al. 2012, The Astrophysical Journal Supplement Series, 203, 23, doi: 10.1088/0067-0049/203/2/23

Hubble, E. 1929, Proceedings of the National Academy of Sciences, 15, 168, doi: 10.1073/pnas.15.3.168

Ilbert, O., Capak, P., Salvato, M., et al. 2009, The Astrophysical Journal, 690, 1236, doi: 10.1088/0004-637X/690/2/1236

Ilbert, O., McCracken, H. J., Le Fèvre, O., et al. 2013, Astronomy and Astrophysics, 556, A55, doi: 10.1051/0004-6361/201321100

Inoue, A. K. 2011, Monthly Notices of the Royal Astronomical Society, 415, 2920, doi: 10.1111/j.1365-2966.2011.18906.x

Inoue, A. K., Hasegawa, K., Ishiyama, T., et al. 2018, Publications of the Astronomical Society of Japan, 70, 55, doi: 10.1093/pasj/psy048

Inoue, A. K., Yamanaka, S., Ouchi, M., et al. 2020, Publications of the Astronomical Society of Japan, 72, 1, doi: 10.1093/pasj/psaa100

Ishikawa, S., Kashikawa, N., Toshikawa, J., & Onoue, M. 2015, Monthly Notices of the Royal Astronomical Society, 454, 205, doi: 10.1093/mnras/stv1927

Ishikawa, S., Kashikawa, N., Toshikawa, J., et al. 2017, The Astrophysical Journal, 841, 8, doi: 10.3847/1538-4357/aa6d64

Ito, K., Kashikawa, N., Toshikawa, J., et al. 2019, The Astrophysical Journal, 878, 68, doi: 10.3847/1538-4357/ab1f0c

—. 2020, The Astrophysical Journal, 899, 5, doi: 10.3847/1538-4357/aba269

Ito, K., Kashikawa, N., Tanaka, M., et al. 2021, The Astrophysical Journal, 916, 35, doi: 10.3847/1538-4357/abfc50

Ivezić, Ž., Kahn, S. M., Tyson, J. A., et al. 2019, The Astrophysical Journal, 873, 111, doi: 10.3847/1538-4357/ab042c

Iyer, K., Gawiser, E., Davé, R., et al. 2018, The Astrophysical Journal, 866, 120, doi: 10.3847/1538-4357/aae0fa

Izumi, T., Matsuoka, Y., Fujimoto, S., et al. 2021, The Astrophysical Journal, 914, 36, doi: 10.3847/1538-4357/abf6dc

Jiang, L., Wu, J., Bian, F., et al. 2018, Nature Astronomy, 2, 962, doi: 10.1038/s41550-018-0587-9

Jones, M. C. 1993, Statistics and Computing, 3, 135, doi: 10.1007/BF00147776

Jurić, M., Kantor, J., Lim, K.-T., et al. 2015. https://arxiv.org/abs/1512.07914

Kalberla, P. M. W., Burton, W. B., Hartmann, D., et al. 2005, Astronomy and Astrophysics, 440, 775, doi: 10.1051/0004-6361:20041864

Kalita, B. S., Daddi, E., D'Eugenio, C., et al. 2021, The Astrophysical Journal Letters, 917, L17, doi: 10.3847/2041-8213/ac16dc

Kawanomoto, S., Uraguchi, F., Komiyama, Y., et al. 2018, Publications of the Astronomical Society of Japan, 70, 1, doi: 10.1093/pasj/psy056

Kawinwanichakij, L., Papovich, C., Quadri, R. F., et al. 2017, The Astrophysical Journal, 847, 134, doi: 10.3847/1538-4357/aa8b75

Kennicutt, R. C. 1998, Annual Review of Astronomy and Astrophysics, 36, 189, doi: 10.1146/annurev.astro.36.1.189

Khostovan, A. A., Sobral, D., Mobasher, B., et al. 2019, Monthly Notices of the Royal Astronomical Society, 489, 555, doi: 10.1093/mnras/stz2149

Kodama, T., Hayashi, M., Koyama, Y., et al. 2012, Proceedings of the International Astronomical Union, 8, 74, doi: 10.1017/S1743921313004353

Komiyama, Y., Obuchi, Y., Nakaya, H., et al. 2018, Publications of the Astronomical Society of Japan, 70, 1, doi: 10.1093/pasj/psx069

Konno, A., Ouchi, M., Nakajima, K., et al. 2016, The Astrophysical Journal, 823, 20, doi: 10.3847/0004-637x/823/1/20

Kovač, K., Lilly, S. J., Knobel, C., et al. 2010, The Astrophysical Journal, 718, 86, doi: 10.1088/0004-637X/718/1/86

Koyama, Y., Kodama, T., Tadaki, K. I., et al. 2013, Monthly Notices of the Royal Astronomical Society, 428, 1551, doi: 10.1093/mnras/sts133

Koyama, Y., Polletta, M. D. C., Tanaka, I., et al. 2021, Monthly Notices of the Royal Astronomical Society: Letters, 503, L1, doi: 10.1093/mnrasl/slab013

Kriek, M., van Dokkum, P. G., Labbé, I., et al. 2009, The Astrophysical Journal, 700, 221, doi: 10.1088/0004-637X/700/1/221

Krishnan, C., Hatch, N. A., Almaini, O., et al. 2017, Monthly Notices of the Royal Astronomical Society, 470, 2170, doi: 10.1093/mnras/stx1315

Kubo, M., Tanaka, M., Yabe, K., et al. 2018, The Astrophysical Journal, 867, 1, doi: 10.3847/1538-4357/aae3e8

Kubo, M., Uchimoto, Y. K., Yamada, T., et al. 2013, The Astrophysical Journal, 778, 170, doi: 10.1088/0004-637X/778/2/170

Kubo, M., Toshikawa, J., Kashikawa, N., et al. 2019, The Astrophysical Journal, 887, 214, doi: 10.3847/1538-4357/ab5a80

Kubo, M., Umehata, H., Matsuda, Y., et al. 2021, The Astrophysical Journal, 919, 6, doi: 10.3847/1538-4357/ac0cf8

Kusakabe, H., Shimasaku, K., Nakajima, K., & Ouchi, M. 2015, The Astrophysical Journal, 800, L29, doi: 10.1088/2041-8205/800/2/L29

Kusakabe, H., Shimasaku, K., Ouchi, M., et al. 2018, Publications of the Astronomical Society of Japan, 70, 1, doi: 10.1093/pasj/psx148

Laigle, C., McCracken, H. J., Ilbert, O., et al. 2016, The Astrophysical Journal Supplement Series, 224, 24, doi: 10.3847/0067-0049/224/2/24

Landy, S. D., & Szalay, A. S. 1993, The Astrophysical Journal, 412, 64, doi: 10.1086/172900

Lawrence, A., Warren, S. J., Almaini, O., et al. 2007, Monthly Notices of the Royal Astronomical Society, 379, 1599, doi: 10.1111/j.1365-2966.2007.12040.x

Le Fèvre, O., Deltorn, J. M., Crampton, D., & Dickinson, M. 1996, The Astrophysical Journal, 471, L11, doi: 10.1086/310319

Le Floc'h, E., Aussel, H., Ilbert, O., et al. 2009, The Astrophysical Journal, 703, 222, doi: 10.1088/0004-637X/703/1/222

Lee, K.-G., Hennawi, J. F., White, M., Croft, R. A. C., & Ozbek, M. 2014, The Astrophysical Journal, 788, 49, doi: 10.1088/0004-637X/788/1/49

Lee, K.-G., Hennawi, J. F., White, M., et al. 2016, The Astrophysical Journal, 817, 160, doi: 10.3847/0004-637x/817/2/160

Lehmer, B. D., Alexander, D. M., Bauer, F. E., et al. 2010, The Astrophysical Journal, 724, 559, doi: 10.1088/0004-637X/724/1/559

Lehmer, B. D., Alexander, D. M., Geach, J. E., et al. 2009, The Astrophysical Journal, 691, 687, doi: 10.1088/0004-637X/691/1/687

Lehmer, B. D., Basu-Zych, A. R., Mineo, S., et al. 2016, The Astrophysical Journal, 825, 7, doi: 10.3847/0004-637x/825/1/7

Lemaux, B. C., Le Fèvre, O., Cucciati, O., et al. 2018, Astronomy and Astrophysics, 615, A77, doi: 10.1051/0004-6361/201730870

Lemaux, B. C., Cucciati, O., Fèvre, O. L., et al. 2020, arxiv. https://arxiv.org/abs/2009.03324

Leslie, S. K., Schinnerer, E., Liu, D., et al. 2020, The Astrophysical Journal, 899, 58, doi: 10.3847/1538-4357/aba044

Lewis, I., Balogh, M., De Propris, R., et al. 2002, Monthly Notices of the Royal Astronomical Society, 334, 673, doi: 10.1046/j.1365-8711.2002.05558.x

Liang, Y., Kashikawa, N., Cai, Z., et al. 2021, The Astrophysical Journal, 907, 3, doi: 10.3847/1538-4357/abcd93

Lidman, C., Suherli, J., Muzzin, A., et al. 2012, Monthly Notices of the Royal Astronomical Society, 427, 550, doi: 10.1111/j.1365-2966.2012.21984.x

Lin, L., Capak, P. L., Laigle, C., et al. 2016, The Astrophysical Journal, 817, 97, doi: 10.3847/0004-637x/817/2/97

Lin, Y.-T., Hsieh, B.-C., Lin, S.-C., et al. 2017, The Astrophysical Journal, 851, 139, doi: 10.3847/1538-4357/aa9bf5

Long, A. S., Cooray, A., Ma, J., et al. 2020, The Astrophysical Journal, 898, 133, doi: 10.3847/1538-4357/ab9d1f

Lovell, C. C., Thomas, P. A., & Wilkins, S. M. 2018, Monthly Notices of the Royal Astronomical Society, 474, 4612, doi: 10.1093/mnras/stx3090

Lovell, C. C., Vijayan, A. P., Thomas, P. A., et al. 2020, Monthly Notices of the Royal Astronomical Society, 500, 2127, doi: 10.1093/mnras/staa3360

Lusso, E., Comastri, A., Simmons, B. D., et al. 2012, Monthly Notices of the Royal Astronomical Society, 425, 623, doi: 10.1111/j.1365-2966.2012.21513.x

Macuga, M., Martini, P., Miller, E. D., et al. 2019, The Astrophysical Journal, 874, 54, doi: 10.3847/1538-4357/ab0746

Madau, P., & Dickinson, M. 2014, Annual Review of Astronomy and Astrophysics, 52, 415, doi: 10.1146/annurev-astro-081811-125615

Magdis, G. E., Gobat, R., Valentino, F., et al. 2021, Astronomy and Astrophysics, 647, A33, doi: 10.1051/0004-6361/202039280

Magnelli, B., Elbaz, D., Chary, R. R., et al. 2011, Astronomy and Astrophysics, 528, A35, doi: 10.1051/0004-6361/200913941

Magnelli, B., Popesso, P., Berta, S., et al. 2013, Astronomy and Astrophysics, 553, A132, doi: 10.1051/0004-6361/201321371

Magnelli, B., Ivison, R. J., Lutz, D., et al. 2015, Astronomy and Astrophysics, 573, 45, doi: 10.1051/0004-6361/201424937

Maiolino, R., Gallerani, S., Neri, R., et al. 2012, Monthly Notices of the Royal Astronomical Society: Letters, 425, L66, doi: 10.1111/j.1745-3933.2012.01303.x

Man, A. W. S., Greve, T. R., Toft, S., et al. 2016, The Astrophysical Journal, 820, 11, doi: 10.3847/0004-637x/820/1/11

Marchesi, S., Civano, F., Elvis, M., et al. 2016a, The Astrophysical Journal, 817, 34, doi: 10.3847/0004-637x/817/1/34

Marchesi, S., Lanzuisi, G., Civano, F., et al. 2016b, The Astrophysical Journal, 830, 100, doi: 10.3847/0004-637x/830/2/100

Marchesi, S., Gilli, R., Lanzuisi, G., et al. 2020, Astronomy and Astrophysics, 642, A184, doi: 10.1051/0004-6361/202038622

Marrone, D. P., Spilker, J. S., Hayward, C. C., et al. 2018, Nature, 553, 51, doi: 10.1038/nature24629

Marsan, Z. C., Marchesini, D., Brammer, G. B., et al. 2015, The Astrophysical Journal, 801, 133, doi: 10.1088/0004-637X/801/2/133

Martig, M., Bournaud, F., Teyssier, R., & Dekel, A. 2009, The Astrophysical Journal, 707, 250, doi: 10.1088/0004-637X/707/1/250

Mawatari, K., Inoue, A. K., Hashimoto, T., et al. 2020, The Astrophysical Journal, 889, 137, doi: 10.3847/1538-4357/ab6596

McConachie, I., Wilson, G., Forrest, B., et al. 2021. https://arxiv.org/abs/2109.07696

McCracken, H. J., Capak, P., Salvato, M., et al. 2010, The Astrophysical Journal, 708, 202, doi: 10.1088/0004-637X/708/1/202

McCracken, H. J., Milvang-Jensen, B., Dunlop, J., et al. 2012, Astronomy and Astrophysics, 544, A156, doi: 10.1051/0004-6361/201219507

McCracken, H. J., Wolk, M., Colombi, S., et al. 2015, Monthly Notices of the Royal Astronomical Society, 449, 901, doi: 10.1093/mnras/stv305

Meiksin, A. 2006, Monthly Notices of the Royal Astronomical Society, 365, 807, doi: 10.1111/j.1365-2966.2005.09756.x

Merlin, E., Fontana, A., Castellano, M., et al. 2018, Monthly Notices of the Royal Astronomical Society, 473, 2098, doi: 10.1093/MNRAS/STX2385

Merlin, E., Fortuni, F., Torelli, M., et al. 2019, Monthly Notices of the Royal Astronomical Society, 490, 3309, doi: 10.1093/mnras/stz2615

Merloni, A., Heinz, S., & Di Matteo, T. 2003, Monthly Notices of the Royal Astronomical Society, 345, 1057, doi: 10.1046/j.1365-2966.2003.07017.x

Meurer, G. R., Heckman, T. M., & Calzetti, D. 1999, The Astrophysical Journal, 521, 64, doi: 10.1086/307523

Miley, G. K., Overzier, R. A., Tsvetanov, Z. I., et al. 2004, Nature, 427, 47, doi: 10.1038/nature02125

Miller, T. B., Chapman, S. C., Aravena, M., et al. 2018, Nature, 556, 469, doi: 10.1038/s41586-018-0025-2

Mitsuhashi, I., Matsuda, Y., Smail, I., et al. 2021, The Astrophysical Journal, 907, 122, doi: 10.3847/1538-4357/abcc72

Miyaji, T., Griffiths, R., & C-COSMOS Team. 2008, in AAS/High Energy Astrophysics Division #10, Vol. 10, #04.01. https://ui.adsabs.harvard.edu/abs/2008HEAD...10.0401M/abstract

Miyaji, T., Hasinger, G., Salvato, M., et al. 2015, The Astrophysical Journal, 804, 104, doi: 10.1088/0004-637X/804/2/104

Momose, R., Shimasaku, K., Nagamine, K., et al. 2021a, The Astrophysical Journal Letters, 912, L24, doi: 10.3847/2041-8213/abf04c

—. 2021b, The Astrophysical Journal Letters, 912, L24, doi: 10.3847/2041-8213/abf04c

Momose, R., Ouchi, M., Nakajima, K., et al. 2014, Monthly Notices of the Royal Astronomical Society, 442, 110, doi: 10.1093/mnras/stu825

Momose, R., Shimasaku, K., Kashikawa, N., et al. 2021c, The Astrophysical Journal, 909, 117, doi: 10.3847/1538-4357/abd2af

Moneti, A., McCracken, H. J., Shuntov, M., et al. 2021, 1. https://arxiv.org/abs/2110.13928

Mortlock, A., Conselice, C. J., Hartley, W. G., et al. 2015, Monthly Notices of the Royal Astronomical Society, 447, 2, doi: 10.1093/mnras/stu2403

Mukai, K. 1993, Legacy, 3, 21

Muldrew, S. I., Hatch, N. A., & Cooke, E. A. 2015, Monthly Notices of the Royal Astronomical Society, 452, 2528, doi: 10.1093/mnras/stv1449

Muzzin, A., Wilson, G., Yee, H. K. C., et al. 2009, The Astrophysical Journal, 698, 1934, doi: 10.1088/0004-637X/698/2/1934

Muzzin, A., Marchesini, D., Stefanon, M., et al. 2013, The Astrophysical Journal, 777, 18, doi: 10.1088/0004-637X/777/1/18

Naab, T., Johansson, P. H., & Ostriker, J. P. 2009, The Astrophysical Journal, 699, L178, doi: 10.1088/0004-637X/699/2/L178

Nakajima, K., Ouchi, M., Shimasaku, K., et al. 2012, The Astrophysical Journal, 745, 12, doi: 10.1088/0004-637X/745/1/12

Nantais, J. B., van der Burg, R. F. J., Lidman, C., et al. 2016, Astronomy and Astrophysics, 592, A161, doi: 10.1051/0004-6361/201628663

Nantais, J. B., Muzzin, A., van der Burg, R. F. J., et al. 2017, Monthly Notices of the Royal Astronomical Society: Letters, 465, L104, doi: 10.1093/mnrasl/slw224

Newman, A. B., Ellis, R. S., Andreon, S., et al. 2014, The Astrophysical Journal, 788, 51, doi: 10.1088/0004-637X/788/1/51

Oguri, M., Lin, Y. T., Lin, S. C., et al. 2018, Publications of the Astronomical Society of Japan, 70, 1, doi: 10.1093/pasj/psx042

Oke, J. B., & Gunn, J. E. 1983, The Astrophysical Journal, 266, 713, doi: 10.1086/160817

Olsen, K. P., Rasmussen, J., Toft, S., & Zirm, A. W. 2013, The Astrophysical Journal, 764, 4, doi: 10.1088/0004-637X/764/1/4

Ono, Y., Ouchi, M., Harikane, Y., et al. 2018, Publications of the Astronomical Society of Japan, 70, 2, doi: 10.1093/pasj/psx103

Onoue, M., Kashikawa, N., Uchiyama, H., et al. 2018, Publications of the Astronomical Society of Japan, 70, 1, doi: 10.1093/pasj/psx092

Oteo, I., Sobral, D., Ivison, R. J., et al. 2015, Monthly Notices of the Royal Astronomical Society, 452, 2018, doi: 10.1093/mnras/stv1284

Oteo, I., Ivison, R. J., Dunne, L., et al. 2018, The Astrophysical Journal, 856, 72, doi: 10.3847/1538-4357/aaa1f1

Ouchi, M., Shimasaku, K., Akiyama, M., et al. 2005, The Discovery of Primeval Large-Scale Structures with Forming Clusters at Redshift 6, Tech. Rep. 1, doi: 10.1086/428499

Ouchi, M., Harikane, Y., Shibuya, T., et al. 2018, Publications of the Astronomical Society of Japan, 70, 13, doi: 10.1093/pasj/psx074

Overzier, R., & Kashikawa, N. 2019, Astro2020 Science White Paper, 1. https://arxiv.org/abs/1903.04980

Overzier, R. A. 2016, The Astronomy and Astrophysics Review, 24, 14, doi: 10.1007/s00159-016-0100-3

Overzier, R. A., Bouwens, R. J., Cross, N. J. G., et al. 2008, The Astrophysical Journal, 673, 143

Peebles, P. 1980, The large-scale structure of the universe

Peng, C. Y., Ho, L. C., Impey, C. D., & Rix, H. W. 2010a, The Astronomical Journal, 139, 2097, doi: 10.1088/0004-6256/139/6/2097

Peng, Y.-j., Lilly, S. J., Kovač, K., et al. 2010b, The Astrophysical Journal, 721, 193, doi: 10.1088/0004-637X/721/1/193

Pozzetti, L., Bolzonella, M., Zucca, E., et al. 2010, Astronomy and Astrophysics, 523, A13, doi: 10.1051/0004-6361/200913020

Reddy, N. A., & Steidel, C. C. 2009, The Astrophysical Journal, 692, 778, doi: 10.1088/0004-637X/692/1/778

Reeves, A. M. M., Balogh, M. L., van der Burg, R. F. J., et al. 2021, Monthly Notices of the Royal Astronomical Society, 21, 1, doi: 10.1093/mnras/stab1955

Ricci, C., Trakhtenbrot, B., Koss, M. J., et al. 2017, The Astrophysical Journal Supplement Series, 233, 17, doi: 10.3847/1538-4365/aa96ad

Roche, N., & Eales, S. A. 1999, Monthly Notices of the Royal Astronomical Society, 307, 703, doi: 10.1046/j.1365-8711.1999.02652.x

Rowe, B. T., Jarvis, M., Mandelbaum, R., et al. 2015, Astronomy and Computing, 10, 121, doi: 10.1016/J.ASCOM.2015.02.002

Salpeter, E. E. 1955, The Astrophysical Journal, 121, 161, doi: 10.1086/145971

Santos, S., Sobral, D., Matthee, J., et al. 2020, Monthly Notices of the Royal Astronomical Society, 493, 141, doi: 10.1093/mnras/staa093

Saracco, P., Marchesini, D., Barbera, F. L., et al. 2020, The Astrophysical Journal, 905, 40, doi: 10.3847/1538-4357/abc7c4

Sawicki, M., Arnouts, S., Huang, J., et al. 2019, Monthly Notices of the Royal Astronomical Society, 489, 5202, doi: 10.1093/mnras/stz2522

Schechter, P., & Press, W. H. 1976, The Astrophysical Journal, 203, 557, doi: 10.1086/154112

Schinnerer, E., Smolčić, V., Carilli, C. L., et al. 2007, The Astrophysical Journal Supplement Series, 172, 46, doi: 10.1086/516587

Schlegel, D. J., Finkbeiner, D. P., & Davis, M. 1998, The Astrophysical Journal, 500, 525, doi: 10.2478/dema-2014-0019

Schombert, J. M. 1986, The Astrophysical Journal Supplement Series, 60, 603, doi: 10.1086/191100

Schreiber, C., Pannella, M., Elbaz, D., et al. 2015, Astronomy and Astrophysics, 575, A74, doi: 10.1051/0004-6361/201425017

Schreiber, C., Glazebrook, K., Nanayakkara, T., et al. 2018, Astronomy and Astrophysics, 618, A85, doi: 10.1051/0004-6361/201833070

Scoville, N., Abraham, R. G., Aussel, H., et al. 2007, The Astrophysical Journal Supplement Series, 172, 38, doi: 10.1086/516580

Sérsic, J. L. 1963, Influence of the atmospheric and instrumental dispersion on the brightness distribution in a galaxy

She, R., Ho, L. C., & Feng, H. 2017, The Astrophysical Journal, 842, 131, doi: 10.3847/1538-4357/aa7634

Shi, D. D., Cai, Z., Fan, X., et al. 2021, The Astrophysical Journal, 915, 32, doi: 10.3847/1538-4357/abfec0

Shi, K., Toshikawa, J., Cai, Z., Lee, K.-S., & Fang, T. 2020, The Astrophysical Journal, 899, 79, doi: 10.3847/1538-4357/aba626

Shi, K., Huang, Y., Lee, K.-S., et al. 2019a, The Astrophysical Journal, 879, 9, doi: 10.3847/1538-4357/ab2118

Shi, K., Lee, K.-S., Dey, A., et al. 2019b, The Astrophysical Journal, 871, 83, doi: 10.3847/1538-4357/aaf85d

Shibuya, T., Ouchi, M., & Harikane, Y. 2015, The Astrophysical Journal Supplement Series, 219, 15, doi: 10.1088/0067-0049/219/2/15

Shimakawa, R., Kodama, T., Hayashi, M., et al. 2017, Monthly Notices of the Royal Astronomical Society: Letters, 468, L21, doi: 10.1093/mnrasl/slx019

—. 2018, Monthly Notices of the Royal Astronomical Society, 473, 1977, doi: 10.1093/mnras/stx2494

Shimasaku, K., Ouchi, M., Okamura, S., et al. 2003, The Astrophysical Journal, 586, L111, doi: 10.1086/374880

Shimasaku, K., Kashikawa, N., Doi, M., et al. 2006, Publications of the Astronomical Society of Japan, 58, 313, doi: 10.1093/pasj/58.2.313

Silk, J., & Rees, M. J. 1998, Astronomy and Astrophysics, 331, L1, doi: 10.1046/j.1365-8711.2001.04259.x

Smail, I., Ivison, R. J., & Blain, A. W. 1997, The Astrophysical Journal, 490, L5, doi: 10.1086/311017

Smolčić, V., Novak, M., Bondi, M., et al. 2017, Astronomy and Astrophysics, 602, A1, doi: 10.1051/0004-6361/201628704

Sobral, D., Santos, S., Matthee, J., et al. 2018, Monthly Notices of the Royal Astronomical Society, 476, 4725, doi: 10.1093/mnras/sty378

Sobral, D., Smail, I., Best, P. N., et al. 2013, Monthly Notices of the Royal Astronomical Society, 428, 1128, doi: 10.1093/mnras/sts096

Sobral, D., Matthee, J., Best, P., et al. 2017, Monthly Notices of the Royal Astronomical Society, 466, 1242, doi: 10.1093/mnras/stw3090

Sohn, J., Geller, M. J., Rines, K. J., et al. 2018, The Astrophysical Journal, 856, 172, doi: 10.3847/1538-4357/aab20b

Song, M., Finkelstein, S. L., Ashby, M. L. N., et al. 2016, The Astrophysical Journal, 825, 5, doi: 10.3847/0004-637x/825/1/5

Speagle, J. S., Steinhardt, C. L., Capak, P. L., & Silverman, J. D. 2014, The Astrophysical Journal Supplement Series, 214, 15, doi: 10.1088/0067-0049/214/2/15

Springel, V., White, S. D., Jenkins, A., et al. 2005, Nature, 435, 629, doi: 10.1038/nature03597

Steidel, C. C., Adelberger, K. L., Dickinson, M., et al. 1998, The Astrophysical Journal, 492, 428, doi: 10.1086/305073

Steidel, C. C., Adelberger, K. L., Shapley, A. E., et al. 2005, The Astrophysical Journal, 626, 44, doi: 10.1086/429989

—. 2000, The Astrophysical Journal, 532, 170, doi: 10.1086/308568

Steidel, C. C., Giavalisco, M., Pettini, M., Dickinson, M., & Adelberger, K. L. 1996, The Astrophysical Journal Letters, 462, L17

Stockmann, M., Toft, S., Gallazzi, A., et al. 2020, The Astrophysical Journal, 888, 4, doi: 10.3847/1538-4357/ab5af4

Straatman, C. M. S., Labbé, I., Spitler, L. R., et al. 2014, The Astrophysical Journal, 783, L14, doi: 10.1088/2041-8205/783/1/L14

Strazzullo, V., Gobat, R., Daddi, E., et al. 2013, The Astrophysical Journal, 772, 118, doi: 10.1088/0004-637X/772/2/118

Strazzullo, V., Pannella, M., Mohr, J. J., et al. 2019, Astronomy and Astrophysics, 622, A117, doi: 10.1051/0004-6361/201833944

Suchyta, E., Huff, E. M., Aleksić, J., et al. 2016, Monthly Notices of the Royal Astronomical Society, 457, 786, doi: 10.1093/mnras/stv2953

Suzuki, T. L., Kodama, T., Tadaki, K.-i., et al. 2015, The Astrophysical Journal, 806, 208, doi: 10.1088/0004-637X/806/2/208

Tacconi, L. J., Genzel, R., Smail, I., et al. 2008, The Astrophysical Journal, 680, 246, doi: 10.1086/587168

Tanaka, M. 2015, The Astrophysical Journal, 801, 20, doi: 10.1088/0004-637X/801/1/20

Tanaka, M., Valentino, F., Toft, S., et al. 2019, The Astrophysical Journal, 885, L34, doi: 10.3847/2041-8213/ab4ff3

Taniguchi, Y., Scoville, N., Murayama, T., et al. 2007, The Astrophysical Journal Supplement Series, 172, 9, doi: 10.1086/516596

Taniguchi, Y., Kajisawa, M., Kobayashi, M. A., et al. 2015, Publications of the Astronomical Society of Japan, 67, 104, doi: 10.1093/pasj/psv106

Tejos, N., Morris, S. L., Finn, C. W., et al. 2014, Monthly Notices of the Royal Astronomical Society, 437, 2017, doi: 10.1093/mnras/stt1844

Thomas, D., Maraston, C., Bender, R., & Mendes de Oliveira, C. 2005, The Astrophysical Journal, 621, 673, doi: 10.1023/A:1019504712938

Tinker, J. L., Robertson, B. E., Kravtsov, A. V., et al. 2010, The Astrophysical Journal, 724, 878, doi: 10.1088/0004-637X/724/2/878

Toft, S., Smolčić, V., Magnelli, B., et al. 2014, The Astrophysical Journal, 782, 68, doi: 10.1088/0004-637X/782/2/68

Tomczak, A. R., Quadri, R. F., Tran, K.-V. H., et al. 2016, The Astrophysical Journal, 817, 118, doi: 10.3847/0004-637X/817/2/118

Tomczak, A. R., Lemaux, B. C., Lubin, L. M., et al. 2017, Monthly Notices of the Royal Astronomical Society, 472, 3512, doi: 10.1093/MNRAS/STX2245

Toshikawa, J., Malkan, M. A., Kashikawa, N., et al. 2020, The Astrophysical Journal, 888, 89, doi: 10.3847/1538-4357/ab5e85

Toshikawa, J., Kashikawa, N., Ota, K., et al. 2012, The Astrophysical Journal, 750, 137, doi: 10.1088/0004-637X/750/2/137

Toshikawa, J., Kashikawa, N., Overzier, R., et al. 2016, The Astrophysical Journal, 826, 114, doi: 10.3847/0004-637x/826/2/114

Toshikawa, J., Uchiyama, H., Kashikawa, N., et al. 2018, Publications of the Astronomical Society of Japan, 70, 1, doi: 10.1093/pasj/psx102

Trebitsch, M., Dubois, Y., Volonteri, M., et al. 2021, Astronomy and Astrophysics, 653, A154, doi: 10.1051/0004-6361/202037698

Uchiyama, H., Toshikawa, J., Kashikawa, N., et al. 2018, Publications of the Astronomical Society of Japan, 70, 1, doi: 10.1093/pasj/psx112

Uchiyama, H., Akiyama, M., Toshikawa, J., et al. 2020, The Astrophysical Journal, 905, 125, doi: 10.3847/1538-4357/abc47b

Ueda, Y., Akiyama, M., Hasinger, G., Miyaji, T., & Watson, M. G. 2014, The Astrophysical Journal, 786, 104, doi: 10.1088/0004-637X/786/2/104

Umehata, H., Hatsukade, B., Smail, I., et al. 2018, Publications of the Astronomical Society of Japan, 70, doi: 10.1093/pasj/psy065

Umehata, H., Fumagalli, M., Smail, I., et al. 2019, Science, 366, 97, doi: 10.1126/science.aaw5949

Utsumi, Y., Goto, T., Kashikawa, N., et al. 2010, The Astrophysical Journal, 721, 1680, doi: 10.1088/0004-637X/721/2/1680

Valentino, F., Tanaka, M., Davidzon, I., et al. 2020, The Astrophysical Journal, 889, 93, doi: 10.3847/1538-4357/ab64dc

van der Burg, R. F. J., Hildebrandt, H., & Erben, T. 2010, Astronomy and Astrophysics, 523, A74, doi: 10.1051/0004-6361/200913812

van der Burg, R. F. J., McGee, S., Aussel, H., et al. 2018, Astronomy and Astrophysics, 618, A140, doi: 10.1051/0004-6361/201833572

van der Burg, R. F. J., Muzzin, A., Hoekstra, H., et al. 2013, Astronomy and Astrophysics, 557, A15, doi: 10.1051/0004-6361/201321237

van der Burg, R. F. J., Rudnick, G., Balogh, M. L., et al. 2020, Astronomy and Astrophysics, 638, A112, doi: 10.1051/0004-6361/202037754

Venemans, B. P., Kurk, J. D., Miley, G. K., et al. 2002, The Astrophysical Journal, 569, L11, doi: 10.1086/340563

Venemans, B. P., Röttgering, H. J. A., Miley, G. K., et al. 2007, Astronomy and Astrophysics, 461, 823, doi: 10.1051/0004-6361:20053941

Vulcani, B., Poggianti, B. M., Oemler, A., et al. 2013, Astronomy and Astrophysics, 550, A58, doi: 10.1051/0004-6361/201118388

Weaver, J. R., Kauffmann, O. B., Ilbert, O., et al. 2021, arXiv e-prints, arXiv:2110.13923. https://arxiv.org/abs/2110.13923

Wetzel, A. R., Tinker, J. L., & Conroy, C. 2012, Monthly Notices of the Royal Astronomical Society, 424, 232, doi: 10.1111/j.1365-2966.2012.21188.x

Whitaker, K. E., Williams, C. C., Mowla, L., et al. 2021, Nature, 597, 485, doi: 10.1038/s41586-021-03806-7

Wilson, G., Muzzin, A., Yee, H. K. C., et al. 2009, The Astrophysical Journal, 698, 1943, doi: 10.1088/0004-637X/698/2/1943

Wuyts, S., Labbe, I., Franx, M., et al. 2007, The Astrophysical Journal, 655, 51, doi: 10.1086/509708

Wylezalek, D., Galametz, A., Stern, D., et al. 2013, The Astrophysical Journal, 769, 79, doi: 10.1088/0004-637X/769/1/79

Yajima, H., Abe, M., Khochfar, S., et al. 2021, Monthly Notices of the Royal Astronomical Society, 509, 4037, doi: 10.1093/mnras/stab3092

Yang, G., Brandt, W. N., Vito, F., et al. 2018, Monthly Notices of the Royal Astronomical Society, 475, 1887, doi: 10.1093/mnras/stx2805

Yonekura, N., Kajisawa, M., Hamaguchi, E., Mawatari, K., & Yamada, T. 2021. https://arxiv.org/abs/2109.02019

York, D. G., Adelman, J., Anderson, Jr., J. E., et al. 2000, The Astronomical Journal, 120, 1579, doi: 10.1086/301513

Yoshida, M., Shimasaku, K., Kashikawa, N., et al. 2006, The Astrophysical Journal, 653, 988

Yun, M. S., Scott, K. S., Guo, Y., et al. 2012, Monthly Notices of the Royal Astronomical Society, 420, 957, doi: 10.1111/j.1365-2966.2011.19898.x

Zamojski, M. A., Schiminovich, D., Rich, R. M., et al. 2007, The Astrophysical Journal Supplement Series, 172, 468, doi: 10.1086/516593

Zavala, J. A., Casey, C. M., Scoville, N., et al. 2019, The Astrophysical Journal, 887, 183, doi: 10.3847/1538-4357/ab5302

Zavala, J. A., Casey, C. M., Manning, S. M., et al. 2021, The Astrophysical Journal, 909, 165, doi: 10.3847/1538-4357/abdb27

Zehavi, I., Contreras, S., Padilla, N., et al. 2018, The Astrophysical Journal, 853, 84, doi: 10.3847/1538-4357/aaa54a

Zhao, D., Aragón-Salamanca, A., & Conselice, C. J. 2015, Monthly Notices of the Royal Astronomical Society, 453, 4444, doi: 10.1093/mnras/stv1940

A

Appendix for Chapter 2

A.1 Impact of photometric uncertainty on the shape of PC UVLF

Here, we examine the effect of the photometric uncertainty on the shape of the UVLF.

We first check the uncertainty of the PC UVLF due to the photometric uncertainty. For each galaxy, we generate mock $M_{\rm UV}$ by adding Gaussian noise whose 1σ corresponds to the observed photometric error to the observed magnitude. The PC UVLF is recalculated from this $M_{\rm UV}$ distribution with 1000 times iteration. The right panel of Figure A.1 shows the recalculated PC UVLF (called pseudo PC UVLF) compared with the original PC UVLF. These two UVLFs are consistent, so this implies that the uncertainty of the PC UVLF due to the photometric uncertainty is negligible.

We then assess the Eddington Bias. We first derive the difference between the original magnitude and that with artificially noise, estimated in the previous paragraph. Followed by the method in the previous works (e.g., Ilbert et al., 2013) which estimate

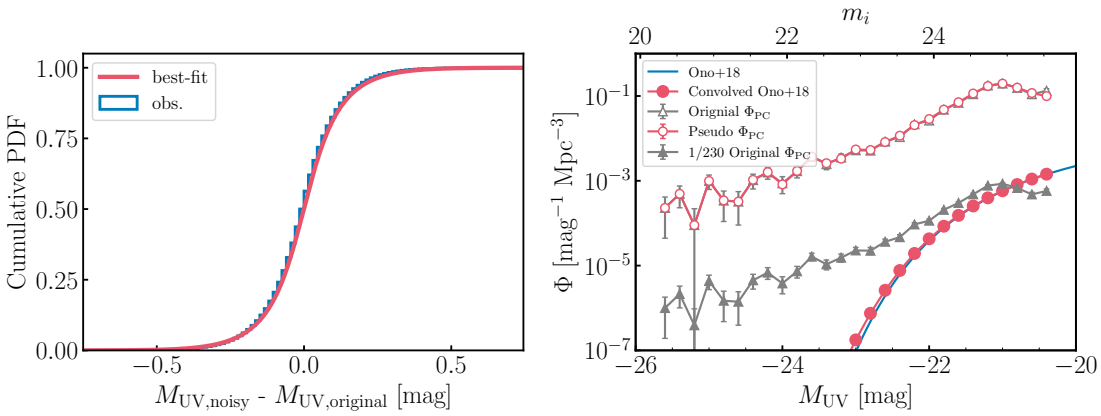

Figure A.1: Left panel: The distribution of the difference between the original magnitude and the noise added one, which is shown as blue histogram. The best-fit of the product of the Gaussian distribution and the Lorenzian distribution is shown in the red line. Right panel: The convolved (red filled circles) and original (blue line) field UVLF (Ono et al., 2018) and the shifted (gray triangles), pseudo (red open circles), and original (gray open triangles) PC UVLF in this work.

the effect of the Eddington Bias on the stellar mass function, the product of the Gaussian distribution $G(x) = \frac{1}{\sigma\sqrt{2\pi}} \exp\left(-\frac{1}{2}\frac{x^2}{\sigma^2}\right)$ and the Lorentzian distribution $L(x) = \frac{\tau}{2\pi}\frac{1}{\left(\frac{\tau}{2}\right)^2+x^2}$ is fitted to the magnitude difference distribution, which is shown in the left panel of Figure A.1, and we obtain the best-fit parameters (σ and τ). Convolving the observed field UVLF with the best-fit functions provides us how significant the Eddington bias is in our photometry quality. Here, we employ the best-fit Schechter function of the field UVLF obtained in Ono et al. (2018).

The right panel of Figure A.1 shows the convolved field UVLF. Compared with the original field UVLF, it has indeed slightly higher amplitude than the original one, but it has still steep shape than our estimated PC UVLF. This implies that our photometric quality does not make the bright-end excess seen in the PC UVLF from the field UVLF.

A.2 Robustness of UV slope-magnitude relation

To assess the robustness of our measurement of UV-slope β and the sample selection, we measure the β of field galaxies in the same manner as described in Section 2.4.3 to

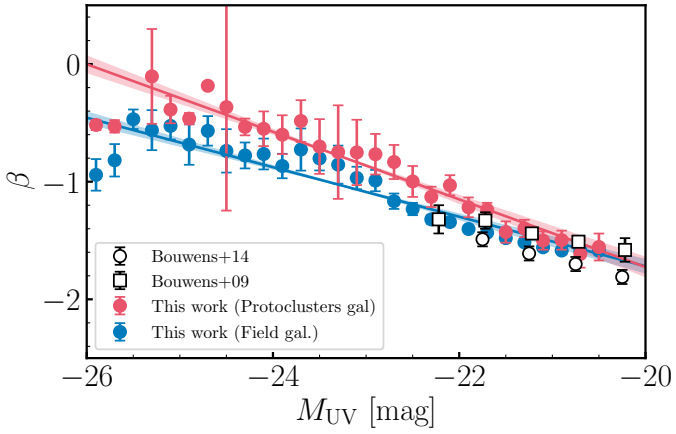

Figure A.2: $\beta - M_{\rm UV}$ relations estimated in this study. The red circles represent the median value of UV slope of protocluster galaxies and the red line represents its best-fit. The blue circles and the blue line represent those of field galaxies. The shaded regions of each best-fit lines represent their 1σ uncertainty. Relations from the literature (Bouwens et al., 2014, 2009) is also shown, our estimation for field galaxies is consistent with it, suggesting the robustness of our UV slope estimation.

compare it with the relation in the literature. The $\beta - M_{\rm UV}$ relation our field galaxies as well as in the literature (Bouwens et al., 2014, 2009) are shown in Figure A.2. Our $\beta - M_{\rm UV}$ relation for field galaxies is consistent with the literature at $-22.3 < M_{\rm UV} < -20.3$, suggesting that our measurement and sample selection is robust.

A.3 Completeness affected by a possible confusion limit in overdense regions

In Chapter 2, we focus on overdense regions of galaxies. In such regions, the image blending of galaxies might frequently occur due to the high local number density and this could lead an inaccurate photometry of galaxies. The blending also could decrease the sample completeness. This effect is closely related to the number density of galaxies that we focus on. Here, we examine how significantly the blending effect affect the photometry and the completeness by inserting mock galaxies into the image to make artificial overdense regions.

Firstly, we make a cut out image with $4' \times 4'$ of a overdense region whose overdensity peak is about 3σ. In Toshikawa et al. (2018), the average and the standard deviation of the number of bright ($m_i < 25$ mag) galaxies within $1'.8$ are 6.4 and 3.2, respectively. According to the field luminosity function of g-dropout galaxies (e.g., Ono et al., 2018), this implies that 1σ of the number density of galaxies with $25 < m_i < 26$ is about 1.8 $\mathrm{mag}^{-1}\mathrm{arcmin}^{-2}$. We make five artificial overdense region image by inserting mock galaxies to the cutout image so that their number densities are equivalent to 1.8, 3.6, 5.4, 7.2, and 9.0 $\mathrm{arcmin}^{-2}\mathrm{mag}^{-1}$, corresponding to the overdensity significance of 4σ, 5σ, 6σ, 7σ, and 8σ, respectively, which is the same overdensity range of our protocluster sample. The morphological and physical properties of mock galaxies are the same as that we did in estimating the completeness in Section 2.3.3. We fix the redshift as $z = 3.8$ since we only aim to see the difference induced by the number density of galaxies in the field. The detection and measurement process are also the same as that described in Section 2.3.3.

We compare the output magnitude of the detected objects from `hscpipe` to the input magnitude of mock galaxies in Figure A.3. The magnitude difference between the input and output magnitude are consistent at any overdensities. The peak difference between the input and the output magnitude is lower than the photometric error, suggesting that the magnitudes are accurately recovered. This result implies that the photometry is not affected by the blending due to the overdensity. Even we only focus on faint ($m_i > 24.5$) objects, which can be more blended by other bright objects, they also follow the same trend (the right panel of Figure A.3).

As the same in Section 2.3.3, we construct a completeness function as a function of magnitude. Figure A.4 shows the ratio between these completeness functions and that at $z = 3.8$ estimated in Section 2.3.3. The ratio do not change around one up to 8σ. This suggests that the overdensity in the range of that of our protoclusters does not affect the completeness function.

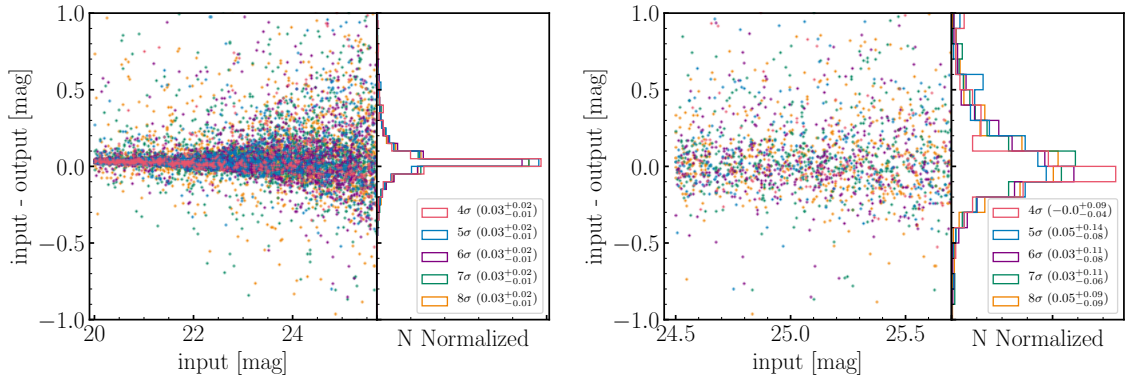

Figure A.3: Comparison of the input magnitude and the output magnitude of mock galaxies. Red, blue, purple, green, and yellow markers show cases in 4σ, 5σ, 6σ, 7σ, 8σ regions. The left panel plots all detected mock galaxies, and the right panel plots only faint galaxies with $m_i > 24.5$. In each panel, the median value and 16/84th percentile uncertainty is shown, and all of them is consistent, suggesting that the blending due to the overdensity does not affect the photometry.

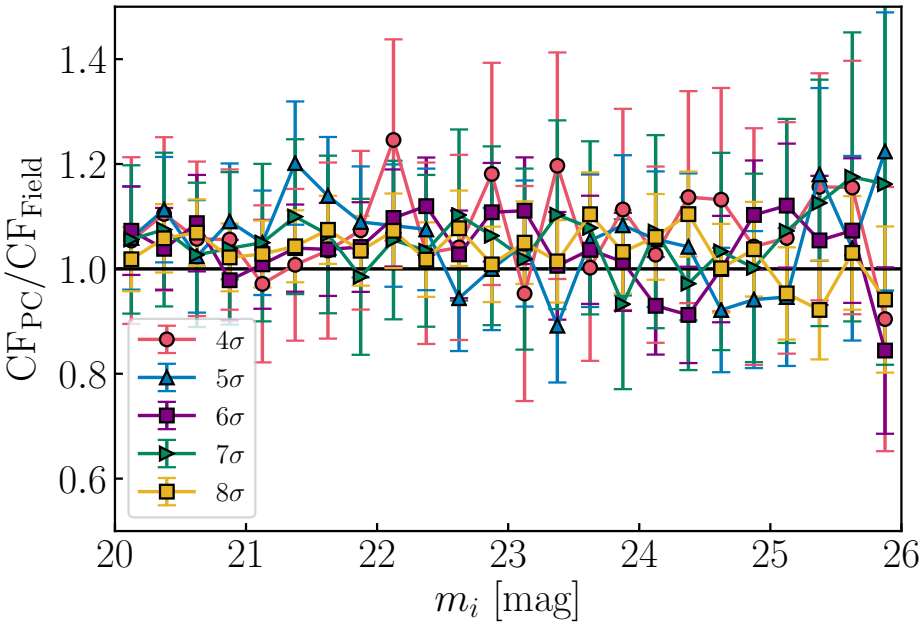

Figure A.4: Ratio of the completeness function in overdense regions to that in the blank field. Red, blue, purple, green, and yellow lines correspond to cases in 4σ, 5σ, 6σ, 7σ, 8σ regions, respectively. Error bars represent the Poisson error of the number of detected mock galaxies for each bins.

A.4 Quality assessment of size measurement by HSC-SSP image

We evaluate the quality of the size measurement based on HSC-images. Here, we conduct two tests. One is to compare the size measured by HSC images with those of Hubble Space Telescope (HST) images, which have better image resolution. The other is to measure the sizes of mock galaxies and compare it with the input effective radius. The former aims to confirm that the quality of the HSC size is consistent with those from HST, and the latter aims to determine how faint and how accurate we can measure sizes.

Firstly, we compare the size from HSC with those from HST. Here, a size measurement catalog of Griffith et al. (2012), which conduct the GALFIT fitting to the HST F814W image. Objects whose photo-z of Chapter 3 is $3 < z < 4.5$ are further discussed, which is the similar to the effective redshift distribution of g-dropout galaxies. Moreover, to mimic g-dropout galaxies, we restrict objects with $\log(M_\star/M_\odot) > 10.0$ classified as SFGs ($\mathrm{sSFR}_{1\sigma,\mathrm{lower}} > 10^{-9.5}\ \mathrm{yr}^{-1}$). Their size is measured from HSC images with the same method in Section 2.5.2. The same quality cut in Section 2.5.2 is applied to them. The measured size is compared with those of Griffith et al. (2012) in Figure A.5. You can see that the size from HSC correlates with those of HST and is consistent with them considering with their uncertainty. The mean offset ($b = \log(r_{e,\mathrm{output}}/r_{e,\mathrm{input}})$) is $b = 0.01$ dex and the scatter ($\sigma_{\mathrm{MAD}} = 1.48 \times \mathrm{median}(|\log(r_{e,\mathrm{output}}/r_{e,\mathrm{input}}) - \mathrm{median}(\log(\mathrm{r_{e,output}}/\mathrm{r_{e,input}}))|)$) is 0.1dex. These suggest that HSC can provide the fair size consistent with HST.

Secondly, we measured the size of mock galaxies. The quality of the size measurement is expected to be largely affected by the image quality, which differs from patch to patch. Therefore, the bias and scatter of the size measurement are estimated for all tract/patches in the HSC-SSP field. We insert mock galaxies and derive their size using the same method as described in Section 2.5.2. Mock galaxies are followed by the Sérsic profile, whose sérsic index is fixed as $n = 1.5$, and the axis ratio is random. Their effective radius and the magnitude is varied in the range of $0.02 < r_{\mathrm{e,major}} < 2$ and $22 < i\ \mathrm{mag} < 26$, respectively. Mock galaxies which are inside of mocked regions or overlapped with real objects are excluded for further discussion. Figure A.6 and Figure A.7 show the map of the offset and scatter of the size measurement for all mock galaxies in four regions of the HSC-SSP UltraDEEP/DEEP layer. Similar to the first

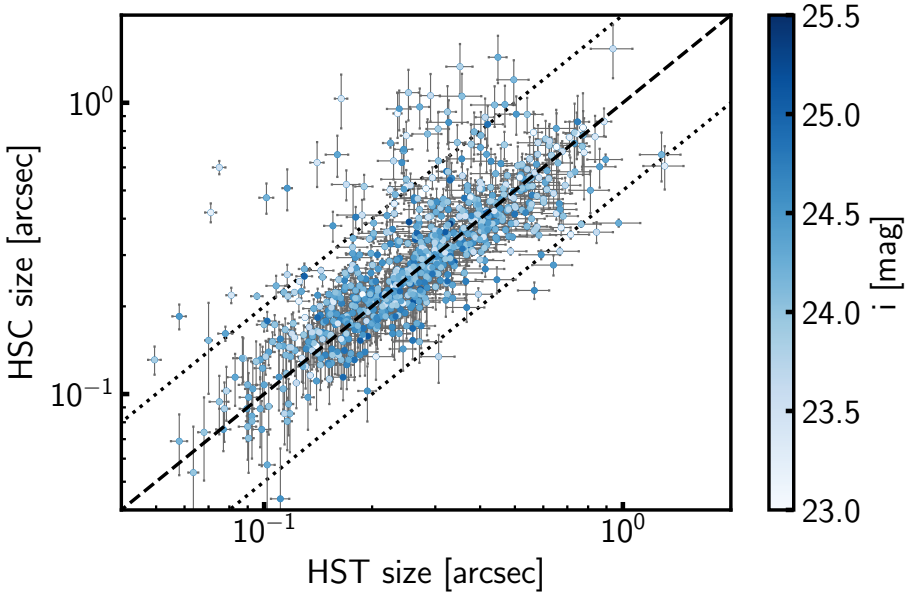

Figure A.5: Comparison of the size measurement between HSC and HST. The color represents the i band magnitude. The dashed line shows the one-to-one relation between the HSC size and HST size. Dotted lines show half and twice of HST sizes.

test, the offset is negligible (~ 0.015 dex on average), but the edge of pointings (i.e., shallower images) has a slightly larger value. Scatter is almost uniform ($\sigma_{\rm MAD} < 0.2$ dex), except for one pointing in the DEEP2-3 field. This pointing has worse depth and seeing, which might be a reason for the large scatter. We exclude these regions.

This mock simulation provides the offset and the scatter as a function of the output size and magnitude, which are shown in Figure A.8. Both the bias and the scatter are dependent on the magnitude. Especially, the scatter strongly increases towards a fainter magnitude and it reaches to 0.3dex for $0.2 < r_e[\mathrm{arcsec}] < 2$ objects, which are majority of $z \sim 4$ galaxies (c.f., Figure A.5). Based on these results, we only focus on galaxies with i mag < 25 to discuss their sizes. This criterion achieves the offset ≤ 0.05 dex and the scatter ≤ 0.2 dex. The offset is corrected for each galaxy by dividing its value estimated for each patch shown in Figure A.8.

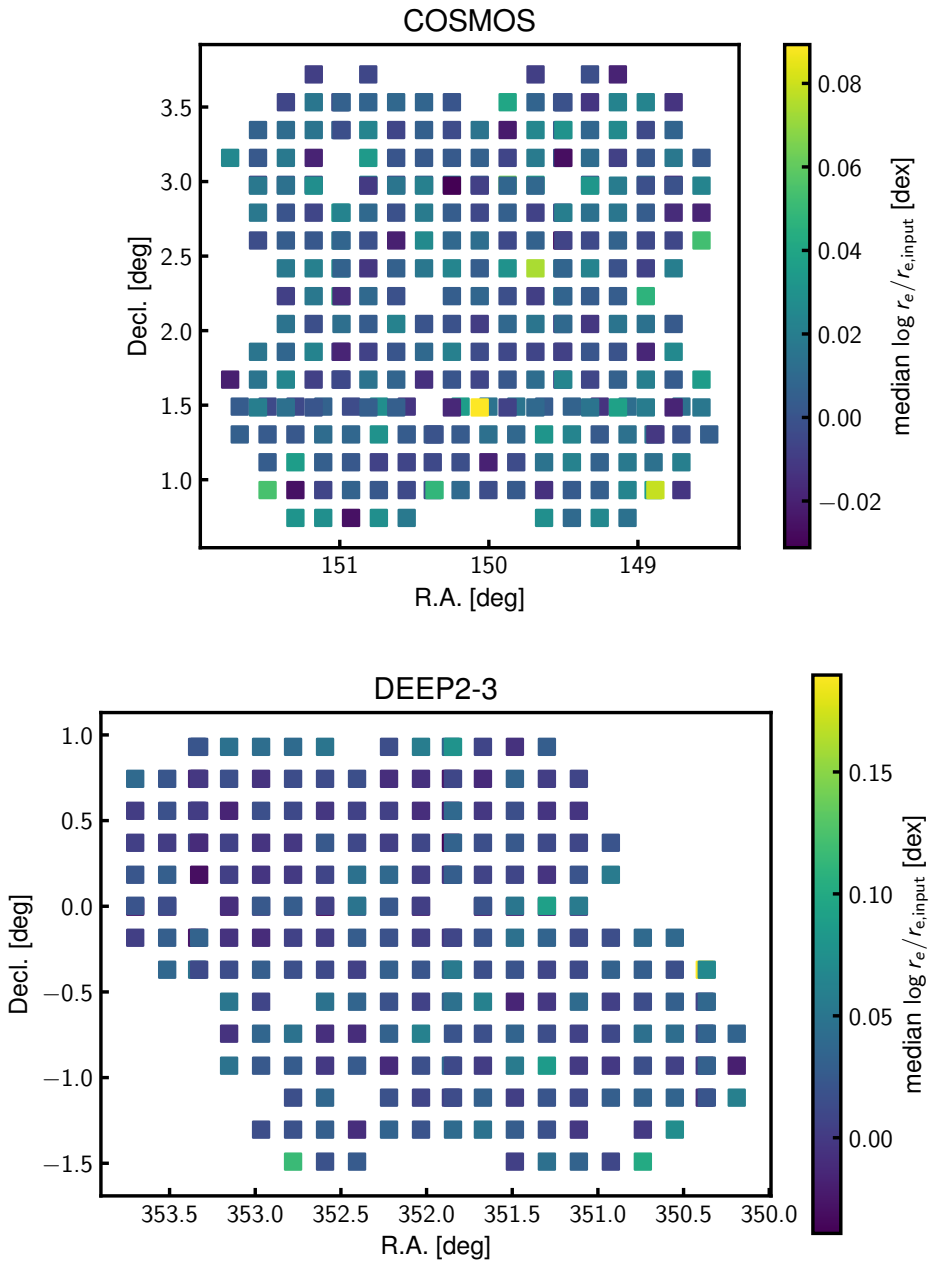

Figure A.6: Map of the bias of the size measurement for four fields of the HSC-SSP UltraDEEP/DEEP layer. Each marker corresponds each patch and its colors show the value of the median offset from the correct size. Some patches are missing because they are largely affected by the bright stars.

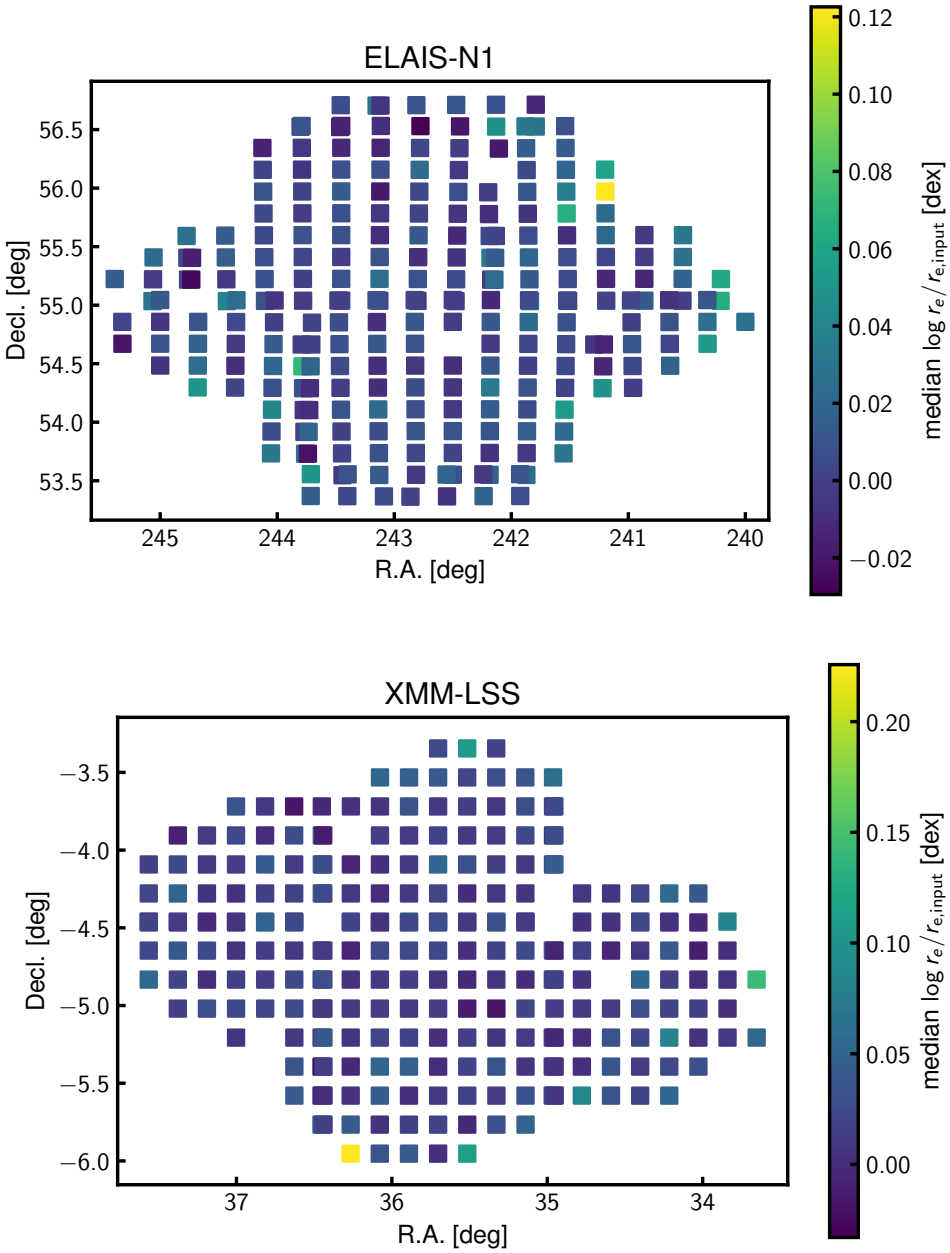

Figure A.6: (continued.)

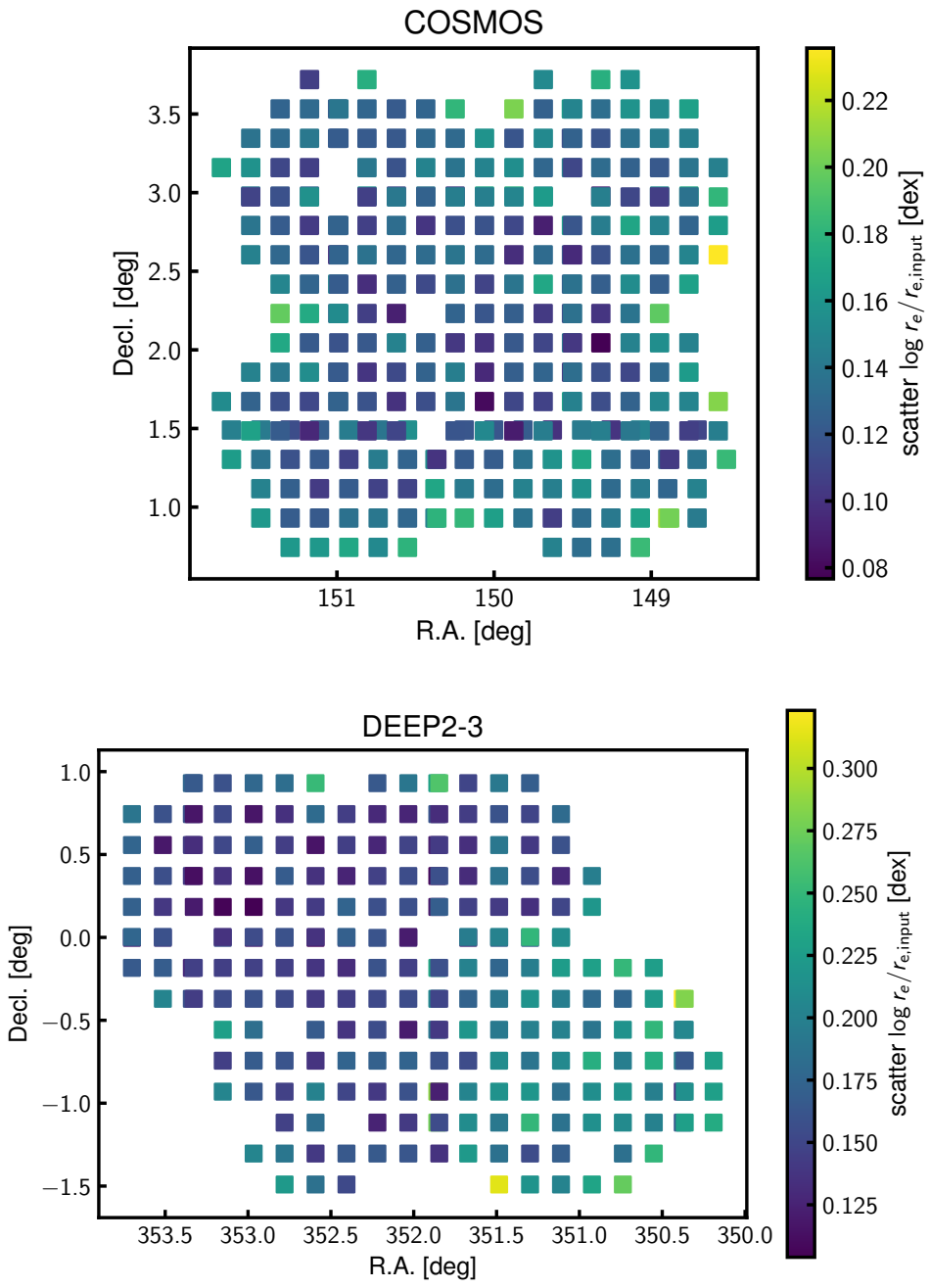

Figure A.7: Map of the bias of the size measurement for four fields of the HSC-SSP UltraDEEP/DEEP layer. Each marker corresponds each patch and its colors show the value of the median offset from the correct size. Some patches are missing because they are largely affected by the bright stars.

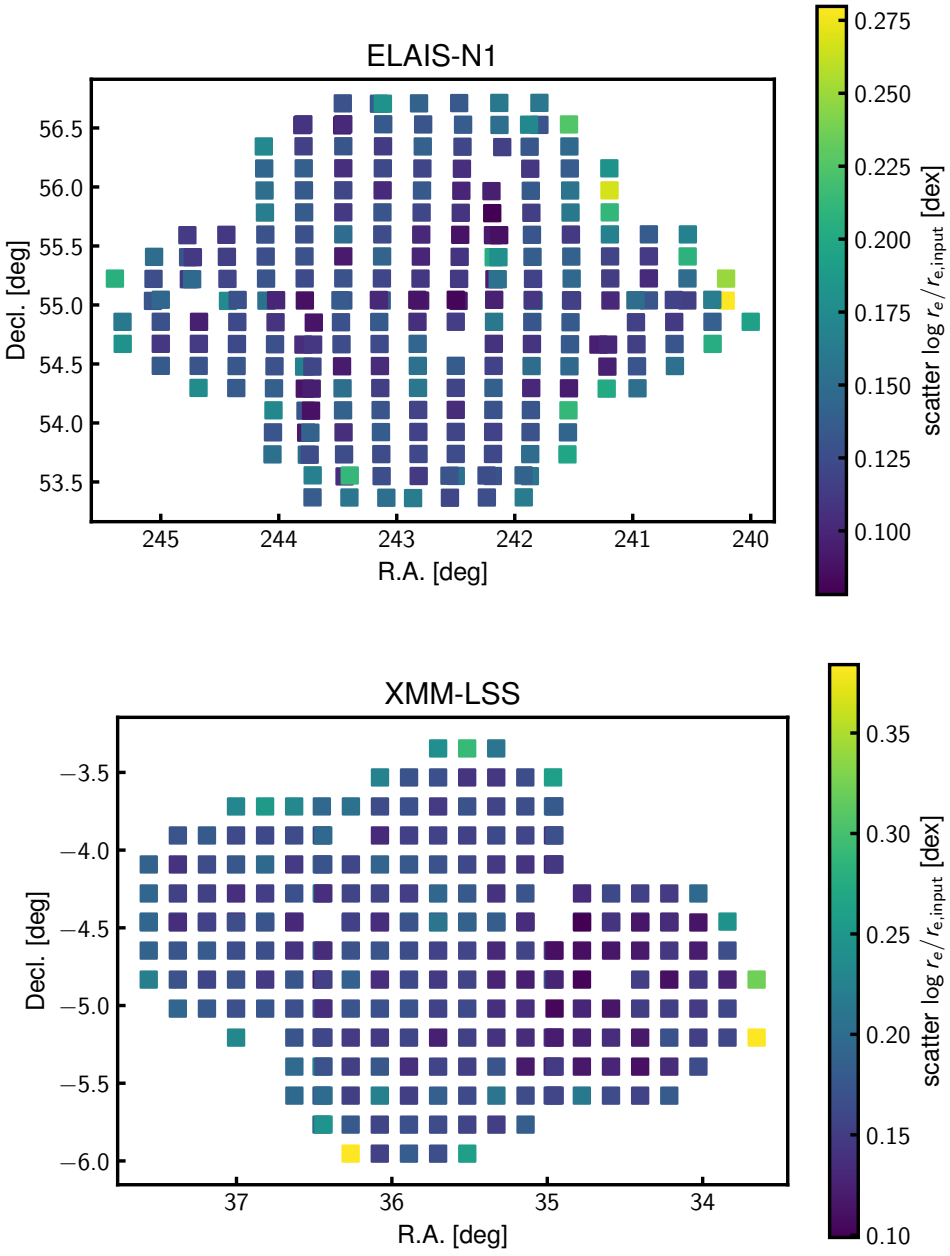

Figure A.7: (continued.)

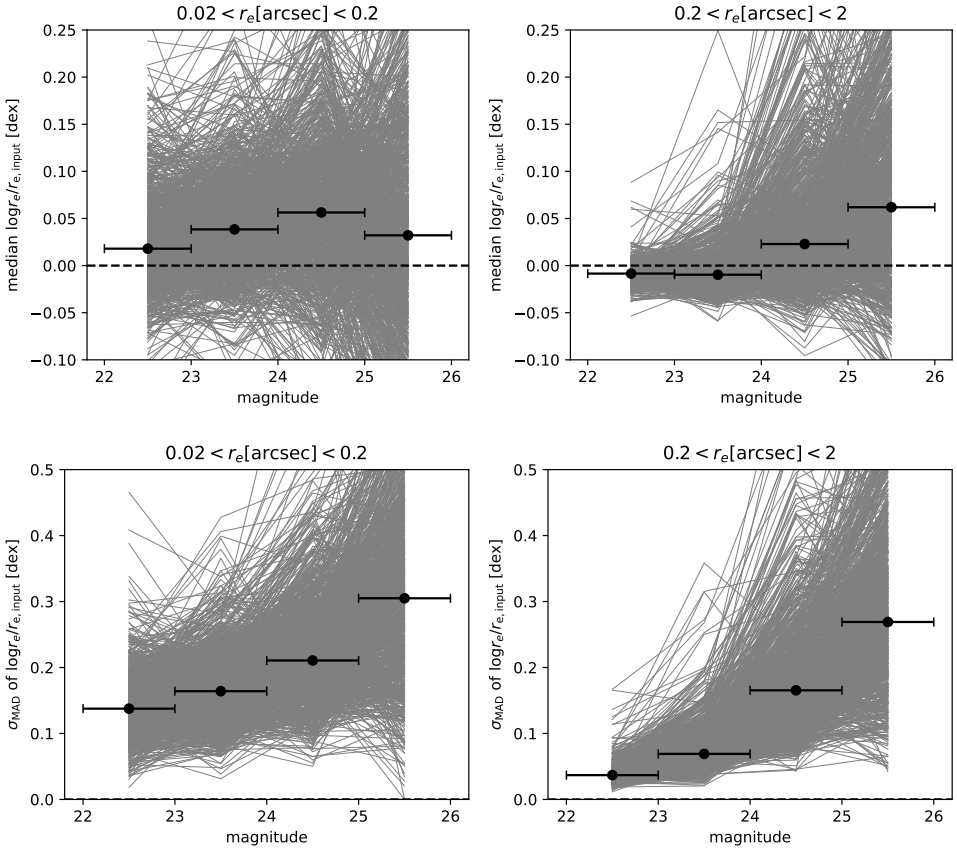

Figure A.8: Bias (top panel) and scatter (bottom panel) of HSC-SSP size as a function of the output size and observed magnitude. The gray lines represents the result for each patches and black marker show its average value for each 1 mag bin.

B

Appendix for Chapter 4

B.1 Impact of removing 24μm detected sources

Here, we show the result when we remove objects with $S/N > 4$ detection in MIPS 24μm (Le Floc'h et al., 2009) from the sample by allowing the separation of 2" (see Section 4.2). Figure B.1 and Figure B.2 show the AGN luminosity in the X-ray and radio as a function of redshift and stellar mass, which correspond to Figure 4.8 and Figure 4.13 of the original case, respectively. Their trend is the same, i.e., the AGN luminosity of QGs is higher than that of SFGs at $z > 1.5$. Therefore, we conclude that the 24μm detected sources do not affect the entire conclusion of this paper.

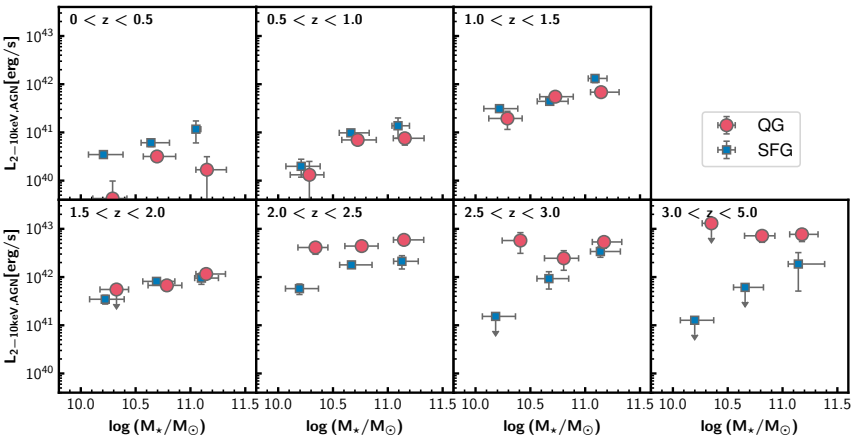

Figure B.1: The same for Figure 4.8, but in the case of excluding the 24μm detected sources of Le Floc'h et al. (2009).

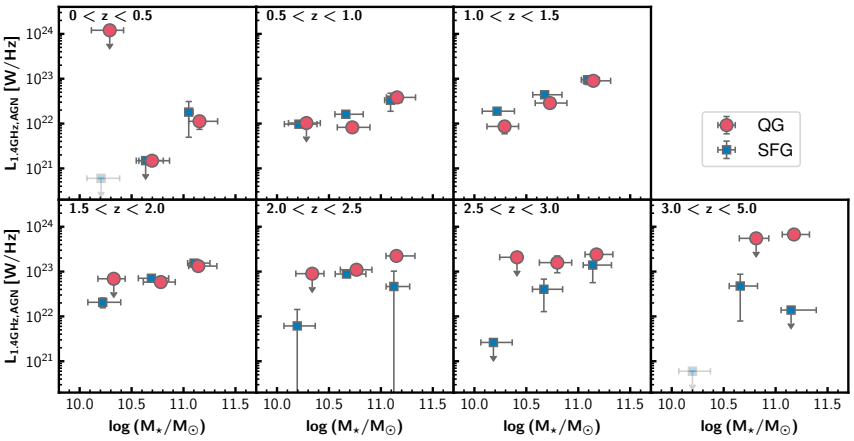

Figure B.2: The same for Figure 4.13, but in the case of excluding the 24μm detected sources of Le Floc'h et al. (2009).

B.2 Effect of different XRB scaling relations on X-ray AGN luminosity

In Section 4.3, we estimate the X-ray AGN luminosity from the observed X-ray luminosity by using the XRB scaling relation derived in Lehmer et al. (2016). As seen in Equation 4.2, this relation considers two terms, each proportional to the stellar mass and the SFR. On the other hand, there are other suggested function forms. Especially, Aird et al. (2017) and Fornasini et al. (2018) used the form which set the index of SFR free defined as follows:

$$L_{X,\mathrm{XRB}} = \alpha(1+z)^{\gamma} M_{\star} + \beta(1+z)^{\delta} \mathrm{SFR}^{\theta}. \tag{B.1}$$

In, Aird et al. (2017), the parameters are estimated as $\log \alpha = 28.81 \pm 0.08$, $\log \beta = 39.50 \pm 0.06$, $\gamma = 3.90 \pm 0.36$, $\delta = 0.67 \pm 0.31$, and $\theta = 0.86 \pm 0.05$. Also in Fornasini et al. (2018), the parameters are estimated as $\log \alpha = 29.98 \pm 0.12$, $\log \beta = 39.78 \pm 0.12$, $\gamma = 0.62 \pm 0.64$, $\delta < 0.2$, and $\theta = 0.84 \pm 0.08$. The difference of the method of these two studies is whether the luminosity corrects the intrinsic absorption and the sample selection, such as the redshift range. In addition, it should be noted that Fornasini et al. (2018) mentioned that we should consider the XRB luminosity derived by their best-fit value as the upper limit since their sample can contain low-luminosity AGN.

We here use these scaling relations and examine whether the picture obtained in Section 4.3.4 is changed. The AGN luminosity is derived in the same manner as in Section 4.3.4. Figure B.3 and Figure B.4 show the AGN luminosity in the case of the XRB scaling relation of Aird et al. (2017) and Fornasini et al. (2018), respectively. Though the exact value changes in both cases, but the overall trend does not change significantly. The AGN luminosity of QGs is generally higher than that of SFGs at $z > 1.5$ and their difference gets smaller at $z < 1.5$. This result suggests that the trend of the AGN luminosity is robust to the assumed XRB scaling relation.

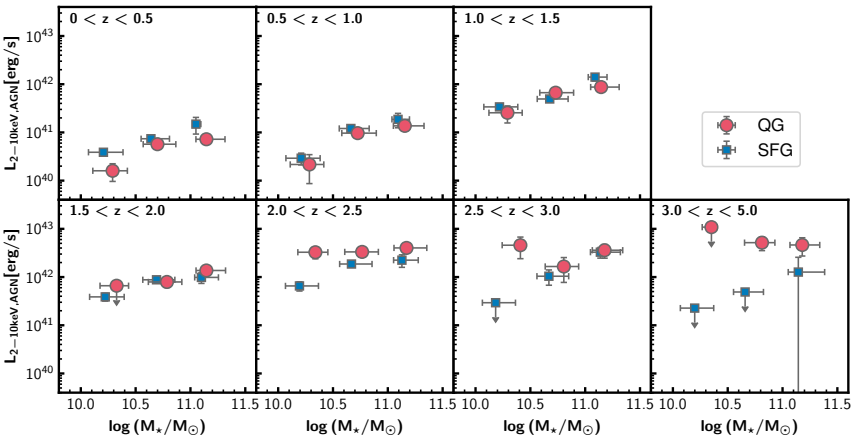

Figure B.3: The same for Figure 4.8, but in the case of using the XRB scaling relation in Aird et al. (2017).

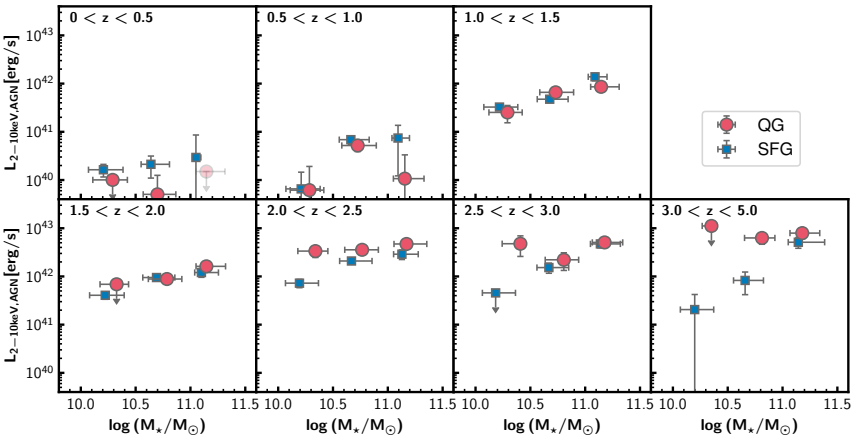

Figure B.4: The same for Figure 4.8, but in the case of using the XRB scaling relation in Fornasini et al. (2018)